UNIVERSITÀ DI PARMA

UNIVERSITÀ DEGLI STUDI DI PARMA

DOTTORATO DI RICERCA IN
Scienze del Farmaco, delle Biomolecole e dei Prodotti per la Salute

CICLO XXXIII

INHALATION DRUG PRODUCTS OF LOADED CALCIUM PHOSPHATE NANOPARTICLES FOR HEART TARGETING

Coordinatore:
Chiar.mo Prof. Marco Mor

Tutore Accademico:
Chiar.mo Prof. Fabio Sonvico

Tutore Aziendale:
Emerito Prof. Paolo Colombo

Dottorando: Eride Quarta

Anni Accademici 2017/2018 – 2019/2020

Table of Contents

List of Symbol and Abbreviations

α	Alfa
β	Beta
δ	Delta
ζ	Zeta
ABS	Acrylonitrile Butadiene Styrene machining
ACN	Acetonitrile
ACVI	Adenylate Cyclase VI
ANOVA	Analysis of Variance
API	Active Pharmaceutical Ingredient
ASD	Amorphous Solid Dispersion
AUC	Area Under the Curve
BBB	Blood-Brain Barrier
BSA	Bovine Serum Albumin
CaPs	Calcium Phosphate Nanoparticles
CF	Cystic Fibrosis
CFC	Coarse Fraction Collector
CFCs	Chlorofluorocarbons
CMA	Critical Material Attribute
COPD	Chronic Obstructive Pulmonary Disease
CPP	Critical Process Parameter
CQA	Critical Quality Attribute
CUPIDO	Cardio Ultraefficient nanoParticles for Inhalation of Drug prOducts
DAPI	4′,6-Diamidino-2-Phenylindole
DCCM-1	Defined Cell Culture Medium-1
DCFDA	2’,7'-Dichlorodihydrofluorescein Diacetate
DLS	Dynamic Light Scattering
DMF	Dimethylformamide
DMSO	Dimethyl Sulfoxide
DoE	Design of Experiments
dpCaPs	Dry Powder of Calcium Phosphate Nanoparticles
DPI	Dry Powder Inhaler
DSC	Differential Scanning Calorimetry
DUSA	Dosage Unit Sampling Apparatus
ED	Emitted Dose
EDTA	Ethylenediaminetetraacetic Acid
EF	Emitted Fraction
ELISA	Enzyme-Linked Immunosorbent Assays

EMA	European Medicines Agency
EPAC	Exchange Protein Activated by cAMP
FBS	Fetal Bovine Serum
FDA	Food and Drug Administration
FFC	Fine Fraction Collector
FI	Interaction Factor
FIB	Focused Ion Beam
FPD	Fine Particle Dose
FPF	Fine Particle Fraction
FSI	Fast Screening Impactor
FT-IR	Fourier Transform Infra-Red Spectrometry
GSD	Geometric Standard Deviation
HBSS	Hanks' Balanced Salt Solution
HFrEf	Heart Failure with Reduced Ejection Fraction
ICH	International Council for Harmonization of Technical Requirements for Pharmaceuticals for Human Use
ICP-OES	Inductively Coupled Plasma Optical Emission Spectroscopy
IFR	Inspiratory Flow Rate
ISO	International Organization for Standardization
HFAs	Hydrofluoroalkanes
HPMC	Hydroxypropylmethyl Cellulose
HPLC	High Pressure Liquid Chromatography
LOD	Limit of Detection
LOQ	Limit of Quantification
LPN	Lipid Nanoparticles
LPS	Lipopolysaccharide
LTCC	L-type Calcium channel
MD	Metered Dose
MDI	Metered Dose Inhaler
MMAD	Mass Median Aerodynamic Diameter
MOC	Micro-orifice Collector
MP	Mimetic Peptide
MRN	Milrinone
MTT	3-(4,5-Dimethylthiazol-2-yl)-2,5-Diphenyltetrazolium Bromide
MWCO	Molecular Weight Cut-Off
NCS	Newborn Calf Serum
NGI	Next Generation Impactor
NPs	Nanoparticles
NTA	Nanoparticle Tracking Analysis
PAH	Pulmonary Arterial Hypertension

PALS	Phase Analysis Light Scattering
PBS	Phosphate Buffered Saline
PD	Pharmacodynamic
PdI	Polydispersity Index
PET	Polyestere Membrane
Ph.Eur.	European Pharmacopoeia
PK	Pharmacokinetic
PKA	Protein Kinase A
PLGA	Polylactic-co-glycolic Acid
PMA	Phorbol Myristate Acetate
pMDI	Pressurized Metered Dose Inhaler
PP	Polypropylene
PSD	Particle Size Distribution
PSG	Penicillin/Streptomycin/Glutamine
PXRD	X-ray Powder Diffraction
QbD	Quality by Design
QbT	Quality by Testing
QRM	Quality Risk Management
QTPP	Quality Target Product Profile
RES	Reticuloendothelial System
RFU	Relative Fluorescent Intensity
ROS	Reactive Oxygen Species
RSD	Relative Standard Deviation
RSM	Response Surface Methodology
RWC	Residual Water Content
SAED	Selected Area Electron Diffraction
SD	Standard Deviation
SEM	Scanning Electron Microscopy
SLA	Stereo Lithography Apparatus
SPC	Statistical Process Control
SQC	Statistical Quality Control
TEM	Transmission Electron Microscopy
TFA	Trifluoroacetic Acid
TGA	Thermogravimetric Analysis
TMB	3,3′,5,5′-Tetramethylbenzidine
TNF	Tumor Necrosis Factor
USP	United States Pharmacopoeia
XRD	X-Ray Diffraction
ZOL	Zoledronic Acid

Abstract

The aim of this work was to pharmaceutically develop an innovative nanomedicine consisting in highly respirable microparticulate dry powder (dpCaPs) able to embed and release Calcium Phosphate nanoparticles (CaPs) loaded with mimetic peptide or microRNA to restore the cardiac function. The microparticles, embedding therapeutic nanoparticles delivered by inhalation in deep lung, release the CaPs by carrier dissolution and target the heart by translocation to pulmonary vein blood.

Spray drying technique transformed the nanoparticle dispersion in inhalable microparticles. Mannitol, as water soluble carrier, was used for microparticle construction. A DoE was applied for understanding the effect of the composition and process parameters on selected quality attributes of dpCaPs. *In vitro* respirability was performed using the novel medium resistance Nemera prototype device. The DoE study revealed that the powder having the ratio CaPs/mannitol 1:4 exhibited the best aerodynamic performance for lung deposition and CaP release. The emitted dose was >85%, the FPF >80%. Microparticles had a spherical shape, rough surface and low density. The high fraction (*i.e.* 50%) of extra-fine particles (< 2µm) promotes the CaP deep lung deposition at alveolar region and translocation to the heart. The CaP nanoparticles and microparticles were successfully produced at pilot scale.

In vitro evaluation found that dpCaPs were not toxic for human lung alveolar epithelial cells and macrophages and did not induce cytokine release. The microparticles embedding loaded CaPs tested on murine HL-1 cardiac cells allowed the peptide internalization in the myocytes with a dose dependent mechanism. Finally, the dpCaPs pulmonary *in vivo* administered to diseased mini pigs were able to restore the normal heart contractility.

1 Introduction

1.1 Advantages and challenges of pulmonary route

Pulmonary drug delivery is not limited to the treatment of respiratory diseases but presents a number of positive features extremely useful for the therapy of several systemic diseases, in many cases overcoming in terms of efficacy and safety other classic routes of administration such as oral, parenteral or subcutaneous[1]. These features arise mostly from the particular anatomical and physiological characteristics of the lung.

First and foremost, lungs feature a huge surface area of around 100 m^2 and a relatively pervious barrier to drug absorption. Namely, the respiratory architecture presents at the alveolar region a biological barrier constituted only by an epithelial and an endothelial cell layer. These characteristics providing an ideal location for the deposition and especially the absorption of aerosolized formulations[2]. Additionally, in terms of metabolism drugs are exposed to much more favourable conditions compared to oral administration. The first-pass liver metabolism is avoided as well as the catabolic enzymes of the intestine[3]. Especially in the case of topically delivered drugs, a lower dose can be administered due to the direct delivery of the active substance to the site of action, leading to fewer systemic adverse effects and, in some cases to a rapid onset of action. As far as systemically administered drugs are concerned, delivery via the lungs is available for a large number of molecules from small ones to large proteins. The pulmonary route of administration is less invasive than parenteral administration and it could be a desirable alternative for patients when drugs are being administered only intravenously. Thus, systemic administration of peptides, antibiotics, vaccines, anti-cancer substances or other drugs via the lung is favoured and is expected to broaden the inhalation medicinal products market considerably in the near future[4]. Another secondary but notable advantage of pulmonary route is that, differently from oral administration, it is independent from food intake and metabolic interpatient variability, providing more stable absorption kinetics[5].

Despite the aforementioned advantages, it is surprising that only very few systemically acting inhaled drugs have been marketed so far. On the contrary, pulmonary drug delivery is typically used for the treatment of chronic respiratory diseases, such as asthma, chronic obstructive pulmonary disease (COPD) and orphan diseases, such as pulmonary arterial hypertension (PAH) and cystic fibrosis (CF). Significant challenges emerge from the lung physiology and pathology together the complexity during the inhalation product development. In fact, an

inhaled product needs to satisfy plenty of requirements in terms of formulation and device design.

Furthermore, as well as other parts of our organism, the lung has evolved to prevent the invasion of undesired airborne particles in the body. The geometry of airway, humidity and clearance mechanisms contribute to this elimination process. Once deposited on the airways surface, the fate of the particles will depend on their solubility and the landing site. After the inhalation, the particles can be dissolved in lung fluid, acting locally or passing into the systemic system as well as can be translocated out of the respiratory tract when insoluble. The mucus and surfactant that lines the pulmonary epithelium (1.0-10.0 μm thick) and alveoli (0.1-0-2 μm thick), respectively, constitute physical barriers to pulmonary adsorption of drugs. The mucus movement rate is determined by the number of ciliated cells and their beat frequency. For insoluble matter, clearance is governed mainly by mechanical removal of particles via phagocytosis by alveolar macrophages and mucociliary transport. Moreover, in cases of respiratory diseases such as inflammations, CF or COPD alterations in airways lead to poor aerosol deposition and penetration[6].

Dose uniformity and reproducibility, patient's compliance, proper use of inhalers, differences in breathing patterns are some of the major problems that need to be addressed in order to assure therapeutic effectiveness of aerosolized medications.

Although not without barriers, as briefly above described, the lung is a very desirable target for drug delivery. Airway geometry, humidity, clearance mechanism and the presence of lung disease influence the deposition of an aerosol and therefore the therapeutic effectiveness of inhaled medications.

1.1.1 Aerosols deposition and drug absorption in the lungs

Inhalation therapies, either for topical or systemic diseases, are characterized by the fact that only a fraction of the inhaled dose reaches the target area, mainly due to deposition issues. Mechanisms that determine the conduction and deposition of aerosols in the respiratory tract have been a subject of study for more than 50 years and their understanding is a key aspect in developing inhaled products capable of delivering the required dose of active substance to the patient[7]. Deposition indeed can be influenced by several factors ranging from aerosol properties such as particle size, shape, density and surface energy, to physiological factors, such as interpatient differences related to airways geometry, pulmonary conditions and breathing patterns, in terms of frequency, tidal volume and breath-holding[8].

In terms of particle properties, size is the main parameter for the successful delivery of an aerosol in a specific region of the lungs. At this point it is important to note that in the case of aerosol deposition, we care for the aerodynamic particle size expressed as aerodynamic diameter (d_{ae}) which is the indicator of how the particle sediment in a fluid. It is an important factor for the evaluation of *in vivo* performance of particles to dissolve in the lung fluids. Aerodynamic diameter is given by Equation 1,

$$d_{ae} = d_v \sqrt{\frac{\rho}{\rho_0 \cdot \chi}} \quad (1)$$

where d_v is the equivalent volume diameter, ρ is the particle density, ρ_0 is the unit density, and χ is the dynamic shape factor. The aerodynamic diameter of a particle is the diameter of an equivalent sphere, whose density (ρ_0) is 1 $g \cdot cm^{-3}$, which settles in still air at the same velocity as the particle in question[9].

Considering Equation 1 it is easy to understand that particles with a lower density and geometric size have a smaller aerodynamic diameter, hence a deeper lung deposition. At the same time, an increase in dynamic shape factor leads to a smaller aerodynamic diameter. The dynamic shape factor is the ratio of the resistance force experienced by the actual non-spherical falling particle, to the resistance force experienced by a sphere having the same volume. It can be determined either experimentally or using complex models[10]. For instance, non-spherical particles such as cube-shaped, needle-shaped and plate-shaped have a higher dynamic shape factor (χ) compared to spherical particles, leading to a smaller aerodynamic diameter. Nevertheless, in some cases, such as needle-shaped particles, deviations from sphericity result in large contact areas hence stronger inter-particulate forces that lead to poor powder flowability[11]. Ultimately, surface energy of the particles is a parameter affecting aerosol performance. High surface energy typical smooth surfaces increase particle interactions thus leading to poor flow properties due to higher cohesiveness between particles. As a result, efforts are being done in order to reduce surface energy by producing particles with a rougher surface[12].

Due to the gradual reduction of the airways diameter in the respiratory tract, a deposition dependent on the aerodynamic particle size could be observed: 30–70 μm particles deposit in the nasal cavity, 20–30 μm in the pharynx, 10–20 μm in the larynx, 8–10 μm in the trachea, 5–8 μm in the bronchi, 3–5 μm in the bronchioles, and 0.5–3 μm in the alveoli[13]. In general, particles with a mean aerodynamic diameter between 1-5 μm are considered suitable for

pulmonary administration[9]. It is essential to clarify that, depending on the target location, different particle size and hence a different deposition is desired. For instance, salbutamol, an extensively used bronchodilator for the treatment of asthma, has an agonistic effect on β2-adrenergic receptors on the surface of smooth muscle cells in the lungs and not present in the alveolar region. Thus, in order to achieve a more efficient deposition for salbutamol, a mean particle size of 3 μm is preferred over one of 1.5 μm that reaches in a higher percentage the alveolar region.

Particle deposition in lungs is governed by the mechanisms of inertial impaction, gravitational sedimentation, Brownian diffusion, and, to a lesser extent, by electrostatic precipitation or interception Figure 1.1.

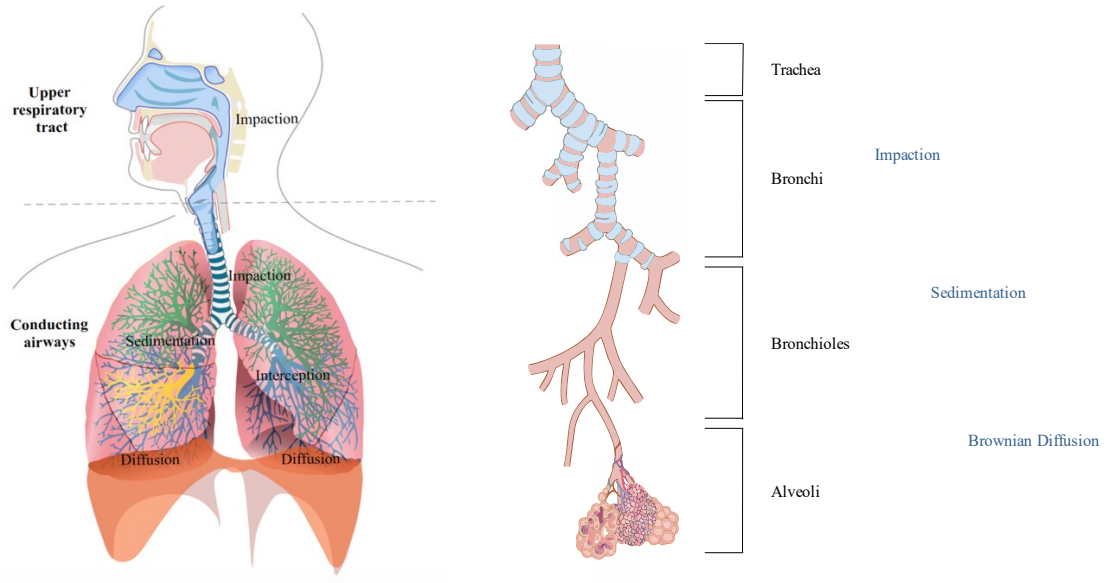

Figure 1.1 Mechanisms of particle deposition in the respiratory tract: inertial impaction, sedimentation and diffusion. Creative Commons "Respiratory system complete no labels.svg " by Bibi Saint-Pol, Jmarchn, used under CC BY-SA 3.0/Added labels.

The first and predominant mechanism, as particles flow through the primary airways of the upper respiratory tract, is inertial impaction. In this case, some particles fail to follow the airflow when sudden changes of flow direction occur, colliding with airway walls because of their high momentum. These effects usually happen in the first ten generations of the tracheobronchial tree, where airflow is turbulent and fast and applies to particles larger than 10 μm[14]. The deposition efficiency is function of the Stokes Number (Stk) given by Equation 2,

$$Stk = \frac{d_{ae}^2 Q C_c}{9\eta D} \quad (2)$$

where d_{ae} is the aerodynamic particle diameter, Q is the volumetric air flow rate, Cc is the Cunningham correction factor, η is the viscosity of air, and D is the characteristic dimension of the obstacle (typically its diameter). The product $d_{ae}^2 \cdot Q$ ($\mu m^2 \cdot L \cdot min^{-1}$) is referred to as the 'inertial impaction parameter'[15]. The higher the Stokes number is, the more readily particles will be deposited by inertial impaction.

Moving deeper in the respiratory tract a second mechanism of particle deposition may occur. Sedimentation is the gravitational settling of particles and mainly affects particles in the size range between 0.1 and 8 μm[16]. Particles that escape inertial impaction in the upper airways are characterized by a velocity of sedimentation that is proportional to their size. This size, called terminal settling velocity (V_s) derives from Stoke's drag force and is given by Equation 3,

$$V_s = \frac{(\rho_0 - \rho_\alpha) d_a^2 g}{18\eta} \quad (3)$$

where ρ_0 and ρ_α are the densities of particles and air respectively, d_{ae} is the aerodynamic diameter, g is the gravitational acceleration and η is viscosity of air. This equation is applied for particles with a Reynolds number (R_e) lower than 0.1 since for values close to 1, Stoke's law collapses due to the increase of air inertia[17]. Reynolds number is given by Equation 4,

$$R_e = \frac{\rho_\alpha d U_o}{\eta} \quad (4)$$

where ρ_α is the density of air, *d* is the particle diameter and U_0 is the air velocity and basically, expresses the ratio between air inertia and viscosity (η)[18].

It is important to note that breathing manoeuvres, such as breath holding, tend to favour sedimentation especially for small particles that need more time in order to settle on the walls of airways. Such strategies are applied in cases that a specific site of deposition in the respiratory tract is desired[19].

For particles smaller than 0.5 μm, Brownian diffusion is the primary mechanism of deposition; it refers to the random motion of particles (Brownian motion) in locations such as the alveolar region, where air velocity is practically zero. Brownian diffusion is characterized by the diffusion coefficient (D_{if}) that is given by the Stokes-Einstein equation (Equation 5),

$$D_{if} = \frac{kT}{3\pi\eta d_{ae}} \quad (5)$$

where k is the Boltzmann's constant, T is the absolute temperature, η is the viscosity of air and d_{ae} is the aerodynamic particle diameter. Particles with such a small diameter rarely manage to deposit and usually, come out of the body via exhalation[20] (Figure 1.2).

As far as interception phenomenon is concerned, this primarily refers to elongated particles such as fiber with dimension comparable with the airway diameter. Furthermore, electrostatic precipitation is likely to occur for particles that carry electrostatic charges during the generation and transport of the aerosol. Aerosol charge status is affected by many variables including formulation and materials used in the devices. Depending on the amount of electrostatic charges that are produced, deposition may be affected accordingly. In general, electrostatic effects, tend to enhance particle deposition only if the number of charges on particles is sufficient. Finally, as mentioned before, although it cannot be seen as a mechanism of deposition, the high humidity of air present in lungs may promote aggregation leading to large particles with a different deposition profile compared to the original particles[7].

Once deposited in alveolar region, drugs encounter a variety of physicochemical and biological barriers. These include pulmonary lung surfactant, *i.e.* a surface lining fluid that acts as a reservoir for lung surfactant, alveolar epithelium, the extracellular space inside tissues (interstitial and basement membrane) and the vascular endothelium along with the catabolic enzymes in the tracheobronchial region. In addition, macrophages in the alveolar region that threaten the drug absorption[21,22].

In order to cross the cellular barriers, the particles must firstly dissolve and then the drug can reach the blood stream following mainly two mechanisms depending on its physicochemical properties. Namely, the mechanisms are the transcytosis (through the cells) either passively or actively (carrier-mediated) and the paracellular transport (through the cell junctions). For instance, small lipid-soluble molecules are rapidly absorbed because they can easily enter the phospholipid bilayer surrounding the cells, while hydrophilic molecules pass through aqueous pores in the intercellular tight junctions. Ionization degree and molecular weight seem to determine the rate at which molecules can pass through these pores. Thus, for molecules from 100-1000 Da, ionization degree prevails. The less ionized a molecule, the faster is absorption rate, because of fewer interactions with the pore constituents, whereas for larger molecules, molecular weight becomes an influential factor, too[23].

In the case of macromolecules, such as peptides and proteins, pulmonary route has shown to offer higher bioavailability, as long as protection from peptidases. Furthermore, the lung possesses a large surface area and an extensive vascular network for adsorption. However, the

macromolecule absorption rate is mainly dictated by size- the larger the size the slower the absorption[24]. For these reasons the lungs are an attractive route for peptide administration.

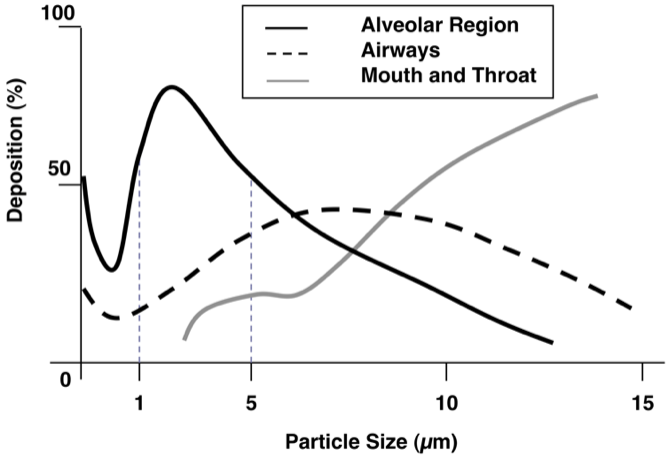

Figure 1.2 Particles mass fractional deposition into the lungs as an aerodynamic diameter function, assuming that particles are spherical with unit density. Adapted by permission from Springer Nature Customer Service Centre GmbH, Springer Nature, Nature Reviews Drug Discovery, Inhaling medicines: delivering drugs to the body through the lungs[25], Copyright® 2017.

1.2 Dry powder inhalers (DPIs)

1.2.1 Features and devices

According to EMA, dry powder inhalers (DPIs) are inhalation delivery systems consisting of a dry powder formulation and a container closure system capable of delivering drugs in the lungs for the treatment of topical or systemic diseases[26]. There is a wide range of device types on the market, but the basic components of a DPI are: powder formulation, dose measuring system and mouthpiece.

They feature plenty of positive characteristics such as high lung deposition, consistent and precise dose, independence from hand-to-breath coordination, durability to microbial contamination, high chemical stability of drug, absence of propellants, simple inhalation technique and portability[27]. Conversely, as formulations are in form of dry powder, they are sensitive to moisture, and there is a strong dependence between the airflow generated by the patient and the aerosol performance. If the airflow is not the appropriate, the user, such in the

case of children below five-year-old or patients with low inhalation capacity, de-aggregation of formulation to fine particles for lung deposition may not occur[28].

In regard to the relationship of the inhalation effort with the aerosol generation, this is also affected by an intrinsic property of the device, called device resistance ($kPa^{1/2}\cdot L\cdot min^{-1}$) that differs from one device to another, in reason of the different manufacturing design (turbulent shear zones, whirl and circulation chambers). The higher the air resistance of the device is, the lower the inspiratory flow rate (IFR) that the patient can apply is. United States Pharmacopoeia (USP) suggests to determine the air resistance by measuring at which air flow the device produces a pressure drop of 4kPa. According to that measurement DPIs are classified as: high resistance (~30 L/min), medium resistance (~60 L/min) and low resistance (~90 L/min). Low resistance DPIs work on a broad range of in IFRs (50-100 L/min) to produce pressure drop of 2-4 kPa, instead of high resistance DPIs work with lower inspiratory flow rates (30-40 L/min), and thus are appropriate for more types of patients. However, high IFRs can lead to high oropharyngeal deposition, due to impaction and that may also jeopardize the performance of high resistance DPIs, if IFR exceeds the optimum[29].

There are two main classifications for the DPIs, namely the dosing system and the aerosolization mechanism. The former include *pre-metered DPIs* in which previously metered amounts of drug formulation are loaded and *device-metered DPIs* in which there is a reservoir containing multiple doses of formulation that are metered by a dose-metering system. *Pre-metered DPIs* may be single-dose (a capsule loaded either by the patient before use) or multi-dose using replaceable blisters, cartridges or dosing discs[28]. The classification based on the aerosolization mechanism include *passive* and *active* devices. *Passive* devices were the first developed DPIs and are breath-actuated, meaning that they require inspiration effort by the patient in order to initiate the deagglomeration process and extract the dose from the device. Limitation of such devices was mentioned before and is that patient with insufficient inhalation capacity may not extract the entire dose, reducing therapeutic effect. Conversely, *active* devices use either a battery-operated propeller or pressurized air that is mechanically decompressed in order to induce powder dispersion. These devices don't depend on patient's inspiration capacity and are dose consistent. Nevertheless, passive devices still prevail in the market as no active DPI is currently marketed as they are expensive, bulky and require many operational steps[30].

1.2.2 Dry powder formulations

A DPI must always be considered as a combination of the device and the drug formulation. Interpreting these two components as a single entity, during development along with the proper

use by the patient, ensures the effective delivery of active substance (API) at the site of action and, thus, its therapeutic effectiveness. There is a wide variety of APIs that are in use for the treatment of chronic respiratory diseases, like asthma, COPD, (β2-agonists, corticosteroids), cystic fibrosis, lung infections (antibiotics, antifungals) or have been proposed to treat systemic diseases like migraine (triptans), pulmonary arterial hypertension (sildenafil) or to induce analgesia (morphine) and anaesthesia. They, also, vary in molecular weight, solubility, hydrophobicity, crystallinity and other physicochemical properties resulting in different formulation and particle engineering strategies[31].

During development of a DPI many parameters need to be taken into account. Drug formulation is one of the most critical and serves undoubtedly as a starting point of the development. First of all, it is important to remember that drug particles for an efficient lung deposition must have a size between 1-5 μm. However, powders with such a small particle size are strongly cohesive due to inter-particulate forces (van der Waals, electrostatic) or to capillary condensation that derives from the presence of moisture. Thus, particles form large agglomerates that may be difficult to de-aggregate to fine particles during aerosolization[32]. Moreover, as mentioned earlier, pulmonary drug delivery gives the opportunity of using lower doses than oral route and thus making it difficult to meter the dose and manipulate the bulk powder[33]. In order to resolve issues like these several formulation strategies are applied namely *carrier-based* formulations and *carrier-free* formulations[34].

1.2.3 Particle engineering

Dry powder formulations are generally simple in terms of ingredients due to the limited number of excipients allowed for inhalation delivery as lung safety justification must be provided in depth. In order to compensate for this restriction in excipient use, sophisticated “lean” dry powder formulations must be developed with particles capable of combining fine size, narrow size distribution, low surface energy and density. In addition, enhanced drug stability, high bioavailability, precise targeting and/or sustained release[35] are sought. This activity is called “particle engineering” and is one of the biggest challenges concerning DPI development. According to the drug properties and the delivery target, different methods may be used to obtain fine respirable particles with the aforementioned properties.

Milling is the classical technique used for particle micronization and is widely used. With the term milling we encompass a number of so-called top-down techniques used to mechanically grind large drug crystals into particles within a respirable size range[36]. The particle size

reduction can be achieved by pressure, friction, attrition, impact or shear. The three main types of mills are fluid-energy mills, such as the jet mill that uses high-pressure air to accelerate particles that collide each other and break; high-peripheral-speed mills, such as the pin-mill that uses a series of concentrically mounted pins on which particles impact due to centrifugal forces in the milling chamber and the ball mill that uses spheres of extremely hard materials as "milling media" that break down the particles due to friction[37].

Jet milling is the most common method as it is industrially well-established, and it is able to provide particles between 1-15 μm with a narrow particle size distribution. The milling apparatus is easy to use, inexpensive and during operation little to no contamination in the final powder occurs. However, jet milling presents difficulties in controlling the size, shape and morphology of particles[38]. Dry conditions combined with mechanical forces lead to the development electrostatic forces and local distortions of the crystal lattice (amorphization) which leads to agglomeration and thus, poor flowability and dispersibility of the powder[36]. Partial amorphization results in powders with regions that possess different physicochemical properties (solubility, thermodynamic stability) than the original particles. A solution to partial amorphization is to process the particles in presence of increased humidity (30-70%), called *wet milling*. Because of the partial solubility of the drug in moisture, any amorphous regions will undergo recrystallization and thus, drug particles are expected to present higher crystallinity[39].

The inverse manufacturing approach is provided by the bottom-up techniques. Contrary to top-down methods, these techniques can control not only the size distribution, but also the particle shape and (surface) morphology. The basic difference is that the particles are built up (grow in size) by dissolving or suspending the drug in various solvents (water, ethanol, o/w or w/o emulsions) and then, recovered by solvent evaporation or anti-solvent precipitation[34]. Apart from spray drying that will be analysed in depth in the next section, spray freeze drying, and supercritical fluid technology are the most commonly used bottom-up techniques.

1.3 Spray drying

1.3.1 Concept and hardware

Spray drying as mentioned in the previous section is one of the bottom-up techniques that is widely used to prepare fine or even ultra-fine particles with desirable characteristics. The spray

drying process allows the production of dry powders by spraying a feed solution in which the drug is dissolved or dispersed, by mean of a hot gas (usually air). After solvent evaporation the produced ultra-fine powder is collected[40].

More specifically, the process starts with the atomization of the feed solution by an appropriate device (atomizer, nozzle). The produced droplets are propelled into a drying chamber where interact with a heated gas at a high temperature selected according to the desired particle properties. As the droplets are exposed to the hot gas, solvent evaporates and solid product particles are obtained. Finally, air is aspirated and particles, separated by collection systems (cyclone, filter bag, scrubber), are collected[41]. Thus, the basic components of a spray drying apparatus are the drying chamber, atomizer, aspirator and collection cyclone (Figure 1.3). Depending on the solvent (organic/aqueous) different modifications may be done. *Open-cycle systems* are applied to dry aqueous feed solutions while *closed-cycle* systems with the use of nitrogen as a drying gas, are applied in order to avoid release of organic solvents into the environment, decrease the risk of explosion and the chance of product oxidation or recover solvents for reuse. The latter is based on the recycling of the inert gas and the condensation of the organic solvent through a condenser.

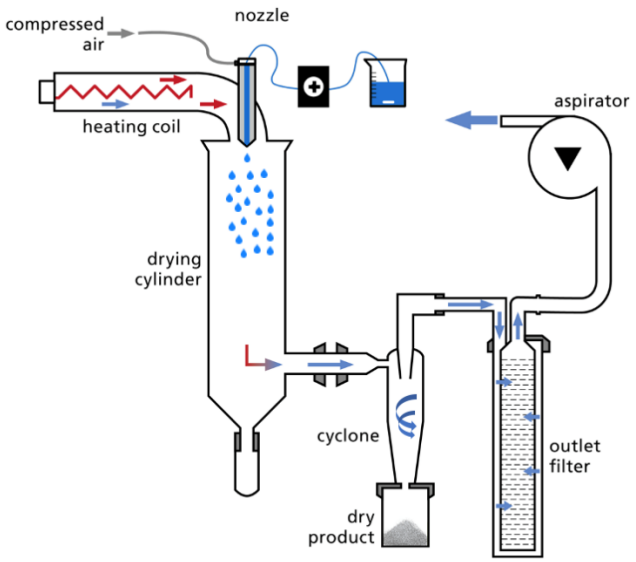

Figure 1.3 Schematic representation of an open-cycle spray drying system.

Starting from the atomization procedure, generation of small droplets (5-1000 μm) leads to the formation of large surface areas and thus, droplets reach within seconds the temperature of the inert gas due to high heat transfer that results in instant solvent evaporation. Several

atomization systems have been developed, namely rotary atomizers, hydraulic (pressure) nozzles, pneumatic nozzles and ultrasonic nozzles. Depending on the principle of operation and the properties (nozzle diameter) of apparatus, different droplet size distribution can be achieved. This is important because droplet size affects the final particle size and moisture content of the obtained powder. For instance, in pneumatic nozzles (multi-fluid) feed is atomized by a gas stream which produces extremely fine droplets (10–100 μm), while in ultrasonic nozzles, due to lower velocity produced during vibration, final droplets are within a size range of 5–1000 μm[42].

Moving on in the drying chamber, different flow patterns may be used based on the properties of the starting material, namely *co-current, counter-current* and *mixed* flow. In the *co-current* arrangement, material is sprayed in the same direction as the flow of hot air. In general, such an arrangement is preferable for heat sensitive products as they are heated the least; however, this may lead to insufficient solvent evaporation. In the *counter-current* arrangement, material is sprayed against the direction of air flow. The droplets hit initially the air that travels a distance significant enough to reduce its temperature. As the droplets move to the bottom of the drying chamber, the air gets hotter and drier. This leads to a higher temperature in the final product compared to the *co-current* configuration which can be good in terms of high thermal efficacy and low moisture content but not the optimum choice for heat sensitive molecules. In addition, extremely dry products tend to agglomerate due to electrostatic forces and thus, particle size is larger than *co-current* flow. Finally, *mixed* flow combines the aforementioned two flows. Material is sprayed upwards and remains in the hot zone for a short time to eliminate the residual moisture. Gravity then pulls the product into a cooler zone. This arrangement offers flexibility for materials with varying degrees of thermal stability[42].

In the last stage of the process, particles are separated from the air stream either by precipitation on the bottom of the chamber, from which particles are removed with a scraper, or by using a cyclone and bag filters. The latter is the most usual system and particles through the cone-shaped cyclone are collected in a flask by centrifugal forces[43]. Ultra-fine particles (<1μm), that are not heavy enough to escape the air stream, are collected through a woven fabric filter (bag filters)[44].

1.3.2 Particle formation

Spray drying is a simple, single-step process of low cost and easy to scale up. One of the most attractive features of spray drying is that, by controlling several process parameters and

attributes of the feed solution, it is possible to control particle characteristics. Size, shape, surface charge, roughness, morphology and moisture content can be adapted to improve the performance of the dry powder during inhalation[45]. For many of those factors it is now well-known their impact on particle formation.

First of all, it is important to understand how the particles are formed via spray drying. Particle formation is governed by the radial distribution of components during the drying process of droplets. As the solvent evaporates, droplet shrinks proportionally to the solvent evaporation rate (k) and its surface is enriched by the solute components. This causes a solute diffusive flux from the surface to the center of droplet[44]. Surface enrichment (E_i), which is the concentration of component i ($C_{s,i}$) in relation to its average concentration in the droplet ($C_{m,i}$) is given by Equation 6,

$$E_i = \frac{C_{s,i}}{C_{m,i}} = \frac{e^{0.5 \cdot Pe_i}}{3\beta_i} \quad (6)$$

where Pe_i is the dimensionless Peclet number and β is a function that must be integrated numerically for each Pe number. Peclet number (Pei) is related to the ratio of solvent evaporation rate (k) and diffusion coefficient of solute component i in the liquid phase (D_i), as shown in Equation 7[46].

$$Pe_i = \frac{k}{8D_i} \quad (7)$$

Equations 6 and 7 show that distribution of components of a droplet is driven mainly by solvent evaporation rate and their diffusion coefficient. In general, when $P_e \leq 1$, radial concentration profile of the solute component is expected to be flat, because the diffusion coefficient higher than the rate of droplet shrinkage will homogeneously distribute the solute in the final particle. This leads to spherical particles with little or no void space and high density[47]. On the contrary when $P_e > 1$, diffusional movement of the component is slower compared to the speed of the receding droplet surface by evaporation. This leads to particles with low density, large void internal spaces and hollow or wrinkled shape due to a shell formation. Thus, it is becoming obvious that surface enrichment could be manipulated by solute properties, solvents and process factors[48].

1.3.3 Critical factors affecting dry powder properties

The critical factors that affect particle formation and other dry powder properties can be separated in those that concern the feed solution and those of the spray drying process parameters[46].

Feed solution properties

Solvent properties, excipients and concentration of the components in the feed solution highly influence the final powder characteristics. Solvent volatility is the primary attribute in order to achieve lower residual solvent, better flow properties and reasonable yield of powder particles. If an organic volatile solvent is included in the feed solution, less of inlet temperature energy is exhausted by solvent evaporation, due to the lower boiling point of the solvent. This leads to higher outlet temperatures and therefore to a greater thermal efficiency of the process[49]. Other properties, such as high dielectric and dipole moments, have shown to increase amorphic state of the final solid dispersion. Hence, solvents containing better tendency of dispersion can produce solid dispersions of higher solubility[50].

In fact, one of the main uses of spray drying is the production of amorphous solid dispersions (ASD), due to instant evaporation that results in an insufficient time for the molecules to re-arrange and pack into the crystal lattice[51]. ASDs are one-phase systems in which API molecules are fully dissolved in an amorphous carrier (usually a polymer). ASDs are advantageous in terms of solubility and dissolution rate while the excipients used stabilize the amorphous state of the API during storage and prevent recrystallization during the dissolution. The choice of the polymer should be based on several properties such as glass transition temperature (T_g), nature of polymer (anionic/cationic), presence of functional groups, hygroscopicity, solubility in organic solvents, molecular weight and thermal stability. For instance, a high T_g (~75°C) leads to more stable ASDs particles with enhanced flowability since they remain at glassy state at room temperature and are highly viscous preventing recrystallization of the API[42]. In addition, high hygroscopic polymers absorb water during spray drying which weakens molecular hydrogen bonding thus leading to a lower miscibility of the drug in the polymer and decreased T_g of the formulation[52].

Last but not least, feed concentration is a parameter strongly related with the evaporation time. High solid concentrations (>5% w/v) lead to droplets containing lower solvent amounts, thus leading to higher P_e values and therefore, to the production of large, porous, wrinkled particles[53]. Moreover, at high concentrations lower moisture content has been reported due to the increase in solid content and reduction in the total moisture to be evaporated[54].

Process parameters

During spray drying, operator controls five process parameters, *i.e.* the inlet temperature, the rate of the feed solution (ml/min), the flow (or pressure) of atomizing air (L/h), the nozzle

diameter (μm) and the gas flow rate at aspirator (m^3/h). These parameters have a direct impact on the outlet temperature, droplet size, drying efficiency and final product performance.

Initially, the inlet temperature determines the solvent evaporation rate and thus particle formation. High inlet temperatures lead to high P_e numbers and therefore porous particles. Apart from that, rapid shell formation at the droplet surface may occur due to high inlet temperatures causing solvent entrapment. During solvent evaporation the outer layer may collapse or rupture, resulting in cracked, broken particles. A reduction in inlet temperature may lead to higher moisture content in the particles which may stick on the walls of the drying chamber, leading to lower yield of the process[46]. Finally, although it is not clear yet, it has been reported that increasing inlet temperature could result in a higher aerodynamic diameter due to either denser particles or an agglomeration[55,56].

Feed rate is another critical parameter that affects outlet temperature, droplet size, drying velocity and distribution of components. Increase of feed rate has shown to decrease outlet temperature, since the volume of liquid to be evaporated increases[57]. In practice, outlet temperature is the highest temperature to which the product will be heated and plays a critical role in particle size and morphology. This point, along with the enlarged droplets that are produced in high feed rates and the less time available for evaporation, lead to higher moisture contents, as well as lower yields[58].

Continuing to the process parameter, air flow rate is defined as the volume of drying air supplied to the system per unit time. A slow airflow rate is expected to give a better thermal efficiency, due to the slower passage through the drying chamber and the longer action of the drying air upon droplets. Nevertheless, very slow flow rates can also affect yield as larger particles may deposit through gravitational sedimentation on the bottom of the drying chamber. As a result, it is advisable to adjust the drying air flow rate to the maximal value available, also in order to maximize the cyclone operation efficiency[59]. Lastly, it is also an issue that a reduction in airflow may reduce the sheer forces at the nozzle; this may create larger droplets in the spray and thus, generate larger particle. Regarding the nozzle diameter it makes sense that, increasing its diameter, larger size of the droplets and thus larger particles are produced[60].

Finally, aspiration rate is a parameter influencing drying efficiency as well. A high aspiration rate means a shorter residence time of air in the spray dryer and thus, less time available for drying, resulting in a higher moisture content. On the contrary, increasing aspiration rate also leads to better cyclone operation efficiency and therefore increases yield.

Table 1.1 summarizes the effect of the aforementioned feed solution properties and spray drying process parameters when increased, on some of the critical quality attributes of a dry

powder for inhalation. As a general rule, in order to produce particles appropriate for inhalation, a relatively high feed concentration should be spray dried using a low feed rate, a high airflow rate, a reasonably high aspirator rate, and a proper inlet temperature to adjust outlet temperature in order to achieve reasonable moisture content in the final product[49].

Table 1.1 Effect of the Spray-Drying Conditions on the Process Outputs.

Impact / Process parameters	Outlet T	Moisture Content	Particle size	yield
Feed Concentration	↑	↓	↑	↑
Non-aqueous solvent	↑	↓	↓	↑
Inlet T	↑	↓	↑ possibly	↑
Feed rate	↓	↑	↑	↓
Air flow rate	↓	-	↓	-
Aspirator rate	↑	↑	-	↑

1.4 Quality by design (QbD)

1.4.1 Basic principles and tools

The term Quality by Design (QbD), even though framed by Joseph M. Juran in 1992, was conceptually introduced by Shewhart in 1930, in reason of his major contribution to the industry with the introduction of control charts in the industry[61]. Shewhart realized that the only way to ensure product quality is by controlling its manufacturing process. In that way, it became clear for the first time that just testing quality in the final product (Quality by Testing-QbT) is not efficient. On the contrary, quality should be built in the product by design[62]. QbD is a multidimensional and holistic approach as states its modern definition based on the work of many scientists in the field of quality such as Deming, Juran, Montgomery, Feigenbaum, Ishikawa. These scientists introduced theories and principles that are the pillars of QbD, such as the theory of knowledge, systems theory, Total Quality Management (TQM), statistical thinking and risk management[63]. Therefore, QbD is officially defined in ICH Q8 (R2) guideline for the pharmaceutical development as "A systematic approach to development that begins with predefined objectives and emphasizes product and process understanding and process control, based on sound science and quality risk management" (ICH harmonized tripartite

guideline. Pharmaceutical development Q8-Q9-Q10. https://www.ich.org/page/quality-guidelines, visited May 21th, 2020).

QbD has been introduced and implemented in the global industry for many years. However, it found its way in the pharmaceutical industry only in the recent years after the FDA initiative for a change in the 21st century, by realizing how patient's safety can be enhanced by integrating science and risk assessment/management into development and manufacturing activities[64]. Of course, there are other drivers towards that initiative, such as the need to abandon the monolithic blockbuster business model and turn to personalized medicine. Moreover, high development costs, tightening of regulations and the pressure from governments to decrease healthcare costs don't allow defects in the final product that are produced by old manufacturing paradigms still adopted by the pharmaceutical industry.

Regarding the QbD approach in the pharmaceutical development, everything must begin and end with the patient whose unmet needs must be fulfilled, having always in mind that is the one and only reasoning behind the whole development process of any drug product. Based on that idea the primary elements of QbD are[65]:

1. A quality target product profile (QTPP) that is the quality characteristics of a drug product that ideally will be achieved to ensure the desired quality. This is translated to the critical quality attributes (CQAs) of the drug product, *i.e.* physical, chemical, biological, or microbiological property or characteristic of an output material;
2. Product design and understanding through the identification of the critical material attributes (CMAs);
3. Process design and understanding through risk assessment for the identification of critical process parameters (CPPs) and a thorough understanding of the relation between CMAs and CPPs to CQAs;
4. A control strategy that includes specifications for the drug substance(s), excipient(s) and drug product as well as controls for each step of the manufacturing process;
5. Process capability and continual improvement.

In order to achieve the aforementioned goals, QbD implements several tools that derive basically from the approach of statistical thinking. To begin with, ICH Q9 guideline "Quality risk management (QRM)" uses risk assessment to identify and prioritize potential risks of formulation and process parameters of each unit operation. Some of the main methods used for risk assessment are the Failure Modes and Effects Analysis (FMEA) or Cause and Effect diagrams (Ishikawa diagrams) that are ways to evaluate a system, design process or service for

possible ways in which known or potential failures (problems, errors, risks, concerns) can occur[66]. After that, with the addition of extra information on the process along with prior knowledge and statistically designed experiments, these potential risks of failure can be refined and adequately addressed through interventions for assuring quality[62].

Other tools that QbD uses arise from the statistical quality control (SQC) first introduced by Woodall and Montgomery that includes statistical process control (SPC), process capability and design of experiments (DoE). Especially DoE is an extremely useful tool during product and process design that came to replace the traditional one factor at a time approach (OFAT) by implementing other statistical tools like response surface methodology (RSM), multivariate analysis and analysis of variance (ANOVA)[63]. Experimental design is applied to determine the impact of each CMA and CPP on the CQAs as well as the potential interactions that may exist between CMAs and CPPs that affect CQAs. Factorial designs (full or fractional), mixture designs and RSM are predominantly used for screening of factors, process characterization and optimization[67]. After the calculation of the effects, it is possible to define the optimum value for each chosen factor (CMA, CPP) that results in the desired range of values for the responses (CQAs) with the minimum variability. This last part is essentially important in order to map the process behaviour at different factor levels and to define the design space, *i.e.,* the multidimensional combination and interaction of input variables (*e.g.*, material attributes) and process parameters that have been demonstrated to provide assurance of quality (ICH Q8)[67].

1.4.2 Implementing QbD in the development of DPIs

As in all dosage forms, implementing a QbD approach provides an assurance to the control of the final formulation and manufacturing process. In the case of DPIs, however, it becomes more compelling the need of using QbD for several reasons. Firstly, as mentioned in a previous section, DPIs must be considered as a result of the interaction between the device and the drug formulation, thus making the development of such a product a rather complex effort. On top of that, proper use or not of the DPI by the patient affects in a high extent product effectiveness and that is something that should be always kept in mind from the first steps of product development through QRM. Finally, manufacturing of DPIs has shown low process capability during processes such as powder dosing or capsule/blister filling. At the same time, *in vitro* analytical methods for the evaluation of CQAs have shown low robustness, as *in vivo-in vitro* correlation (IV/IVC) in the case of the impactors that are essentially used for the evaluation of aerodynamic performance of the DPIs.

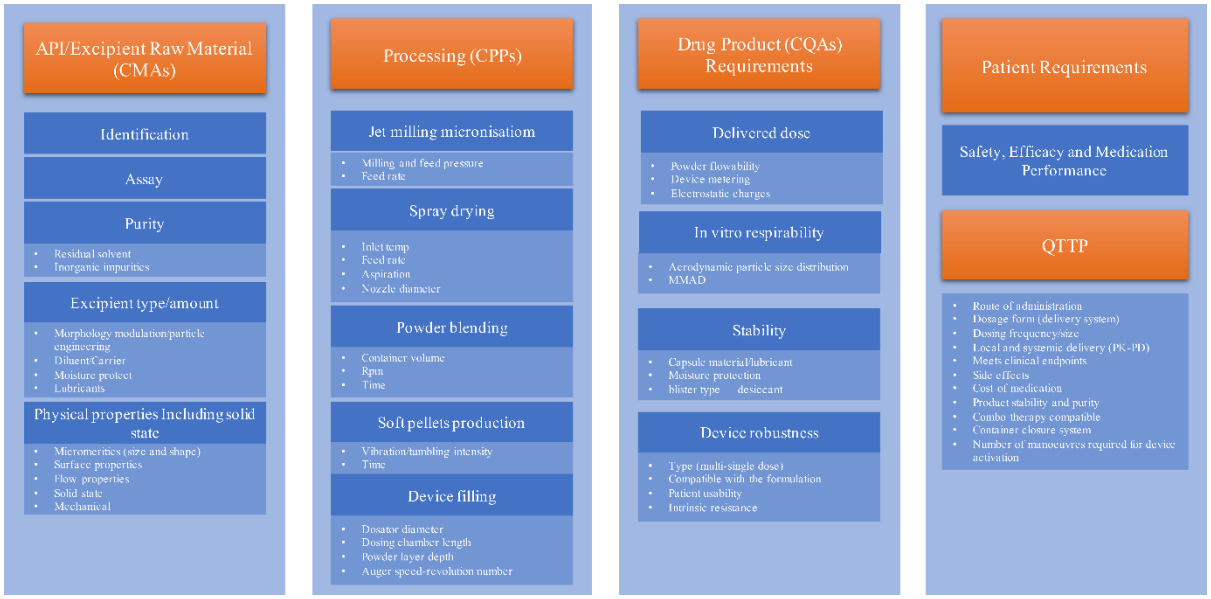

Figure 1.4 A QbD roadmap for a dry powder inhaler product. Adapted from: The application of Quality by Design framework in the pharmaceutical development of dry powder inhalers, European Journal of Pharmaceutical Sciences, Buttini F. *et al.*[68], Copyright® 2018, with permission from Elsevier.

Figure 1.4 by Buttini *et al.* shows briefly a QbD roadmap that decodes the general aspects during a DPI development. Behind every title and bullet of that roadmap, a plethora of *in vitro* analytical methods, quality controls, statistical analysis and prior knowledge has been applied in order to ensure that every aspect is properly included, justified and controlled. Starting from the patient requirements, in the first stages of product development it is important to assure safety and effectiveness of the product. These primary aspects have to be considered throughout the whole DPI product lifecycle from inception, from design and manufacture, to service and disposal of products (lifecycle management). In order to do that, a QTPP must be established in which fundamental product characteristics are described along with the proper justification for each choice. Those are the route of administration, dosage form, strength, dosing regimen, delivery device, PK-PD profile depending on the therapeutic target, side effects, cost of medication, product stability and other important characteristics that, if achieved, assure product quality[62]. Afterwards, a translation of QTPP in CQAs follows. For DPIs some common CQAs exist such as device metering, moisture content, aerodynamic performance that includes powder flowability, aerodynamic particle size distribution, and device robustness. Other CQAs common in all dosage forms exist such as API content uniformity and stability. Finally, as defined by the QbD approach, it is important by risk assessment to determine the independent variables, *i.e.* the CPPs and CMAs, the control of which can lead to the manipulation of the dependent variables, *i.e.* the CQAs[62,69].

In the previous section the CPPS of spray drying were analyzed but depending on the method used for particle engineering, different CPPs may exist. Furthermore, typical CMAs for the raw materials used are API or excipients crystal form, purity, stability and particle size distribution. Implementing a QbD approach is the only way to link all these aspects together, given the complexity, variability and interactions that are hidden in the variables that affect the quality of the final DPI product[62].

1.5 Cupido Project

1.5.1 Purpose and Consortium

The present thesis was conducted in the context of Cupido Project which has received funding from the EU's Horizon 2020 research and innovation program under the Grant Agreement 720834. The title of the project was CUPIDO, acronym of Cardio Ultraefficient nanoParticles for Inhalation of Drug prOducts. It started in February 2017 with its main purpose of the application of nanotechnologies to the cardiovascular field. The incidence of cardiovascular diseases (CD) has increased over the last decades, primarily because of the expansion of the "modern" lifestyle in wealthy countries and the lengthening of life expectancy. It is estimated that the world's population aged 60 years and over will reach 2 billion by 2050 (three times more than in 2000). Another complication is that according to the World Health Organization, in 2005 there were 2.3 billion people around the world with a body mass in the overweight or obese range.

Taken together, this indicates a huge increase in the numbers of those at risk of developing CD in the next 40-50 years. Despite advancements in its management, CD still remains a major cause of death worldwide, claiming 17.1 million lives a year and accounting for estimated 31% of all deaths globally. Treatment of CD costs 139 billion euros for the EU annually, with hospitalizations comprising 60-70% of direct treatment costs. Up to 40% of all deaths occur among the elderly (65 years of age or older), who are expected to reach approximately 20% of the whole population by the year 2030. Additionally, the cost to treat CD will triple by that time.

The economic impact of CD on the overall European healthcare currently stands at 192 € billion annually, and this figure continues to rise every year. In spite of all medical efforts, the 5-year mortality of heart failure (HF) has decreased significantly less than that of cancer. In fact, the day-to-day management of individual end-stage patients is still challenging with only short-

term benefits, and heart transplantation is available only to a minority of patients. Altogether, this situation highlights the urgent need to overcome the difficulties associated with the use of conventional pharmacological therapies (*i.e.* drug instability, insufficient efficacy, collateral side effects due to unspecific tissue targeting, and invasive drug administration in end-stage disease) by developing novel ground-breaking therapeutic strategies that go far beyond any current conventional medical approach. For this to occur, it is critical to further understand the underlying mechanisms leading to CD and properly stratify the patients. In particular, new approaches for safe, efficient, and cardiac-specific delivery of therapeutic drugs are strongly required. CUPIDO is a new milestone in the fight against CD. It brings additional and concrete evidence for the need of EU-wide policy actions for CD treatment.

CUPIDO project aims to hit the core of the cardiovascular disease, developing inhalable nanoparticles that can deliver a therapy directly to the diseased heart. Exploiting nanoparticles as a targeted delivery system can revolutionize the cardiovascular field, becoming the first non-invasive heart-targeting therapy. CUPIDO consortium is working to develop biocompatible and biodegradable nanoparticles that can self-assemble and encapsulate drugs (novel or available) for cardiovascular disease. The nanoparticles, once inhaled, will first reach the lungs' alveoli and later will translocate to the heart, where the drug will be finally released to cardiomyocytes. Finally, the heart-specificity will be ensured thanks to chemical and magnetic guidance, reducing the chances of adverse side effects.

Cupido project consists of a multidisciplinary team extended to six countries. CUPIDO consortium ranges from National Research Centers (CNR, Italy) and universities (Charité University Medicine Berlin, Imperial College of London) to financial companies (IN s.r.l, Italy), technology companies (Simula, Norway; Cambridge Innovation Technologies Consulting Ltd, United Kingdom; Nemera, France; L.I.F.E, Italy; Bioemtech, Greece) and pharmaceutical companies (Sanofi, France; Finceramica, Italy; PlumeStars s.r.l., Italy). The 12 Cupido partners can cover the complete chain that brings an idea into a feasible product and cover expertise in: cardiovascular and nanotechnology research, bioengineering and molecular imaging, pulmonology and lung cell biology, *in silico* computational models, wearable electronics, drug delivery solutions and pharmaceutical products (https://www.cupidoproject.eu/our-goal, visited May 22th, 2020).

1.5.2 Calcium phosphate nanoparticles for targeted nanomedicine

Currently, modern medicine is going through a paradigm shift from the widespread disease managements to more tailored and customized treatments, exploiting specified therapeutic agents' interactions at molecular level. About this, promising results come from the emerging field of nanomedicine, that could be defined as the employment of nanotechnology to overcome healthcare problems. In this field, the remarkable and novel properties shown by nanomaterials are exploited to achieve specificity, accomplishments and biological activities not exhibited by their counterparts at larger dimensional scales[70].

The nanometric dimensions of nanoparticles/nanosystems offer several advantages over formulations containing larger particles. First of all, nanoparticles (NPs) are characterized by a large surface area and thus, a faster dissolution rate. In addition, as the particle size decreases, saturation solubility of a particle increases[71]. This is particularly interesting in order to enhance bioavailability of hydrophobic drugs by encapsulation in water dispersed NPs while on the same time NPs can provide protection against *in vivo* drug early degradation[72]. Furthermore, it has been shown that small size particles can penetrate into tissues and reach the cytoplasm or other intracellular target[73]. Last but not least, NPs that function as drug carriers, can be used to evade capture by cells of the reticuloendothelial system (RES), and to target specific tissues. Consequently, avoidance of the rapid clearance from bloodstream, and reduction of drug side effects are met[74 75]. However, there are concerns about the potential long-term toxicity of NPs that needs to be studied. Moreover, the complexity of the NPs preparation process may be difficult to scale-up[76].

The use of NPs has been widely studied for cancer management. Nowadays some NPs-based formulations are clinical approved for the treatment of a variety of cancer types. Several authors have highlighted that innovative NPs-mediated formulations of conventional chemotherapeutics can enhance their efficacy[77].

Among other nanoparticulate drug delivery systems, such as liposomes, polymeric NPs, micelles, dendrimers, niosomes and lipid-based carriers, calcium-phosphate nanoparticles (CaPs) exhibit several attractive features that make them a useful tool for targeted nanomedicine[78]. CaPs are the inorganic constituent of normal (bone, dentin) and pathological calcifications mainly in the form of ionic substituted and poorly crystalline apatite. As a result, they possess excellent biocompatibility, bioactivity, osteoinductivity and non-immunogenicity. Bioceramics have been used as biomaterials for manufacturing biomedical devices in orthopaedics and dentistry[79]. Additionally, except for a potential increase of the intracellular

calcium concentration after an uptake and a limited local inflammatory reaction, there are no adverse effects of calcium phosphate nanoparticles[80]. Consequently, if a proper method for the preparation of CaPs is applied, there is a chance of producing CaPs having excellent biocompatibility due to its chemical similarity to human hard tissue (bone and teeth). This characteristic makes them recognizable by organisms as endogenous materials[81].

In terms of functionality, CaPs feature a faster degradation than other commonly used NPs and, by changing synthesis parameters, their physicochemical properties (morphology, surface charge, crystallinity, colloidal stability) can be flexibly manipulated. Furthermore, CaPs can act as carriers for various APIs including biomolecules, either by surface adsorption or encapsulation, protecting them from the biological environment[82]. After that, due to their pH dependent solubility, CaPs can self-assemble and remain stable in blood plasma (pH=7.4) until they reach regions with acidic pH (< 5) as inflammatory regions or endosomes and lysosomes after cellular intake[83]. Nevertheless, some of the main drawbacks of CaPs are their low drug payload values and their tendency to form aggregates in aqueous suspensions. This makes difficult to achieve a high colloidal stability and bioavailability, as the aggregates are easily removed by macrophages. The latter issue could be resolved by the addition of ionic organic molecules (citrate ions, amino acids or macromolecules) that stabilize the size of CaPs at the early stage of crystallization, due to the binding of ions to CaP surface[81,84].

Since today CaPs have been mainly used for the treatment of cancer as carriers of APIs or in combination with external stimuli to produce a therapeutic effect, as imaging agents or even designed to produce both therapeutic and diagnostic effect (theragnostic agents).

Doxorubicin, platinum complexes and methotrexate are the main chemotherapeutic agents that have been loaded in calcium phosphate nanoparticles[85 86].

Because of their small size, they are able to target cancers due to enhanced permeation and retention (EPR) effect resulting in accumulation in over-vascularized cancerous tissues. Apart from that, due to the high negative surface charge, CaPs are able to adsorb electrostatically on their surface targeting ligands with high tissue specificity. Bisphosphonates drugs selectively target bone apatite and have been widely used for skeletal diseases (osteoporosis, osteosarcoma, etc.). The calcium of CaP nanoparticles attracts the zoledronic acid, a bisphosphonate molecule, modifying its typical bone tissue drug disposition[87]. Various other active moieties have been studied and attached on the surface of CaPs from small molecules to macromolecules such as nucleic acids, peptides and antibodies by exploiting several interaction mechanisms between the NPs and the API (Figure 1.5).

Targeted CaP nanoparticles were also used for the delivery of nucleic acids in the form of siRNA, exogenous genes, plasmids and suicide genes. Targeting moieties can exclusively target desired cells by enhancing their therapeutic efficacy or target the apoptotic genes delivery or siRNAs to malignant cells[88].

Efficient and selective was the targeted transfection of nucleotides or suicide genes by calcium phosphate nanoparticles. In details, it was demonstrated that cancer cells, *i.e.* the human colon cancer cells LoVo[89] and human gastric cancer cells SGC7901 were selectively destroyed with suicide genes on CaPs. The silencing of specific genes resulted from siRNAs delivered to human lung cancer cells NCI-H-460[90], human colon carcinoma cells HT29-luc and murine melanoma cells B16F10. Furthermore, in the works of Hu *et al.*[91] and Roy *et al.*[92], the success of CaP *in vivo* targeted transfection of exogenous genes to murine hepatocyte cells has been reported. It must be mentioned that the main findings of these reports are only at the proof-of-concept level and further evidences are needed.

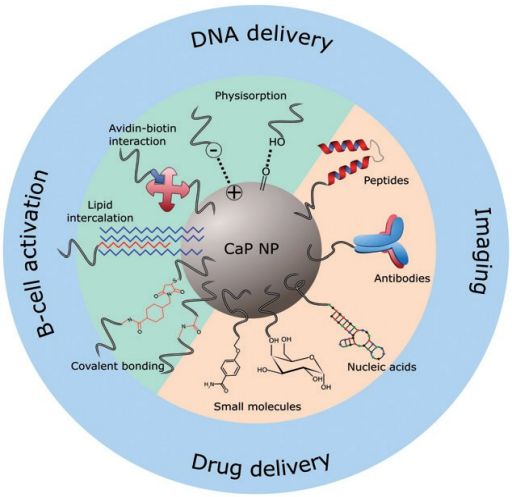

Figure 1.5 Schematic representation of functions (outer ring), moieties (right sector) and surface decoration methods (left sector) of targeted CaPs. Adapted by permission from Taylor & Francis, Calcium phosphate-based nanosystems for advanced targeted nanomedicine, Degli Esposti L. *et al.*[72], Copyright® 2018.

Porru *et al.* proposed an innovative strategy for glioblastoma treatment based on transferrin (Tf) targeted self-assembled calcium phosphate nanoparticles (NPs) incorporating zoledronic acid (ZOL) (NPs-ZOL-Tf). NPs-ZOL-Tf have been tested on the glioblastoma cell line U373MGLUC showing higher *in vitro* cytotoxic activity than the treatment by free ZOL. ZOL-Tf calcium phosphate nanoparticles also *in vivo* administered to immunosuppressed mice carrying intramuscular U373MG-LUC xenografts, showed a significant inhibition of tumour

weight. Therefore, the ZOL encapsulation in transferrin (Tf) targeted self-assembled calcium phosphate nanoparticles enhanced the anticancer efficacy of this drug in glioblastoma thanks to the acquisition of the ability to cross the BBB[93].

The consequence of CaP nanoparticles agglomerations could lead to a macrophage capture and clearance. Nevertheless, the decoration of the surface with ionic organic molecules (*e.g.* citrate ions, amino acids or macromolecules) stabilize CaP NPs in their colloidal form. A further CaP nanoparticle common issue is their rapid surface degradation that could lead to a burst release of the payload in the organism, hampering the applications requiring a more sustained and prolonged release. This matter could be overcome since CaP NPs could be engineered to encapsulate the drug within the crystalline matrix preventing the burst release effect.

1.5.3 Peptide-loaded CaPs for the treatment of heart failure

The research about the potential uses of CaPs in diseases different from cancer is still in its infancy. In 2018 Miragoli *et al.* published a work in which they demonstrated that inhalation of calcium phosphate nanoparticles (CaPs) (<50 nm) allows for rapid translocation of CaPs from the pulmonary tree to the bloodstream and to the myocardium, where their cargo is quickly released. For the first time an attempt was made in order to use an alternative route of administration other than the traditional oral and intravenous for the treatment of myocardial disease. Briefly, negatively charged CaPs were produced via a biomineralization-inspired strategy in the range of 20-50 nm, capable of delivering bioactive molecules after crossing the cardiomyocytes cellular membrane without promoting toxicity or interfering with any functional properties of cardiomyocytes[94,95].

In 2016, Rusconi *et al.* demonstrated the therapeutic effect of a cell-penetrating mimetic peptide (R7W-MP). This peptide by targeting the $Ca_v\beta2$ cytosolic subunit of the L-type calcium channel (LTCC), improves cardiac contractility. Some pathological heart conditions are associated with alterations of LTCC levels and function (diabetic cardiomyopathy). The R7W-MP peptide by restoring of LTCC density at the plasma membrane, preserves its physiologic channel function. More specifically, R7W is an oligoarginine (R7W) cell-penetrating peptide that is fused to the N-terminus of the 11 aminoacidic peptide (MP), the active component of the therapeutic molecule, and acts as a carrier for the MP without affecting its function[96]. MP mimics an amino acidic stretch of the C-terminal tail of the $Ca_v\beta2$ cytosolic chaperone and is designed to target specifically the Tail Interacting Domain (TID) within the $Ca_v\beta2$ globular

domain. This facilitates the restoration of $Ca_V\alpha1,2$ protein density at the plasma membrane in heart conditions associated with altered LTCC levels and function[97].

In the absence of R7W sequence, MP loses its potential to enter the cardiac cells. Its efficiency in rescuing cardiac contractility requires that the CaPs mediate its crossing of the pulmonary barrier and subsequent myocardial cell internalization. CaPs were proved to successfully encapsulate the MP and *in vivo* administered by nebulization were able to internalize the cardiomyocyte. The peptide release led to a complete recovery of cardiac function. Based on this targeted heart treatment and taking advantage of the attractive features of pulmonary route compared to other delivery routes, a more selective cardiac accumulation of CaPs is possible. As a result, a significant dose reduction of the active biomolecule, as well as less adverse effects due to heart-specificity, can be achieved[98].

1.6 Lung-to-heart route

1.6.1 Comparison between the intravenous route of administration and the lung-to-heart delivery

The nanoparticles administered by the intravenous (IV) route are in succession conveyed by the blood stream to the right heart, to the lungs and to the left heart. In the context of the first blood passage in the pulmonary circulation, the fraction of IV administered nanoparticles reaching the left heart, of which 4-5 % will be directed to the coronary arteries, is difficult to measure. The left heart blood concentration is not representative of the pulmonary vein concentration due to the very efficient capture of the nanoparticles in the systemic circulation. In fact, the fraction of nanoparticles lost before and after the right heart attainment should be high enough to explain the better accumulation observed in the case of pulmonary administration. This is particularly true considering the low bioavailability usually observed after pulmonary administration (Figure 1.6).

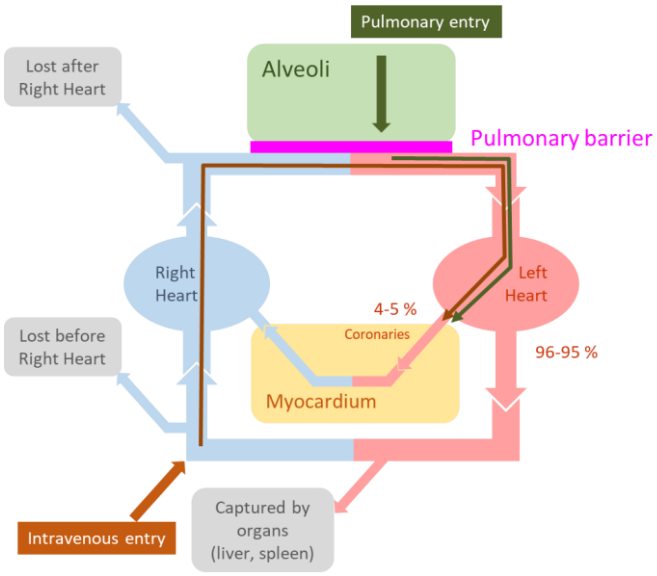

Figure 1.6 Comparison of the intravenous and pulmonary routes.

1.6.2 CaP nanoparticles lung to heart delivery

The comparison of the fate of the CaP nanoparticles deposited in the airways embedded in microparticulate powder or in nebulized micro-droplets will be addressed in an attempt to assess the potential impact of pulmonary administration procedure on lung-to-heart delivery of Ca-P nanoparticles and the associated peptides. The lung-to-heart route and the intravenous route, depicted in the Figure 1.7, will be compared, from the anatomical features of the systemic and pulmonary circulations, to address the potential of the pulmonary route to promote accumulation of inhaled drugs in the heart.

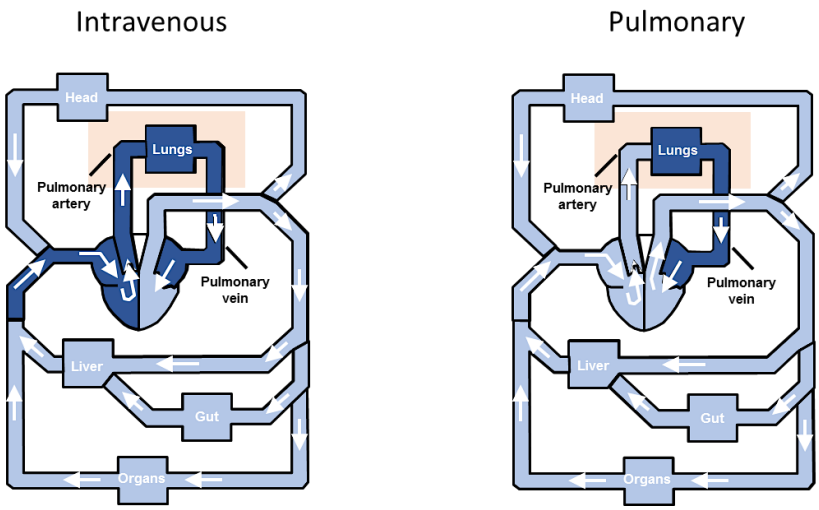

Figure 1.7 Nanoparticle routing as a function of the route of administration.

The accumulation of the CaP nanoparticles and of the nano-associated peptide in the heart is dependent on:

- the fraction of CaP nanoparticles in microparticles delivered to the alveoli (the absorptive part of the lung);
- the administration time, which may be significantly different for continuous nebulization compared to inhalation of discrete puffs of powder;
- the release of CaP nanoparticles from the microparticles delivered as inhalable powder;
- the ability of the CaP nanoparticles to be translocated through the type I pneumocytes to reach the blood;
- the specificity of the lung-to-heart transport, in particular the shorter pathway that may limit the loss of drug into the blood stream, better directing the absorbed material to the coronary arteries.

Nanoparticles cannot be directly delivered to the lung as individual particles because alveolar deposition efficiency is uncertain and medical devices to generate nanoparticles aerosols are not market ready. Based on ICRP (International Commission on Radiological Protection) lung deposition model, 20 nm particle size allows a theoretical efficient deposition in the alveoli (around 50%) but there is no available medical device generating this particle size aerosol. Few prototypes of inhaler have been described in different papers to generate submicronic particle (around 200 nm)[99] but a high fraction of these particles was exhaled (80%)[100]. Therefore, the direct inhalation of nanoparticles suffers from unlikely deposition at the intended site for action. A technique to overcome this drawback is to embed nano-sized particles in micron-sized carriers suitable for inhalation down to the deep lung, and capable to restore, in the alveoli fluid, the nanoparticles exhibiting the original size distribution deemed necessary for the expected nano-carrier performance.

Two procedures can be adopted to fulfil this aim:

- dispersion of the nanoparticles in micro-droplets of aqueous medium as suspensions;
- embedding of the nanoparticles into micro-sized solid matrix particles.

In terms of inhalation product, this means to manufacture a drug suspension for nebulization, or to construct a dry powder for inhalation.

1.6.3 Expected influence of the pulmonary administration protocol on the pharmacokinetics

Dry Powder Inhalers have the advantage to be portable and to deliver the dose in one or few inhalation acts, reducing the administration time in comparison with nebulizers with access to a more patient-friendly therapy. Compared to nebulizers, their main limitation is the inspiratory flow rate by the patient. DPIs require a minimum inspiratory flow to ensure the particle deagglomeration and the delivered dose to the patient (20 L/min; 1 kPa pressure drop).

In this inhalation product, low or large amount of formulation can be delivered. The amount inhaled is therefore reliable and the size of the aerosolized powder can be adjusted to deliver extra fine particles (< 3 µm), adapted for deep deposition into the lung.

As mentioned before, nano-sized particles cannot be dried and delivered as they are. They should be temporarily enlarged by embedding in microparticles. The risk of irreversible aggregation of the nanoparticles as a consequence of the microparticles manufacturing process is significant. The dry powder manufacturing principle is based on the assembly as solid microparticles of the nanoparticles using a water-soluble non-toxic carrier substance tolerated by lung tissue. The reversibility of nanoparticles embedded, *i.e.* nanoparticles release, when in contact with the pulmonary fluid, is one of the critical aspects of this thesis project.

Scientific literature reports various manufacturing principles aimed at producing inhalable microparticles exhibiting the aptness to restore, after deposition on wet surface, embedded nanoparticles respecting the initial size distribution. A first technique is to agglomerate the nanoparticles in a larger structure called “Trojan particles”. A second technique, adopted in this work, is to construct microparticles starting from the dispersion of the nanoparticles in a solution of carrier substances (*i.e.* lactose, leucine, trehalose or mannitol). The suspension is transformed by spraying or lyophilization into a dried powder exhibiting the appropriate microparticles size (< 5 µm) for inhalation and deposition in the deep lung. The obtained microparticles consist in a matrix of water-soluble substance embedding the nanoparticles. The restoration of nanoparticles characteristics results from the dissolution of the microparticles in the hydrophilic fluid. In addition to the size, the surface properties governing the ability of released nanoparticles to be translocated through the lung epithelium to systemic circulation is a key quality attribute.

The dry powder, as for the solution for nebulization, requires a device for administration of the dose. There are many DPI devices available on the market. For most of them, the powder is administered as a single dose in a hard capsule. The patient inhales through the mouthpiece of

the device, generating the air flow rate needed (> 20 L/min) (i) to extract the powder from the previously pierced capsule, (ii) to aerosolize it and (iii) to drive the particles into the lung where they are deposited according to their aerodynamic diameter. The maximum of amount of powder inhalable without cough is around 20-30 mg. However, where higher doses are required, successive inhalation acts allow the delivery of the entire dose in smaller puffs. Therefore, the DPI technology is expected to be robust enough to be adopted for the lung-to-heart drug routing.

By embedding nanoparticles in microparticles to produce a dry powder for inhalation, the expectation is that the rapid/easy dose administration and lung deposition, together with quick dissolution and high local concentration, will lead to an improved pulmonary blood translocation, as compared to nebulized liquid formulations.

Since the objective of this thesis project is to direct the drug to the cardiomyocytes, the dry powder is designed to promote the translocation of the drug-loaded nanoparticles from the apical alveolar epithelium of lung, to the blood flowing in alveolar capillaries to the heart.

Consequently, the absorption of nanoparticles is seminal for their translocation. For deposition to take place, various alveolar defence mechanisms activated against foreign materials in the respiratory units have to be overcome. The first one is a physical mechanism dependent on the size of inhaled material. When environmental particles or droplets have a size compatible with their access to the airways (aerodynamic diameter <5 μm; *i.e.* "respirable" particles), they may deposit in the airway secretions in the conducting airways and be cleared via the mucociliary escalator. This is a major bronchial airway defence mechanism that transports foreign material back to the throat where it is swallowed or expectorated. This mechanism is particularly efficient for larger respirable particles and insoluble or poorly soluble substances; it is based on specialized ciliated epithelial cells that push back the particles trapped in the mucus in large airways from the site of particle deposition to the throat.

Particles escaping bronchial capture, in particular those having a diameter < 3 μm, continue their travel to the deep lung and are deposited in alveoli, as expected for this research project microparticles. The alveolar deposition exposes the microparticles to phagocytic clearance by alveolar macrophages. However, since the microparticles of this project are designed for prompt dissolution and release of nanoparticles into the pulmonary secretions, their residence time in the alveoli is expected to be short and, as a consequence, the associated probability of macrophage engulfment is expected to be low.

Finally, possible degradation of the peptide loaded onto the nanoparticles in the pulmonary fluid is expected to be mitigated by the presence of calcium phosphate nanoparticles, likely by limiting the drug exposure to enzymes.

1.6.4 Translocation of nanoparticles from the alveoli into the blood

Even though the mechanism of crossing the pulmonary epithelium by nanoparticles is generally accepted as the mechanism of pulmonary entry of particulate matter into the blood circulation[101], the *in vivo* measurement of translocation faces methodological difficulties. For example, the poor stability of carbon nanoparticle labelling (with 99m-technetium) was shown to lead to artefactual results[102 103], whereas the unavoidable parallel absorption by oral route in the whole-body inhalation exposure protocol can induce a bias in the interpretation of data[104]. As a consequence, there is not, as yet, a complete consensus about: (i) the proportion of deposited nanoparticles that translocate across the pulmonary gas-blood barrier, (ii) the mechanism of translocation and (iii) the key quality attributes (size, zeta-potential, surface properties) deemed appropriate to favour this route.

1.6.4.1 Influence of nanoparticles size

The potential impact of particulate air pollution on human health has been a primary driver of the preclinical and clinical studies aimed at evaluating the entry of particles into the body by the pulmonary inhalation route. Particular attention has been paid to nanoparticles with a size < 100 nm, referred to as ultrafine particles. In fact, since alveolar macrophage phagocytosis of ultrafine particles is thought to be significantly less efficient than uptake of micron-sized particles[104], this protection process from nanoparticle inhalation is less effective, and further routing to the bloodstream is conceivable. In this context, accumulation of nanoparticles in the liver is viewed as a proof of the pulmonary barrier crossing toward the blood circulation. In fact, the accumulation in the liver after intravenous administration is typical of particulate materials in blood. Accumulation in the heart would be also expected, considering the lung-to-heart routing, but is not addressed in a systematic manner in these experiments.

Using technetium-99m labelled albumin nanoparticles with a diameter below 80 nm, Nemmar *et al.* studied the passage in blood of 1, 10 and 100 µg doses in hamsters after intratracheal instillation[105]. The labelling was not altered in the blood, as shown by thin-layer chromatography. Up to 1.24 ± 0.27 % of the radioactivity was found in the liver, 30 minutes

after the administration of 100 µg dose. Interestingly, 0.22 ± 0.11 % of the radioactivity was found in the heart whereas only 0.002 ± 0.0004 % was found in the spleen (also known as an organ capturing circulating nanoparticles).

On the opposite, ultrafine organic particles of ^{13}C with a diameter in the 20-29 nm range were also found to accumulate in the liver, after 6 h of whole-body inhalation exposure of rats, but not in the heart. However, oral absorption due to mucociliary clearance, as well as post exposure cleaning of their fur by the model animals, may have induced a bias in the biodistribution.

Since the materials representative of the ultrafine particles used in environmental toxicology are poorly soluble in water and poorly biodegradable, the artifacts due to their degradation or dissolution are thought to be mitigated. Used as pollutant surrogate, elemental silver (EAg) particles, with a diameter in 4-10 nm range, were inhaled by rats in a whole-body chamber[106]. EAg particles were located by transmission electron microscopy in the alveolar macrophages and in the alveolar wall. A significant amount of Ag was detected in the blood, which shows that the EAg particles crossed the pulmonary barrier. Significant amounts were found in the liver and the heart. However, the Ag accumulation in the heart was approximately 75 times lower than the accumulation in the liver, whereas it was only 6 times lower for technetium-99m labelled albumin nanoparticles. Therefore, favoured accumulation in the heart is not likely is this particular models.

1.6.4.2 Influence of nanoparticles surface properties

The uptake of particles by the epithelial cells was also evidenced by imaging using polystyrene latex beads with a 240 nm diameter[107]. Even though these particles are too big to be categorized as ultrafine particles, it is interesting to note that lecithin-coated beads were incorporated by type I and II cells, while uncoated beads were not incorporated. Therefore, this study shows that inhaled exogeneous particles can be processed differently as a function of their surface properties, although the mechanism of recognition is not yet elucidated. Even though the polystyrene beads could not be observed in the endothelial cells, which constitutes a missing link in the routing process. These experiments support the hypothesis of the transport of inhaled particles to the capillary space by translocation.

As alluded earlier, the surface properties of the nanoparticles are also prone to influence their immersion into the lung's surface-lining layer[108]. It may be part of the explanation of the better capture of the lecithin-coated beads, as compared to the uncoated ones. In practice, a

disintegration test has been included in the certificate of analysis of CUPIDO products, with the expectation that the appropriate wetting of the nanoparticles conditioning their incorporation in the surface-lining layer is assessed.

1.6.4.3 Microparticles disintegration and Ca-P nanoparticles recovery

The bioavailability of a drug administered by inhalation in powder form depends on several steps that cumulate to reduce the amount of drug available for absorption. Starting from the powder manufactured to obtain a respirable powder, the drug content in the formulation is dependent on the pharmaceutical process. The formulation introduced in the device is expected to be inhaled by the patients but, in practice, part of the formulation does not leave the device. Then, the deposition of the powder in the lung depends on the aerodynamic particle size distribution and may be done in sections of the respiratory tract not relevant for absorption. According to the CUPIDO products design, the deposited microparticles are expected to be dissolved to release the embedded nanoparticles. This process should be effective to avoid additional drug loss. Finally, free nanoparticles have to translocate from the lung fluid to the blood stream through lung epithelium, another possible site of drug loss.

In summary, as depicted in Figure 1.8, the bioavailability of a particulate drug in the lung is affected by all the previously described steps that cumulate to reduce the absorption. The quantification of the drug lost at each step is necessary for proper comparison of the nebulization and the dry powder inhalation.

Bioavailability: η process * η delivery * η deposition *η adsorption

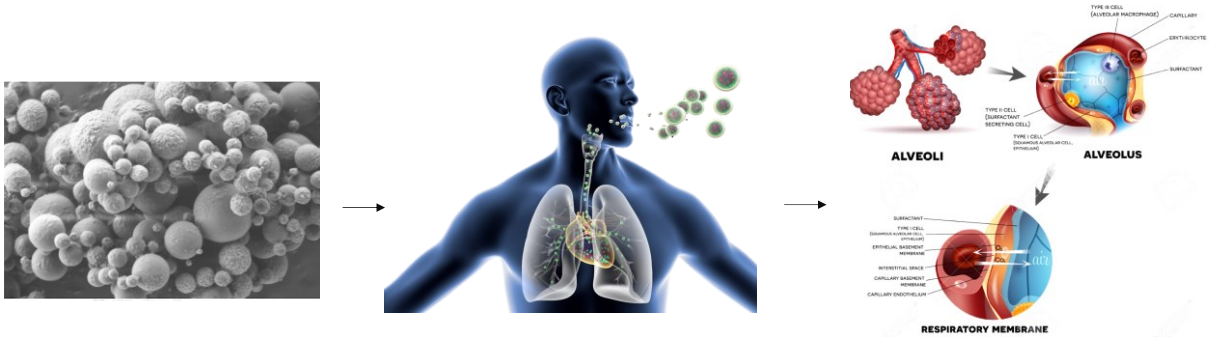

Process technology | Aerosol deposition | Adsorption (dissolution/permeability)

Figure 1.8 Processes of bioavailability construction following a dry powder inhalation from a dry powder inhaler.

The dose of microparticles deposited on the lung epithelium is lower than the dose metered in the reservoir of the dry powder inhaler, as previously described. If the objective is a systemic action, only the part of drug deposited in the deep lung can translate into significant blood levels of the drug. The portion deposited in the tracheobronchial region makes a small contribution to the systemic level of drug. The portion deposited in the mouth and swallowed can contribute to the level of drug in the blood, but it is not useful for the therapeutic objective of CUPIDO product.

As illustrated in Figure 1.9, there are several kinetics constants driving the deposition and absorption of drug, as a function of the section of respiratory tree. The drug adsorption process from pulmonary region can be carrier mediated (Michaelis-Menten type) active and/or passive in the lung, while adsorption from the trachea-bronchial region is assumed to be first-order only. Mucociliary escalator kinetics from the pulmonary to the tracheo-bronchial region is represented by a first-order rate constant (K_e). For CUPIDO products, the release of nanoparticles from the microparticles has to be considered as an additional kinetics constant.

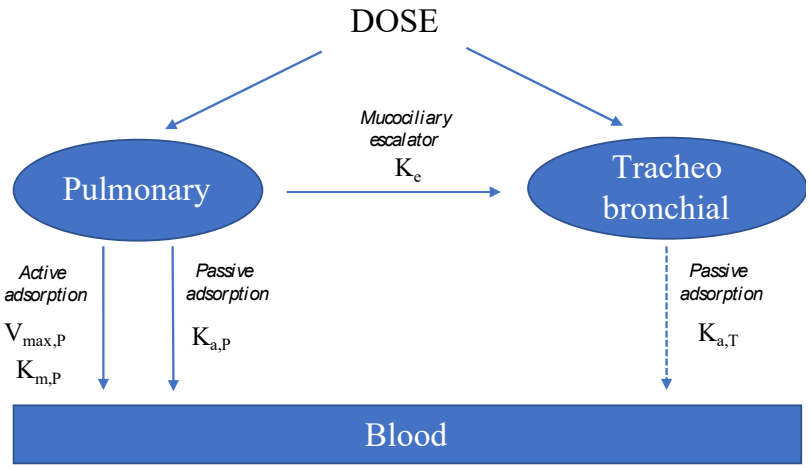

Figure 1.9 Schematic kinetic model of the drug deposition and absorption in the lung. $V_{max,P}$ and $K_{max,P}$ are the maximum rate and "affinity" of the Michaelis-Menten-type, carrier-mediated active adsorption process; $K_{a,P}$ and $K_{a,T}$ are the first-order rate constants for passive adsorption from the pulmonary and the tracheo-bronchial regions, respectively. K_e is the first order rate constant for mucociliary escalator.

2 Aim and objectives

Calcium phosphate nanoparticles have several intrinsic characteristics that make them a promising material for targeted drug delivery. In fact, CaP NPs are totally biocompatible, non-immunogenic and degraded in the cells into non-toxic bioproducts, *i.e.* calcium and phosphate ions[80]. CaP NPs can bind and deliver a wide range of drugs, from antitumor agents, antimicrobials, nucleic acids, peptides, and many others[109,110]. The preparation of CaP NPs is a simple and inexpensive process easily scaled up at industrial level and fully compliant to the principles of green manufacturing. Finally, CaP NPs possess a pH-dependent solubility that makes them naturally stimuli-responsive, since drug release is associated to nanoparticles dissolution triggered by a decrease of pH under 5.0.

Therapeutic agents, adsorbed to or encapsulated within the nanoparticle, can be protected from degradation in the biological environment. This feature is particularly relevant for therapeutic biomolecules such as nucleotides or peptides. Indeed, the *in vivo* delivery, stabilization and cell targeting have resulted so far to be inadequate due to degradation before reaching the active site. Hence, for these therapeutic biomolecules the use of CaP NPs as drug carrier is particularly favoured, since the protective action of CaP NPs is well-known[111,112]. All the above-mentioned features can be tailored for the desired application by changing nanoparticles physicochemical properties, like their morphology, size, surface properties, and chemical composition.

Despite these benefits of nanoparticles, their administration by inhalation remains a challenge since a delivery system able to create a respirable aerosol for nanomedicine deposition in the deep lung, where absorption can take place, is required. Therefore, the aim of this research project was to scale up at industrial level a novel microparticulate inhalation powder drug embedding CaP nanoparticles loaded with drug to be given by inhalation with a Dry Powder Inhaler. The powder aerosol must be able to deposit into the deep lung, release the nanoparticles for their translocation across the gas-blood barrier in pulmonary vein with the goal to target the release to heart.

2.1 First objective

The first objective of the project has been the design and manufacturing of a novel drug loaded CaP nanoparticles having suitable properties for efficient delivering of the therapeutic payload to the heart that is the target organ. Thus, the research was focused on loading of small drugs or biomolecules as therapeutic agents for cardiovascular diseases. Clinically available drugs or

innovative therapeutic compounds for cardiovascular disease (CD) have been loaded in CaP nanoparticles-mediated inhalation heart therapy. CaP nanoparticles must enter the pulmonary-heart blood circulation from where directly reach the heart. After the cardiac tissue targeting, the internalization in cardiomyocytes allow the nanoparticles to release their cargo. This first objective was accomplished in partnership with CNR.

2.1.1 Drug and biomolecules loaded

2.1.1.1 Milrinone

Milrinone (MRN) is a cardiac inotropic and vasodilator drug, commonly used for congestive heart failure treatment. It increases the intracellular cAMP concentration and high calcium supply influx to make a positive inotropic effect, selectively inhibiting the enzyme phosphodiesterase III action. Systemic contractility, vascular resistance, left ventricular filling pressure and pulmonary arterial pressure are decreased and myocardial contractility increased by milrinone thereby improving the thorough heart function. The main milrinone advantage over other cardiac inotropes, such as captopril, nitroprusside and dobutamine, is that significantly downsizes pulmonary capillary wedge and right atrial pressures, atrial pressure left ventricular end-diastolic pressure, jointly with raised stroke work index. MRN is clinically administered by intravenous injection (Primacor®, Sanofi-Aventis, Chilly-Mazarin, France) or orally to adult and pediatric patients for failing heart conditions. Nevertheless, its clinical efficacy may be limited due to lack of target specificity and low bioavailability, besides the side effects, *e.g.,* arrhythmias and renal dysfunction[113].

The development of a milrinone inhalation product may be relevant to overcome the issues related to side effects due to intravenous injection and to improve the low bioavailability of oral milrinone administration.

2.1.1.2 miR-Neg5 (miRNA)

MicroRNAs (miRNAs) are small regulators involved in several biological processes and have been recognized as potential novel therapeutic targets for the treatment and prevention of cardiovascular diseases. The cardiac enriched miR-133 (Figure 2.1), which is inversely related to failing heart conditions, is involved in several aspects of pathological cardiac remodelling and its potential role as therapeutic compound was shown by Castaldi *et al.*[114]. In detail, miR-

133 controls many components of the β_1 adrenergic receptor transduction cascade and is cardioprotective during heart failure.

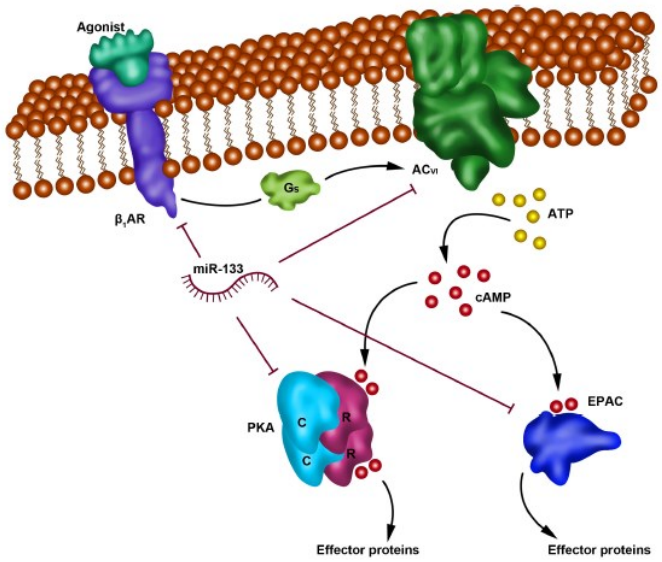

Figure 2.1 Schematic representation of microRNA-133 (miR-133) targeting key components of the β1-adrenergic receptor (β1AR) transduction cascade. ACVI indicates adenylate cyclase VI; C, catalytic subunit; EPAC, exchange protein activated by cAMP; Gs, stimulatory G protein; PKA protein kinase A; and R, regulatory subunit. Reprinted by permission from Wolters Kluwer Health, Inc., Circulation Research, MicroRNA-133 Modulates the β1-Adrenergic Receptor Transduction Cascade, Castaldi A. *et al.*[115], Copyright® 2014.

In previous activities, miRNAs were loaded in synthesized CaPs[82]. In this study Di Mauro *et al.* developed negatively surface charged nanoparticles, which are able to encapsulate and carry miRNAs into cardiac cells both *in vitro* and *in vivo*. In the arising field of nanomedicine, controlling the negative charge of the nanocarriers in terms of surface potential can be beneficial in facilitating the targeting of hyperpolarized and excitable organs. The excitable cells are prone to (electro) toxicity. In fact, by measuring passive and active electrophysiologic properties of cardiomyocytes subjected to charged synthetic nanoparticles, it was discovered that polarized cells have a selective compatibility for negatively charged nanoparticles[116,117]. In agreement with these results, Di Mauro *et al.*[82] demonstrated that negatively charged CaP nanoparticles did not affect the functional measured parameters in cardiac cells. In particular, no changes in passive membrane properties, known to be a signature of arrhythmogenesis, were observed. In the first part of this thesis project, the miR-133 was loaded in Calcium phosphate nanoparticles, prepared following a novel protocol and envisioned to be a new miR-133 drug delivery system by inhalation for heart targeting.

2.1.1.3 Mimetic peptide (MP)

The mimetic peptide MP (11 AA, MW: 1326 Da, α-helix structure, Figure 2.2) is a novel therapeutic tool that selectively targets the cytosolic $Ca_v\beta2$ chaperon subunit of the cardiac L-type Calcium Channel (LTCC) complex. By enhancing/recovering the protein interaction between the subunits of the LTCC complex, MP restores the physiologic protein density of LTCC at the plasma membrane and thus, recovers the altered myocardial function due to various acquired and genetic cardiac pathological conditions[96]. MP was loaded in CaPs synthesized following Miragoli *et al.* dedicated protocol, by adding the peptide in the reactant solutions. The association of MP was successful, producing loaded CaPs with a negative surface charge at physiological pH (-32.0 ± 5 mV), and a mean hydrodynamic diameter of about 80 nm[95].

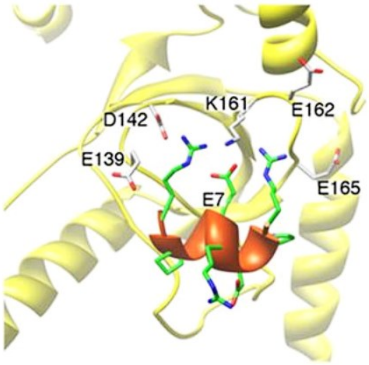

Figure 2.2 Molecular model of the MP (orange) docked onto the tail-interacting domain (TID) region of $Ca_v\beta2$ (yellow), revealing the formation of electrostatic interactions. Reprinted by permission from Wolters Kluwer Health, Inc., Circulation, Peptidomimetic Targeting of $Ca_v\beta2$ Overcomes Dysregulation of the L-Type Calcium Channel Density and Recovers Cardiac Function, Rusconi *et al.*[96], Copyright® 2016.

In the first section of this research thesis, the MP was loaded in Calcium phosphate nanoparticles, prepared following a novel protocol. The nanoparticles preparation preceded the final goal to design and construct a respirable product to be delivered via inhalation to reach the diseased heart.

2.2 Second objective

Nanoparticles for inhalation would be easily administered as water dispersion using nebulizers that transform the liquid in micro-droplets containing nanoparticles. However, the liquid dispersion of nanoparticles suffers for physical and chemical stability. In dry form, individual

nanoparticles are too small for lung deposition following a respiratory act, since nanoparticles could be inhaled, but the risk of exhalation is very high. Microparticulate powder aerosols can deposit into the lung higher amount of drug compared to droplets from the nebulization of dispersion. Then, they can attain on the respiratory epithelium a drug concentration higher than by the systemic route. However, the aerosol inhalation introduces constraints related to powder delivery and lung deposition. Deposition of aerosol microparticles anticipates the drug dissolution and permeation processes in the lung. The combination of drug formulation and aerosolizing device governs the mass of drug aerosolized and inhaled. The drawbacks of the prior art concerning the aerosol products containing nanoparticles, are overcome by a drug powder aerosol made by composite microparticles embedding drug loaded nanoparticles. Then, the manufacturing technology can substantially provide aerodynamic properties to nanoparticles.

Consequently, the second objective of the research was to embed the Calcium phosphate nanoparticles in a dry microparticulate powder able to deliver and release the nanoparticles to the lung epithelium. The strategy adopted was to produce microparticles (between 1-5 μm) by spray drying a water solution of a carrier in which calcium phosphate nanoparticles loaded with active substances have been dispersed. The composition and structure of microparticles are designed to allow the incorporated drug-loaded nanoparticles to target the heart, starting from the aerosol entrance and deposition in the lung. Then, the administration sequence proceeds with the deposition of extra-fine microparticles in the pulmonary alveoli, the release of drug-loaded nanoparticles by dissolution of microparticles and the translocation of nanoparticles into the blood of the pulmonary veins[95,118,119] (Figure 2.3).
In 2017 Torge[120] described the preparation of polymeric nanoparticles embedded by spray drying in mannitol microparticles. The microparticles' structure, respirability and capability to release the nanoparticles protecting the original size, was different from microparticles for inhalation carrying drug loaded calcium phosphate nanoparticles of this thesis. The microparticle formulative process in this thesis was optimized by applying a DoE for discovering the effect of the liquid dispersion composition and spray-drying process parameters on selected Critical Quality Attributes (CQAs) of the microparticles embedding unloaded CaPs (dpCaPs). The unloaded and loaded dpCaPs were tested *in vitro* and *in vivo* for a full spectrum of biocompatibility, toxicity, blood-interaction, air/blood flow-interaction at pulmonary barrier, inflammatory responses, and pharmacokinetics. These activities were

performed in collaboration with CNR (Italy), Imperial College (United Kingdom) and Charitè Universitätsmedizin Berlin (Germany).

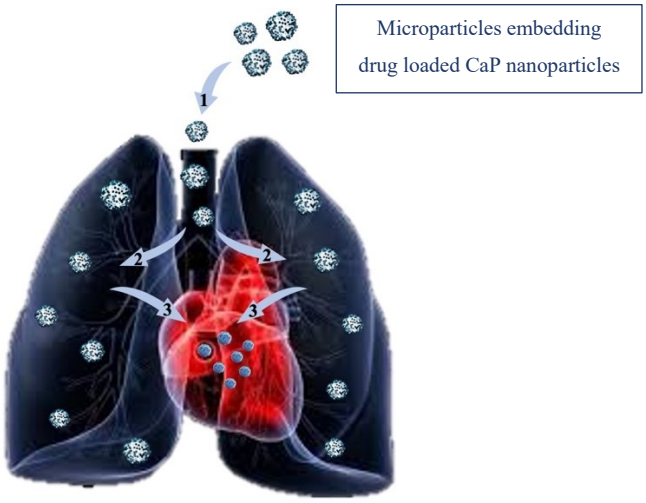

Figure 2.3 Schematic illustration of the concept of microparticles embedding CaP nanoparticles delivered to lung for heart targeting. 1: microparticles inhalation; 2: microparticles deposition in lungs and release of CaP NP that translocate through the air-blood pulmonary barrier; 3: heart targeting and drug release into the heart.

2.3 Third objective

The third objective of this project was to support the study and development of a novel pulmonary device for the dry powder administration (DPI) useful for extra-fine particle delivery, accomplished by the industrial partner of the project Nemera (France).

The administration and absorption of inhaled drugs depends on several factors, among these, the technical characteristics of the inhaler have a fundamental role, beyond the usability by each person. The most recent clinical evidence, highlighted by the main pneumological scientific societies, indicate that inhalation therapy can lose effectiveness if not correctly executed[121,122]. This can occur due to both the characteristics of the inhalers and the patients' ability to take the drug correctly. Hence, in a new pulmonary product, the combination between drug formulation and inhaler is pivotal also for the patient's adherence to the therapy[123]. For the dose administration the use of a pre-metered device has been suggested since the target is not a chronic disease requiring continuous drug administration. Considering the status of patients with a partially impaired pulmonary function, an inhaler with a medium resistance (*i.e.* 60 L/min at 4 kPa pressure drop) was realized.

2.4 Fourth objective

The fourth objective was to assist the industrial manufacturing of the product required for pre-clinical and clinical studies, providing physico-chemical and analytical support. Pilot-scale manufacturing of best performing drug-loaded CaP nanoparticles with initial stability tests, microparticle manufacturing process in industrial environment and formulations combination with the inhalation devices were the steps assisted. The nanoparticles and microparticles obtained were analysed in order to identify any critical steps and potential risks associated with the scale up process. This goal was shared with the industrial partner Finceramica (Faenza, Italy). The optimized microparticles embedding CaPs loaded with therapeutic substance were tested *in vitro* on pulmonary and cardiac cells. Finally, the powder was administered by inhalation to mini-pigs, in order to assess the therapeutic effect of microparticles embedding CaP loaded with mimetic peptide in the heart.

A timetable of PhD program development plan is reported in Figure 2.4.

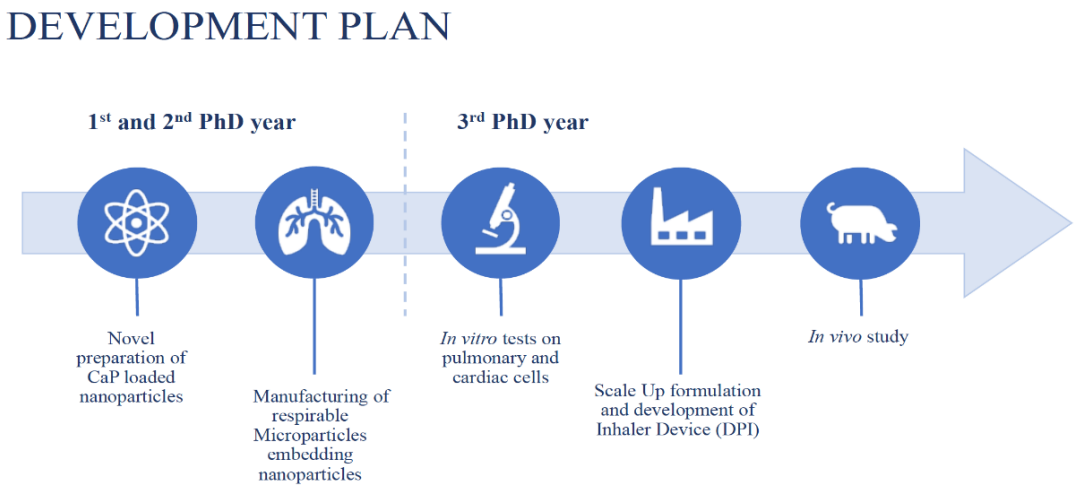

Figure 2.4 Development plan of the three PhD program years.

3 Materials and Experimental Methods

3.1 Materials

To prepare the calcium phosphate nanoparticles, calcium chloride dihydrate ($CaCl_2 \cdot 2H_2O$, > 99.5%, Lot: A1052302649, Emprove®, Merck KGaA, Darmstadt, Germany); disodium hydrogen phosphate dihydrate ($Na_2HPO_4 \cdot 2H_2O$, > 99.0%, Lot: K47479136632, Emprove®, Merck KGaA, Darmstadt, Germany); trisodium citrate dihydrate ($Na_3(C_6H_5O_7) \cdot 2H_2O$, > 99.0%, Lot: K93697842636, Emprove®, Merck KGaA, Darmstadt, Germany); sodium hydroxide NaOH 0.1 N (FU XII Ed.) and ultrapure water purified by reverse osmosis (MIlliQ, Millipore, Molsheim, France) were used. The active API and biomolecules were: milrinone (USP Reference Standard, MW 211.02 g/mol, batch number M781194316, Merck KGaA, Darmstadt, Germany); self-internalized R7W mimetic peptide (purity 97.4%, MW 1326.38 Da, 11 amino acids: DQRPDREAPRS, batch number U8665EG110-1/PE2815, GenScript Biotech, Piscataway, NJ, USA); mimetic peptide MP (purity 95.5%, MW 2605.9 Da, 19 amino acids: RRRRRRRWDQRPDREAPRS, batch number U8459DB280-17PE9065, GenScript Biotech, Piscataway, NJ, USA); miRNA negative control 5 (batch number 345432126, miRNA strand: GAUGCUACGGUCAAUGUUCAAG, miRCURY LNA™ miRNA Mimic 20, Qiagen Sciences, Germantown, MD, USA). For the NPs purification by dialysis, molecular porous membrane tubing (15 cm, diameter 22 mm, MWCO 3.5 kDa, Part number: 132724, Spectra/Por®, Spectrum Laboratories Inc., Rancho Dominguez, Canada) were employed. To manufacture the microparticles, mannitol ($C_6H_{14}O_6$, Emprove® Essential, Parteck M 100 Lot: M781194316, Merck KGaA, Darmstadt, Germany) has been chosen as excipient. Acetonitrile (CH_3CN, VWR International, Fontenay-sous-Bois, France), trifluoroacetic acid (CF_3COOH, 100%, Lot: ON657456, CHROMANORM® VWR International, Fontenay-sous-Bois, France) and hydrochloric acid (37%, HCl, batch number: 17K154012, VWR International, Fontenay-sous-Bois, France) were the component of mobile phase of HPLC developed analytical methods. All solvent used were of analytical grade.

3.2 Experimental Methods

These activities research were performed in collaboration with Dr. Lorenzo Degli Esposti in Laboratory of Bioceramics and Bio-hybrid Composites, CNR - Institute of Science and Technology for Ceramics (Faenza, Italy) headed by Dr. Michele Iafisco.

3.2.1 Calcium phosphate nanoparticles (CaPs) preparation

To obtain the unloaded calcium phosphate nanoparticles (CaPs), two aqueous solutions were prepared: one containing $CaCl_2$ 0.1M and trisodium citrate 0.2 M (pH 6.8) and of disodium phosphate 0.12 M (pH 8.7). The pH of each solution was adjusted to 10.0 using NaOH 0.1 M. Subsequently, the phosphate solution was added to the calcium-citrate solution at a fixed mixing volume ratio of 1:1 (v/v). The final solution was kept to 37°C for 5 minutes to allow the precipitation of CaP nanoparticles. Finally, the flask containing nanoparticles dispersion was put in an ice bath to stop the reaction. The dispersion of precipitated nanoparticles was dialyzed overnight to remove unreacted salts at 25°C for 24 hours across a cellulose dialysis membrane with a cut-off of 3500 Da and immersed in 500 mL of Milli-Q water followed by multiple water exchanges. To assess the CaPs concentration, 1.0 mL of dispersion was collected inside a weighted Eppendorf vial, in triplicate, and centrifuged for 15 minutes at 13000 rpm. The supernatant was removed, and the residual was dried and weighted. The dispersion was recovered and stored at 4°C in a sealed vial.

3.2.1.1 Milrinone (MRN) loading

Several tests were performed to assess the interaction of drugs with the nanoprecipitation environment and the conditions of drug concentration and pH of the solution for nanoparticles preparation method were optimized. Milrinone (Figure 3.1) is soluble in DMSO (20 mg/mL), warm 100% ethanol (3 mg/mL), and DMF (~0.3 mg/mL). It is very low soluble in water. The pK_a of milrinone is 7.21 and pK_b is 5.72.

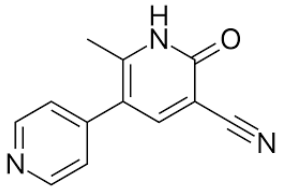

Figure 3.1 Chemical structure of milrinone.

In a second step of optimization, the maturation time was increased, with the aim to lead to the improvement of the interaction of drugs during CaP formation and the minimization of the desorption of drugs during the dialysis purification. Additionally, NaOH 0.1 M was added also to the calcium solution in order to create an environment that is alkaline enough to solubilize the drug. Drug was used at its solubility limit in highly alkaline solution (3 mg/mL) and was dissolved both in calcium or in phosphate phases. To identify the critical aspects in term of drug loading in CaPs, a study was conducted to monitor the milrinone content during nanoparticle loading steps using a specific HPLC assay method.

3.2.1.2 miR-Neg5 (miRNA) and Mimetic Peptide (MP) loading

As in the case of the unloaded calcium phosphate nanoparticles (CaPs) preparation (see Section 3.2.1) the exact same procedure was followed for the preparation of loaded with miR133- and mimetic peptide (MP; 11 AA, MW: 1326 Da, α-helix structure)-loaded CaPs nanoparticles. The only difference of this preparation was that 0.014 mg/mL of micro-RNA (Neg-5) or 0.6 mg/mL of MP were added into phosphate solution.

The lab scale protocol of CaPs loaded with mimetic peptide was transferred at the pilot scale using a five times higher concentration of the reagents than lab scale quantities. However, in order to optimize the mimetic peptide content while remaining compliant with the CaPs good quality, particularly in terms of size (*i.e.* purification from citrate excess) and surface charge, the dialysis time was fixed to 48 hours.

3.2.2 CaP nanoparticles physico-chemical characterization

3.2.2.1 Dimensional analysis and surface charge by Dynamics Light Scattering (DLS)

Hydrodynamic diameter (d_H) and surface charge of the final formulations were measured using Zetasizer Nano ZS operating Zetasizer Software 7.12 (Malvern Instruments Ltd., Malvern, UK). Z-Average diameter, Polydispersity Index (PdI) and ζ-potential were determined using Dynamic Light Scattering (DLS) and Phase Analysis Light Scattering (PALS), respectively.

Dynamic Light Scattering is a non-invasive, well-established technique for measuring the size of particles typically in the submicron region, lower than 1 μm. The principle of DLS for size measurement of fine particles and molecules resides on the constant random thermal motion, called Brownian motion. The Brownian motion is the random movement of particles due to the bombardment by the solvent molecules that surround them. The larger the particle or molecule,

the slower the Brownian motion will be. The hydrodynamic diameter of a particle is calculated from the translational diffusion coefficient by using the Stokes-Einstein Equation 8:

$$d_H = \frac{kT}{3\pi\eta D} \quad (8)$$

where D is the translational diffusion coefficient, k is the Boltzmann's constant, T is the absolute temperature, η is the viscosity of the medium. As reference material, the hydroxyapatite (HA) with a refractive index of 1.63 was selected with backscatter detection of ατ 630 nm and 173° backscatter angle. Since the water has been chosen as dispersion medium, the refractive index of 1.33 and viscosity of 0.887 cP were set-up.

The particle size was expressed as Z-Average diameter, a parameter reported as suitable for quality control as reported by the ISO 22412:2017 guidelines of Particle size analysis — Dynamic light scattering (DLS). Z-average is the intensity-weighed mean particle diameter derived from the cumulants analysis. The polydispersity index (PdI), *i.e.* the dimensionless measure of the broadness of the size distribution, is calculated from the cumulants analysis. Polydispersity Index values smaller than 0.05 are rarely seen other than with highly monodisperse standards. Values greater than 0.07 indicate that the sample has a very broad size distribution and is probably not suitable for the dynamic light scattering technique.

The samples used for DLS measurements were the CaPs dispersions and the CaPs nanoparticles restored from the embedding microparticles dissolved in water. A *restoration protocol* was established to evaluate the influence of the spray-drying procedure and excipient addition on the properties of the restored nanoparticles dispersion (Figure 3.2).

Regarding particle size measurement protocol in the case of the nanoparticles, 1 mL of the dispersion was diluted with 1 mL of ultrapure water, to obtain a CaP concentration of 0.5 mg/mL. Then, the diluted solution was slowly introduced in a cuvette (ZEN0040 in polystyrene, 10x10x45 mm, Sarstedt AG & Co., Nümbrecht, Germany) in order to avoid the formation of air bubbles. Instead, for the restoration protocol, 10 mg of microparticles were dissolved in 4 mL of ultrapure water to release the original NPs concentration of feed solution before spray-drying, i.e. 0.5 mg/mL. Then, a gentle shaking was performed to obtain a clear solution that was then carefully introduced into a polystyrene cuvette. Three measurements for each sample were performed and the run duration was 10s, while the equilibration time was set up at 120s (n=3 ± std.dev.).

Phase Analysis Light Scattering (PALS) measurement was used to determine the nanoparticle surface charge. The ζ-potential was measured using Smoluchowki method for aqueous solution. Briefly, the sample was introduced between two electrodes in a cell of the Zetasizer

(Folded Capillary Zeta Cell, DTS1070, Malvern Instuments Ltd., Malvern, UK). The presence of the dispersed CaP modifies the pattern of electro osmosis between the electrodes when a field is applied. The zeta potential is measured at several distances from the surface of the material. As in the Z-Average diameter measurements, the same procedure for sample preparation was followed for ζ-potential measurement with the liquid samples introduced in the cuvette without dilution. Three measurements for each sample were performed. The run duration was 10s while the equilibration time was set up at 120s (n=3 ± std.dev.).

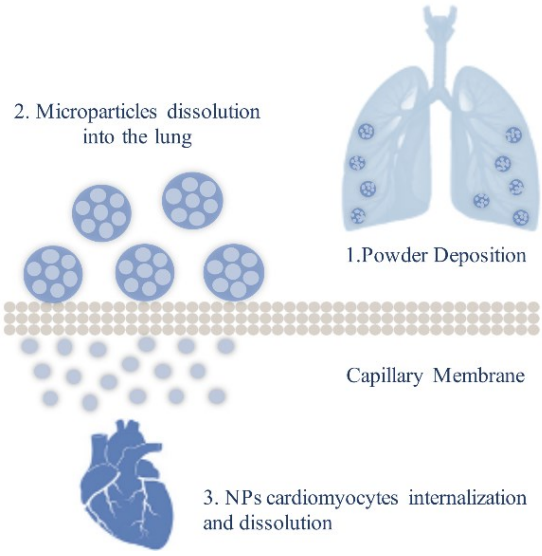

Figure 3.2 Schematic representation of CaP restoration from microparticles embedding nanoparticles.

3.2.2.2 Nanoparticle Tracking Analysis

In order to confirm the particle size distribution and have an evaluation of particle concentration in suspension, a measurement by nanoparticles tracking analysis (NTA) experiment was conducted using NanoSight NS300 (Malvern Instruments Ltd., Malvern, UK) equipped with a 480 nm laser light source, and a 20× magnification microscope with a field of view of approximately 100×80×10 μm. The nanodispersion was diluted to 0.5 mg/mL with ultrapure water in order to obtain a sufficient dilution suitable for single particle tracking. After that, sample was drawn with 1 mL plastic syringe and injected into the instrument sample chamber. Nanoparticles' images were acquired using a video capture mode for three analysis time of 60 seconds each. Measurement was carried out at a defined temperature (25°C) and viscosity (0.828-0.832cP). The built-in sCMOS camera recorded videos and the particle tracking were carried out by NTA 3.1 software. NTA tracks single particles in Brownian

motion due to the light scattered. In detail, the videos of particle's tracks, projected on the x–y plane and observed through a 20× microscope, are analyzed by the software that locates and follows the centre of each individual particle moving in the observation volume. The average distance moved by each particle in the x and y directions is measured. This value is then converted into particle size on the basis of a variation of Stokes–Einstein equation taking into account that the motion is tracked in two dimensions Equation 9:

$$\overline{(x,y)}^2 = \frac{4TK_B}{3\pi\eta d_h} t \quad (9)$$

where k_B is the Boltzmann constant and $\overline{(x,y)}^2$ is the mean squared displacement of a particle during time *t* at temperature T, in a medium of viscosity η, with a hydrodynamic diameter of d_h[124].

The results values were expressed as mean and standard deviation of three runs analysis. Furthermore, knowing the volume of the suspension and the dilution, the associated NTA software can calculate an approximate concentration of the nanoparticles inside the colloidal dispersion[125].

3.2.2.3 Morphology analysis by Transmission Electron Microscopy (TEM) and Cryo-TEM

Transmission electron microscopy (TEM) was used to study the morphology of nanoparticulate samples using bright field imaging in collaboration with IMEM–CNR (Parma, Italy). In addition, selected area electron diffraction (SAED) modality was used to study the crystallinity of single nanoparticles. TEM micrographs and SAED patterns of the samples were collected with a Tecnai F20 microscope (FEI Company, Hillsboro, OR, USA) equipped with a Schottky emitter operating at 120 keV. The dry powder samples were ultrasonically dispersed in ultrapure water and then a few droplets of the slurry were deposited on 200 mesh copper TEM grids covered with thin amorphous carbon films and left in dryer to evaporate for 10 minutes under a fume hood.

The CaP-NPs morphology was evaluated also using cryo-Transmission Electron Microscopy (cryo-TEM), in collaboration with University of Siena (Siena, Italy). The analysis was performed with a TEM CM200 FEG (FEI Company, Hillsboro, OR, USA) equipped with Tem Cam F224HD (TVIPS) and cryotransfer specimen holder 626 DH. The cryo-TEM generates images of nanoparticle in a frozen-hydrated state essentially as they exist in solution. Briefly, 2.3 mL of CaP nanoparticles suspension were frozen before TEM analysis using a Vitrobot

Mark IV (FEI Company, Hillsboro, OR, USA) on copper grid Quantifoil applying the instrument parameters: blot force -2, blotting time 3 sec, humidity 100%, T 20°C.

3.2.2.4 Chemical composition analysis by Inductively coupled plasma optical emission spectroscopy (ICP-OES)

Inductively coupled plasma optical emission spectroscopy was used to determine elemental composition of the samples. Quantification of Ca and P in the nanoparticles was carried out by ICP-OES spectrometer Agilent 5100 ICP-OES (Agilent Technologies, Santa Clara, CA, USA). Samples were prepared by dissolving 500 µL of CaPs sample in 200 µL of 1% HNO_3 solution then diluted to 10 mL (Nitric Acid HNO_3 65%, batch number: 7697372, Merck KGaA, Darmstadt, Germany). Standard solutions obtained by dilution of certified 1000 ppm standards (Sigma Aldrich, St. Louis, MO, USA) of investigated atoms were used for creating a concentration/emission calibration curve in the concentration range 1–100 ppm.

3.2.2.5 Powder X-ray Diffraction (PXRD)

Powder X-ray Diffraction was used as a non-destructive analytical technique for solid state analysis and discrimination between crystalline and amorphous samples. The PXRD patterns of the samples were recorded on a D8 Advance diffractometer (Bruker, Karlsruhe, Germany) equipped with a Lynx-eye position sensitive detector using Cu Kα radiation (λ = 1.54178 Å) generated at 40 kV and 40 mA as X-ray source. Spectra were recorded in the 2θ range from 10 to 60° with a step size (2θ) of 0.02° and a counting time of 0.5 s.

3.2.2.6 Fourier transform infrared spectroscopy (FT-IR)

Fourier transform infra-red spectrometry was used to characterize the vibrational structure of the samples, to assess the presence of functional groups, and to study variations in local order. For spectroscopic characterization, the FT-IR analyses were carried out on a Nicolet iS5 spectrometer (Thermo Fisher Scientific Inc., Waltham, MA, USA) with a resolution of 2 cm^{-1} by accumulation of 32 scans covering the 4000 to 400 cm^{-1} range, using a diamond ATR accessory model iD7.

For vibrational peak deconvolution the FT-IR analyses were carried out with a resolution of 2 cm^{-1} by accumulation of 64 scans covering the 4000 to 400 cm^{-1} spectral range with the same

instrument in transmission mode using the KBr pellet method. In detail, during preparation about 1 mg of the lyophilized CaPs sample was ground finely along with 100 mg of anhydrous KBr to remove scattering effects from large crystals. This powder mixture was then pressed at 8,000 psi into 7 mm diameter disc to form a translucent pellet through which the beam of the spectrometer can pass through. A pure KBr disk was used as a blank. Curve fitting, peak deconvolution, and quantification of integral areas using Gaussian and/or Lorentzian functions were done using MagicPlot software (Magic Plot Systems LLC, Saint Petersburg, Russia).

3.2.3 Microparticles embedding CaP nanoparticles (dpCaPs) manufacturing

3.2.3.1 Unloaded dpCaPs Design of Experiments (DoE) study

Preliminary, the preparation of spray-dried microparticles embedding unloaded CaPs (dpCaPs) was studied by applying a Design of Experiment (DoE). In particular, a two-level full Factorial Design with 3 factors (2^3=8) was applied allowing for the investigation of all the possible combinations between the selected levels. In addition, 3 center points were added in order to check for a possible curvature. The design was of resolution V meaning that since it is a full factorial all the possible combinations are investigated in the design. Therefore, there is no confounding effect between the main parameters and interactions[126]. Thus, in total 11 experiments were generated in a randomized way to avoid bias using Design-Expert Software® Version 12 (Stat-Ease Inc., Minneapolis, MN, USA).

The three factors selected for this DoE and their respective levels were:

A: CaPs concentration (mg/mL) [0.5-7.0],

B: Mannitol concentration (mg/mL) [0.5-2.0],

C: Feed rate (mL/min) [3.5- 7.0] (Table 3.1, Figure 3.3).

In the current study the selected responses (Critical Quality Attributes, CQAs) evaluated after the preparation of the 11 powders using Design Expert® software were: yield of the process, moisture content, CaPs hydrodynamic diameter (d_H) after restoration in water (Z-Average diameter), microparticles size distribution (median volume diameter, Dv_{50}), microparticles aerodynamic performance measured as Emitted Dose (ED) and Fine particle mass (FPD).

The analysis of each response was performed using primarily statistical graphs (Pareto charts, half-normal probability plots) and ANOVA (Confidence Interval = 95%) in order to evaluate the significance of the mathematical model as well as the impact of each factor on the response. Furthermore, several other graphs were used as auxiliary means to visualize and detect potential interactions and curvature.

Table 3.1 Matrix of the full-factorial design.

Std	Run	Factor A: CaPs conc. (mg/mL)	Factor B: Mannitol conc. (mg/mL)	Factor C: Feed rate (mL/min)
6	1	7.0	2.0	3.5
4	2	7.0	0.5	3.5
7	3	0.5	2.0	3.5
1	4	3.75	1.25	5.25
8	5	0.5	0.5	3.5
11	6	7.0	0.5	7.0
5	7	0.5	0.5	7.0
9	8	3.75	1.25	5.25
3	9	0.5	2.0	7.0
10	10	3.75	1.25	5.25
2	11	7.0	2.0	7.0

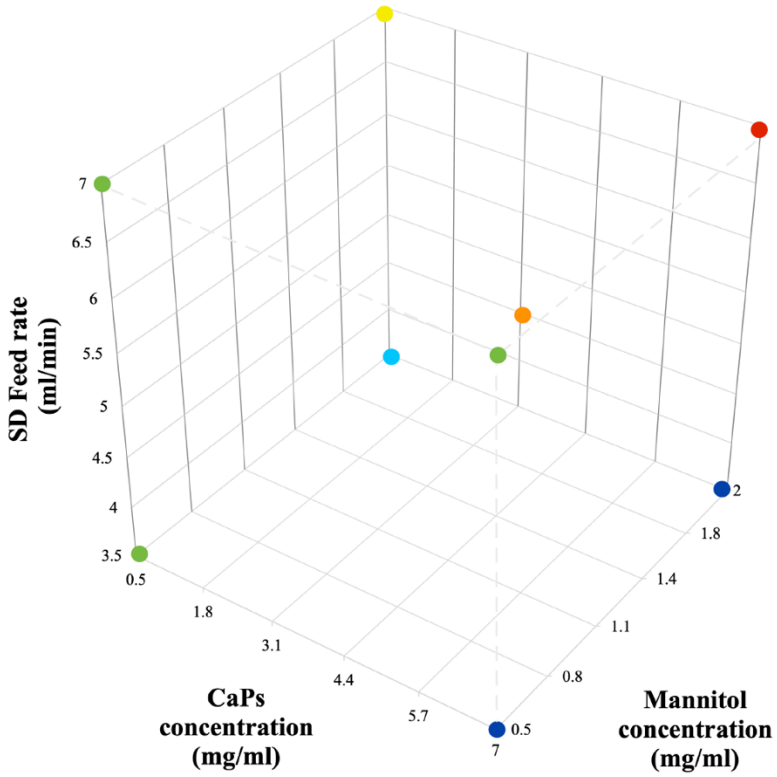

Figure 3.3 Schematic representation of the Full factorial design matrix (Design-Expert Software® Version11).

3.2.3.2 Preparation of spray-dried microparticles embedding unloaded CaPs (dpCaPs)

The dry powders for inhalation were produced using a Büchi Mini Spray Dryer (SD) B-290 (Büchi Laboratory Equipment, Flawil, Switzerland). In detail, the aqueous dispersions to be dried were obtained starting from nanoparticle dispersions concentrated 7.0 mg/mL and diluted to obtain a concentration from 0.5 mg/mL to 7.0 mg/mL. Subsequently, amounts of mannitol were added and dissolved in the CaPs dispersion in order to achieve a mannitol concentration from 0.5 mg/mL to 2 mg/mL. The final solid concentration of feed solutions to be dried was in a range between 1.0 and 9.0 mg/mL. The feed rate was set from 3.5 mL/min to 7 mL/min, according to the factor combinations generated by the Design Expert® (Table 3.1). All aqueous dispersions to be dried were kept under constant magnetic stirring at 250 rpm throughout the drying process. Initially, CaP unloaded samples were spray-dried at 150°C of Inlet Temperature. Then the Inlet T was reduced to 125°C envisioning to preserve, during drying of the biomolecule loaded nanoparticles, the stability of biomolecules. The selected spray drying operating parameters are reported in Table 3.2.

Table 3.2 Spray drying operating parameters for dpCaPs preparation.

Inlet Temperature	125°C
Atomizer Air Flow rate	600 L/h
Aspiration	100% (35 m^3/h)
Nozzle	0.7mm

3.2.3.3 Preparation of microparticles embedding drug loaded CaPs nanoparticles (loaded dpCaPs) by spray drying

In reference to the results of the DoE performed on the spray-dried unloaded CaPs, inhalable microparticles embedding the unloaded CaPs nanoparticles (dpCaPs), drug loaded calcium phosphate nanoparticles were diluted with purified water to 0.5 mg/mL. Mannitol, as particle former, was dissolved in the nanoparticles' dispersion in ratio CaPs: mannitol 1:4. The concentration of the feed solution to dry was 2.5 mg/mL. Then, a spray drying process was carried out with a mini spray-dryer Büchi B-290. The spray dried powders were manufactured in the following drying conditions: inlet air temperature, 125°C; outlet temperature in range

between 70-75°C; pump feed rate, 3.5 mL/min; aspiration rate, 35 m^3/h (100%); atomizing air flow rate, 600 L/h. A nozzle of 0.7 mm was employed. Finally, the dry powders were recovered from the collection vessel and stored in a sealed glass vial at 20-25 °C.

3.2.3.4 Yield of spray drying process

Yield of the process was calculated for all the powders using the Equation 10:

$$Yield\ (\%) = \frac{W_A}{W_T} * 100 \qquad (10)$$

where W_A is the weight of the actual amount of powder collected (product collection vessel plus cyclone) and W_T is the theoretical amount of the powder based on the total weight of the solids in the dispersion to be dried.

3.2.4 Microparticles embedding CaP nanoparticles physico-chemical characterization

3.2.4.1 Scanning electron microscopy (SEM)

The microparticles morphology and the surface characteristic of the powders were investigated by scanning electron microscopy (SEM), in collaboration with IMEM-CNR in Parma, Italy. The instrument employed was a Field Emission Scanning Electron Microscope - Focused Ion Beam (FESEM-FIB, Auriga Compact, Zeiss, Jena, Germany) equipped with different resolution fields emission microscope and working distances. The samples were prepared by placing 1-2 mg of microparticles into a carbon tape on an aluminium sample stab.

In order to study the interior structure of the microparticles embedding CaPs for tailored porosity analysis, the particles were cut by FIB etching (course-line) with an operating voltage of 1 kV and a current of 1 nA, followed by FIB polishing (fine-line) with an operating voltage of 30 kV and a current of 100 pA. In few cases, prior to the FIB etching process, a platinum coating process (30 kV,50 pA) was performed for 60 s in the FIB instrument to protect the sample from electrical damage, that may lead to the change in the surface morphology (less spiky). Images were taken in SEM mode with the same SEM operating conditions after FIB processing at magnifications ranging from 5.000x to 70.000x.

3.2.4.2 Particle size distribution analysis by Laser Diffraction

The measurement of particle size distribution (PSD) of dried powders was done using the diffractometer Spraytec (Malvern Instruments Ltd., Malvern, UK). It was equipped with 300

mm focal lens, which measure particle size in the range from 0.1 to 900 μm. Spraytec is based on the principle of laser diffraction that measures particle size distributions, by measuring the angular variation. This is assessed in intensity of light scattered as a laser beam passes through a particulate sample that is dispersed in a liquid, in which the particles are not soluble. Large particles scatter light at small angles relative to the laser beam and small particles scatter light at large angles. The angular scattering intensity data, is then analyzed to calculate the size of the particles responsible for creating the scattering pattern, using the Mie theory of light scattering. The particle size is reported as a volume equivalent sphere diameter.

Briefly, 10 mg of powder were dispersed in 10 mL of Span 85 (batch number: 1302944, Merck KGaA, Darmstadt, Germany) 0.1% w/v in cyclohexane (C_6H_{12}, VWR International, Fontenay-sous-Bois, France). The dispersion was placed in ultrasonic bath (Ultrasound bath, USC 300T VWR International, Fontenay-sous-Bois, France) for 1 min and subsequently analyzed. The particle size distribution was measured with 5% threshold obscuration. Data were expressed as volume diameter of 10^{th} (Dv_{10}), 50^{th} (Dv_{50}) and 90^{th} (Dv_{90}) percentiles of the particle population and as Span value [(Dv_{90} -Dv_{10})/Dv_{50}].

3.2.4.3 *In vitro* aerodynamic assessment by DUSA, FSI and NGI

The aerodynamic performance of the powders was evaluated using a Fast Screening Impactor (FSI) (Copley Scientific, Nottingham, UK). FSI is an abbreviated impactor based on the proven Next Generation Impactor (NGI) technology the pre-separator of which, is the natural basis for this FSI. FSI is used for a first screening of the formulations and is characterized by easiness for automation, reduced time that allows more samples to be measured and less complex mechanism, tending to decrease handling errors. Four components compose this specific impactor. A mouthpiece adapter that is useful for the airtight seal-connection of the DPI under test with the induction port, which is fitted in a right angle and imitates the human throat. A vacuum pump is connected to the outlet of the impactor by a tube of appropriate length and is utilized to drag the aerosol cloud. The fourth component is the main part of the impactor and it consists of two-stages. The first one that is called Coarse Fraction Collector (CFC) is employed for the capture of large non-inhalable particles (>5 μm), namely coarse fraction. This is equipped with an interchangeable insert, enabling a cut-off of 5μm at 60 L/min. The second one is the Fine Fraction Collector (FFC) for particles with an aerodynamic diameter lower than 5 μm. Particles that are not captured in the CFC keep following the airstream and deposit on a glass fiber filter (Type A/E glass fiber disc filter 76.0 mm in diameter, 100/PK, batch number: T70857, Pall SRL, Buccinasco, IT) of the fine fraction collector (FFC).

More specifically, a quantity for each powder (40±0.5 mg) was weighed on an analytical balance (sensitivity 0.1 mg, Gibertini Crystal, Novate Milanese, Italy) directly into size 3 capsules (provided by Qualicaps® QUALI-V I, HPMC based capsule) Lot: E1403210). The capsule was then inserted into the holder chamber of the RS01® (Medium Resistance Monodose Dry Powder Inhaler, Plastiape, Lecco, Italy) device or Nemera device (medium resistance) and pierced. The whole system device-capsule was weighed. Subsequently, the filter was weighed and the entire system was connected to a vacuum pump (Mod. 1000, Erweka GmbH, Langen, Germany) which created the air flow to aerosolize the powder and distribute it in the FSI. The flow rate used during each test was adjusted, according to current USP monograph, with a Critical Flow Controller TPK (Copley Scientific, Nottingham, UK) in order to produce a pressure drop of 4 kPa over the inhaler. Thus, flow rate was set at 60 L/min before each experiment using a Flow Meter DFM 2000 (Copley Scientific, Nottingham, United Kingdom). The flow activation time (in seconds) was calculated according to Equation 11:

$$Activation\ time = 240/Q \quad (11)$$

where Q (L/min) is the test flow rate.

Therefore, the pump was activated for 4 seconds for each test so that a volume of 4 L of air was withdrawn from the inhaler. After aerosolization the FFC was dismantled and the filter as well as the system device-capsule was weighed. The difference of the weight before and after actuation for the system device-capsule results in the Emitted Dose (ED) of the powder which expresses the amount of powder leaving the device after actuation and entering the impactor. The ratio between the ED and the initial weight of the powders gives the Emitted Fraction (EF). Finally, the difference of the weight before and after actuation for the filter results in the Fine Particle Dose (FPD) of the powder (aerodynamic diameter < 5 mm) while the ratio of the FPD with the ED gives the Fine Particle Fraction (FPF). ED, EF, FPD and FPF are all considered CQAs and indicators of the powder aerodynamic performance. Each experiment was performed in triplicate and the data are expressed as the mean.

Aerodynamic particle size distribution of the most promising microparticles embedding loaded with peptide CaP nanoparticles was further investigated using a Next Generation Impactor (NGI) equipped with a rubber adaptor to fit RS01® and Nemera devices in the induction port and a micro-orifice collector (MOC) fitted with a glass fiber filter (Paper filters, Whatman, Sigma- Aldrich, St. Louis, MO, USA, 934-AH grade, 82 mm, 435 μm). The apparatus, as described in the Ph. Eur. 9th ed, consists of a sequence of metal collection cups, with nozzles of distinct cut-off diameters, interconnected to form successive stages. The aerosol is

transported through the apparatus stages following a controlled airflow and is fractioned in function of the aerodynamic diameter.

Before running the experiment, 2 mL of a solution of Tween 80 in ethanol (1% w/v) was applied on the particle collection surface of each stage; after complete solvent evaporation a thin layer of surfactant was obtained on the stage surfaces that ensured efficient particle capture (avoided particle bouncing). For each experiment, 3 capsules (loaded with 40 mg of powder) were discharged into the NGI. Flow rate generated by a vacuum pump (SCP5, Copley scientific Ltd, Nottingham, UK) was set at 60 L/min, using a Flow Meter DFM 2000 (Copley scientific Ltd, Nottingham, UK), and activated for 4 seconds through a Critical Flow Controller TPK (Copley scientific Ltd, Nottingham, UK). Since each stage corresponds to a specific size range, the data obtained, plotted as particle size distribution versus size, allow to calculate the MMAD (Median Mass Aerodynamic Diameter) and geometric standard deviation (GSD) of the aerosol. During the NGI experiment, the aerosol moved along seven size stages according to the diameter of the particles and upon deposition, drug was collected by washing the impactor with HCl 0.1 M to obtain the total release of peptide from CaPs. After the powder aerosolization, samples were collected with 25 mL of HCl 0.1 M volumetric flasks for device plus capsule and 10 mL for induction port samples. Powder deposited on stages was solubilized with 5 mL of HCl 0.1 M. Filter was removed from the system and put in a crystallizer, 7 mL of HCl 0.1 M were added, and the crystallizer was put 2 minutes in an ultrasonic bath. The solutions obtained from filter and device plus capsule were filtered with 0.45 μm cellulose acetate syringe filters (Labservice Analytica S.r.l., Bologna, Italy), before injection in HPLC.

Different aerodynamic performance parameters were calculated: the MD (metered dose) is the amount of drug loaded in the device; the ED (emitted dose) is the amount of peptide from the induction port to the filter; EF (emitted fraction) as percentage ratio between the ED and amount of powder loaded in the capsule (MD); Fine Particle Dose (FPD), the mass of the aerosolized peptide with an aerodynamic diameter lower than 5 μm; Fine Particle Fraction (FPF) was determined as percentage of the FPD with respect to the ED. Moreover, Mass Median Aerodynamic Diameter (MMAD) defined as the diameter which separates the powder in two populations with equal weight was determined by plotting the cumulative percentage of mass less than the cut-off diameter for each stage on a probability scale versus the aerodynamic diameter of the stage on a logarithmic scale. Geometrical Standard Deviation (GSD) is a parameter indicating how wide particle size distribution as reported in USP41 chapter 601.

The GSD was calculated according to USP41 Equation 12:

$$GSD = \sqrt{\frac{sizeX}{sizeY}} \quad (12)$$

where size X is the aerodynamic diameter at 84.13% of the particle population and size Y is the aerodynamic diameter at 15.87% of the particle population.

The GSD (geometric standard deviation) gives a measure of how much the particle diameters are different from each other; it is a value between 1.2 and 2. When the value is equal to 1 indicates a monodisperse aerosol consisting of equal particles. The desirable values are those close to 1.2 because it indicates a polydisperse aerosol but composed of particles with similar granulometry. MMAD and GSD were calculated based upon the inverse normal of the cumulative percentage under the stated aerodynamic diameter versus the log of the effective cut-off diameter. Linear regression of the five data points closest to 50% of the cumulative particle mass that entered the impactor was performed to compute the MMAD and GSD. The cut-off diameter of NGI stages was calculated and corrected for the different flow rates.

To test the novel inhaler device, the emitted dose uniformity was tested using a Dosage Unit Sampling Apparatus (DUSA) operating for the duration of time to allow 2 L of air, as specified in USP41, at flow rates of 30,60 and 90 L/min. In all the cases, dose collection was carried out under critical flow control conditions (TPK Copley S/N 02043440, Copley Scientific Ltd, Nottingham, UK). The test was performed on Nemera prototype device for each condition of misuse examined. DUSA apparatus consisted of a filter support base with an open-mesh filter support in which a glass microfiber filter (Type A/E 47 mm, Pall SRL, Buccinasco, IT) was inserted to collect the micro or submicron fraction of aerosol. A collection tube of 115.4 cm^3 aluminium was screwed, from one side, to the filter support base and on the other side to the mouthpiece adapter. The filter support base was connected to the Critical Flow Controller TPK, which was in turn connected with the vacuum pump. On the opposite side, the Dry Powder Inhaler was connected to the mouthpiece adapter. At the beginning of each experiment, flow meter (Copley Scientific Mod DFM 2000 S/N 4043 1302 005, Copley Scientific Ltd, Nottingham, UK) was used to measure and adjust the flow at 30,60 and 90 L/min. Before discharging the dose from the device, the vacuum pump (SCP5, Copley Scientific Ltd, Nottingham, UK) was turned on and the inhaler was loaded. The powder recovered on the filter was gravimetric determined before and after the aerosolization together with the device. Data are expressed as Emitted fraction that is the percentage referred to the amount of 40 mg of microparticles loaded in a HPMC size 3 capsule.

3.2.4.4 Thermogravimetric analysis (TGA)

Thermogravimetric analysis for the calculation of the residual solvent content in the powders was performed with a TGA/DSC (METTLER Toledo, Worthington, OH, USA). The principle of operation for TGA is that it measures weight changes in a material as a function of temperature (or time) under a controlled atmosphere. A TGA analysis is performed by gradually raising the temperature of a sample in a furnace as its weight is measured on an analytical balance that remains outside of the furnace. In TGA, mass loss is observed if a thermal event involves loss of a volatile component. Finally, the weight of the sample is plotted against temperature or time to illustrate thermal transitions in the material. For the analysis of the dry powder formulations 3-5 mg of each spray-dried powder were weighed in 70 μL alumina pan with a pierced cover (crucibles) using the balance of the instrument (sensitivity 1.0 μg). The analysis was performed by heating the sample under a flux of dried nitrogen (80 mL/min) from 25ºC to 150ºC at a rate of 10ºC/min. The weight loss and therefore, the residual solid content was measured in the range between 25ºC and 150ºC.

3.2.4.5 Differential scanning calorimetry analysis (DSC)

DSC is a thermo-analytical technique which measures the difference in the heat flow rate to the sample and to a reference sample while they are subjects to a controlled temperature program. It was conducted to detect spay dried powders melting point, therefore, to investigate solid state. The powder differential scanning calorimetry analysis was performed using DSC model 821e instrument driven by a STARe software (METTLER Toledo, Worthington, OH, USA). Measurements were preceded by a calibration with Indium (onset of melting T_m=157.1°C, enthalpy of melting DH_m = 27.84 $J \cdot g^{-1}$). DSC traces were recorded by placing accurately weighed quantities (4–6 mg) of powder in a 40 μL aluminium pan which was then sealed and double pierced. Scans were performed between 25 and 200°C using a heating rate of 10 °C/min under purging nitrogen atmosphere at a flow rate of 100 mL/min.

3.2.4.6 Bulk and tapped density determination

Bulk and tapped densities were determined following Ph. Eur. 9th ed. prescriptions. For bulk density, 500 mg of spray dried powder were gently introduced, without compacting, into a 10 mL graduate cylinder (readable to 0.1 mL). Powder was carefully level and the unsettle apparent volume was read. Density was, finally, calculated as ratio between mass (g) on volume

(mL). Tapped density was evaluated employing a tapped density tester (model SVM 122, Erweka GmbH, Langen, Germany). The 10 mL graduate cylinder containing the poured 500 mg of powder was tapped for 10, 500 and 1250 taps. After every tap step volume was read. According to the Pharmacopoeia requirements, since the difference between V_{500} and V_{1250} was > 0.2 mL, others 1250 were performed until the volume read was stable. This test was carried out in triplicate.

3.2.4.7 True density measure through a gas pycnometer

True density of unloaded and loaded microparticles was measured with AccuPyc II 1340 gas pycnometer (Micromeritics Instrument Corporation, GA, USA) driven by an AccuPyc II 1340 V.109 software. Helium (purity 5.0) was used as measuring gas. The measurements were conducted at ambient temperature nearly 30 minutes after the equipment switch on and the saturation of the pipelines with the gas. A cell of 1 cm^3 was used. Before the sample measurements the equipment was calibrated using a stainless-steel sphere (Instrumental kit n. 133-34905-00). To perform the density determination, an amount corresponding to about 500 mg of each sample was accurately weighted (balance E154, Gibertini, Milano, Italy, sensitivity 0.1 mg). Then, the specimen was inserted in the measuring cell; the sample occupied around the ¾ of the cell volume. The instrument was operated, and the density computed on the base of the volume of gas in the cell. Three measurements were performed for each sample.

3.2.4.8 Analytical method for milrinone quantification

The milrinone content was investigated using High Performance Liquid Chromatography (HPLC) readapting the analytical method reported in the specific monography by United States Pharmacopeia (USP41). The equipment used was Agilent 1200 LC Series (Agilent Technologies, Santa Clara, CA, USA), Software ChemStation v. A.04.02 coupled with UV detector. The sample injection volume was set at 10 µL and as stationary phase, Xterra C18 4.6 mm X 30 mm – 2.5 µm (Waters spa, Milano, Italy) thermostated at the temperature of 20°C column was used. The solvent of dissolution was a mixture of ultrapure water (H_2O) and acetonitrile (ACN) in the ratio of 87:13 and few drops of Trifluoroacetic acid (TFA). The mobile phase was made of two different solvents: Solvent A_H_2O + TFA 0.1 (%v/v) and Solvent B_ACN + TFA 0.1 (%v/v). The elution gradient is reported in Table 3.3:

Table 3.3 Gradient elution program of the milrinone.

TIME (minutes)	Solvent A (%)	Solvent B (%)
0	100	0
10	85	15
10.1	100	0
16	100	0

The analyses were carried out at fixed flow rate of 1.0 mL/min, the UV/VIS detector was set at λ 328 nm (wavelength) and the run time was 16 minutes. Each sample was injected 6 times and the 3 closer value were used to calculate mean and standard deviation. Under these conditions, the peak retention time was 2.7 minutes.

Each sample were injected three times and in Table 3.4 are shown the AUC average values, standard deviation and relative standard deviation (RSD%) of milrinone calibration curve.

Table 3.4 AUC values, Standard Deviation and RSD%, calculated for each standard concentration of the milrinone.

Milrinone Concentration (mg/mL)	AUC Average	Standard Deviation	RSD (%)
0.020	969.8	0.15	0.016
0.060	2887.7	3.21	0.111
0.080	3862.7	1.53	0.040
0.120	5797.3	9.45	0.163
0.150	7352.0	5.29	0.072

Linearity of the responses, obtained by injecting five standard solutions at increasing concentration, was assessed between 20.0 µg/mL and 150.0 µg/mL (R^2= 0.999) (Figure 3.4). The limit of detection (LOD) and the limit of quantification (LOQ) were 2.6 µg/mL and 8.0 µg/mL, respectively.

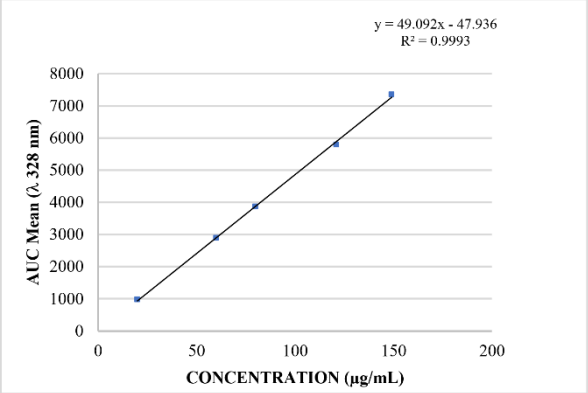

Figure 3.4 Relationship between milrinone concentration and detector response at λ 328 nm in the concentration range 20.0 and 150.0 µg/mL of milrinone in water and acetonitrile in the ratio of 87:13.

3.2.4.9 Analytical method for mimetic peptide MP content determination

In order to quantify the mimetic peptide (MP) content either in the MP loaded CaP nanoparticles dispersion and in the spray dried microparticles embedding MP-loaded CaPs, an HPLC method was developed by using HPLC-UV (Agilent 1200 LC Series, Agilent Technologies, Santa Clara, CA, USA). The separations were performed using a column Alltima C18 (5µm, 250×4.6mm) column (Hichrom, Reading, UK) and a gradient elution using as eluent A an aqueous solution of TFA 0.065% v/v and as Eluent B acetonitrile plus TFA 0.05% v/v. Gradient conditions are reported in Table 3.5.

Table 3.5 Gradient composition of mobile phase as eluent A (H20_TFA 0.065% v/v) and eluent B (ACN_TFA 0.065% v/v) at different time points.

TIME (min)	A (%)	B (%)
0.01	85	15
2.00	85	15
25.00	35	75
25.01	5	95
27.00	5	95
27.01	95	5
30.00	95	5

The flow rate was 1.0 mL/min and the wavelength was set up at 220 nm while the temperature and analysis time for each sample were at 25°C and 30 min, respectively. The injection volume was 100µL. The method has been validated before in terms of precision, accuracy, sensitivity

and linearity in the range from 10.0 to 140.0 µg/mL (Table 3.5). The LOD was 1.4 µg/mL and LOQ is 4.4 µg/mL.

According to ICH Q2[127] recommendations, the accuracy was determined by assessing the percentage recovery of known concentrations of mimetic peptide injected with unloaded CaPs nanoparticles. Pre-analysed standards at three levels of concentration (10.0, 69.5 and 140.0 µg/mL) were spiked with 250.0 µg/mL of unloaded CaPs nanoparticle formulation. The experiment was conducted in triplicate and percentage recoveries and RSD were calculated.

For the three concentration levels tested, recovery was within the 100 ± 1% limit with RSD values lower than 2%, precisely 1.99%. The method is accurate for the mimetic peptide, as percentage recovery and RSD values obtained indicate an intimate concordance between theoretical and experimental results.

The method precision was assessed in terms of intermediate precision (inter-day) and repeatability (intra-day). The precision was determined at three different concentration levels included in calibration curve: the lower (10.0 µg/mL), intermediate (69.5 µg/mL) and highest (140.0 µg/mL) for CaP loaded MP nanoparticles. Repeatability of the method was demonstrated by the concentration recovery (100 ± < 2 %) and RSD (< 2%) for six repeated injections per sample, of the three samples replicates analysed in the same day. Residual standard deviation of recovered concentrations of 0.6%, *i.e.* lower than 2% for all analytes at the three concentration levels, in three alternated days, confirmed the intermediate precision.

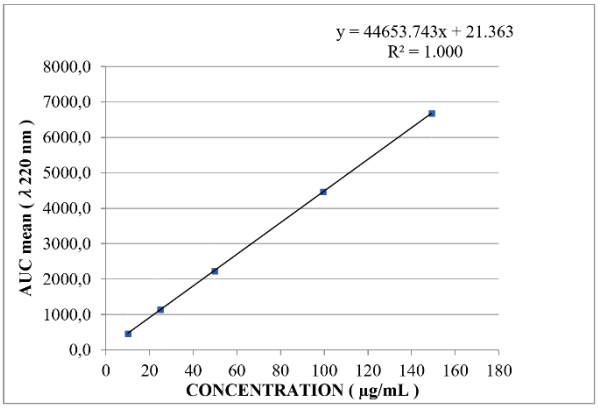

Figure 3.5 Relationship between MP concentration and UV detector response at λ 220 nm in the concentration range 10.0 µg/mL and 140.0 µg/mL of peptide in HCl 0.1 M.

Before every analysis a standard of MP was precisely weighed (sensitivity 0.01 mg) and dissolved in a HCl 0.1M solution in order to achieve a concentration close to the sample to be analyzed and within the linearity concentration range of MP.

Then, for the preparation of the blank sample with no analyte, 1 mL of unloaded CaPs dispersion were dissolved in 1 mL of HCl 0.1 M. After 10 minutes at room temperature for the complete degradation of the CaPs, the sample was shaken gently to obtain a clear solution and the obtained solution was transferred in a glass HPLC vial of 1.5 mL. The same procedure was followed for the preparation of the MP loaded CaPs dispersion.

For the microparticles embedding MP loaded CaPs, 20 mg of each spray-dried powder were weighed and dissolved in 2 mL of HCl in a glass vial of 5 mL. In cases that after 15 minutes at RT the microparticles were not completely dissolved, a gentle shaking or sonication in water bath for 2-3 minutes was performed (Ultrasound bath, USC 300T VWR International, Fontenay-sous-Bois, France) and the obtained clear solution was transferred in a glass HPLC vial of 1.5 mL to be analyzed.

3.3 Pulmonary and extra-pulmonary *in vitro* viability, cytotoxic and apoptotic levels following exposure to dpCaPs

Disclosure

These activities were performed in National Heart and Lung Insitute, Imperial College London (London, UK), by Dr Michele Chiappi in the Lung Cell Biology Group lab, headed by Professor Terry Tetley.

All human lung tissue used in this study was surplus and obtained following lung resection for carcinoma of the lung. Written informed consent was acquired for all patient samples and the research was carried out with approval of the Royal Brompton and Harefield Ethical Committee (Ref: 8/H0708/73).

Reagents and materials

All chemicals used were purchased from Merck KGaA (Darmstadt, Germany) unless stated otherwise.

3.3.1 Culture of immortalized human alveolar type 1-like epithelial (transformed type 1; TT1) cells

Human pulmonary TT1 cells are an immortal alveolar type 1(AT1)-like epithelial cell line derived from primary human alveolar type 2 (AT2) epithelial cells. TT1 cells were cultured in Defined Cell Culture Medium-1 (DCCM-1) (Biological Industries, Kibbutz Beit Haemek, Israel) supplemented with 10% newborn calf serum (NCS) or 10% fetal bovine serum (FBS; Gibco®, Thermo Fisher Scientific, Gloucester, UK) and 1% penicillin/streptomycin/glutamine (PSG).

Trypsin-EDTA was used to dissociate the TT1 monolayers into a single cell suspension, followed by the addition of 10% serum-supplemented DCCM-1 to neutralize the trypsin; this suspension was centrifuged at 317 g for 10 minutes. The pelleted cells were seeded at a density of 100,000 cells per mL DCCM-1 + 10% NCS/FBS + 1% PSG. Once the cells had reached confluence, they were serum starved for 24 hours prior to NP exposure.

3.3.2 Primary human pulmonary epithelial alveolar type 2 (AT2) cells

Primary AT2 cells were isolated from healthy regions of lung tissue following surgical resection using the protocol established by Witherden and Tetley[128 129]. Briefly, pieces of human lung tissue were perfused with sterile normal saline (>10 times, until the saline ran clear). Once excess blood and macrophages had been lavage out of the tissue, it was digested using trypsin (Type I, bovine pancreas) and 250 µg/mL DNase I in Hanks' Balanced Salt Solution (HBSS). The tissue was then finely chopped and passed through a series of filters – final filter size 40 µm mesh – to allow isolated cells to be separated from tissue debris.
The cell suspension was centrifuged at 317 g for 10 minutes then resuspended in DCCM-1. Any residual primary human alveolar macrophages (AM), and blood cells, were removed by differential adherence. Medium containing AT2 cells and fibroblasts was removed, plated and incubated for another two hours to remove contaminating fibroblasts (see below for details). Non-adherent AT2 cells were collected and seeded, at a density of 1000000 cells per mL DCCM-1 + 10% NCS + 1% PSG, on tissue culture plates which had been pre-treated with 1% PureCol collagen solution (Advanced BioMatrix, Carlsbad, CA, USA). Once the AT2 cells had formed a monolayer, after 2-3 days, they were serum starved for 24 hours prior to NP exposure.

3.3.3 Cell viability

3.3.3.1 MTT assay (mitochondrial activity)

After 24 hours exposure to NPs, the washed cells were incubated with 100 µL 500 µg/mL 3-(4,5-dimethylthiazol-2-yl)-2,5-diphenyltetrazolium bromide (MTT) (Amresco, Cleveland, OH, USA), prepared in serum-free DCCM-1 medium, for 25 minutes at 37oC (5% CO2). The MTT solution was replaced with 200µL dimethyl sulfoxide (DMSO), in order to disrupt the cells and aid solubilization of formazan, and transferred to conical well plates, which were centrifuged at 1690 g for 15 minutes to remove residual CNTs. The production of formazan demonstrates metabolic activity, thus cell viability, as it is a result of reduction of MTT by metabolic enzymes in the mitochondria. Supernatant absorbance was measured at 570 nm in an Infinite® F50 spectrophotometer (TECAN, Männedorf, Switzerland) using Magellan™ software.

3.3.3.2 Enzyme-linked immunosorbent assay (ELISA)

Measurement of IL-6/IL-8/TNF-α

Interleukin 6 (IL-6), interleukin 8 (IL-8) and tumor necrosis factor (TNFα) are cytokines that are produced by cells during inflammatory processes thus are used as markers of inflammation. Enzyme-linked immunosorbent assays (ELISA) were performed, to quantify protein expression, using the centrifuged conditioned medium (free of MWCNTs) collected following 24 hours exposure to the NPs.

Briefly, 96 well microtiter plates were coated with the relevant human capture antibody (R&D Systems, UK and PeproTech, London, UK) in PBS and incubated overnight at RT. After 24 hours, the plates were washed with wash buffer (0.05% Tween 20 in PBS) followed by adding blocking buffer (1% BSA in PBS) and incubating at RT for 2 hours or at 4oC overnight followed by another wash stage.

Standard solutions, prepared in serial concentrations in serum-free medium, and the test samples were added to the microtiter plates in duplicate and incubated at RT for 2 hours. The plates were then washed with wash buffer followed by adding detection antibody in diluent (0.1% BSA, 0.05% Tween 20 in PBS) and incubating at RT for 2 hours.

Subsequently, streptavidin-horseradish peroxidase solution was added and the plates incubated for 20 minutes at RT, whilst protecting from light. TMB substrate reagent was added and the plates left to incubate for a further 20 minutes at RT. Stop solution (1 M HCl) was added and the absorbance was measured at 450 nm in an Infinite® F50 spectrophotometer (TECAN, Switzerland).

3.3.3.3 Reactive Oxygen Species (ROS) detection

Fluorescent probe

2',7'-dichlorodihydrofluorescein diacetate (H_2DCFDA), a chemically reduced form of fluorescein, is used as an indicator for most ROS. Oxidants and intracellular esterases cleave the acetate groups of H_2DCFDA resulting in a highly fluorescent product, 2',7'-dichlorofluorescein (DCF). Cells were exposed to NPs for 4, 8 and 24 hours. Post NP-exposure, cells were washed twice with warm PBS and incubated with 25 μM H_2DCFDA in serum-free medium for 30 minutes at 37°C (5% CO_2). 1 μg/mL PMA was used as a positive control for ROS generation; TT1 cells were exposed to PMA for 45 minutes prior to H_2DCFDA incubation. Any residual dye was washed off with PBS and DMSO was added to solubilize the

cells. The solution was centrifuged in a conical plate at 1690 g for 15 minutes. The supernatant was transferred to black 96 well plates and the fluorescence measured at excitation wavelengths 485 ± 12 nm and emission wavelengths 520 ± 35 nm in a FLUOstar OPTIMA Microplate reader (BMG LABTECH, Ortenberg, Germany) using MARS Data Analysis software.

3.4 *In vitro* cardiac functional test of Mimetic Peptide-loaded dpCaPs

These research activities were performed at the Institute of Genetic and Biomedical Research (IRGB) - UOS Milan, by Dr Jessica Modica in Signal Transduction in Cardiac Pathologies Lab - Humanitas Research Hospital (Milano, Italy), headed by Dr. Daniele Catalucci.

3.4.1 Materials and experimental methods

Murine cardiac muscle cells (HL-1) were grown in Claycomb medium (Sigma- Aldrich, St. Louis, MO, USA) supplemented with 10% FBS (Sigma-Aldrich St. Louis, MO, USA), 1% of penicillin-streptomycin (Pen-Strep 10,000 U/mL, Lonza, Milan, Italy), 1% of ultraglutamine (200 mM, Lonza, Milan, Italy) and 0.1 mM of norepinephrine (Sigma-Aldrich St. Louis, MO, USA) in gelatine/fibronectin precoated T75 flasks. The treatment with peptide R7W-MP, self-internalized by cardiomyocytes, used as positive control or different concentrations of dpCaPs loaded with MP was performed in serum-free medium. After 24 h of treatment, the Fluo-4 Direct Calcium Assay was performed as described by the manufacturer (Thermo Fisher Scientific Inc., Waltham, MA, USA). HL-1 cells were stimulated with Fluo-4Direct calcium reagent (Thermo Fisher Scientific Inc., Waltham, MA, USA) and signals were detected one hour post-treatment. Bay K8644 (Sigma) was added to cells at the final concentration of 1μM and signals were detected for 30minutes using a Synergy H4 instrument (BioTek Instrument, Winooski,VT, USA). Results were analyzed using (Prism, Version 7.0a; GraphPad Software Inc., La Jolla, CA, USA).

3.5 Therapeutic effect of Mimetic Peptide loaded dpCaPs formulation for the treatment of cardiovascular function in porcine model

Disclosure

The experimental protocol was approved by the local bioethics committee of Berlin, Germany (G 0064/19), and conforms to the Guide for the Care and Use of Laboratory Animals published by the U.S. National Institutes of Health (NIH publication no. 85-23, revised 1996).

3.5.1 Materials and experimental methods

Aim of the study was the investigation of the efficacy of the inhalation of microparticles embedding CaPs nanoparticles loaded with mimetic peptide as a novel treatment for heart failure with reduced ejection fraction (HFrEF) in Göttingen mini-pigs. HFrEF was induced in Göttingen mini-pigs by continuous right-ventricular pacemaker stimulation (tachypacing). The induced chronic tachycardia causes within three weeks a severe progressive ventricular dysfunction with dilatation of the left ventricle, contractile dysfunction of the heart and activation of the neuro-humoral system. These changes are usually reflected by clinical signs of congestive heart failure, showing the *in vivo* phenotype of HFrEF. After pacemaker implantation, all animals were given a recovery period of 7 days before the tachypacing was initiated. In addition, the animals underwent a continuous telemetric monitoring (ECG and respiratory rate) until the end of the examination. The telemetric system is an important refinement measure in which heart rate (and thus stimulation rate) and respiratory rate can be measured without restraining the animal, *i.e.* with better reproducibility of the data as well as less stress for the animals. The echocardiography (once a week) and the pacemaker programming were carried out in conscious animals. Pigs were exposed to ventricular tachycardia for a total of 6 weeks, with 180 beats/min 2-weeks long followed by 200 beats/min for further 4 weeks. Clinical signs of heart failure such as dyspnoea, cough, pathological findings of heart auscultation, cyanosis, ascites and cachexia were recorded in a protocol. After 4 weeks of pacing, in the presence of clinical evidence of congestive heart failure, the therapy with MP loaded dpCaP was performed over 2 weeks. The animals inhaled 12 mg/kg of microparticles loaded with 60 µg/kg of mimetic peptide through a mask for 14 days of treatment. The unloaded microparticles were used as control. The effect of treatment was monitored by means of transthoracic echocardiography once weekly (Vivid I; GE Healthcare,

Vienna, Austria) as well as with a final invasive left ventricular pressure-volume assessment, as previously described[130].

The dry powder was aerosolized using a commercially available device provided by the Covance company (Laboratories Ltd. Woolley Road, Alconbury, UK). The animals continued to breathe spontaneously during inhalation and did not need sedation. The unloaded dry powder formulation had been tested to characterize the minipig inhalation system to be used on subsequent studies at the facilities in Berlin. The trials demonstrated that the target aerosol concentrations were consistently generated with a respirable particle size using the test items. The system efficiency was of 30%. The system has been developed and tested to minimize animal distress.

The study design was divided in i) pilot and ii) main experiments. The pilot experiments (pharmacokinetics) were dose-finding. A catheter was implanted in one of the jugular vein for serial blood sampling without animal discomfort. It was planned to test two different doses (60 and 220 µg/kg bw/day), which were derived from previous study in rodents and represented the lowest and highest range of activity of the compound[95]. However, given the strong improvement of cardiac contractility after inhalation of 60 µg/kg bw/day of MP, it has been skipped the highest dose and moved to the main study, consisting of 3 group of animals for a total of 24 animals, as follows:

- Group 1 heart failure pigs n = 8, with daily dpCaPs-MP inhalation;
- Group 2 heart failure pigs n=8, daily dpCaPs-NP without MP vector only;
- Group 3 healthy pigs n=8, Control.

Primary endpoint of the study was the left ventricular ejection fraction (LVEF), while secondary endpoints were: Calcium transient amplitude in single cardiomyocytes, left ventricular fibrosis (Picrosirius red staining), Respiratory rate and serum biomarkers.

Referring to previous murine data on LVEF and Calcium transient amplitude after inhalation of dpCaPs-MP, the software G*Power 3.1 [Faul, F., Erdfelder, E., Lang, A.-G., & Buchner, A. (2007). G*Power 3: A flexible statistical power analysis program for the social, behavioural, and biomedical sciences. Behaviour Research Methods, 39, 175-191)] was used to calculate the sample size (Effect size d= 0.55, α=0.05 und Power 1-β=0.80).

Hemodynamic, cardiac functional, histological, and molecular changes at different time points were compared by 1-way analysis of variance (ANOVA) for repeated measures and comparisons between groups by 2-way ANOVA, in both cases followed by Bonferroni post

hoc test. When samples are not normally distributed, a nonparametric test was used. For all statistical analyses, significance was defined as $p < 0.05$.

3.6 Statistical analysis

For the *in vitro* pulmonary and cardiac cells tests the results were reported as mean and SD of at least three replicates. The differences between data were tested using Student's t-test (paired, two-tailed). Differences were considered to be statistically significant at $p<0.0001$using (Prism, Version 7.0a; GraphPad Software Inc., La Jolla, CA, USA).

4 Results and Discussions

4.1 Calcium Phosphate nanoparticles (CaPs) preparation and characterization

4.1.1 Unloaded CaP nanoparticles

In a first step, biomimetic unloaded CaPs were synthetized and characterized according to the original established and patented protocol (PCT/EP2015/080991 and Di Mauro *et al.*[131]). Briefly, an aqueous solution of $CaCl_2$ (100 mM) containing trisodium citrate (400 mM) at pH 8.5 adjusted with NaOH, was mixed (1:1 v/v) with a solution of Na_2HPO_4 (120 mM). The mixture was kept in a water bath at 37°C for the precipitate maturation time of 5 min. To remove unreacted reagents, the CaP suspension was dialyzed overnight across a cellulose dialysis membrane with a molecular weight cut-off of 3500 Da. This method of purification was preferred to centrifugation to avoid strong aggregation of CaP nanoparticles. Fourier-transform infrared (FT-IR) spectroscopy and X-Ray diffraction (XRD) analyses performed before the dialysis (Figure 4.1) showed very broad signals indicating that the nanoparticles have an amorphous structure, similar to that of the mineral phase of very young bones[132].

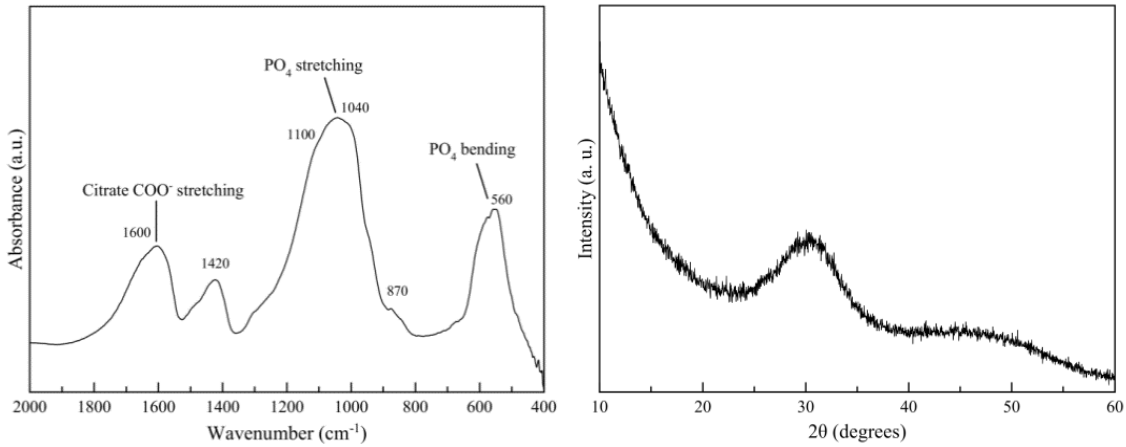

Figure 4.1 FT-IR spectra (left) and XRD pattern (right) of amorphous CaPs synthesized immediately after precipitation, before dialysis.

Dynamic light scattering (DLS) and ζ-potential analyses performed immediately after the dialysis, demonstrated that CaP nanoparticles showed a Z-Average of about 70 nm and negative surface charge (-42.5 ± 5 mV). The Ca/P molar ratio, determined by ICP-OES

analysis, was 1.6 according to theoretical value of stoichiometric hydroxyapatite between 1.5-1.67[133].

The CaP dispersion at concentration 0.5 mg/mL, was analysed by Cryo-EM to evidence the nanoparticle morphology. Two morphologically different particles populations were evidenced (Figure 4.2). CaPs were mostly observed as individual particles with a small presence of clusters. The most represented population was characterized by spherical particles with diameter from 20 to 60 nm (Figure 4.2C). Needle-like particles instead were mainly present on the border of the deposited sample drop. Needle-like particles were from 5 to 10 nm thick and with a variable length ranging from 50 to 120 nm (Figure 4.2B).

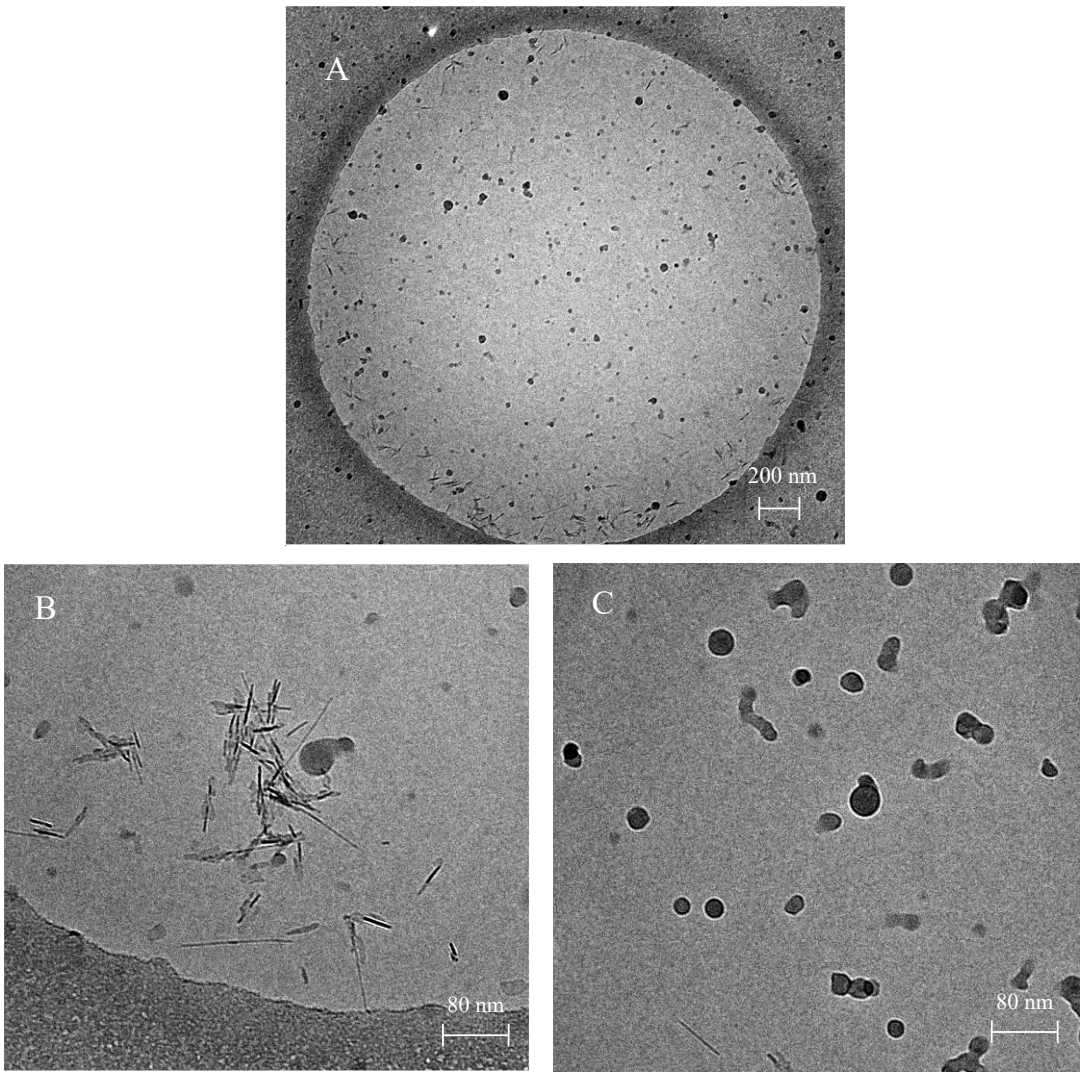

Figure 4.2 Cryo-EM image of a CaP nanoparticles sample at different magnification. A: whole nanodispersion at low magnification; B: details of spherical nanoparticles morphology C: close-up of needle-like CaP shape.

The Cryo-EM images suggested that the nature of the nanoparticles was not exclusively amorphous as implied from the FT-IR spectra and X-ray pattern.

One of the basic requirements for clinical studies, regulatory approval and marketing is the stability of the medicine and in particular of the drug substance. Typically, new drug candidates enter the pharmaceutical development process in a crystal or amorphous state. Crystallinity ensures a high level of purity and stability, particularly if the crystal formed is the most thermodynamically stable form. Whereas crystals exhibit long-range molecular order, molecules in the amorphous state have no long-range order but retain the short-range order typical of liquids. From a pharmaceutical perspective, if amorphous material is present there must be significant concern since, relative to the crystalline state, the amorphous state is less thermodynamically stable. Consequently, molecules in the amorphous state generally exhibit greater chemical instability, altered mechanical properties, greater hygroscopicity but enhanced dissolution rates[134]. If these properties are not predicted or controlled, they can lead to difficulty on processing, storage and pharmaceutical products use. Moreover, since the amorphous state is metastable relative to the crystalline state, there is often the potential for unexpected crystallization during storage, leading to macroscopic changes in specific surface area, flow, solubility and dissolution rate. Such observations led to the hypothesis that most solid-state instabilities of pharmaceuticals preferentially occur in the disordered non-crystalline regions of the solid[134]. Both to overcome these concerns and since the CaP produced following Di Mauro *et al.* protocol[131] showed both crystalline and amorphous characteristics, a modified CaP preparation to obtain only crystalline nanoparticles was developed. Briefly, the above reported protocol was slightly modified reducing the amount of citrate during the preparation, namely the molar citrate to calcium ratio was modified from 4 to 2 and adjusting the pH to 10.0. The modifications introduced in this new protocol were carried out also in prevision of the scale-up activities. In fact, the reduction of the nominal amount of citrate improves the yield of the process, increasing the quantity of precipitated nanoparticles. Moreover, these CaP preparation changes were optimized in order to generate nanoparticles with particle size distribution comparable to that of nanoparticles prepared with the previous protocol. The Ca/P molar ratio, assessed by ICP-OES analysis, was 1.6 in agreement as previous with the theoretical value of stoichiometric hydroxyapatite[133].

FT-IR and XRD analyses (Figure 4.3 and Figure 4.4) for the CaP nanoparticles obtained with the new protocol showed more defined signals suggesting that particles are crystalline. In fact, the change from amorphous to crystalline was quantitatively evaluated by means of the splitting factor, that was found to be 4.0. This is a well-reported index for the evaluation of crystallinity

degree of CaP-based materials from FT-IR spectra[135]. The splitting factor, which quantifies the degree of splitting of the PO_4 bond bending peaks, is known to increase with increasing crystallinity[136,137]. In detail, the sum of the heights of the stretching of phosphates peaks at 603 and 560 cm^{-1}, measured above a baseline drawn from approximately 780–495 cm^{-1} (Figure 4.3), divided by the height of the valley between them at ~588 cm^{-1}, allows to obtain the splitting factor value. In fact, while in the case of CaPs synthesized with original protocol the splitting factor was not measurable, conversely it was perfectly measured in the FT-IR spectra of CaPs prepared with the new protocol.

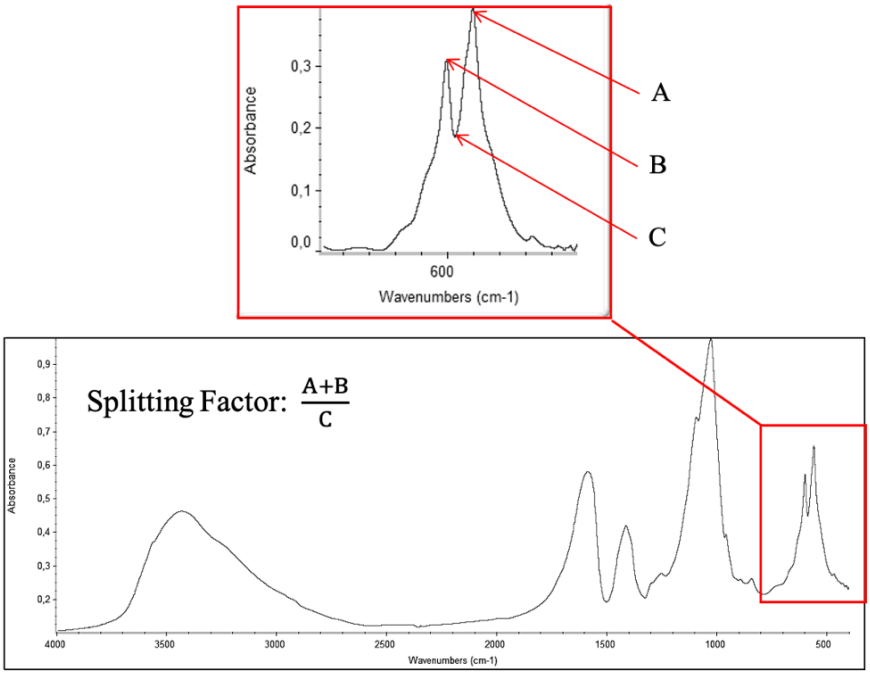

Figure 4.3 FT-IR spectra of crystalline CaP nanoparticles and splitting factor measurment based on the sum of the heights of the stretching of phosphates peaks (named A and B at 603 and 560 cm^{-1}, respectively and divided by the height (C) of the valley between them at ~588 cm^{-1}.

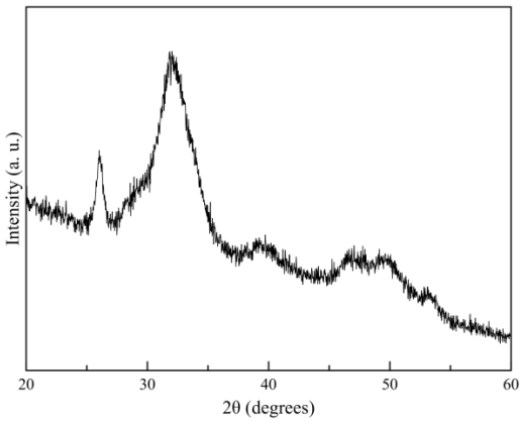

Figure 4.4 XRD pattern of the CaP nanoparticles synthesized with novel protocol.

The CaP structure of solid phase in bone was first identified by De Jong as a crystalline calcium phosphate, close to geological apatite by chemical analyses, the most importantly, by X-ray diffraction that were also confirmed few years later[138]. The XRD pattern obtained from manufactured CaP nanoparticles, displayed the most intense peaks at 25.88° and at about 32° (broad band), fingerprints of crystalline hydroxyapatite[139]. The diffraction peaks are broad and not well defined. This broadness suggests a relatively low degree of crystallinity and nanodimensions[138] (Figure 4.4).

DLS analysis demonstrated that the CaPs in the dispersion, immediately after dialysis, have a mean hydrodynamic diameter of about 250 nm, which decreases with time to about 80 nm that is in line with Di Mauro *et al.* CaP protocol. The PDI of 0.2 suggested not a monomodal distribution. The surface charge of CaPs in water was negative (-40.0 ± 3 mV). In conclusion, results revealed that the size and surface charge of the crystalline nanoparticles synthesized with the new protocol with lower sodium citrate content, are in line with the quality of previous protocols. The TEM image (Figure 4.5) confirmed the needle like crystal morphology; the needle showed a length from 20 to about 100 nm and a thickness in range between 5-10 nm.

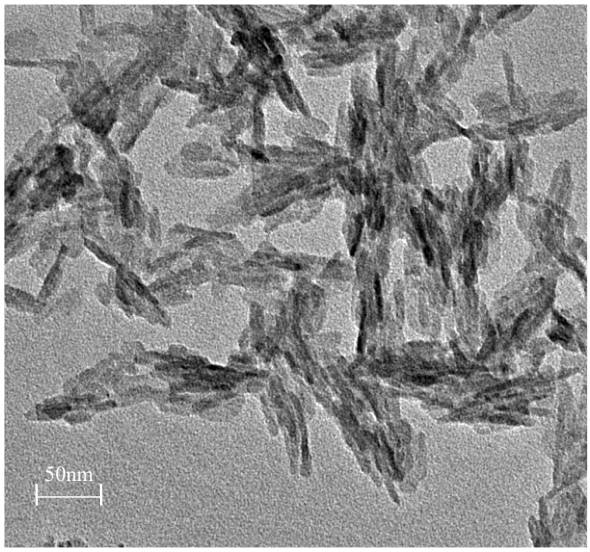

Figure 4.5 TEM image of unloaded crystalline CaP nanoparticles after dialysis.

The optimized protocol to prepare crystalline CaP was applied for the generation of nanoparticles loaded with different category of drugs, namely i) milrinone, a small drug already in clinical use; ii) a cardiac-enriched microRNA; iii) a mimetic peptide (MP).

4.1.2 Milrinone loading

Milrinone is a small size molecule, inhibitor of the enzyme phosphodiesterase III, clinically administered orally or by injection. It increases the intracellular cAMP concentration by improving the calcium supply influx and consequently, it has a positive inotropic effect. The study and development of an inhaled milrinone product may be relevant to directly targeting the heart muscle reducing the systemic collateral effects due to the current administration routes, especially intravenous injection[140].

In a first trial, the loading of CaPs with MRN was assessed by adding the drugs in the reactant solutions, but this approach led to the precipitation of milrinone calcium salts. To overcome this issue and prevent the formation of salts, a higher amount of citrate was employed, with the aim to complex calcium ions. Not even this approach resulted satisfactory, as drug loading measured by HPLC was below 0.1% w/w (milrinone content over total nanoparticles amount).

In order to improve drug loading, the CaP nanoparticles were prepared by increasing the maturation time to favour the interaction of drug during CaP formation and focusing on a minimization of drug desorption during dialysis. In fact, in order to identify the criticality in term of drug loss during the precipitation process, a study was conducted to monitor the MRN content during nanoparticle loading step by step, by assaying milrinone by HPLC at the different production steps. This evidenced that the dialysis step determined the quasi-total depletion of MRN from the formulation (< 0.1% w/w). Hence, this process drastically affected the loading of milrinone, which is massively lost during nanoparticles purification. An ultrafiltration equipment and centrifugation were tested as contingency plan, but also after the employment of these methods, the recovered MRN in CaP dispersion was lower than 0.1 % w/w.

4.1.3 miR-Neg5 (miRNA) and Mimetic Peptide (MP) loading

MicroRNAs (miRNAs) are regulators involved in several biological processes and have been recognized as potential novel therapeutic drugs for the treatment and prevention of cardiovascular diseases. The cardiac enriched miR-133, which is inversely related to failing heart conditions, is involved in several aspects of pathological cardiac remodeling and its potential role as therapeutic compound was recently shown by Castaldi *et al.*[115].

Calcium phosphate nanoparticles were prepared as reported in the Section 4.1.1, but adding 0.014 mg/ml of micro-RNA (Neg-5) to phosphate solution.

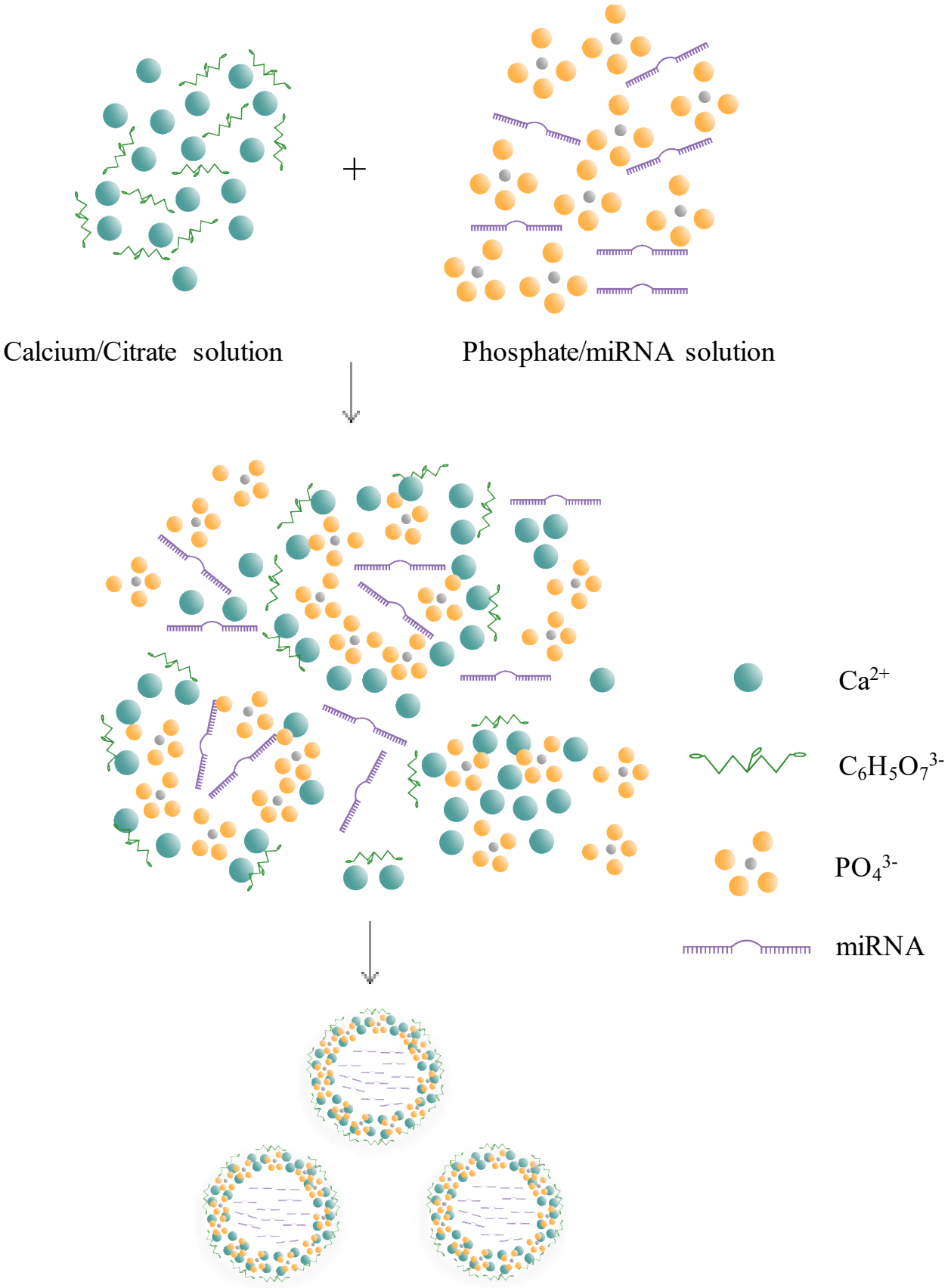

Figure 4.6 Schematic representation of the CaP-miRNA formation mechanism.

The incorporation mechanism consists of a first step of interaction in which, within the basic reaction environment (pH 8.5-8.7), the PO_4^{3-} ions interact via a strong electrostatic interaction with the chemical groups (carboxylate and amine) of the biomolecule. The negative charge of miRNA, which has a calculated isoelectric point of about 7.0[141], it is expected to interact with Ca^{2+} ions. Afterward, the reaction of PO_4^{3-} with Ca^{2+} ions trigger the nucleation of particles and their growth, resulting in the mineralization of biomolecules. During this process, citrate stabilizes the nanoparticles and modulates their growth through its binding on the surface at the early stage of crystallization (Figure 4.6)

The obtained miRNA loaded CaPs nanoparticles showed, by dynamic light scattering analysis, a Z-average of 1900 ± 50 nm and a PDI of 0.3 suggesting the presence of nanoagglomerates (Figure 4.7), exhibiting hence a polydisperse multimodal size distribution. The nanoparticle surface charge was negative (-17 ± 5 mV).

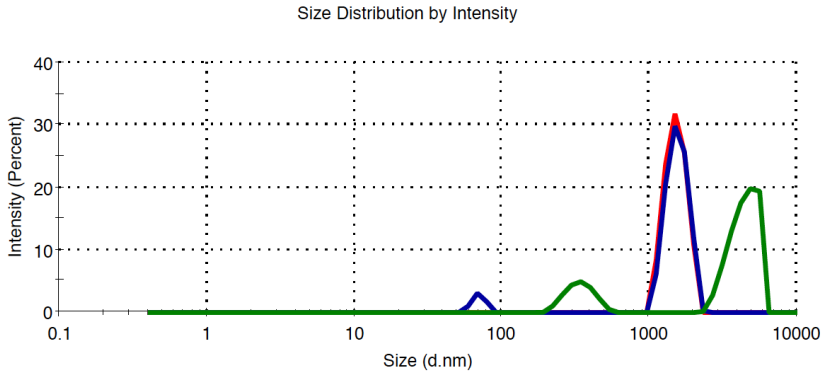

Figure 4.7 Particle size distribution (nm) in Intensity (%) measurements of 3 different batches of CaP loaded with miRNA nanoparticles by DLS.

The Ca/P molar ratio of miRNA loaded CaP nanoparticles, calculated by ICP-OES analysis, was 1.67. The miRNA loaded nanoparticles concentration was about 1.0 mg/mL. The crystallinity index, in terms of splitting factor, was 4.0, the same value of the unloaded CaPs. These crystalline nanoparticles miRNA loaded revealed needle-like morphology. The miR-CaPs appear organized in a sort of network that could be an artefact due to the sample drying for SEM analysis preparation (Figure 4.8).

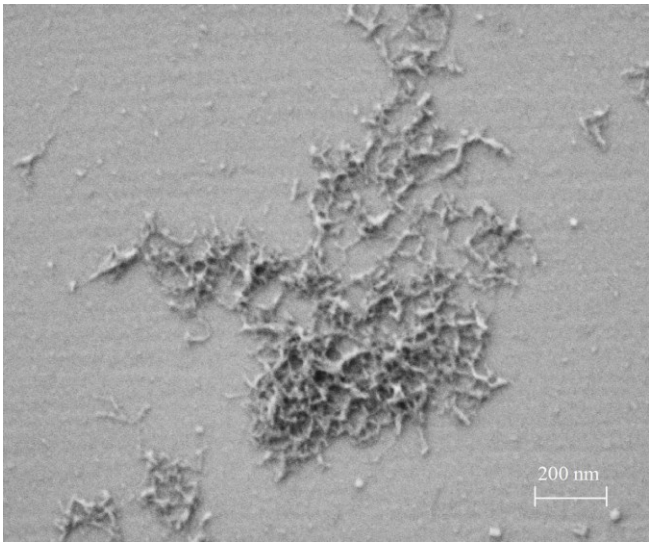

Figure 4.8 SEM micrograph of CaP nanoparticles loaded with miRNA.

Successively, CaP nanoparticles loaded with the mimetic peptide (MP; DQRPDREAPRS, MW: 1326 Da, α-helix structure) targeting the $Ca_v\beta 2$ calcium channel[95] were prepared following the reported procedure (paragraph 4.1.1) in which the peptide active substance was dissolved at 0.6 mg/mL in the Na_2HPO_4 0.12 M solution.

Notably, the incorporation mechanism for mimetic peptide into CaP NPs was similar to the one previously observed for microRNA (Figure 4.6). In the basic reaction environment (pH ~ 9.0), the phosphate ions electrostatically interact with the carboxylate and amine groups of the mimetic peptide. At the pH of the reaction, the MP peptide, having a calculated isoelectric point of 7.06[141], generally interacts with Ca^{2+} ions. Afterward, the reaction between phosphate and Ca^{2+} ions lead to particles nucleation. The precipitated nanoparticles after dialysis were concentrated 1.0 mg/ml. Ca/P molar ratio of stoichiometric MP loaded CaP nanoparticles was found to be 1.67, confirming a hydroxyapatite nanostructure. The measured peptide concentration in the nanodispersion, determined by HPLC analytical method, was about 0.06 mg/mL. The peptide content expressed as peptide amount over total nanoparticles amount in the dispersion was 6.0 ± 2.0% w/w.

The peptide-loaded CaPs showed an average hydrodynamic particle size of 115 ± 20 nm, PDI of 0.15 ± 0.05, an almost monomodal dispersion, with low amounts of nanoparticles aggregated. The nanodispersion stability was supported by zeta potential measurement that indicated a negative surface charge of -25± 10 mV (Figure 4.9).

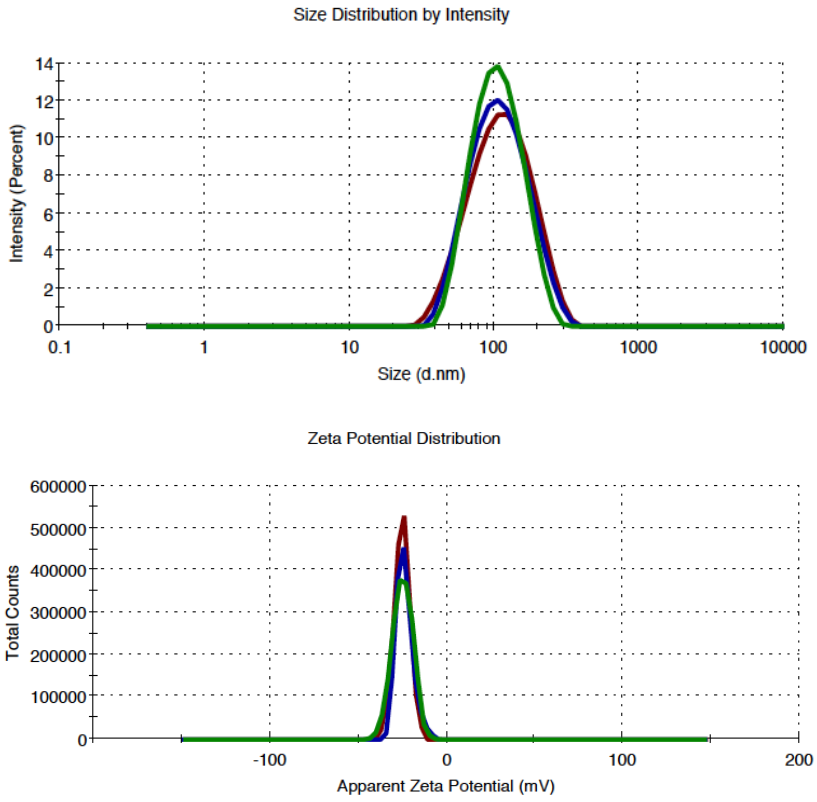

Figure 4.9 Size distribution (nm) in Intensity (%) and Zeta Potential distribution (mV) vs Total counts (kcps) measurements of 3 different batches of CaP loaded with Mimetic peptide (MP), 3 hours after preparation, by DLS.

The DLS is a powerful and accessible tool, even if is also known to have several drawbacks, which are mostly inherent to the technique principles. The fluctuations in scattered light intensity due to the Brownian movement of the particles, determines the size of the particle[142]. Considering that the intensity of the scattered light is proportional to the sixth power of the particle diameter makes this technique highly sensitive to the presence of large particles[143]. This is an advantage if the aim is to detect small amounts of large particles; on the contrary it can be a major drawback for accurate size determination. Dust particles or small amounts of large aggregates can hinder the size determination if the main component exhibits a distinctly smaller size[144]. Hence, the high value of Z-Average is mostly determined by the presence of agglomerates, while the diameter of individual particles, even if abundant, has a lower weight. Nanoparticle Tracking Analysis (NTA) is a method that allows to monitor and analyze single nanoparticles in liquids, relating the Brownian motion to the size of the particles and offering a frequency distribution by number. In addition, the actual nanoparticles concentration in the sample can be determined. Particle motion is related to liquid viscosity, temperature and

particle size and is not affected by particle density or refractive index[125]. As reported in methods, the movement of the particles depends on the hydrodynamic diameter of the equivalent sphere and is calculated through the Stokes-Einstein equation. The accurate monitoring by the NTA in real time of events such as agglomeration and dissolution performed appears optimal for the characterization of calcium phosphate nanoparticles.

In order to further explore the particle size distribution, nanoparticles tracking analysis (NTA) was carried out on MP-loaded CaP nanoparticles particle size distribution and obtained results compared to those from DLS analysis. The nanodispersion was diluted to 0.5 mg/mL with ultrapure water for allowing single particle tracking. Results are shown in Figure 4.10. Particle size distribution showed a peak at 137.7 ± 1.1 nm, 90% of the particles being below 206.3 ± 0.7 nm and 50% of particles were less than 122.7± 1.7 nm, confirming the narrow size distribution of the nanoparticles. The mean particle size value obtained by NTA was very close to DLS results, despite the different weighting functions: the intensity scattered by particles for DLS, larger for large particles, the number of particles for NTA. NTA provides complementary information for both DLS and microscopy. In fact, as it follows individual particles during their movement, it enhances the resolution of polydisperse particle population usually obtained by DLS. The technique still operates on a statistically significant number of particles, larger than for microscopy, although not accessing their morphology[145]. The good correlation between NTA and DLS, suggests that the calcium phosphate nanoparticles are present as agglomerates and almost no individual particles are present. This could be due to the presence of the peptide that structures the small particles triggering the formation of agglomerates.

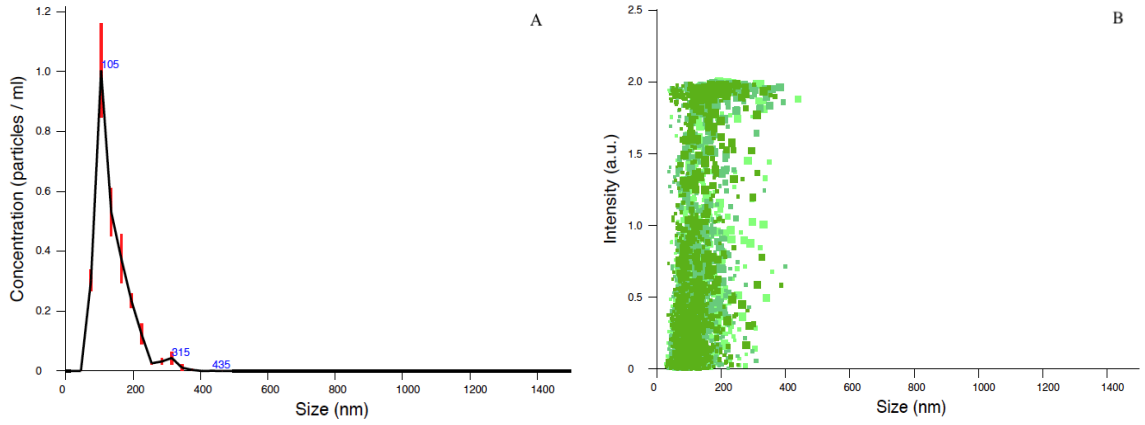

Figure 4.10 Particle size distribution vs nanoparticles concentration and intensity of scattered light obtained by NTA. Particle size distribution is expressed as average and standard error of the mean of nanoparticle concentration (n=3) (A). Different colors and sizes of markers represent measures of particle size and scattered light intensity of single particles from the three independent experiments (B).

4.2 Scale-up of Calcium Phosphate nanoparticles manufacturing and characterization

Currently, the development of CaP nanoparticles is affected by the low replicability and technical issues of their manufacturing procedure, as often occurs for other nanomaterials. Hence, the translation from laboratory to industrial scale production is challenging, particularly to control morphology, size, purity and degree of particle aggregation in order to achieve products with robust quality and to comply specifications.

The development of a continuous flow synthesis of CaP loaded with drug can overcome these troubles, supplying homogenous reaction conditions and highly reproducible process. A design of experiment approach of a continuous flow process to prepare calcium phosphate nanoparticles at large scale was carried out and discussed in detail in an original scientific paper published and reported in Section 5 "Calcium Phosphate Nanoparticle Precipitation by a Continuous Flow Process: A Design of Experiment Approach"[135].

Because miRNA is expensive, the feasibility of scale-up procedure was assessed only for CaP NPs loaded with the mimetic peptide. However, the scaled CaP nanoparticles manufacturing with a continuous process was abandoned due to the low peptide payload obtained, with most of the loss related to the purification step (*i.e.* centrifugation). As a consequence, it was decided to perform the scale up of nanoparticles production process with a more traditional approach in batch.

For the pilot scale batch manufacturing of CaP loaded with mimetic peptide, 3.0 liters five times the volume of the reagents than lab scale quantities were treated. For peptide quantitative determination a HPLC method was developed and validate as reported in subsection 3.2.4.9. Chromatogram of MP reference standard and HCl blank solution are reported in Figure 4.11A-B. The HPLC method, based on a C18 partitioning column, provided a sufficient separation of the MP peak from the other components of the nanoparticles (Figure 4.11C).

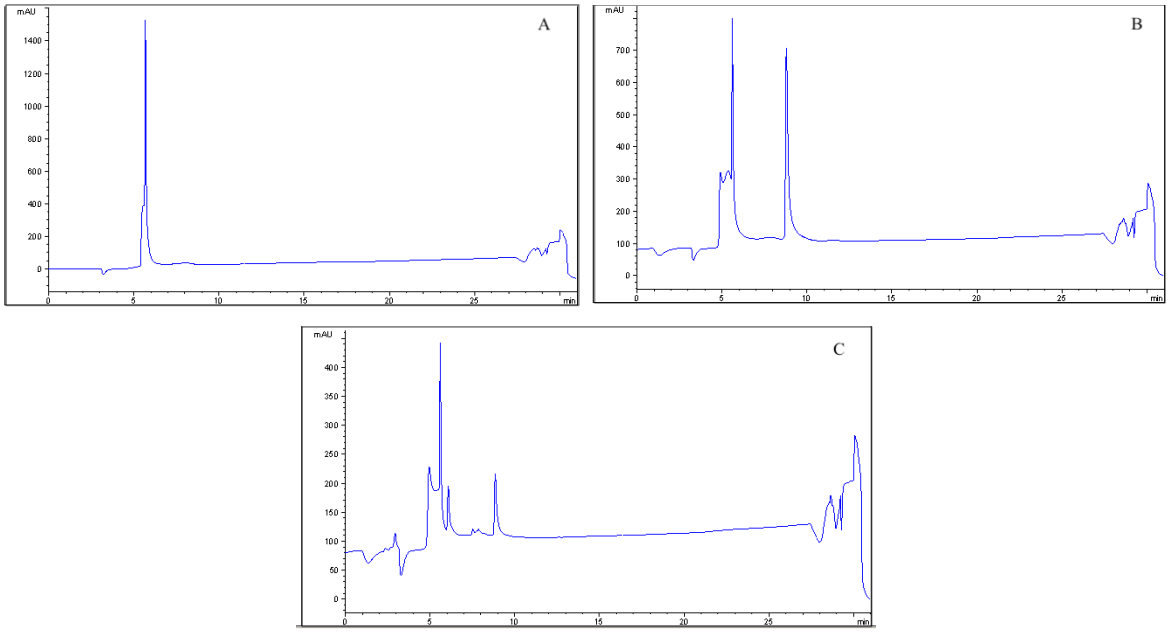

Figure 4.11 Chromatograms of HCl 0.1 M blank solvent (A), MP reference standard at concentration 0.2 mg/mL (B). The MP peak retention time was 9.3 minutes. MP loaded CaPs 0.084 mg/mL (C).

To optimize the scaled MP/CaP nanoparticles, in terms of size, surface charge, concentration and improving the peptide loading, a number of experiments was carried out.

The first goal was to achieve an acceptable compromise between NPs purification and MP loss. The concentrations of nanoparticle CaPs and MP concentration in the dispersion, as function of dialysis time, were quantified at different dialysis times using cellulose membrane with 3.5 kDa molecular weight cut-off. The results are reported in Figure 4.12. The impact of membrane cut-off on MP concentration was also evaluated with a cellulose membrane having 12-14 kDa cut-off. Data analysis showed comparable trend for both membranes, *i.e.* MWCO 3.5 and 12-14 kDa in terms of purification efficiency versus time (data not shown).

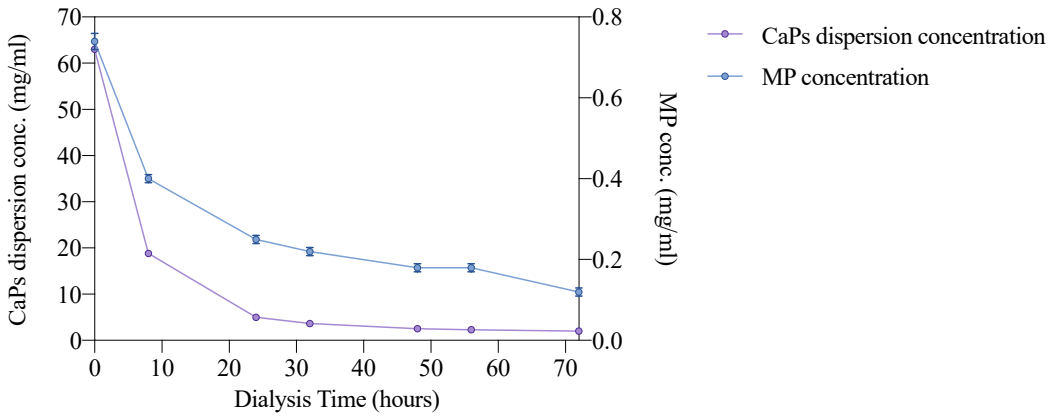

Figure 4.12 Trend of mimetic peptide and CaP nanodispersion concentration (mg/mL) over dialysis time. All results are reported as mean and standard deviation of 3 replicates.

As revealed by the data reported of Figure 4.12, the measured concentration of the MP in CaPs dispersion decreased from 0.74 ± 0.02 mg/mL at time 0 to 0.12 ± 0.01 mg/mL after 72 hours of dialysis together the reduction of solid content in nanoparticles dispersion from 63 ± 0.02 to 2 ± 0.01 mg/mL. Thanks to dialysis process, the elimination of unreacted salts allows to obtain a dispersion of purified nanoparticles, resulting in a concentration much lower than those of dispersion before dialysis. The peptide concentration reached a plateau of 0.18 mg/mL between 48 and 56 hours of dialysis, in correspondence to a nanoparticle concentration around 5.0 mg/mL; then, the content further decreased to 0.12 mg/mL after 72 hours later. The plateau of MP concentration in NPs, between 48 and 56 hours of dialysis, suggested a quasi-equilibrium dialysis achievement. Hence, at this time point, the measured quantity of mimetic peptide, that is 0.12 mg/mL, is reasonably the MP fraction associated to the CaP nanoparticles 2.0 mg/mL. In fact, the concentration of nanodispersed solid decreased during dialysis process by revealing an asymptotic concentration between 48 and 72 hours. The constant concentration of about 2.0 mg/mL at the end of the process, is due to the total depletion of unreacted salts.
Based on the results, the dialysis time was fixed at 48 hours in order to obtain a quality of the CaPs accomplishing an optimization in terms of peptide content and NPs purification from unreacted ions, mostly citrate excess. In detail, for these analyses, performed on two different batches, gave rise to peptide concentration in NPs dispersion after 48 hours of dialysis of 0.18 ±0.01 mg/mL and of nanoparticles 2.0 mg/mL (Figure 4.12).

To further understand the influence of CaP nanostructures on MP release and study how the MP kinetics release is influenced by the CaPs presence, the biomolecule concentration was monitored and measured at different dialysis times comparing CaP-MP suspension and free MP solution. In details, MP loaded nanoparticles and a peptide aqueous solution were dialysed in two different dialysis tubes having 3.5 kDa cut-off submerged into a beaker containing ultrapure water. At established time intervals from 0 to 72 hours, an aliquot of each sample (*i.e.* free MP solution and MP in CaP dispersion) was withdrawn from the dialysis tubing. Each sample was dissolved in HCl 0.1 M (pH 2.5) to provide the dissolution of NPs. The MP content was assayed using HPLC (Figure 4.13).

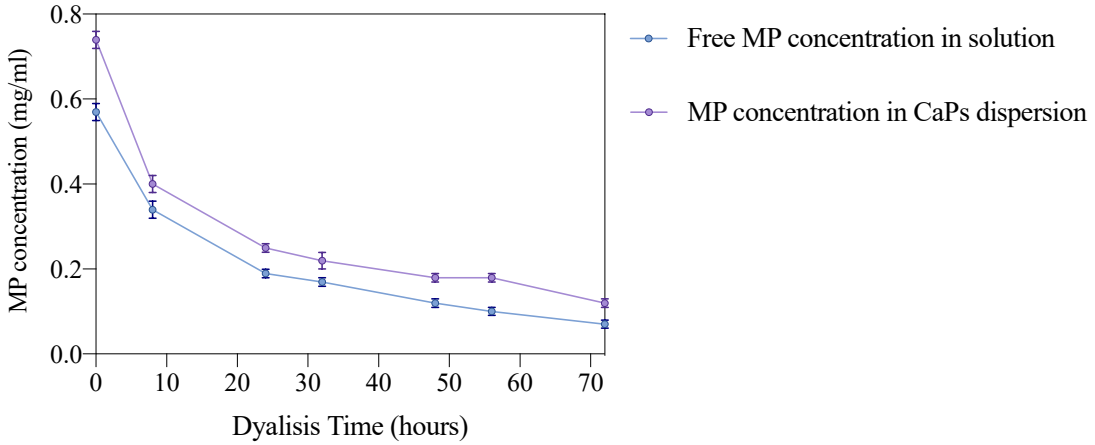

Figure 4.13 Mimetic peptide concentration (mg/mL) in CaPs nanodispersion dissolved in acid solution compared to free peptide concentration (mg/mL) in acid solution measured by HPLC. There was no significant difference between the two data trend (p value= 0.48). All results are reported as mean and standard deviation of 3 replicates. The differences between data were tested using Two-Way ANOVA, considering significant differences with $p < 0.05$ (Prism, Version 7.0a, GraphPad Software Inc., La Jolla, CA, USA).

Dialysis is a common method for the determination of release kinetics from nanoparticle drug delivery systems[146]. Plotting the cumulative percentage of peptide (free in water solution and in CaPs dispersion) remained in dialysis tubing versus time, the MP release kinetics fits to a first order equation in both cases (Figure 4.14). The drug release from the nanoparticles into the dialysis chamber diffused across the dialysis membrane. The drug was expressed as percent remaining to diffuse by Equation 12:

$$MP\ remained\ \% = \frac{[MP]_t}{[MP]_{total}} \cdot 100 \qquad (12)$$

where $[MP]_t$ refers to the concentration of peptide remaining in the dialysis tube at time t and $[MP]_{total}$ is the total amount of peptide into the CaP nanoparticles dispersion at time 0, immediately after precipitation.

A first order equation describes the drug release kinetics that is diffusant concentration-dependent (Equation 13):

$$\frac{dC}{dt} = -kC \qquad (13)$$

where C refers to drug concentration in the dialysis sachet and k is the first order rate constant. This equation can also be written in logarithmic form as Equation 14:

$$logC = log\ C_0 - \frac{kt}{2.303} \qquad (14)$$

where C_0 corresponds to the initial concentration of drug[147]. This means that for both release profiles, the peptide release rate was dependent on the concentration of free peptide in the

dialysis bag, meaning the greater the concentration, the faster the process. However, after a superposed MP amount dialyzed in 32 hours, either in presence or absence of CaPs, between 30 and 72 hours there was evidence of slower dialysis rate of the CaPs MP, signalling an influence of nanoparticles on MP dialysis. However, the MP release kinetics constant was not significantly different (p= 0.11) in presence of CaP nanoparticles.

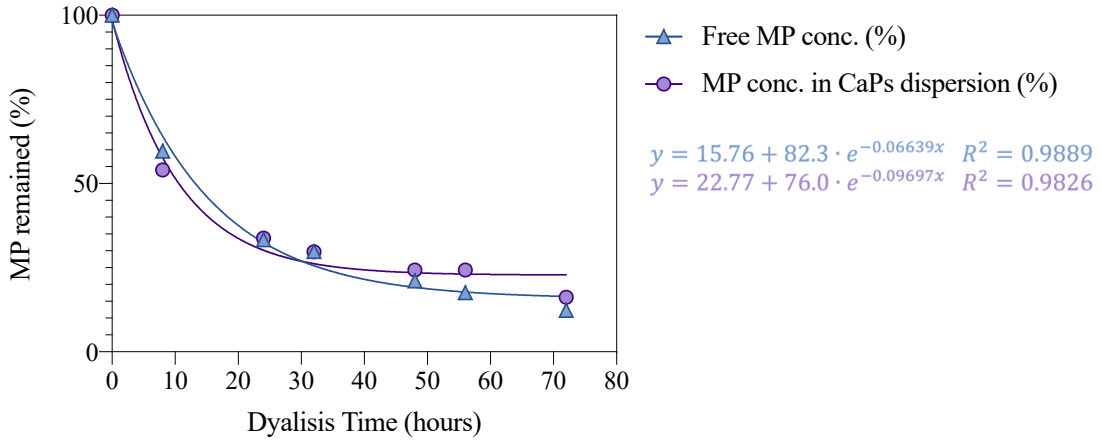

Figure 4.14 Cumulative percentage of mimetic peptide remaining in dialysis tube over the time. Blue and violet lines are referred to MP as it is in water solution and in nanoparticles dispersion, respectively. First order kinetic fitting of mimetic peptide release. Nonlinear regression analysis applying exponential one phase decay and one sample t and Wilcoxon test between the slopes of nonlinear regression (p value= 0.11) were performed by Prism, Version 7.0a, GraphPad Software.

Finally, the scale up protocol was set at 48 hours of dialysis of MP/NPs dispersion, allowing to manufacture nanoparticle with concentration of 1.6 ± 0.2 mg/mL and MP concentration in range between 0.07 and 0.08 mg/mL. The Ca/P molar ratio value of 1.6 assessed by ICP-OES analysis for scaled NPs was in agreement with those typical of hydroxyapatite.

To evaluate the peptide association with calcium phosphate nanoparticles, the FT-IR spectra of mimetic peptide and those of MP/CaPs dispersion were compared. Examining the FT-IR spectrum (Figure 4.15) of MP raw material (violet line), the high amide bands of MP between 1300 and 1800 cm^{-1}, were clearly visible. Comparing this spectrum with the CaP MP loaded spectrum (blue line, FT-IR analysis on five MP/CaP samples), MP amide bands were shifted at higher wavenumbers typical of CaP phosphate bands between 1000 and 600 cm^{-1} meaning the presence of the MP interaction with Ca/P ions (Figure 4.15).

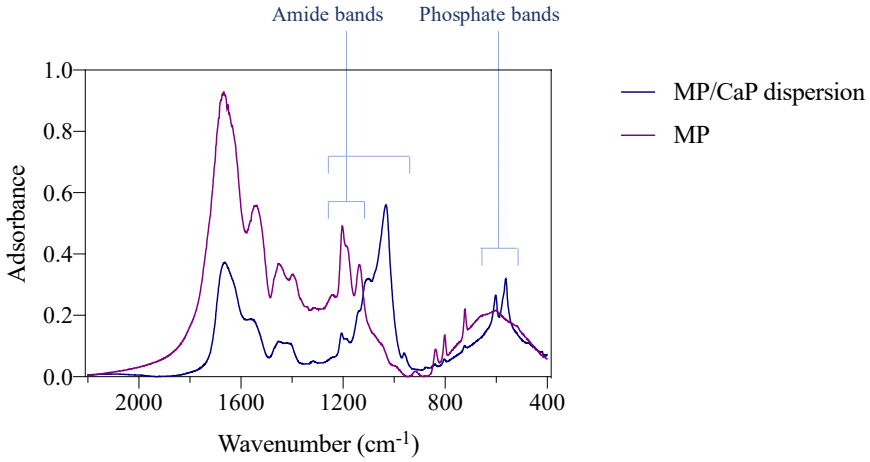

Figure 4.15 FT-IR spectrum of mimetic peptide raw material (violet line) and hydroxyapatite nanoparticles loaded with MP (blue line).

The crystalline structure of MP loaded CaP nanoparticles was also confirmed calculating the Splitting factor, that was 4, based on the sum of the heights of the stretching of phosphates peaks of FT-IR spectrum. As shown by TEM micrograph (Figure 4.16) the crystallized hydroxyapatite nanoparticles with MP revealed a morphology close to needle-plates, sometimes aggregated each one, about 50 nm in length and 10-15 nm in width.

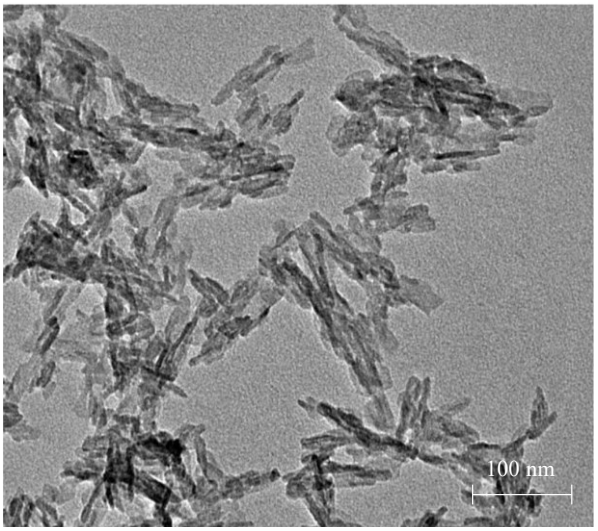

Figure 4.16 TEM micrograph of CaP nanoparticles loaded with MP after purification by dialysis.

4.2.1 MP loaded CaPs stability study

Two batches of 3.0 L each one dispersion of MP-loaded calcium phosphate nanoparticles were produced and stored at 4°C and at 25°C/40% RH conditions, to evaluate the peptide stability

over the time. The measured mimetic peptide concentration in the dispersion immediately after precipitation before dialysis, was 0.104 ± 0.002 mg/mL.

Table 4.1 Mimetic peptide conc. (mg/mL) monitored over the time from 24 hours to 30 days after production and stored at 4°C and 25°C/40% RH. Each sample aliquot was dissolved in HCl 0.1 M before the HPLC analysis. All data are expressed as mean and standard deviation of two different MP/NPs batches.

	MP concentration in CaPs dispersion (mg/mL)	
TIME (hours)	**stored at 4°C**	**stored at 25°C/40%RH**
24	0.092 ± 0.002	0.082 ± 0.004
48	0.076 ± 0.001	0.067 ± 0.003
120	0.068 ± 0.003	0.023 ± 0.002
168 (1 week)	0.053 ± 0.001	0.006 ± 0.001
192 (10 days)	0.044 ± 0.001	< LOQ
360 (15 days)	0.031 ± 0.001	< LOQ
720 (30 days)	< LOQ	< LOQ

As reported in Table 4.1 the peptide concentration rapidly decreased when the nanodispersion was stored at room temperature, namely 10 days after the preparation the concentration was under the limit of quantification. Instead, the peptide demonstrated better stability in refrigerate condition, even if after one week the peptide concentration dropped to 50%. The peptide decrease over the time was function of temperature. A degradation phenomenon often fits with first order kinetic model. Hence, to demonstrate the peptide degradation a nonlinear regression was studied for both CaPs storage conditions (Figure 4.17).

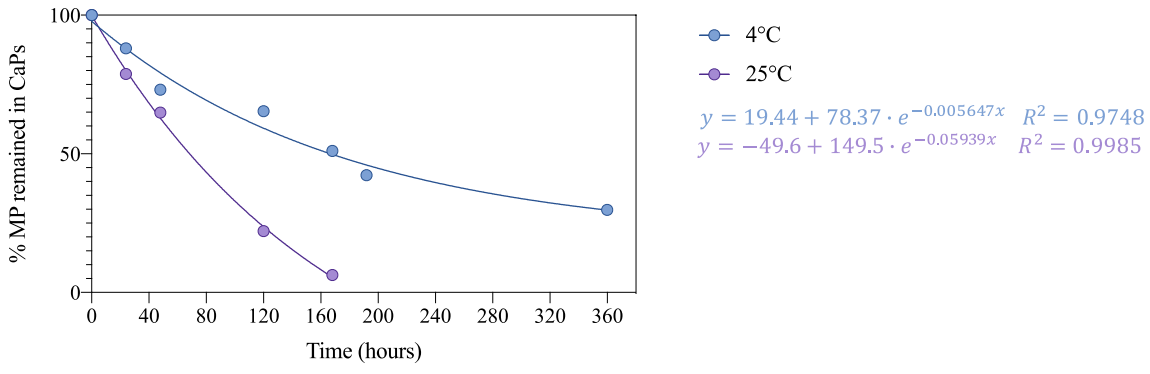

Figure 4.17. Mimetic peptide cumulative percentage over the time (hours) quantified by HPLC. Blue and violet dots are referred to NPs dispersion stored at 4 or 25°C/40%RH, respectively. The analytical data under the LOQ are not reported in graph. Nonlinear regression analysis applying exponential one phase decay was performed by Prism, Version 7.0a, GraphPad Software. The slopes of two nonlinear regressions were significantly different ($p < 0.0001$).

The MP decrease fitting a first order kinetic model explains the decrement of peptide, stored both in refrigerate conditions or at room temperature, was due to a degradation. MP was slightly stable in nanodispersion. The MP half-life $t_{1/2}$ stored at 4°C has been calculated as ln2/k, *i.e.* about 123 hours. The $t_{1/2}$ of NPs stored at 25°C was about 12 hours, approximately a tenth than refrigerate storage. As well, the size of nanoparticles increased during test days because of agglomerate formation. Therefore, room temperature negatively affected the peptide stability in solution.

In this research project, the prepared loaded nanoparticles were envisioned to be dried and transformed in inhalable microparticles, also to overcome the issue of poor chemical-physical stability in liquid nanodispersion and to preserve the mimetic peptide. This stability test results underline the relevance to dry the NPs dispersion quickly after their preparation or store the dispersion at 4°C and dry them within 24 hours to preserve the nanoparticles and peptide stability.

To conclude the first part of this research work, beyond the CaPs/miRNA, crystalline CaPs loaded with ~7%w/w of mimetic peptide with a Z-Average of 160 ± 30 nm, and negative surface charge, *i.e.* ζ-potential of -23 ± 7 mV were successfully produced at pilot scale as well as at lab scale.

4.3 Microparticles embedding CaP nanoparticles (dpCaPs)

The CaPs nanoparticles (hydrodynamic mean diameter less than 200 nm) are difficult to be administered by inhalation in dry form, since their size is too small for deposition in lung after pulmonary administration. The technical solution here proposed to obtain the lung deposition is to increase the apparent size of the nanoparticles by embedding them in microparticulate water soluble structures. This technology substantially assigns to NPs aerodynamic properties. Microparticles were manufactured by spray drying of a carrier water solution in which calcium phosphate nanoparticles loaded with pharmacological active substances are dispersed. Mannitol was employed as carrier. The composition and structure of microparticle embedding the drug loaded nanoparticles activate the heart targeting process via their aerosol deposition in deep lung. After the deposition of the microparticles in the lung alveoli, their dissolution releases the drug-loaded nanoparticles that can translocate in the blood of pulmonary veins.
Mannitol was selected as carrier excipient serving as a matrix in which the CaPs are homogeneously dispersed. The final spray dried product exhibits enhanced flow properties and aerodynamic performance due to its physicochemical properties and low hygroscopicity[148 149]. Mannitol acts as a stabilizing agent for the nanoparticles providing an efficient nanoparticles re-dispersion simply by carrier dissolution. For instance, according to water replacement theory, mannitol exerts a stabilizing effect during lyophilization by replacing in the solid state water as the hydrogen-bonding agent[150]. A spray dried form of mannitol, as inhalation powder, has been approved by EMA and recently also by FDA for cystic fibrosis patient's treatment. Spray dried mannitol is marketed as Bronchitol® (Chiesi Farmaceutici S.p.A., Parma, Italy).

4.3.1 Design of experiments (DoE) to optimize the unloaded dpCaPs manufacturing

To optimize the manufacturing of microparticles embedding CaP nanoparticles, a DoE was applied on a scaled batch of nanoparticles dispersion concentrated 7.0 mg/mL. This CaPs dispersion showed a Z-Average diameter of 80 ± 15 nm, a PdI of 0.2 and a ζ-potential of -25 ± 2 mV.
A two-level full Factorial Design with 3 factors (2^3=8) was applied to investigate of all the possible combinations between the selected levels. In addition, 3 center points were added to check for a possible curvature. In total 11 experiments were generated in a randomized way to

avoid bias using Design-Expert Software® Version 12 (Stat-Ease Inc., Minneapolis, MN, USA). The three process and composition factors and the corresponding low and high levels chosen for the DoE were the following: A: CaPs dispersion concentration (mg/mL) [0.5, 7.0], B: Mannitol concentration in feed solution (mg/mL) [0.5, 2.0], C: Feed rate (mL/min) [3.5, 7.0]. The three factors and the corresponding level (named medium level) chosen by Design-Expert Software® for the center points were: A: CaPs concentration (mg/mL) [3.75], B: Mannitol concentration (mg/mL) [1.25], C: Feed rate (mL/min) [5.25]. The measured selected responses (Critical Quality Attributes) were evaluated after the manufacturing of the 11 powders were: yield of the process, moisture content, CaPs hydrodynamic diameter (d_H) after restoration in water (Z-Average diameter), microparticles size distribution (median volume diameter, Dv_{50}), microparticles aerodynamic performance measured as Emitted Dose (ED) and Fine particle Dose (FPD).The results after the measurement of the selected responses that were analyzed using Design Expert® are shown in the Table 4.2 for all powders. In this case, the low, middle and high levels of the factors are designated with -1, 0 and +1, respectively, according to the coded representation. Results interpretation will be discussed in the following corresponding subsections.

Table 4.2 Summary of the selected factors with a coded representation and responses.

	FACTOR			RESPONSE					
Run	**A: CaPs conc. (mg/mL)**	**B: Mannitol conc. (mg/mL)**	**C: Feed rate (mL/min)**	**Yield (%)**	**Moisture content (%)**	**Z-Average diameter (nm)**	**Dv_{50} (µm)**	**ED (mg)**	**FPD (mg)**
1	+1	+1	-1	84.4	1.2	313.4	3.0	38.1	11.8
2	+1	-1	-1	62.5	1.3	1787.0	2.1	33.0	17.0
3	-1	+1	-1	58.4	1.5	85.4	1.6	32.1	23.8
4	0	0	0	85.0	3.2	400.0	2.6	34.0	20.0
5	-1	-1	-1	53.2	4.0	839.5	3.1	34.6	24.3
6	+1	-1	+1	75.2	3.6	1992.0	3.3	37.6	12.9
7	-1	-1	+1	34.4	3.2	957.4	2.3	31.5	16.2
8	0	0	0	72.2	2.8	892.0	3.0	32.2	23.4
9	-1	+1	+1	61.8	1.4	428.0	2.8	35.6	15.4
10	0	0	0	85.0	2.5	423.0	2.9	32.7	24.3
11	+1	+1	+1	81.8	1.5	418.4	3.5	37.1	15.4

Notes: (Dv_{50}: mean volume diameter, ED: Emitted Dose, FPD: Fine Particle Dose. The three center points experiments correspond to Runs 4-8-10.

4.3.1.1 Yield of the spray drying process

As it can be evidenced from data reported in Table 4.2, the yield of the process varies from 34.4 to 85.0% which shows an important dependence of the yield from the different levels of the selected factors. The feed rate and both CaPs and mannitol concentration affect yield in the opposite way due to the different impact on the residual solvent. High feed rates lead to large droplets that require more time for solvent evaporation leading to high moisture contents in dried microparticles. Consequently, lower yields due to sticky particles on SD filter or cyclone walls were obtained. On the other hand, at high feed solution concentrations droplets contain lower solvent amounts leading to short drying time, less residual moisture and higher yield. As a result, the lowest yield was observed in run 7 where the total solid content was the minimum (overall 1.0 mg/mL) and the feed rate was at its high level (7.0 mL/min), on the contrary the highest yields were observed in runs 1, 4, 10 and 11 where the total solid content was high (5.0 or 9.0 mg/mL) and the feed rate low (3.5 or 5.0 mg/mL). In any case, in the majority of the experiments relatively high yields were achieved (average 68%). The results are also in agreement with a similar results of Dormenval *et al.* They identified factors of importance for the manufacturing of spray-dried siRNA-loaded lipid nanoparticles (LPNs) for inhalation and evaluated their influence on the resulting powders by using a quality by design approach. In particular, the feedstock concentration, consisting of siRNA loaded nanoparticles and mannitol chosen as stabilizing excipient influenced the yield of the spray drying process. Higher feedstock concentrations resulted in increased the yield [150].

Table 4.3 ANOVA for the selected factorial model for the yield of the process.

Source	Sum of Squares	df	Mean Square	F-value	p-value	
Model	1621.05	2	810.53	15.02	0.0029	significant
A-CaPs conc.	1154.40	1	1154.40	21.39	0.0024	significant
B-Mannitol conc.	466.65	1	466.65	8.65	0.0217	significant
Curvature	613.66	1	613.66	11.37	0.0119	significant
Residual	377.85	7	53.98			
Lack of Fit	268.63	5	53.73	0.98	0.5738	not significant
Pure Error	109.23	2	54.61			
Cor Total	2612.57	10				

As shown in Table 4.3 the ANOVA analysis for significance found the model significant as well as factors A and B ($p < 0.05$), CaPs and mannitol concentrations. However, factor C (feed rate) was found to be insignificant and removed from the model. While the curvature term was

included as it appears to be significant meaning that Response Surface Methodology (design augmentation) needs to be applied in order to explain what is causing the curvature. Finally, the Lack of fit was not significant in relation to the pure error.

CaPs concentration affected positively the yield, more significantly than mannitol concentration as it can be seen by the perturbation plot (Figure 4.18) in which the slope that corresponds to factor A is steeper than B. No interaction between factors A and B seems to occur as in the interaction graph the lines that correspond to factors A and B are parallel to each other (Figure 4.18). However, it has to be underlined that the yield is not always a reliable response. For instance, higher order models may govern the effect of the selected factors on the yield[151].

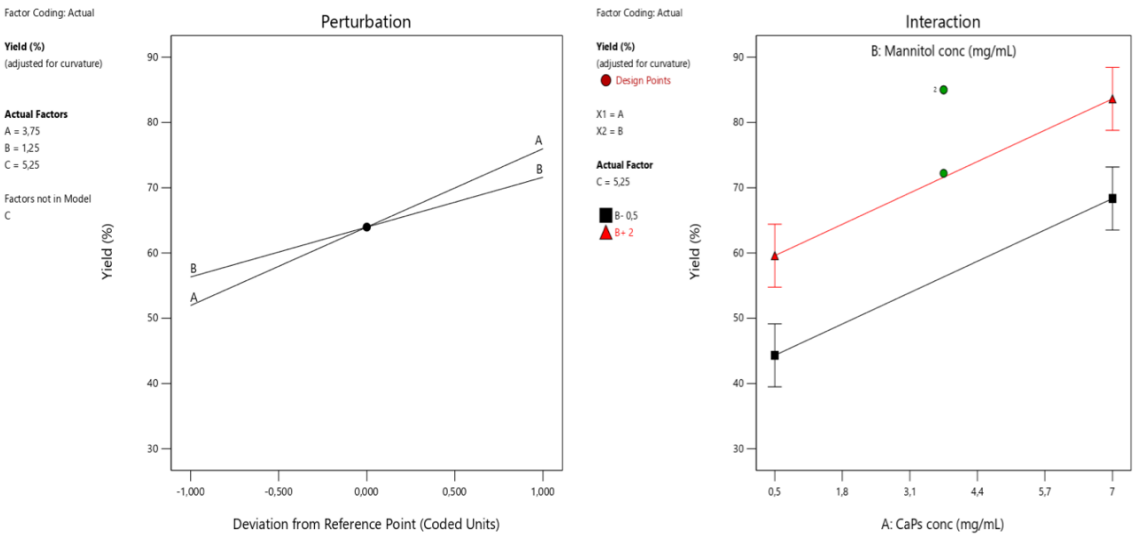

Figure 4.18 a) Perturbation plots for factors A and B b) Interaction graph for factors A and B.

4.3.1.2 Moisture content

The results from the measurement of moisture content using thermogravimetric analysis (TGA) for all 11 powders produced are shown in Table 4.4.

Table 4.4 Moisture content of the spray dried powders.

Run	A: CaPs conc (mg/mL)	B: Mannitol conc (mg/mL)	C: Feed rate (mL/min)	Moisture Content (%)
1	+1	+1	-1	1.2
2	+1	-1	-1	1.3
3	-1	+1	-1	1.5
4	0	0	0	3.2
5	-1	-1	-1	4.0
6	+1	-1	+1	3.6
7	-1	-1	+1	3.2
8	0	0	0	2.8
9	-1	+1	+1	1.4
10	0	0	0	2.5
11	+1	+1	+1	1.5

Apart from the impact of moisture content on powder flow properties as it induces agglomeration of very small particles and decreases de-agglomeration during aerosolization, long-term stability of the product, both physical and chemical, could also be affected [152 153]. Thus, moisture content in the final product should be kept as low as possible not only during production but also during storage. In this study moisture content of all powders ranged from 1.2 to 4.0% (w/w). The lowest values of moisture content were achieved at the high level of mannitol concentration whereas the highest moisture content values were achieved at the low level of mannitol concentration. However, for the other two factors (CaPs concentration and feed rate) no statistically significant effect could be evidenced.

Indeed, after analysis of the response with Design Expert®, Pareto chart reveals a strong effect of mannitol that reduce the moisture content (Figure 4.19). Nevertheless, the importance of mannitol in decreasing the moisture content in dry powder formulation after spray drying was recognized and considered significant. In addition, no other term seems to be significant while the model deriving from the inclusion of factor A only, despite significant, is poor in terms of R^2, adjusted-R^2, and predicted R^2.

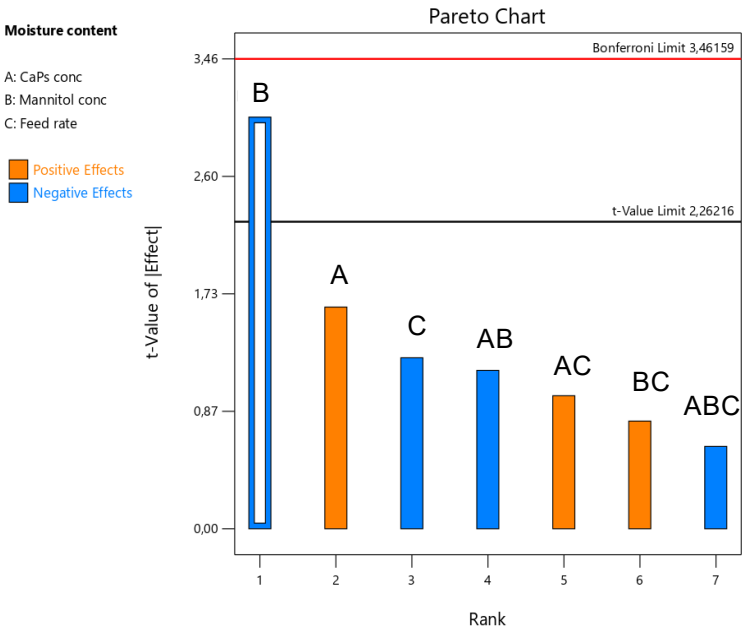

Figure 4.19 Pareto chart illustrating the rank of the t-values corresponding to the effect of each term on Moisture content.

Notes: There are two different t limits plotted on the graph. The highest limit is based on the Bonferroni corrected t-critical value. The lower limit is based on standard t-critical for individual effects tests. When conducting multiple analyses on the same dependent variable, the chance of committing a type I error increases, thus increasing the likelihood of coming about a significant result by pure chance. To correct for this Type I error, a Bonferroni correction has been conducted. To obtain the Bonferroni's correction (α/n), the original p value (α) has to be divided for the number of tests performed (n) [154] [155].

4.3.1.3 Z-Average and ζ-potential after powder restoration in water

The size restoration procedure is the *in vitro* test to assess the quality of CaP NPs released from the dissolved microparticles embedding nanoparticles. The test does not aim to mimic the *in vivo* release of nanosystem from microparticles deposited by inhalation on the wet lung epithelium. The particle size of CaPs dispersions, obtained after powder dissolution in water, is measured as Z-Average diameter, that resulted from dynamic light scattering equipment. Polydispersity index (PdI) and ζ-potential values are reported as well (Table 4.5). Particle hydrodynamic diameter after inhalation microparticle dissolution is a relevant product attribute. It has been shown elsewhere that the lower d_H is, the easier its penetration in a cell tissue can be[156]. A variety of transport barriers in biological tissues has to be overcome for drug delivery nanoparticles. The size, geometry, and surface-attached targeting molecules are the key nanoparticle design features that have been widely studied. Among these, in particular, the size of a particle has important effects on its immune clearance, transvascular delivery, and

intra-tissue dispersion and penetration. As aerosol particles penetrate deeper into the lungs, the absorptive epithelium becomes thinner until the alveolar epithelium is reached. However, the mechanisms by which particles translocate across the alveolar epithelial layer are poorly understood. Tetley *et al*. have shown that uptake and translocation across the pulmonary epithelium is controlled by alveolar type I epithelial cells, whereas not by alveolar type II epithelial cells. Moreover, the phagocytosis by resident alveolar macrophages is the primary mechanism for clearance of micronized foreign bodies. Small, individual, nanosized particles may not be recognized by macrophages and might instead be internalized by the alveolar epithelium. Furthermore, the particle size affects the different penetration mechanism. For example, by using siRNA nanoparticles, 50 nm nanoparticles enter largely by passive diffusion and are found in the cytoplasm, whereas 100 nm nanoparticles enter primarily via clathrin- and also caveolin-mediated endocytosis and are found in endosomes.

However, the size is not the only parameter affecting the alveolar internalization, in fact the nanoparticles functionalization increases their uptake and enhances binding of surfactant which further promotes uptake[119]. As demonstrated by Kato *et al.*, the polystyrene latex beads with a 240 nm diameter were captured by the epithelial cells. While these large particles could not be contemplated as ultrafine particles, it is fair to remark that when coated with lecithin, they were incorporated by type I and II cells. Hence, inhaled exogeneous particles, as function of their surface properties, can be otherwise processed[107].

As a result from these studies, a low diameter is desired for the final pulmonary formulation to be developed.

Table 4.5 Z-average diameter, polydispersity index (PdI) and ζ-Potential of dispersed CaPs after powder dissolution in water.

Run	Z-Average diameter (nm)	PdI	ζ-potential (mV)
1	313.4 ±2	1.0	-21.0
2	1787.0 ±2	1.0	-21.2
3	85.4 ±1	0.5	-18.3
4	400.0 ±2	1.0	-16.4
5	839.5 ±1	0.4	-16.0
6	1992.0 ±1	0.3	-16.5
7	957.4 ±3	0.6	-16.4
8	892.0 ±2	0.9	-15.7
9	428.0 ±2	0.6	-16.5
10	423.0 ±1	0.8	-16.0
11	418.4 ±1	0.2	-13.0

In this study, values between 85.4 and 1992.0 nm were measured with the maximum sizes attributed to the formulations with high CaPs concentration and low mannitol concentration (14:1 w/w ratio). The lowest size was achieved with low CaPs concentration and high mannitol concentration (1:4 w/w ratio), along with a low feed rate. Regarding colloidal stability ζ-potential values ranging from -13.0 to -21.2 mV, indicate colloidal systems relatively stable. In general, the observed zeta-potentials of approximately ≤ -30 mV or > 30 mV are indicative of a colloidal system sufficiently stabilized by electrostatic repulsion in aqueous suspension during short-term storage or further processing[157]. Finally, it is well-established that PdI values > 0.7 are typical for very broad particle size distributions (*e.g.,* polydisperse) distribution of particles[158]. Thus, in certain formulations (1,2,4,8,10) large PdI values suggest an incomplete redispersion for those powders, while in others (3,5,6,11) lower PdI values suggest a more homogeneous redispersion even though a higher Z-Average diameter may exist.

The results are in agreement with the fact that colloidal systems consisting of nanoparticles have a high tendency to agglomerate. Mannitol dissolved in the dispersion acts as a stabilizing agent driving to an efficient powder redispersion as size. The polyol prevents irreversible aggregation of approaching nanoparticles during the drying of droplet. Keil *et al.* formulate the hypothesis that the large amount of water in the nanoparticles, that is lost during the spray drying process, may lead to the need for larger amounts of matrix excipients capable to trigger a better redispersion[159].

ANOVA model was found to be significant as well as factors A, B and the interaction AB ($p < 0.05$). However, factor C (feed rate) was found insignificant and removed from the model as well as the curvature term. In addition, the Lack of fit was not significant relative to the pure error. Regarding the statistical terms of the model, this displays sufficient fitting of the data since R^2 is approximately 0.9. The difference between the Predicted R^2 and the Adjusted R^2 is less than 0.2, implying that a model transformation is not necessary whereas the Adequate Precision value is greater than 4. As a consequence, the model seems to be proper for the navigation in the design space (Table 4.6).

Table 4.6 ANOVA for the selected factorial model for Z-average diameter and fit statistics.

Source	Sum of Squares	df	Mean Square	F-value	p-value	
Model	3.339E+06	3	1.113E+06	18.61	0.0010	significant
A-CaPs conc.	6.053E+05	1	6.053E+05	10.12	0.0155	significant
B-Mannitol conc.	2.344E+06	1	2.344E+06	39.20	0.0004	significant
AB	3.888E+05	1	3.888E+05	6.50	0.0381	significant
Residual	4.186E+05	7	59799.66			
Lack of Fit	2.644E+05	5	52882.59	0.6860	0.6829	not significant
Pure Error	1.542E+05	2	77092.33			
Cor Total	3.757E+06	10				

R^2	0.8886
Adjusted R^2	0.8408
Predicted R^2	0.7802
Adequate Precision	11.0727

The role of mannitol to stabilize and protect CaPs size is to lead to a re-dispersion with small d_H. Its importance can be noticed in the perturbation plot (Figure 4.20a) in which the line slope that corresponds to CaPs concentration (factor B) is steeper than mannitol concentration (factor A) which has a less variable positive effect on particle size. Furthermore, interaction between factors A and B is observed as in the interaction graph the lines corresponding to factor A at different levels of factor B are not parallel. In particular, at the low level of factor B, the effect of CaPs concentration on the particle size moving from low to high level is much higher as when factor B is kept steady at its high level (Figure 4.20). Hence, in order to keep redispersed nanoparticle size low and stable, a high mannitol concentration in the dispersion of low CaPs is required.

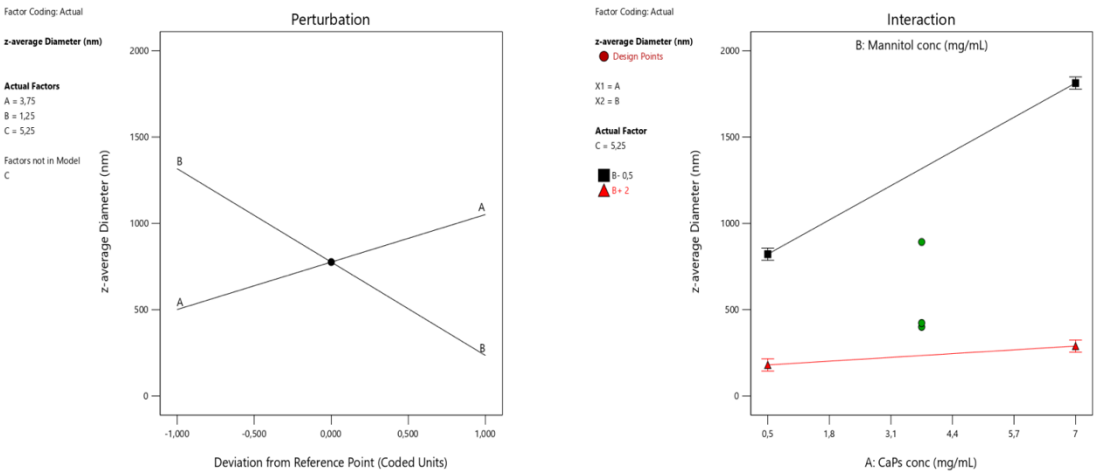

Figure 4.20 a) Perturbation plots for factors A and B; b) Interaction graph for factors A and B.

4.3.1.4 Particle size distribution (PSD) of the dry powders

The PSD of the dry powders that is shown in Table 4.7 is an indicator of the geometric particle size which is proportionally related to aerodynamic particle size. The dried powders obtained showed a Dv_{50} between 1.6 μm and 3.5 μm, which is a range considered extremely suitable for respiratory application[160]. More specifically, high Dv_{50} values resulted when feed solution concentration and feed rate were at their maximum levels (run 11). On the contrary, when these factors were kept at low values, the lowest Dv_{50} value was achieved (run 3). As shown elsewhere, an increase of feed rate leads to a higher particle size[161]. Apart from that it has been pointed out that geometric size (d_g) of the dry particle is given by the Equation 15:

$$d_g = \sqrt[3]{\frac{c_f}{\rho_p}} d_D \qquad (15)$$

where c_f is the feed solution concentration, ρ_p is particle density and d_D is droplet size [162]. Droplet size is positively affected by the feed rate, due to lower atomization energies. Thus, the increases in feed solution concentration and droplet size lead to higher particle size of dried particles. Moreover, feed rate affects negatively outlet temperature which results in a lower drying efficiency that may result to larger particles with high moisture content.

Table 4.7 Median volume diameter (Dv_{50}) and percentiles (Dv_{10}, Dv_{90}) of the spray dried powders.

Run	Dv_{10} (μm)	Dv_{50} (μm)	Dv_{90} (μm)
1	1.6	3.0	5.5
2	1.2	2.1	3.5
3	1.3	1.6	3.1
4	1.7	2.6	4.0
5	1.4	3.1	7.7
6	1.5	3.3	6.8
7	1.1	2.3	6.9
8	1.4	3.0	5.8
9	1.3	2.8	7.5
10	1.3	2.9	6.2
11	1.6	3.5	8.0

Analysis of the response using Design Expert® shows that factors A (CaPs concentration) and C (feed rate) together with interaction AB have a marginal but significant effect on Dv_{50}. They lie slightly above the t-value significance limit in the Pareto chart. Interestingly, the three factor interaction (3FI) ABC has the highest effect among all terms (Figure 4.21). The other

interaction terms (AC, BC) are insignificant; however, they were included in the model to support hierarchy. Subsequently, using ANOVA the model was found to be significant as well as factors A, C and the 3FI ABC ($p < 0.05$), while the curvature term was found to be insignificant and removed from the model. In addition, the Lack of fit was not significant relative to the pure error (Table 4.8). Statistical terms R^2 and adjusted R^2 were sufficiently high (0.9619 and 0.8729 respectively) however the predicted R^2 was found to be negative (-1.4486) meaning that inclusion of all the terms led to a model with poor prediction capacity. Model reductions with simultaneous maintenance of the hierarchy led to insignificant models.

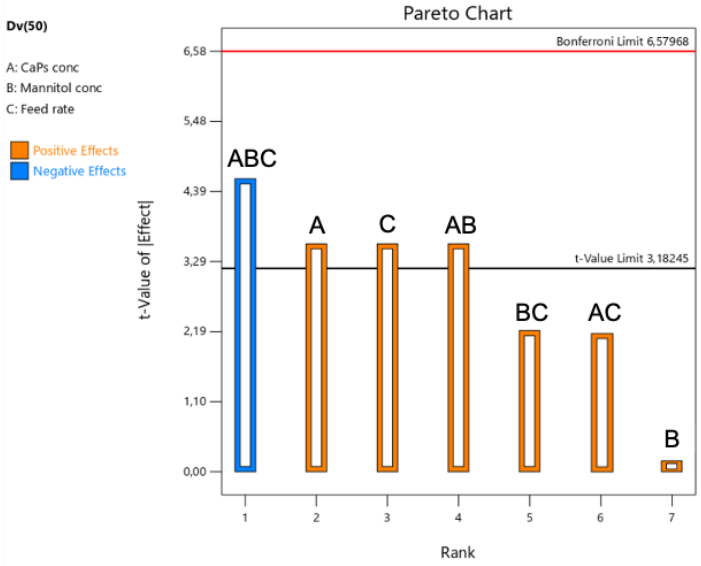

Figure 4.21 Pareto chart illustrating the rank of the t-values corresponding to the effect of each term on the Dv_{50}.

Table 4.8 ANOVA for the selected factorial model for Dv_{50}.

Source	Sum of Squares	df	Mean Square	F-value	p-value	
Model	2.9900	7	0.4270	10.81	0.0382	significant
A-CaPs conc	0.5512	1	0.5512	13.95	0.0335	significant
B-Mannitol conc	0.0012	1	0.0012	0.0316	0.8702	
C-Feed rate	0.5512	1	0.5512	13.95	0.0335	significant
AB	0.5513	1	0.5513	13.95	0.0335	significant
AC	0.2112	1	0.2112	5.35	0.1038	
BC	0.2112	1	0.2112	5.35	0.1038	
ABC	0.9112	1	0.9112	23.07	0.0172	significant
Residual	0.1185	3	0.0395			
Lack of Fit	0.0319	1	0.0319	0.7351	0.4816	not significant
Pure Error	0.0867	2	0.0433			
Cor Total	3.1100	10				

4.3.1.5 Aerodynamic performance

The Critical Quality Attributes selected in order to evaluate powder aerodynamic performance after the *in vitro* experiments were the Emitted Dose (ED) and the Fine Particle Dose (FPD) obtained by using Fast Screening Impactor (FSI). According to European Pharmacopoeia requirements, the ED should exceed 75% of the dose loaded in the device which in this case was 40 ± 0.5 mg. Observing the Table 4.9, in all cases Emitted Fraction (EF) was more than 75% with an average of 86%, meaning that all the formulations possess efficient flow properties during aerosolization. Analysis of the Emitted Fraction response using Design Expert® showed a high effect of factor A (NPs concentration) as well as 3FI ABC. As a result, only factor A was included in the model, which in any case resulted to be insignificant ($p>0.05$) with poor statistical terms and thus ED wasn't analysed further. However, it is obvious that due to high ED values in all formulations the space in which the experiments have been performed, probably provides flexibility in terms of achieving high ED values.

Table 4.9 Summary of the values of the parameters used to characterize powder aerodynamic performance.

Run	ED (mg)	EF (%)	FPD (mg)	FPF (%)
1	38.1	95.3	11.8	31.0
2	33.0	82.5	17.0	51.5
3	32.1	80.3	23.8	74.1
4	34.0	85.0	20.0	58.8
5	34.6	86.5	24.3	70.2
6	37.6	94.0	12.9	34.3
7	31.5	78.8	16.2	51.4
8	32.2	80.5	23.4	72.7
9	35.6	89.0	15.4	43.3
10	32.7	81.8	24.3	74.3
11	37.1	92.8	15.4	41.5

Notes: ED: Emitted Dose, EF: Emitted Fraction, FPD: Fine Particle Dose, FPF: Fine Particle Fraction.

Regarding FPD, this is an indicator of the lung deposition since it expresses the amount of the powder whose particles having an aerodynamic diameter less than 5μm. As mentioned before particles with a mean aerodynamic diameter 1-5 μm are considered to achieve the lung deposition. As it can be noticed in Table 4.9 FPD ranges from 11.8 to 24.3. The value is pushed towards its highest values, as the CaPs concentration and feed rate decreases (runs 3, 5).

Moreover, high FPD values were also achieved at center points (runs 4, 8, 10) whereas the lowest values were observed at high CaPs concentration (runs 1, 6). These results could be correlated with the corresponding results of the particle size distribution (PSD) analysis (4.3.1.4 subsection) where once more factors A and C had a significant positive effect on particle size. As factors A and C increased, particle size increased as well determining a FPD decreases due to a lower fraction of particles less than 5μm. Of course, this may not always be the case as other parameters such as moisture content, particle density and shape can have an impact either on powder dispersibility and aerodynamic diameter and subsequently FPD. For instance, even though run 5 has a Dv_{90} of 7.7μm, however exhibits a high FPD value and inversely run 1 showed a low FPD despite a favourable Dv_{90}.

Analysis of the response using Design Expert® shows that factor A has the highest effect on FPD reaching the more significant Bonferroni limit. The factor C and interaction AC have a significant effect since the t-value limit in the Pareto chart (Figure 4.22) is overcome. The other terms (B, AB, BC, ABC) are most probably insignificant and weren't included in the model. Subsequently, using ANOVA the model was found to be significant as well as factors A, C and the interaction AC ($p < 0.05$). In addition, the Lack of fit was not significant relative to the pure error (Table 4.10). Finally, the curvature term was included as it appears to be significant meaning that Response Surface Methodology (design augmentation) needs to be applied in order to explain what is causing the curvature.

Table 4.10 ANOVA for the selected factorial model for FPD.

Source	Sum of Squares	df	Mean Square	F-value	p-value	
Model	131.97	3	43.99	9.64	0.0104	significant
A-CaPs conc	63.84	1	63.84	13.99	0.0096	significant
C-Feed rate	36.13	1	36.13	7.92	0.0306	significant
AC	32.00	1	32.00	7.01	0.0381	significant
Curvature	65.20	1	65.20	14.29	0.0092	significant
Residual	27.38	6	4.56			
Lack of Fit	17.09	4	4.27	0.8307	0.6103	not significant
Pure Error	10.29	2	5.14			
Cor Total	224.55	10				

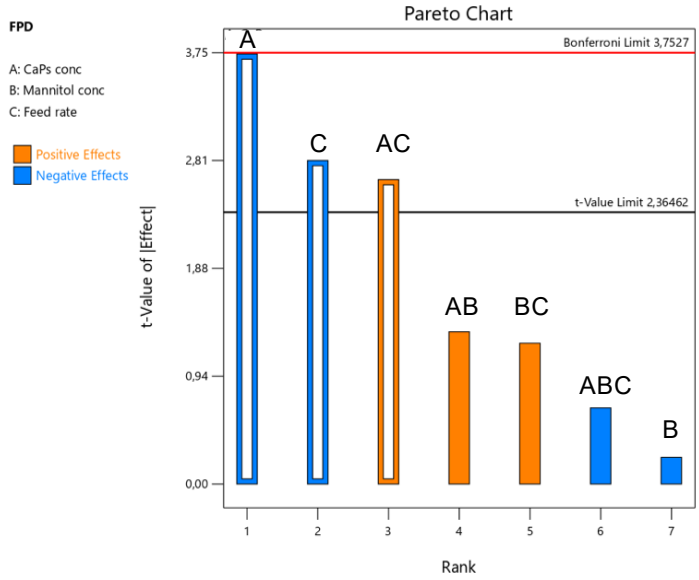

Figure 4.22 Pareto chart illustrating the rank of the t-values corresponding to the effect of each term on the FPD.

The negative effect of factors A and C can also be seen in the perturbation plot (Figure 4.23a) in which the slope for both factors is negative while for factor A is slightly steeper than factor C showing once more the higher effect of factor A. Furthermore, interaction between factors A and C seems to be possible as in the interaction graph the lines that correspond to factor A at different levels of factor C are not parallel to each other. In particular at the low level of factor C, the negative effect of factor A on the FPD moving from low to high level is much higher as when factor C is kept steady at its high level (Figure 4.23b).

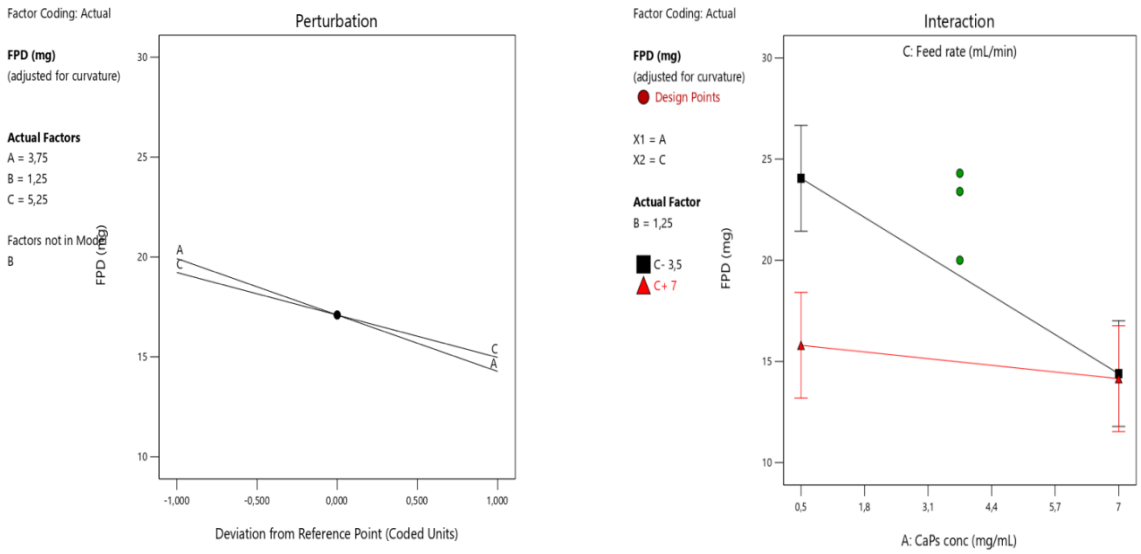

Figure 4.23 a) Perturbation plots for factors A and C b) Interaction graph for factors A and C.

4.3.1.6 Particle morphology

SEM/FIB was used to visualize the particle shape and surface morphology of spray-dried powders. These two micromeritics properties are key factors impacting on the flow properties, the aerodynamic particle size and the dispersibility of a dry powder, due to their effect on the inter-particulate forces. In this study, SEM images from three powders are reported for the analysis of morphology, namely run 1, 3 and 5 because they were particularly distinguished from the others. Runs 1 and 5 exhibited the lowest and highest FPD respectively, while run 3 had the highest FPF. Furthermore, spray-dried mannitol was examined in order to understand the impact of CaPs and mannitol concentrations on particle morphology.

In Figure 4.24 SEM/FIB images illustrate microparticles of spray dried mannitol alone. The dimensional range of the particles is from 200 nm to 1 μm which is considered as a very low PSD while their shape is quite spherical with a very smooth surface. Similar particle morphology has also been described elsewhere[163]. In addition, in the right image it is possible to visualize the internal structure of the particles as obtained by the application of FIB. The focused ion beam-scanning electron microscope (FIB-SEM) system is a new approach to investigate the three-dimensional internal structures of various materials because of its good performance and easy process. The advances of FIB-SEM 3D reconstruction allow to reveal the high and accurate resolution of internal structures of carbon-based materials. Within the particle, a large cavity of around 1.0 μm is formed thus leading to a hollow particle.

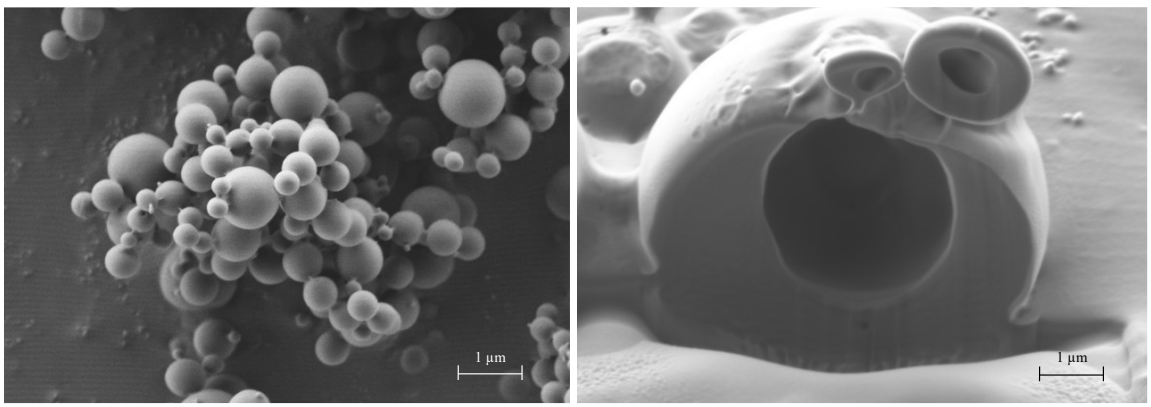

Figure 4.24 SEM micrographs of spray-dried mannitol microparticles.

The content ratio of CaPs and mannitol in the dispersion to spray dry, changed the morphology of dry particles embedding CaPs (dpCaPs). A donut-shaped structure of spray dried microparticles (Figure 4.26) was obtained when the nanoparticle's concentration was high and mannitol low. In particular, to prepare the dpCaPs of run 2, a feed solution having solid

concentration of 7.5 mg/mL, *i.e.* 0.5 mg/mL of mannitol dissolved in the dispersion containing 7.0 mg/mL of nanoparticles was dried at feed rate of 3.5 mL/min. In Figure 4.26 SEM micrographs at different magnifications shows agglomerates of particles with different sizes, mostly below 5µm. The majority of them are spheroidal, a typical shape of particles prepared using spray drying[164]. However, the large particles show a hole in the center that gives them a characteristic donut-like shape. The particle shape is affected by different mechanism of formation. If the shell is hard, but porous enough to allow the residual solvent in the core to evaporate, this could prevent the collapse of the outer solid layer, leading to hollow particle[165]. Torge *et al.* investigated the influence of mannitol on the morphology and aerodynamic properties of nano-embedded microparticles for pulmonary administration. Polylactic-co-glycolic acid (PLGA) nanoparticles and mannitol were spray dried each one as single component and in combination in three different ratios. An influence of the mannitol content on the morphology was evidenced despite all powders were suitable for pulmonary delivery. Hollow morphology and deviation from sphericity were obtained as the PLGA nanoparticles: mannitol ratio increased. Hence, the increase of the percentage of nanoparticles in the formulation leads to high Péclet number. This could be due to the significantly lower diffusion coefficient of the PLGA NPs compared to mannitol that led to the formation of hollow particles with large void spaces[120]. Calcium phosphates nanoparticles have also lower diffusion coefficient than mannitol in water ($2.7 \cdot 10^{-7}$ cm^2/s vs $2.9 \cdot 10^{-6}$ cm^2/s)[166167]. Consequently, the explanation about the particle surface collapse could be attributed to the increased CaPs: mannitol ratio that is 1:0.07 (Patent Application P022017IT-01). P_e justifies if the microparticle structure will be a dense, or rather hollow like "empty particle". As reported in the Equation 7, this dimensionless number results by the ratio between two characteristics rates of the drying process: firstly, the evaporation rate of droplet in drying, and the second one, the rate of solute (nanoparticles or molecules) diffusion to move from the external interface to the core of droplet (Figure 4.25).

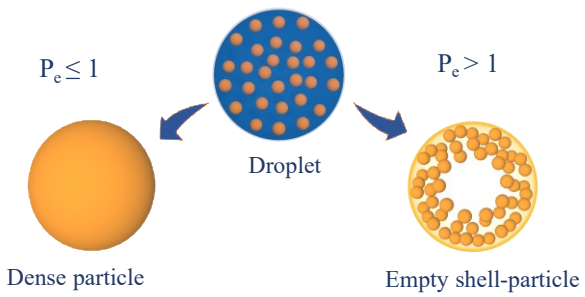

Figure 4.25 Drying of droplets containing particles of low (left) and high (right) Péclet number.

Nevertheless, P_e is also affected by the drying parameters like inlet temperature, pressure, gas flux as well as by the pressure of the spraying, viscosity, chemical nature and concentration of the solute, intermolecular interactions, factors related to the diffusion coefficients and indirectly to the radius of the droplet. Morphology of the particles also depend on the mechanical properties of the material forming the wall together to the colloidal interactions[168] as demonstrated by Tsapis *et al.*[169] and Marty *et al.*[170]. The accumulation of the nanoparticles at the surface in presence of low amount of mannitol made weak the resistance of the curvature of the particle that in dependence on the size, frequently collapse giving rise to the donut shape.

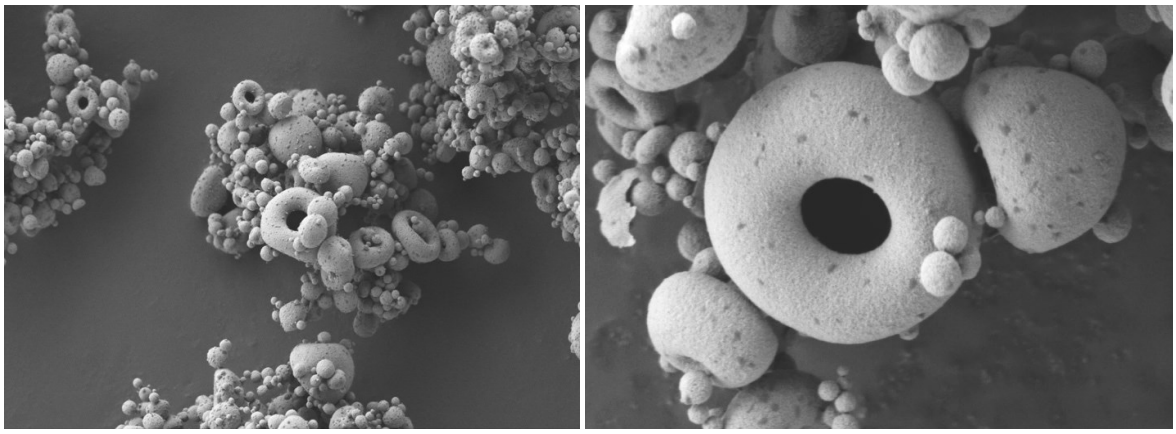

Figure 4.26 SEM micrographs of donut shaped microparticles CaPs: mannitol 1:0.07 embedding unloaded calcium phosphate nanoparticles (run 2 of DoE).

The donuts microparticle structures exhibited acceptable respirability, lower than spherical particles, but with Fine Particle Fraction still higher than 50%.

In order to evaluate the CaPs quality, in terms of size, after the spray drying process, 7.5 mg of donuts shaped microparticles were dissolved in water, to measure the nanometric range by dynamic light scattering. The nanoparticles were restored at nanoparticles concentration of 0.5 mg/mL. The size of the released nanoparticle after restoration resulted increased due to the presence of clusters of nanoparticles, likely an artefact deriving from the higher concentration of nanoparticles in the solution compared to mannitol amount.

In Figure 4.27 SEM images at different magnifications of run 5 obtained at spraying feed rate of 3.5 mL/min from a dispersion of CaPs 0.5 mg/mL and mannitol of 0.5 mg/mL; illustrate aggregates with similar particle shape as in Figure 4.26.

In this case, the donut particles showed an incomplete formation suggesting an effect of the higher amount of mannitol in the formulation. While the particle surface appears rough. Firstly, the particle surface collapse is dependent on the ratio between CaPs and mannitol. On the other

hand, the particle roughness, may explain the better behaviour of dpCaPs of run 5, in terms of FPF that was about 70%. These dpCaPs exhibited similar Dv_{50} value of those of run 1, namely 3.0 and 3.1 μm, respectively and a higher Dv_{90} (7.7 versus 5.5μm). Surface roughness decreases the particle contact area and also increases the distance of separation thus reducing the "cohesive" inter-particulate forces[171, 172].

This observation is also in agreement with Chew *et al.* that demonstrated how the increase in surface roughness of spray-dried bovine serum albumin particles can result in aerodynamic performance enhancement, in terms of fine particle fraction[173].

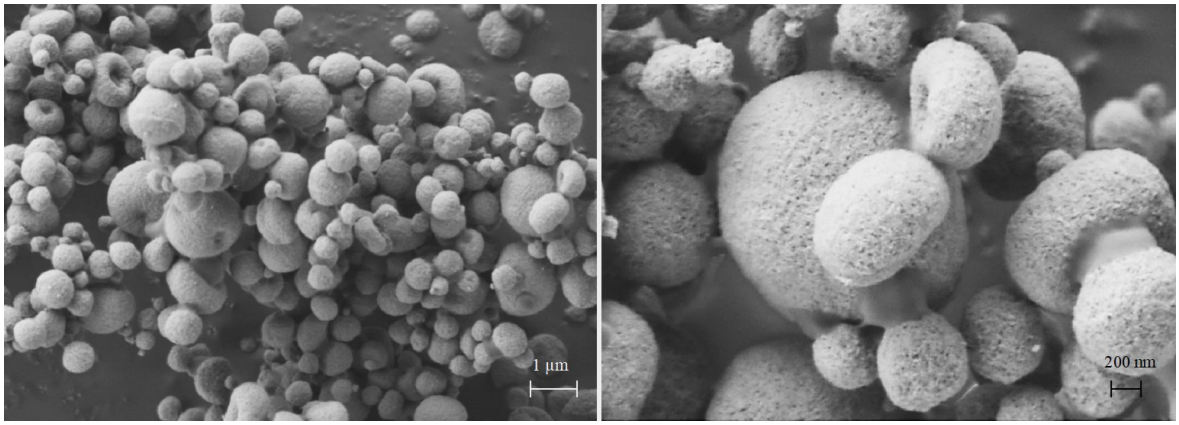

Figure 4.27 SEM micrographs of spray-dried microparticles embedding unloaded CaPs of run 5.

Finally, in Figure 4.28 particle shape, surface morphology and internal structure of run 3 (CaPs concentration of dried solution: 0.5 mg/mL; mannitol concentration: 2.0 mg/mL; feed rate: 3.5 mL/min) is displayed. In this case, dimensional range of the microparticles was from 200 nm to 2.5 μm, as volume diameter measured by laser light diffraction (*i.e,* Dv_{90} of 3.1 μm). The particle shape is quite spherical and close to that of the spray-dried mannitol. This should be explained since the CaPs: mannitol ratio is equal to 1:4. The particle surface appears rough while the internal structure shows again a hollow particle with many small pores spread over the entire inner part of the particle. This is interesting and may be related with the high FPF of this formulation, namely 74.1%. An increase in particle porosity leads to a decrease in particle density that reduces the aerodynamic particle size and thus improves FPF. The true density measured by gas pycnometer was 1.590 ± 0.002 and the apparent tapped density was 0.750 ± 0.002 g/cm^3. Although, the tap density measured value remained over 0.4 g/cm^3, that has been reported in many works as cut-off for determining good aerodynamic characteristics ("aerodynamically light particles")[39]. However, with these manufactured microparticles

embedding nanoparticles, the intraparticle porosity positively affects their respirability properties.

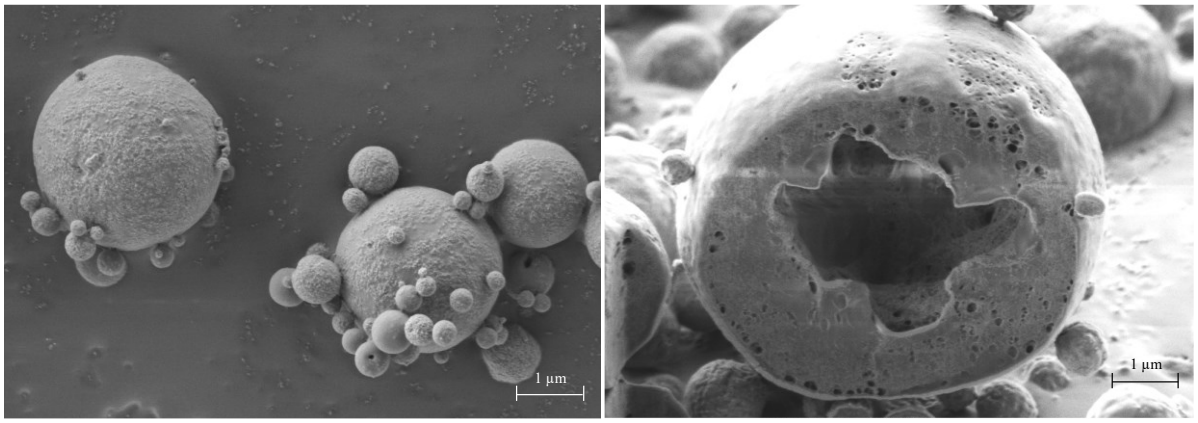

Figure 4.28 Pictures of spherical microparticles embedding calcium phosphate nanoparticles of run 3 by SEM (A) and sectioned by FIB/SEM (B). The ratio CaP: mannitol was 1:4.

In conclusion, the DoE study revealed that mannitol and nanoparticle concentrations significantly affect the fine particle dose (p=0.03) and the restored nanoparticle size (p=0.01). On the contrary, the feed rate parameter was not significant. The quantity of mannitol added to the CaP nano dispersion and the concentration of nanoparticles were crucial for the respirability of microparticles and the size of the restored nanoparticles. Namely, the increase of nanoparticles concentration in the drying droplet and the decrease of ratio between mannitol and nanoparticles lead the microparticle to donuts structure, with respirability decrease and size of the nanoparticles dramatically increase (Figure 4.29).

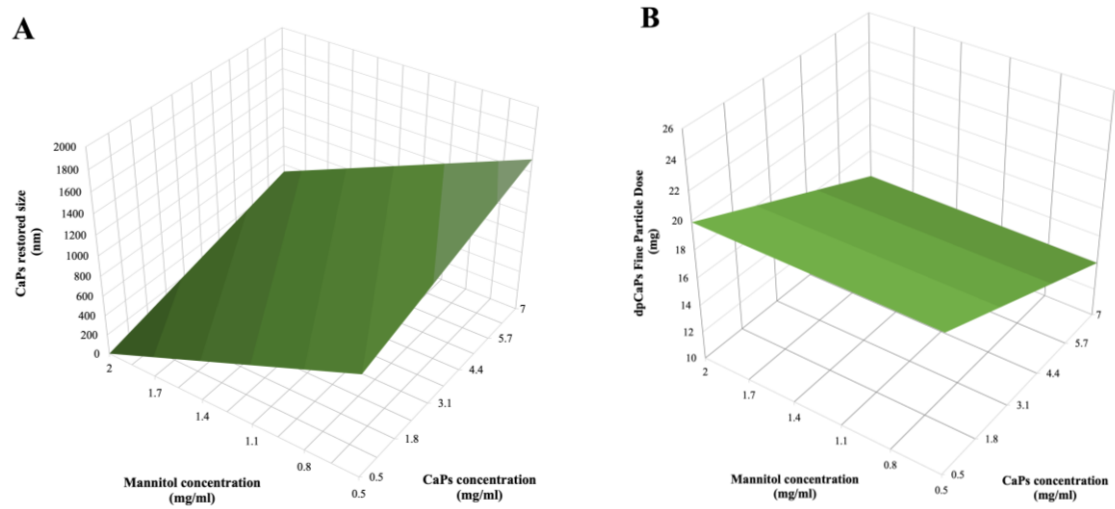

Figure 4.29 3D graphs of mannitol/CaP nanoparticles concentration and restored nanoparticles size (A) or Fine Particle Dose of microparticles (B) at fixed SD Feed rate 5.25mL/min.

4.3.1.7 Process optimization

To summarize all of the above acquired knowledge about the effect of the selected factors on the established CQAs, an effort for process optimization through the DoE was attempted using the desirability function. Desirability function aims to find operating conditions that ensure compliance with the criteria of all the involved responses and, at the same time, to provide the best value of compromise in the desirable joint response. This function has to be 1 to achieve good results[174]. Thus, in order to carried out the appropriate combination of the process parameters for a further improvement of the DPI formulation in terms of optimizing the selected CQAs, the following desirable criteria were set out:

- Maximization for the yield of the process;
- Minimization of Z-Average diameter for CaPs dispersion after powder restoration in water (as it is strongly related with the cell penetration capacity of the CaPs);
- Dv_{90} below 5 μm to provide particles with good aerodynamic properties;
- Maximization of Fine Particle Dose, the *in vitro* indicator of respirable particles.

According to these criteria, 48 solutions were identified by the software with high desirability while in the vast majority of the solutions, factors A, B and C were set at -1, +1 and -1 respectively. The ten solutions with desirability more than 0.860 are presented in Table 4.11. These solutions set the basis for the production of the microparticles embedding mimetic peptide and miRNA loaded CaPs that will be discussed in the Section (4.3.2).

Table 4.11 Parameter combinations that result in the desirable CQAs values with a desirability factor higher than 0.860.

	Factor			Response				
Number	**CaPs conc.**	**Mannitol conc.**	**Feed rate**	**Yield**	**Z-Average Diameter**	**Dv_{50}**	**FPD**	**Desirability**
1	0.50	2.00	3.50	59.58	180.05	1.63	24.050	0.864
2	0.53	2.00	3.50	59.70	180.57	1.64	24.005	0.863
3	0.51	2.00	3.51	59.62	180.21	1.64	24.001	0.863
4	0.50	1.99	3.50	59.49	184.03	1.64	24.050	0.863
5	0.50	1.99	3.50	59.48	184.36	1.64	24.050	0.863
6	0.57	2.00	3.50	59.84	181.20	1.65	23.949	0.862
7	0.50	2.00	3.53	59.59	180.05	1.64	23.974	0.862
8	0.59	2.00	3.50	59.95	181.69	1.65	23.905	0.862
9	0.50	2.00	3.55	59.59	180.05	1.65	23.933	0.861
10	0.50	1.97	3.50	59.32	191.48	1.66	24.050	0.860

4.3.2 Manufacturing optimization of MP-loaded dpCaPs

To optimize the process for the production of microparticles embedding MP loaded CaPs via spray drying, the results obtained from the previous DoE for the unloaded CaPs powders were assumed. Moreover, the solutions of Design Expert® for process optimization (Table 4.12) in combination with the results from Scanning Electron Microscopy (SEM) were elected as reference. Therefore, in order to achieve microparticles embedding MP loaded CaPs, with good aerodynamic performance, a ratio of MP/CaPs: mannitol of 1:4 w/w was established together a feed rate of 3.5 mL/min. The MP loaded CaPs dispersions batches were prepared in scaled-up dimensions (3L). Two levels of solid content of the MP/CaPs dispersions were selected, namely 1.6 mg/mL that was the original concentration of the dispersions, and one more diluted *i.e.* 0.5 mg/mL. The NPs highest concentration has been chosen in the scale up manufacturing, in order to obtain high amount of final powder starting from small volume of NPs dispersion to dry. Finally, the same quality attributes of the unloaded dpCaPs were evaluated for the spray-dried microparticles embedding the peptide (MP/dpCaPs) with the addition of the content determination before and after spray drying. The process parameters applied were the same in the QbD selected as optimized in the previous test.

Table 4.12 Summary table of the selected Critical Quality Attributes.

Run	MP loaded CaPs (mg/mL)	Mannitol (mg/mL)	Yield (%)	Moisture content (%)	Z-Average after restoration (nm)	Dv_{50} (µm)	EF (%)	FPF (%)	MP in dpCaPs Content % w/w
1a	1.6	6.4	67	1.2	169.6	2.99	86.7	52.9	1.0
2a	1.6	6.4	68	2.4	102.5	2.30	75.4	68.1	1.1
3a	1.6	6.4	65	2.8	125.5	2.38	75.6	61.4	1.4
4a	1.6	6.4	69	1.9	133.6	2.46	74.9	69.9	1.1
5a	1.6	6.4	65	1.7	138.6	2.24	79.5	63.4	1.2
Average			67	2.0	134.0	2.47	78.4	63.2	1.2
Std. Dev			1	0.6	24.3	0.30	5.0	6.7	0.1
1b	0.5	2.0	41	3.0	250.1	2.50	78.7	74.0	1.0
2b	0.5	2.0	52	2.4	193.3	2.04	70.2	83.4	1.0
3b	0.5	2.0	55	2.6	209.7	1.89	66.7	80.3	1.3
4b	0.5	2.0	44	1.0	159.0	2.12	76.7	71.2	1.1
5b	0.5	2.0	53	1.5	286.9	2.04	79.0	66.7	1.2
Average			49	2.1	219.8	2.12	74.3	75.1	1.1
Std. Dev			6	0.8	49.8	0.23	5.5	6.8	0.1

Notes: (Dv_{50}: median volume diameter, Z-Average after powder restoration in water, EF: Emitted Fraction, FPF: Fine Particle Fraction, MP/dpCaPs Payload = w/w ratio of mimetic peptide in the dry powder. Runs a. and b. are referred to undiluted and diluted dried CaPs, respectively.

Table 4.12 summarizes the characterization data after the evaluation of the CQAs that derive from the QTPP for all the ten powders that produced using the batches of MP loaded CaPs dispersions prepared in a scale up size. Results interpretation will be discussed in the following corresponding subsections.

4.3.2.1 Yield of the process

Observing Table 4.12, it can be noticed that during spray drying of undiluted MP/CaPs dispersions, higher yields were achieved (average 67 ± 1%) with repeatability that was significantly higher than in the case of diluted MP/CaPs dispersions (average 49 ± 6%). Increase of total solid content of solution to be dried from 2.5 to 8.0 mg/mL clearly positively affected the yield. Less solvent to be evaporated is in each droplet after atomization and thus less moisture content and higher yield is achieved.

In spray drying process, a compromise needs to be done between particle size and yield. It is well known that a mini spray-drying, sometimes has low collection efficiency for fine particles below 2-1 μm as they are not heavy enough to escape the air stream and thus could not deposit in the collection vessel[149]. However, to prepare microparticles in the range of 1-5 μm sufficiently high yields can be obtained. Obviously, in larger scale, spray drying leads to better yields than in lab scale because the fraction lost is an increasingly smaller component of the total production volume[175]. Therefore, without setting aside the superiority of runs 1a-5a in terms of yield, this attribute shouldn't be a limitation in order to select between diluted or undiluted formulations.

4.3.2.2 Moisture content

Regarding moisture content of the replicated formulations, this ranged from 1.0 to 3.0% as shown in Table 4.12. A high variability of moisture content was observed between powders treated in the same conditions, as shown for both undiluted and diluted MP/CaPs dispersions. Furthermore, an increase in moisture content, even though not significant, was measured for runs 1b-5b which could be attributed to the lower mannitol concentration which affects negatively the moisture content as already observed in the DoE presented in Section 4.3.1.

Nevertheless, moisture content for all formulations should be low. The use of mannitol as excipient, due to its particular properties such as low hygroscopicity, results advantageous to obtain powders with low moisture contents[176].

4.3.2.3 Z-Average and ζ-potential after powder restoration in water

Table 4.13 summarizes of the results of the DLS measurements of all MP/dpCaPs formulations after nanoparticles restoration in water compared to the MP/CaPs dispersions before spray drying. The Z-Average of the MP/CaPs before spray drying is more than two times higher than the unloaded CaPs prepared in a scale-up batch size, namely 202.9 and 80.0 nm respectively. It could be speculated that the increase in size could be associated with an effective interaction of mimetic peptide with CaP-NPs.

Table 4.13 Summary table of the DLS measurements.

Run	Z-Average before SD (nm)	Z-Average after restoration (nm)	PdI	ζ-potential (mV)
1a	265.7	169.6	0.8	-11.8
2a	120.8	102.5	0.7	-10.5
3a	197.7	125.5	0.7	-14.2
4a	157.4	133.6	0.7	-16.5
5a	272.8	138.6	0.6	-14.9
Average	202.9	134.0	0.7	-13.6
Std. dev	66.5	24.3	0.1	2.4
1b	266	250.1	0.6	-16.9
2b	124	193.3	0.8	-13.2
3b	195	209.7	0.7	-14.2
4b	150	159.0	0.7	-11.7
5b	276	286.9	0.7	-17.7
Average	202.2	219.8	0.7	-14.7
Std. dev	67.8	49.8	0.1	2.5

Notes: Z-Average of nanoparticles before spray drying (SD) and after powder restoration in water, polydispersity index (PdI) and ζ-potential after microparticles embedding nanoparticles restoration. Runs a. and b. are referred to undiluted and diluted dried CaPs, respectively.

Furthermore, the high inter-batch variability of Z-Average diameter for the MP/CaPs dispersions with an average of 202.9 ± 66.5 nm, was sensibly reduced by the microparticle preparation.

In terms of polydispersity, the average PdI of 0.7 reflects an incomplete re-dispersion of all powders, independently if they were manufactured starting from diluted or undiluted CaPs dispersion. Moreover, ζ-potential values, ranging from -10.5 to -17.7 mV, indicate colloidal systems at risk of agglomeration. An explanation about the colloidal stability of the MP/CaPs dispersions is that during dialysis for 48h a significant amount of sodium citrate is being lost. Sodium citrate is the determinant factor for the stabilization of the colloidal system, as it serves as a crystal-growth inhibitor for the MP/CaPs. In fact, the preparation of nanoparticles with a shorter time of dialysis, *i.e.* 24 or 32h, led to products with higher negative surface charge values, -22.0 ± 3 mV and -20.0 ± 1 mV, respectively.

An average 34% reduction in particle size was achieved after water dissolution of dry powders obtained from the undiluted MP/CaPs dispersions, whereas an average 5% increase in particle size was observed in the case of diluted MP/CaPs dispersions. The mannitol concentration in runs 1a-5a (6 mg/mL) is out of the range of the previous DoE that mannitol concentration in MP microparticles preparation (from 0.5 to 2.0 mg/mL). However, the ratio between nanoparticles and mannitol remains unvaried at 1:4. These results indicate that high solid concentration triggers a better re-dispersion. Similar results were obtained by Wang *et al.* who prepared spray-dried microparticles embedding PLGA nanoparticles using mannitol as a matrix in a ratio PLGA: mannitol 1:4 w/w and a feed solution concentration ~3 mg/mL[157]. Consequently, superiority of spray-dried undiluted MP/CaPs in terms of acquiring colloidal dispersions versus spray-dried diluted MP/CaPs, was found. In fact, the microparticles embedding MP/CaPs at higher content exhibited a significant lower Z-Average after restoration than the diluted MP/CaPs.

4.3.2.4 Particle size distribution (PSD) of the dry powders

In Section 4.3.1.4, a significant positive effect of CaPs concentration on microparticles Dv_{50} was shown after analysis of the data using Design Expert®. In addition, based on Equation 15, the impact of feed solution concentration on the geometric size (d_g) of the dry powder has already been illustrated. Here, in Table 4.14 the results of the measurement of PSD for ten dry powders using laser diffraction, are listed. The results are in agreement with the previous study for the unloaded CaPs. Elversson *et al.* studied the fundamental aspects of the particle

formation during spray drying, related to particle size and density. Particles were prepared starting from carbohydrates having different solubility and different excipient, such as lactose, mannitol, and sucrose/dextran in ratio 4:1. As increasing the droplet size during atomization as well as the feed solution concentration increases, particle size increased[177].

Table 4.14 Particle size distribution of spray-dried microparticles embedding loaded MP/CaPs. Runs a. and b. are referred to undiluted and diluted dried CaPs, respectively.

Run	Dv_{10} (µm)	Dv_{50} (µm)	Dv_{90} (µm)
1a	1.46	2.99	6.02
2a	1.17	2.30	4.74
3a	1.20	2.38	4.92
4a	1.29	2.46	4.57
5a	1.20	2.24	4.19
Average	1.26	2.47	4.89
Std. dev	0.12	0.3	0.69
1b	1.23	2.50	4.96
2b	1.03	2.04	4.34
3b	0.96	1.89	4.16
4b	0.93	2.12	5.60
5b	0.99	2.04	4.82
Average	1.03	2.12	4.78
Std. dev	0.12	0.23	0.57

Almost in all cases the resulted percentiles of volume diameter indicate a size distribution between 1-5 µm thus making the dry powders suitable for respiratory application with the potential to achieve deep lung particle deposition. These results are also reinforced by the fact that MP loading in CaPs didn't lead to products with a particle size outside the desirable range of 1-5 µm. Thus, despite a slight superiority of diluted MP/CaPs, both diluted and undiluted MP/CaPs dispersions are suitable for pulmonary administration.

4.3.2.5 Aerodynamic performance

The aerodynamic performance of the obtained powders was assessed through Fast Screening Impactor (FSI) using RS01® device for inhalation and the parameters related with the lung deposition profile of the dry MP/CaPs are listed in Table 4.15.

As it can be noticed, runs 1b-5b exhibit a higher average FPF compared to runs 1a-5a, namely 75.1% and 63.2% respectively. This could be due to the lower particle size of dry powders coming from diluted MP/CaPs dispersions since PSD is strongly correlated with FPF. The particle size distribution measurements using laser diffraction are metrics for bulk powder, which is essentially completely dispersed to primary particles using, albeit for few minutes, sonication. While the fine particle fraction is a measurement of the particles' d_{ae} after that the deagglomerated aerosol delivered by the inhaler device; moreover, as previously discussed, d_{ae} is function not only of the volume diameter of the particles but also of their density. Thus, even a low PSD can be obtained by laser diffraction, a high FPF may not be able to be achieved if the "cohesive" inter-particulate forces are strong or overcome patient inspiratory flow rate. Therefore, measuring PSD is not enough to predict an efficient powder aerodynamic performance since other parameters such as bulk density and particle shape may also contribute, as mentioned in Section 1. Nevertheless, in this study superiority of spray-dried diluted MP/CaPs in terms of FPF should be considered significant. The results are in agreement with those of the previous DoE for the unloaded CaPs, where high CaPs concentration showed a significant negative effect on FPF.

Table 4.15 Summary of the values of the parameters used to characterize powder aerodynamic performance.

Run	ED (mg)	EF (%)	FPD (mg)	FPF (%)
1a	36.6	86.7	19.4	52.9
2a	30.9	75.4	21.1	68.1
3a	31.1	75.6	19.1	61.4
4a	30.7	74.9	21.3	69.9
5a	32.9	79.5	20.9	63.4
Average		78.4		63.2
Std. Dev		5.0		6.7
1b	25.6	78.7	18.9	74.0
2b	28.4	70.2	23.6	83.4
3b	27.1	66.7	21.7	80.3
4b	31.2	76.7	22.2	71.2
5b	32.0	79.0	21.3	66.7
Average		74.3		75.1
Std. Dev		5.5		6.8

Notes: ED: Emitted Dose, EF: Emitted Fraction, FPD: Fine Particle Dose, FPF: Fine Particle Fraction. Runs a. and b. are referred to undiluted and diluted dried CaPs, respectively.

Regarding Emitted Fraction (EF), this was slightly higher in spray-dried undiluted MP/CaPs where an average 78.4% was measured, anyway, all five formulations exceeded the desirable 75%. On the contrary spray-dried diluted MP/CaPs exhibited an average 74.3% in EF while runs 2b and 3b were found to have an EF below 75%. This discrepancy in EF could be attributed to poorer flow properties of spray-dried diluted MP/CaPs due to lower particle size and higher moisture content than those diluted. The formulations with low Dv_{90} and high moisture content exhibited a low EF (2b, 3b) whereas formulations with high Dv_{90} and low moisture content exhibited a high EF (1a, 4b, 5b). Nevertheless, information about particle shape and surface morphology should be evaluated in parallel as can drastically affect powder flow properties.

4.3.2.6 Peptide content assessment

The results of peptide content, both in the MP/CaPs dispersions before spray drying and in the final formulation, are reported in Table 4.16. MP content over CaPs in the dispersion was calculated as the ratio of the MP found concentration on the CaPs concentration (0.5 mg/mL or 1.6 mg/mL). MP percent in dpCaPs was calculated as the ratio of MP content amount and the powder weighed for the analysis (~20mg).

Table 4.16 Peptide content in CaPs dispersions and in dry powders assessed by HPLC-UV. Runs a. and b. are referred to undiluted and diluted dried CaPs, respectively.

Run	Measured MP/CaPs content (%)	Measured MP/dpCaPs content (% w/w)
1a	6.6	1.0
2a	6.8	1.1
3a	7.5	1.4
4a	6.7	1.1
5a	6.8	1.2
Average	6.9	1.2
Std. Dev	0.4	0.1
1b	6.6	1.0
2b	6.8	1.0
3b	7.5	1.3
4b	6.7	1.1
5b	6.8	1.2
Average	6.9	1.1
Std. Dev	0.4	0.1

Notes: mimetic peptide (MP) content in both nanoparticles dispersions was the same since it was calculated as the ratio of measured MP concentration (*e.g.,* Run 1a: 0.1056 mg/ml, Run 1b: 0.033 mg/ml) on the undiluted or diluted CaPs concentration (*i.e.* 1.6 mg/mL or 0.5 mg/mL).

In all dry powder formulations MP/dpCaPs was between 1.0 %w/w and 1.4 %w/w. Since the ratio CaPs: mannitol was 1:4, the expected peptide content in microparticles was a fifth of MP content in CaPs that was 6.9 ± 0.4. A low inter-batch variability for both diluted and undiluted dpCaPs was observed in agreement with peptide content assessed in NPs batches. Concerning the MP/dpCaPs peptide content of undiluted and diluted formulations, this was slightly higher in the first case without significant difference. Finally, taking into account that the residual solid in the nanoparticles dispersion was not only determined by the CaPs, the peptide content in microparticles embedding the nanoparticles was about one fifth of mimetic peptide content in CaP before drying. Hence, the inlet temperature of 125°C and outlet temperature between 75 and 80°C preserved the mimetic peptide from the degradation.

4.3.2.7 Particle morphology

The particle morphology was investigated for both formulations and performed using SEM and SEM/FIB technique. The micrographs obtained are shown in Figure 4.30.

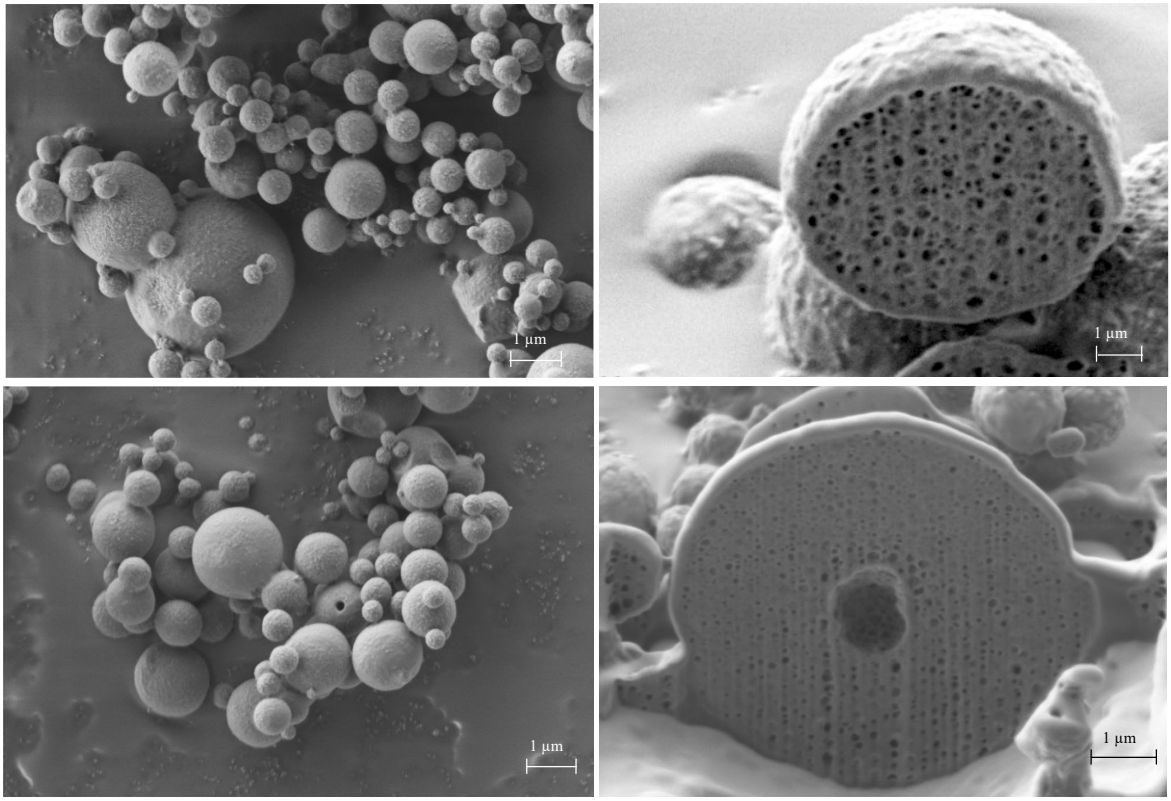

Figure 4.30 Surface and shape (left) SEM image and inner structure (right) FIB/SEM acquisition of microparticles embedding nanoparticles loaded with mimetic peptide. The microparticles of pictures A and B are prepared from undiluted and diluted nanodispersion of CaP, respectively (Patent Application P022017IT-01).

Concerning the particle shape, in both compositions with CaPs content, microparticles exhibited a spherical shape and rough surface as with the unloaded microparticles. The SEM, matched with the Focus Ion Beam technique, allowed to evidence the internal structure of the microparticles embedding the loaded with mimetic peptide calcium phosphate nanoparticles. The inside aspect revealed microparticles with a large number of cavities having 20 nm diameter or smaller, evidently due to the peptide, similarly for both preparations. However, a central evident cavity formed in the case of microparticles produced from undiluted NPs, as with unloaded microparticles. These numerous voids increase the porosity of microparticles, one of the main parameters determining their aerodynamic behaviour. The deposition of aerosolized particles in the airways depends on the aerodynamic diameter that is directly related to particle density. This may explain the high FPF values of all formulations. Finally, this original structure has to be clearly attributed to the peptide presence.

MP/dpCaPs prepared with the diluted CaPs dispersions, exhibited a median volume diameter (Dv_{50}= 2.12 μm) which matches with the increased FPF of those powders, compared to the undiluted ones (75.1% and 63.2% respectively). Similar characteristics for both powders were obtained in terms of moisture and peptide content. Regarding particle morphology, both treatments had a spherical shape and bumpy surface, with an increased number of nano porous on it. The yield and Z-Average size of nanoparticle restored were significantly higher for the microparticles prepared starting from undiluted CaP NPs.

4.3.3 Manufacturing and characterization of loaded with mi-RNA and R7W-MP dpCaPs

Microparticles embedding the micro-RNA nanostructure (dpCaPs/micro-RNA) were prepared by spray-drying technique. Briefly, 2.0 mg/mL of mannitol were dissolved in 0.5 mg/mL of micro-RNA loaded nanoparticle water dispersion. The ratio CaPs micro-RNA: mannitol was 1:4 in the feed solution containing 2.5 mg/mL as residual solid. The mix was stirred for a few minutes at room temperature to allow the carrier dissolution. The set spray dryer parameters were inlet and outlet Temperature 125°C and 70°C, respectively; atomization flow 600 L/h; feed rate 3.5 mL/min; air flow 35 m^3/h. A nozzle with a diameter of 0.7 mm was used. The manufactured microparticles were stored at room temperature in sealed vials. The yield of the spray drying procedure was around 70%.

As reported in the paragraph 4.1.3 the obtained micro-RNA loaded CaPs nanoparticles showed a size of 1900 ± 50 nm, likely as a consequence of agglomerated nanoparticles with surface charge of -17 ± 5 mV. Since the nanoparticles loaded with the mi-RNA appeared to have the tendency to agglomerate, the challenge was to study and construct inhalable microstructure embedding de-agglomerated nanoparticles. In fact, if microparticles dissolution in lung fluid restores cluster of nanoparticles, these could be phagocytosed by macrophages[119].

Table 4.17 Microparticles embedding micro-RNA loaded CaP nanoparticles characterization.

Residual water (w/w%)	EF (%)	FPF (%)	Particle size distribution			Restored Nanoparticles	
			D_{v10} (µm)	D_{v50} (µm)	D_{v90} (µm)	Z-Average (nm)	Z- Potential (mV)
1.0±0.5	89.0±0.1	65.0±0.2	1.3±0.2	2.3±0.6	5.±0.5	250±15	-17±3

The 90% of the microparticles distribution had volume diameter lower than 5 microns (Table 4.17). Spherical microparticles with a rough surface, embedding micro-RNA loaded nanoparticles, were pictured by SEM technique. The sectioned microparticles showed also in this dry composition a porous internal structure with several distributed small cavities having a diameter in nanometric range of 10-50 nm (Figure 4.31). The dry particles have an Emitted Fraction at 89% and Fine Particle Fraction of 65%, suitable for pulmonary administration. Unexpectedly, these microparticles restored nanoparticles with size around 250 nm, only one

eighth of the size of the original nanoparticles. A key role was played by the excipient mannitol to deagglomerate the dpCaPs/micro-RNA calcium phosphate nanoparticles.

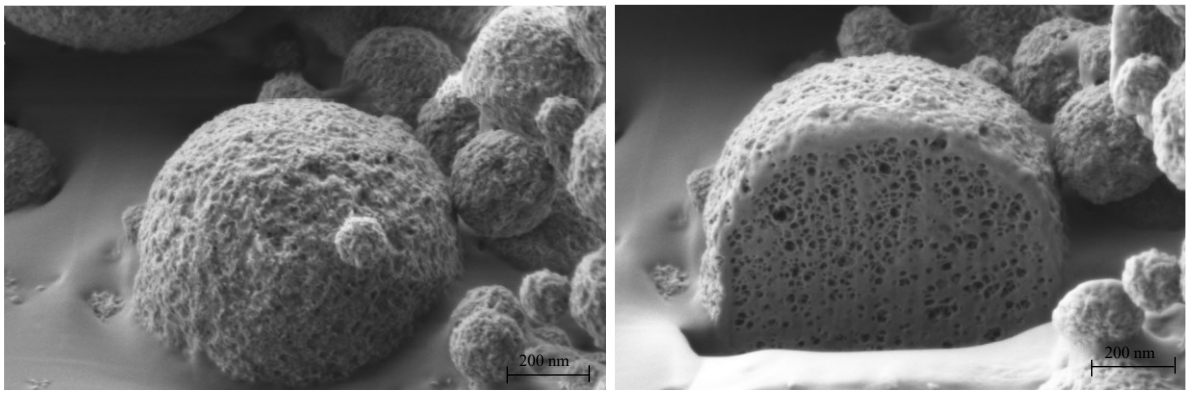

Figure 4.31 SEM image (left) and inner structure FIB/SEM photograph (right) of microparticles embedding nanoparticles loaded with micro-RNA.

To definitely attribute the inner porous structure to the high molecular substance presence as for mimetic peptide and micro-RNA microparticles, calcium phosphate nanoparticles were prepared by precipitation as described in subsection 4.1.3 loading another peptide as the R7W-mimetic peptide (R7W-MP) (19 amino acids, MW 2605.9 Da, α-helix structure). This peptide is different from the mimetic peptide previously loaded, because a terminal arginine amino acid allows the self-internalization into the cardiomyocytes. To manufacture the powder to be inhaled, mannitol was dissolved in the nanoparticle dispersion at CaPs: mannitol ratio 1:4, resulting in a feed solution to be dried containing 2.5 mg/mL of solid. The spray dryer parameters were the same as for mi-RNA CaPs microparticles. The yield of the drying process was 84.4%. Assessment by HPLC-UV revealed that the R7W-MP peptide content of the manufactured microstructure was 1.25 % w/w, as expected.

Table 4.18 Characteristics of Microparticles embedding R7W-MP loaded CaP nanoparticles.

Residual water (w/w%)	EF (%)	FPF (%)	Particle size distribution			Restored Nanoparticles	
			D_{v10} (µm)	D_{v50} (µm)	D_{v90} (µm)	Z-Average (nm)	Z- Potential (mV)
1.5±0.5	86.3± 0.03	68.5± 0.01	1.1±0.2	2.1±0.4	4.5±0.5	60.7±5	-24.5±2

The morphology acquired by SEM analysis showed roundish shape and wrinkled surface microparticles in the range from 200 nm to 2 µm (Figure 4.32). The SEM analysis confirmed

the particle volume diameter smaller than 5 μm, as measured by laser light diffraction analysis (Table 4.18).

The SEM matched with the Focus Ion Beam technique allowed to evidence the internal structure of the microparticles embedding loaded with R7W-MP calcium phosphate nanoparticles. The inside revealed microparticles with a lot of cavities having 20 nm diameter or smaller due to the R7W peptide, similarly to microparticles with mimetic peptide. The regular structure, close to a grid, in which are organized the small cavities, could be an artefact of the ion beam cutting. A value of fine particle fraction 68.5% has been *in vitro* determined by Fast Screening Impactor for the dpCaPs/R7W-MP.

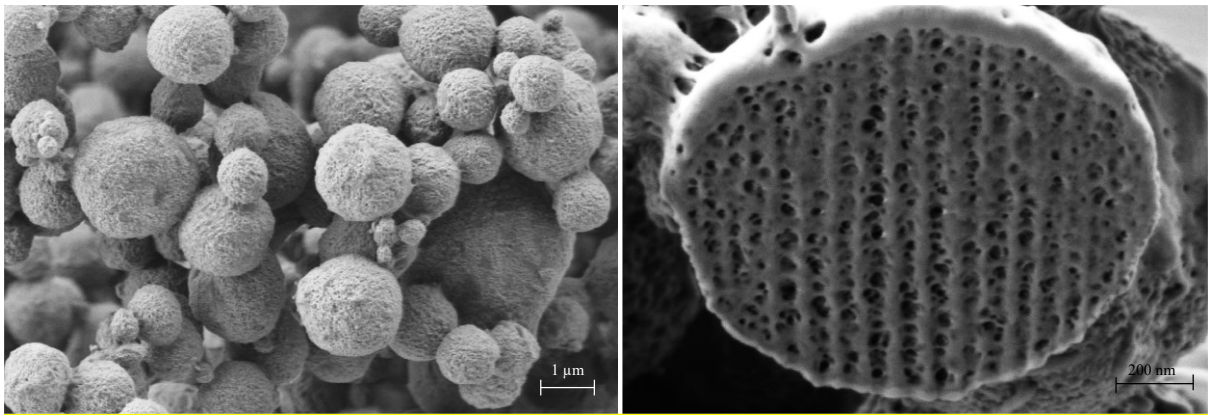

Figure 4.32 Surface and shape SEM image (A) and inner structure FIB/SEM photograph(B) of microparticles embedding nanoparticles loaded with R7W-MP.

4.3.4 Mannitol and Mimetic Peptide role in particle formation

To further understand the role of mannitol in nanoparticles de-agglomeration, a novel preparation of MP/dpCaPs was done. The mannitol was added to the nanoparticle dispersion at CaPs: mannitol ratio 1:0.07. The feed solution solid concentration was 1.7 mg/mL, *i.e.* 0.10 mg/mL of mannitol dissolved in the dispersion containing 1.6 mg/mL of nanoparticles. The spray dryer parameters for microparticle preparation were kept as before: inlet and outlet temperature 125 and 70°C, respectively; atomization flow 600 L/h, feed rate 3.5 mL/min, air flow 35 m^3/h. A nozzle with diameter of 0.7 mm was used. Microparticles obtained showed a lower respirability than microparticles described in Section 4.3.2.5, with a Fine Particle Fraction of 42% (Table 4.19). The low ratio of mannitol to CaPs in the microparticle structure was not enough to keep disaggregated the dispersed nanoparticles resulting from the water dissolution of spray dried microparticles (nanoparticles' restoration).

Table 4.19 Residual water content, respirability, size distribution of microparticles and Z-Average and Zeta Potential of nanoparticles restored. dpCaPs/MP manufactured from CaPs: mannitol ratio 1:0.07.

Residual water (w/w%)	EF (%)	FPF (%)	Microparticle size			Restored Nanoparticles	
			D_{v10} (µm)	D_{v50} (µm)	D_{v90} (µm)	Z-Average (nm)	Z-Potential (mV)
1.6 ± 0.1	91.8 ± 0.01	42.0 ± 0.06	1.5 ± 0.2	2.5± 0.5	5.5 ± 0.7	2800 ±10	-22 ± 2

Finally, to study the role played by MP peptide in microparticle formation, a further spray drying preparation containing free mimetic peptide, unloaded CaP nanoparticles and mannitol was carried out. MP peptide was added to the preformed nanoparticle dispersion; then, mannitol was dissolved to reach CaPs: mannitol ratio of 1:4. The feed solution solid concentration was 8.6 mg/mL and consisted of 0.6 mg/mL of MP, 6.4 mg/mL of mannitol and 1.6 mg/mL of nanoparticles. The spray dryer parameters were inlet and outlet temperature 125 and 70°C, respectively; atomization flow 600 L/h; feed rate 3.5 mL/min; air flow 35 m^3/h. A nozzle with a dimeter of 0.7 mm was used.

Table 4.20 Residual water content, respirability, size distribution of microparticles and Z-Average and Zeta Potential of nanoparticles restored. The microparticles were manufactured starting from a feed solution containing MP as raw material, CaP nanoparticles and mannitol in ratio 1:4.

Residual water (w/w%)	EF (%)	FPF (%)	Microparticle size			Restored Nanoparticles	
			D_{v10} (µm)	D_{v50} (µm)	D_{v90} (µm)	Z-Average (nm)	Z-Potential (mV)
1.5 ± 0.4	91.3 ± 0.03	19.9 ± 0.02	1.3 ± 0.2	2.8± 0.5	5.5 ± 0.3	70 ±15	-21 ± 4

As reported in the Table 4.20, despite the Dv_{90} under 6 µm, the dried microparticles exhibited very low respirability with Fine Particle Fraction lower than 20%. The MP added to previously precipitated unloaded nanoparticles led to a microparticles strongly aggregated, with an internal structure very different from the corresponding preparation in which MP was loaded during CaP nanoparticles precipitation. This spray dried particle formation demonstrates a different interaction of mimetic peptide with nanoparticles. In fact, from morphology analysis performed by SEM/FIB technique, very few internal cavities were observed when the peptide was added to nanoparticles already precipitated (Figure 4.33). The shape of microparticles and the internal structure explain the low FPF measured. In fact, despite the microparticle were in an acceptable range for inhalation, their shape and density are not in conditions to promote their aerodynamic diameters well above that of the previous microparticle preparation.

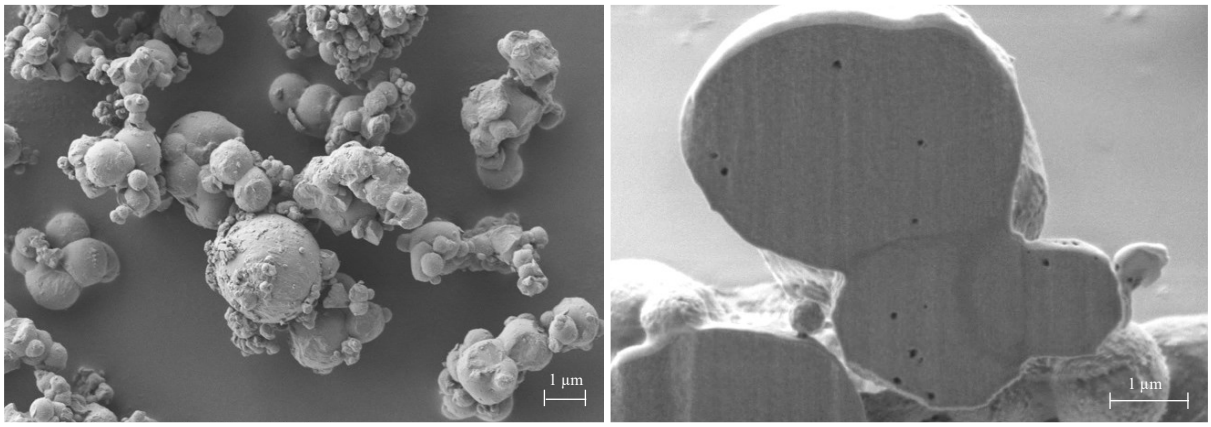

Figure 4.33 Surface and shape SEM image (left, A) and inner structure FIB/SEM photograph (right, B) of microparticles embedding nanoparticles and MP peptide.

Therefore, it was discovered that the reason behind the mannitol crucial role for microparticles respirability is strongly related to the internal structure of the particles and this structure is

linked to the presence of macromolecular substance inside the microparticles. When organized multipores are obtained, due to the presence of a peptide or mi-RNA in microparticle composition and in the process, the aerodynamic size of the highly porous microparticles improves the powder respirability. However, the mannitol function as carrier and stabilizer of the embedded nanostructures relies on a minimum ratio 1 to 4 between nanomaterial and mannitol. Only in these conditions CaPs nanoparticles' size after restoration was very close to the size of nanoparticles freshly prepared. In summary, the restored nanoparticle size from the dissolved microparticles depended on the carrier amount and its ratio with CaPs.

4.3.4.1 Investigation on dpCaPs solid state and stability study

In pharmaceutical field, organic solids presenting polymorphism are widespread, both as single molecular entities and as molecular adducts. The latter include solvates and hydrates and can be of a stoichiometric or non-stoichiometric nature. They generally show different dissolution rates with respect to the corresponding non-solvated ones, as well as a different stability at various temperatures. There are also solids that exhibit polymorphism as single molecular entities with different arrangements of the molecules within the crystal lattice. This phenomenon means that these substances also possess different chemical-physical properties based on the form in which they are used[178]. The polymorphism affects the stability and the dissolution rate of pharmaceutical formulation. During the development of pulmonary drug products, especially the DPIs, the crystalline forms of the carrier or adjuvant influences the interaction with the active ingredient and therefore, the overall product aerosolization performance. An example of this is lactose, since one crystalline form can give less adhesion force so releasing drug more easily and leading to a better dispersion[179]. Formulations consisting of different lactose forms were investigated revealing that fine particle fraction values were found to increase in the following order for lactose as a coarse carrier: α-monohydrate > β-anhydrous > α-anhydrous[180]. One of the most used lactose substitute in this role is the mannitol that is less hygroscopic and lacks Maillard reaction, a property that allows it to also be used in association with peptides and proteins.
As reported in the literature, mannitol can exist in three anhydrous polymorphic forms (α, β and δ) as well as in a hemihydrate form. The crystallization of mannitol in one form or the other depends on several production conditions, such as the type of solvent used and the concentration, temperature and crystallization rate[181]. The molecule can assume six different staggered conformations thanks to the freedom of rotation of the carbon-carbon bonds. Only

three of these are able to minimize the repulsion between the oxygen atoms that are on the same side of the carbon chain and therefore have a lower energy. In all three polymorphic forms, the molecules have the same conformation. In none of the conformations the terminal oxygen atom is aligned with the carbon chain. The polymorphism is therefore determined by the different arrangements of the hydrogen bonds that are established with the surrounding molecules. Thanks to the X-ray diffraction, it was possible to establish the existing mannitol crystalline forms (Figure 4.34)[182].

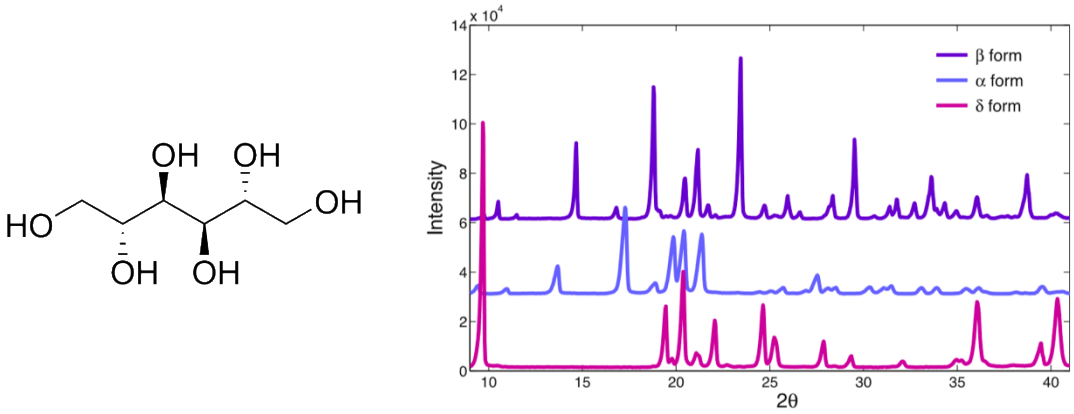

Figure 4.34 D-(-)-mannitol structure (left) and spectra of the polymorphic forms of D-mannitol α, β and δ obtained by X-ray diffractometry (right). Reprinted from Physicochemical characterization of d-mannitol polymorphs: The challenging surface energy determination by inverse gas chromatography in the infinite dilution region, International Journal of Pharmaceutics, MG Cares *et al.*[182], Copyright® 2014, reproduced with permission from Elsevier.

Solid state of unloaded and loaded dpCaPs was investigated by X-ray powder diffraction (PXRD) and DSC. Figure 4.35 displays the X-ray intensity in counts per second (cps) observed for each angle 2θ for the two spray dried powder compared to α, β and δ mannitol. In both powder (Figure 4.35) there are no evidence of extremely intense peak to 9.7 θ angle, fingerprint of δ mannitol in PXRD patterns[183]. A characteristic peak of α mannitol to 13.8 is evidenced in loaded as well unloaded microparticles. The peak shown in loaded dpCaPs spectra at 14.7, distinctive of stable β form is present very weak sometimes in α and δ polymorph[184] and a peak at 2θ value 17.4 typical of α form.

The XPRD peaks were weak, not resolute and sometimes broad, specially over 30° θ angle, highlighting an amorphous state besides the crystalline state for both formulations[183].

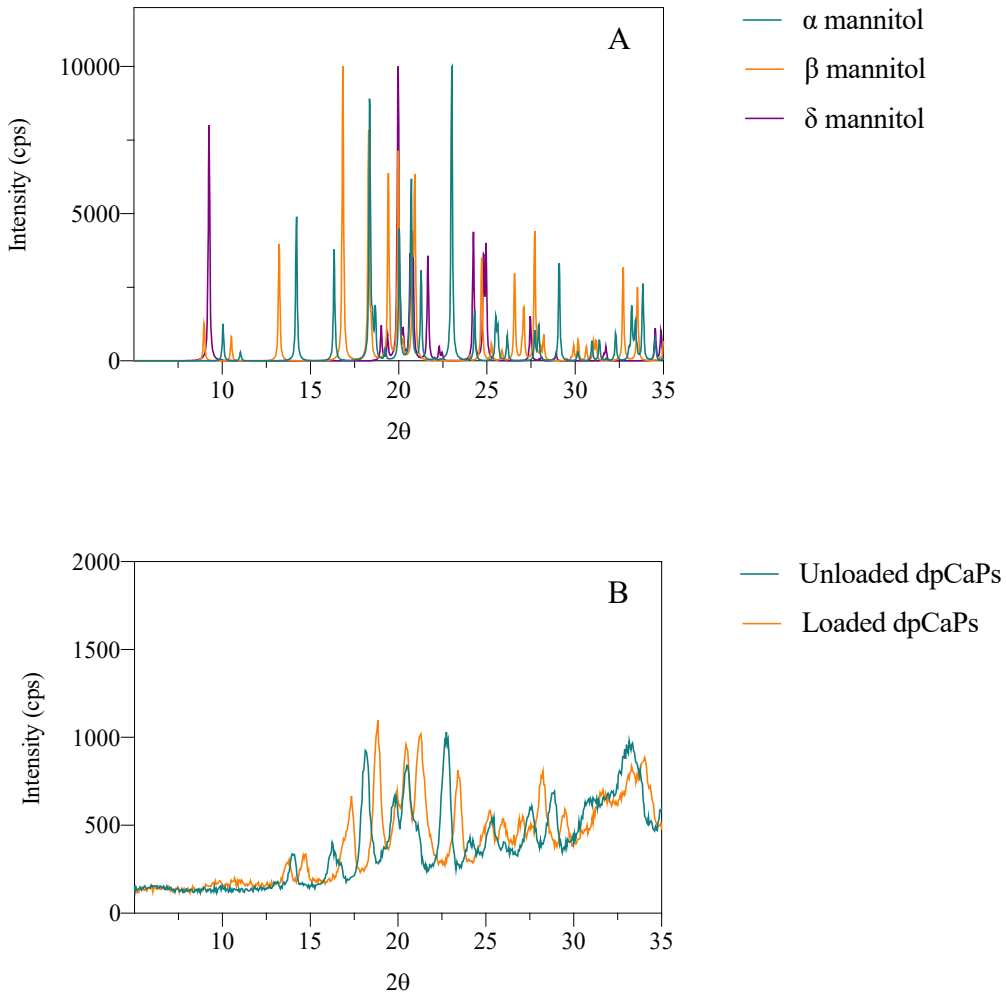

Figure 4.35 X-ray diffraction patterns of unloaded and loaded MP dpCaPs (B). The graphs obtained were compared with the spectra available in the *Cambridge Crystallographic Database, CCDC* (https://www.ccdc.cam.ac.uk) (converted by Prism, Version 7.0a, GraphPad Software Inc., La Jolla, CA, US) to verify the presence of the characteristic peaks of each α, β and δ mannitol forms (A).

Differential Scanning Calorimetry (DSC) technique gives information on the melting point of the spray dried mannitol, as it is compared to unloaded and MP-loaded dpCaPs. The melting processes are graphically represented by the peaks, from which it was possible to derive the onset (temperature of melting begins), the underlying area and the peak temperature which represents the end of the melting process. In details, the integral under the DSC peak, above the baseline, gives the total enthalpy change for the process (ΔH_{sample}).

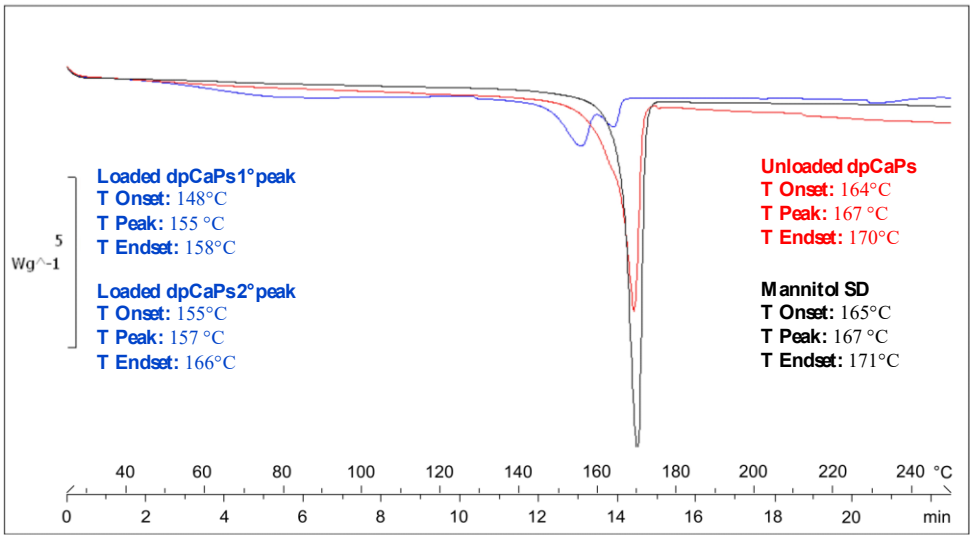

Figure 4.36 Differential scanning calorimetry analysis of spray dried mannitol as it is (black), unloaded microparticles embedding CaPs(red) and loaded with MP dpCaPs(blue). The analysis is representative of three different batches of each sample.

The unloaded microparticles embedding CaPs and spray dried mannitol shown onset of 164 and 165°C, both peak of 167°C and end of 170 and 171°C temperature, respectively. The onset at 164-165°C are ascribed to the melting begin of α and β forms of mannitol. The MP loaded microparticles (blue line in Figure 4.36) revealed an interesting behaviour. After the first melting peak at 155°C, close to that of the meta-stable δ form, it displayed a recrystallization event in more stable α or β form and another endothermic melting peak of the novel α or β forms at 166°C. The structure of δ form is close to that of β form, this being also characterized by a planar zigzag chain and relatively similar bond angles and distances. However, the hydrogen bonds pattern is different.

As revealed by DSC analysis, the mimetic peptide presence and its interaction with CaP nanoparticles and mannitol led to peculiar formulation behaviour during the heating. Crystallization of amorphous excipients can be induced by the environmental conditions during manufacture, storage, temperature and relative humidity in addition to formulation composition (*e.g.,* the peptide). Raut *et al.* using DSC demonstrated temperature induced polymorphic transformation in which the glass transition temperature of mannitol was determined from inferences. The glass transition temperature denotes the stability of amorphous mannitol below which it can be easily re-crystallize and converts to thermodynamically most stable polymorphic form[185].

In conclusion, the intrinsic heating process of DSC analysis of MP loaded dpCaPs formulation lead to a recrystallization event in a more stable α or β form, from δ form. Moreover, this

hypothesis is confirmed from X-ray pattern in which there are no evidence of meta-stable δ form mannitol. Further investigation of manufactured microparticles by solid state analytical methods (*e.g.*, FT-IR and Raman spectroscopy) will be performed.

The microparticles loaded with MP were stored for 1 month in QUALI-V I HPMC capsules at 25°C/40% RH stored in airtight sealed aluminium foils or in a sealed glass vial at 4°C, 25°C/40% RH and 40°C/75% RH in order to evaluate its stability in different conditions.
Stability after storage was assessed measuring the MP content by HPLC and evaluating the aerodynamic performance by Fast Screening Impactor. Microparticles embedding of MP-loaded CaPs proved to provide protection of the peptide, since the formulations were stable in all conditions tested in terms of peptide content. In detail, the results observed that there were no differences after one month of storage in refrigerated condition or 25 °C. A slight (not significant) degradation (below 0.2%) when the powder was stored in accelerate conditions at 40°C was observed (Table 4.21).

Table 4.21 One month stability study in terms of peptide content assessed by HPLC of loaded with MP dpCaPs in different conditions. Data are reported as mean values and standard deviation (N=3).

Mimetic peptide content in dpCaPs (%w/w)				
After production	**After 1month storage**			
	capsules at 25°C/40%RH	**glass vial at 4°C**	**glass vial at 25°C/40%RH**	**Glass vial at 40°C/75%RH**
1.0 ± 0.2	1.1 ± 0.1	1.0 ± 0.1	1.0 ± 0.1	0.98 ± 0.1

The other parameter investigated for evaluating the MP-loaded dpCaPs stability was the aerodynamic performance. The measurement was performed on a capsule loaded with 40 mg of MP/dpCaPs by FSI with RS01® at 60 L/min. Immediately after the production the microparticles, they showed an Emitted Dose of 87 ± 0.2% and Fine Particle Fraction of 70 ± 0.2%. The powder performance resulted stable at refrigerate condition, room temperature and accelerate condition, both stored when stored in capsules or glass vials. Emitted and Fine Particle Fraction were very similar ($p > 0.5$) to those obtained just after the production. The variability between the three *in vitro* aerodynamic assessment of powder stored at 40°C/75%RH showed higher variability (std.dev. 0.5%) than the other conditions (Figure 4.37). The formulation long-term stability will be furthermore examined.

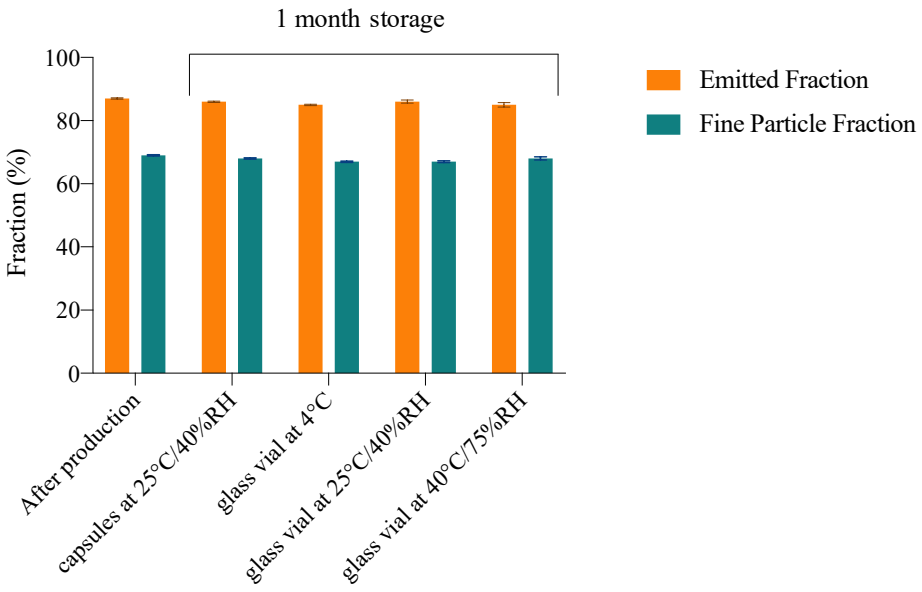

Figure 4.37 Emitted Fraction (EF) and Fine Particle Fraction (FPF) of powder aerosolized by RS01®, after production and storage for 1 month in QUALI-V I HPMC capsules at 25°C/40%RH blistered in aluminium foil and in a sealed glass vial at 4°C, 25°C/40%RH and 40°C/75%RH. Data are reported as mean values and standard deviation (N=3).

4.4 Dry powder inhaler device development

Disclosure

In this Section some materials and experimental methods are not disclosed in detail. Company Confidential Information, property of Nemera (La Verpillière, Lyon, France), *Patent application* in progress.

The possibility to reduce the amount of powder to inhale does not reside only on the composition of the microparticulate powder but also on the inhaler device to use. In fact, the aerosolization performance can be increased and as applied in antibiotic inhalation, administration of larger dose can be shared via several successive inspiration acts.

The medicinal product to target the heart will be administered as an inhalation powder metered in a dry powder inhaler. The inhalation powder of microparticles embedding MP loaded nanoparticles requires a dry powder inhaler for administration. In fact, a dry powder inhaler product is a combination between a formulation and a device, since both the components affect the performance of the administration. In this research, the inhalable formulation has been combined with the prototype of novel dry powder inhaler as a product for lung administration. The scaled-up nanomedicine powder in combination with the novel dry powder inhaler needs to demonstrate the proper aerosol transport, deposit, and release of the loaded nanoparticles (*in vitro* until now) at the pulmonary alveoli level. The optimization of the whole system, *i.e.* drug formulation and device, is compulsory for the successful development of inhalation therapies, for the treatment of local and systemic diseases. Drug–device combinations must aerosolize the drug in the appropriate particle size distribution and concentration, to ensure optimal deposition and dose in the desired region of the lung. However, since the target of the inhalation is to translocate the nanoparticles to blood through the alveoli epithelium, the extra-fine fraction of the aerosol (< 2 μm) has an important role in this project.

For aerosolization and lung deposition, during this development phase a commercial inhalation device based on a hard-capsule reservoir of the dose to be inhaled (RS01®, Plastiape, Lecco, IT), was used for first evaluation. During process of scaling up, the new DPI developed by Nemera has been combined with the powder formulation.

Nemera constructed a novel DPI adopting a similar mechanism of powder aerosolization as RS01®, where powder emission relies on the spinning of the pierced capsule in a chamber of delivery as a result of the inhalation act of the user. The knowledge of the aerosolization

behaviour of an inhalable powder requires the definition of quality parameters along the inhalation act. Using an impactor apparatus, such the compendial Next Generation Impactor, respirability assessment and the aerodynamic particle size distribution can be determined as mass median aerodynamic diameter (MMAD) and geometric standard deviation (GSD).

4.4.1 Prototyping method

The study has been conducted using the capsule reservoir DPI in the final material (proprietary Nemera product made using Acrylonitrile Butadiene Styrene by molding) adopting three prototyping methods applied on the same capsule. The first method was the Stereo Lithography Apparatus (SLA), the second was the Acrylonitrile Butadiene Styrene machining (ABS machining), and the third was the Polypropylene (PP) machining.

The comparison between the final material and the prototyping methods was done in terms of device resistance, emitted dose, and fine particle fraction (data not shown). Based on the device resistance equivalence and FPF equivalence between SLA material and final material, SLA was selected for development purpose (Figure 4.38).

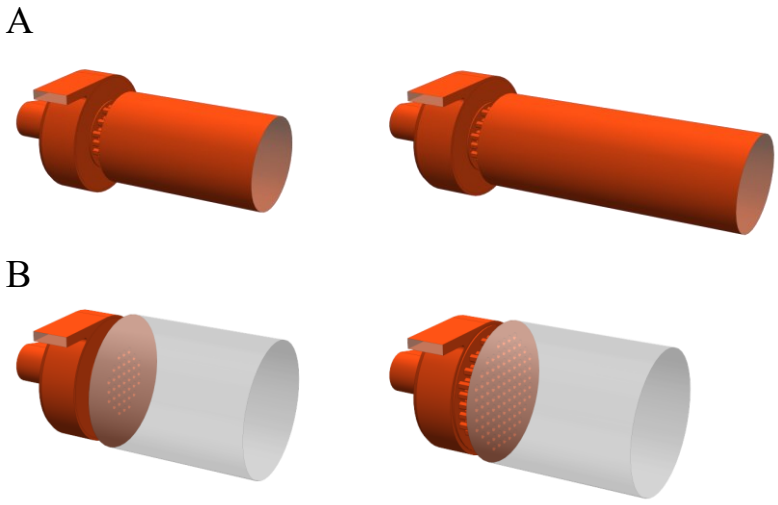

Figure 4.38 Printed prototypes parts obtained with stereolithography (SLA). Varying parameters: mouthpiece length (A), mouthpiece internal diameter and grid surface ratio (B).

4.4.2 Design optimization and molded manufacturing

Table 4.22 presents the defined DPI specifications and performances. During the concept phase, a large amount of unloaded and loaded dpCaPs still in development were tested. In

addition, the device was validated using an alternative powder, a marketed spray dried mannitol (Bronchitol®, Chiesi, Parma, Italy), in terms of Emitted and Fine Particle Fraction.
The influence of the mouthpiece length, mouthpiece internal diameter, grid geometries and the number/size of pins for piercing the capsule were evaluated. In order to optimize the novel device design, an experimental plan and a quadratic model to adjust the optimization was used (data not shown).

Table 4.22 Specifications and performance required for Dry powder inhaler device.

DPI Specifications	DPI performances
• Passive device using capsule • Powder to be loaded in capsule 30-60 mg • Capsule HPMC size 2 or 3 • Device resistance similar to COPD devices • Good usability: max 4 steps before each inhalation	• Emitted dose >75% • Fine Particle Fraction > 50%. • Low variability (<15%) in terms of fine particle dose for inspiratory flow rate ranging from 30 to 100L/min • Low throat deposition (<10%) to reduce the risk of cough.

A soft mold was used to manufacture four components of the DPI without contact with the drug (buttons, button covers, bottom part and cap) and a prototype mold was used to manufacture the DPI body and mouthpiece in contact with the drug to ensure repeatability of these parts. The different parts of the device where then manually assembled. The number of components of the DPI device is 10: body, mouthpiece, bottom part, 2 buttons, 2 springs, 2 pins, one cap.
The prototype device with medium resistance was evaluated by *in vitro* and *in user* tests. For *in vitro* aerodynamic performance test, the measurements were performed aerosolising Bronchitol® capsules. The emitted dose uniformity was tested using a Dosage Unit Sampling Apparatus (DUSA) for DPI operating for the duration of time necessary to allow the flow of 2 or 4 L of air (representing the inhalation volume of a typical patient), as specified in USP42, at flow rates of 30, 60 and 90 L/min. In all the cases, dose collection was carried out under critical flow control conditions (TPK Copley S/N 02043440, Copley Scientific Ltd, Nottingham, UK). The Fine Particle Fraction was measured by laser light diffraction analysis for particle size distribution measurements (Spraytec, Malvern Instruments, Worcestershire, UK) after five consecutive inhalation acts. Approximately 40 mg of mannitol SD powder was directly loaded within capsule and dispersed using Nemera Prototype device and RS01® reference device at 30, 60, and 90 L/min, for a standard total inhalation volume of 4.0 L. Airflow rates were monitored using the TSI digital flow meter (Series 4000, TSI Inc., Shoreview, MN, USA) and

controlled by varying the valve of vacuum pump (Westech Scientific Instruments, Bedfordshire, UK).

The prototype device met the specifications whatever the flow rate (from 30 L/min to 100 L/min). Emitted fraction of 78%, 89% and 89% were obtained for flow rates of 30, 60 and 90 L/min respectively. Fine particle fractions of 70%, 72% and 68% were obtained for flow rates of 30, 60 and 90 L/min respectively. They have been improved for flow rate at 30 L/min in comparison with the RS01® reference device (Figure 4.39). The variability of the Fine Particle Fraction against inhalation flow rates has been reduced close to 15%. Also, the deposition in the mouth has been reduced from 38% to 28% in comparison with the RS01® device.

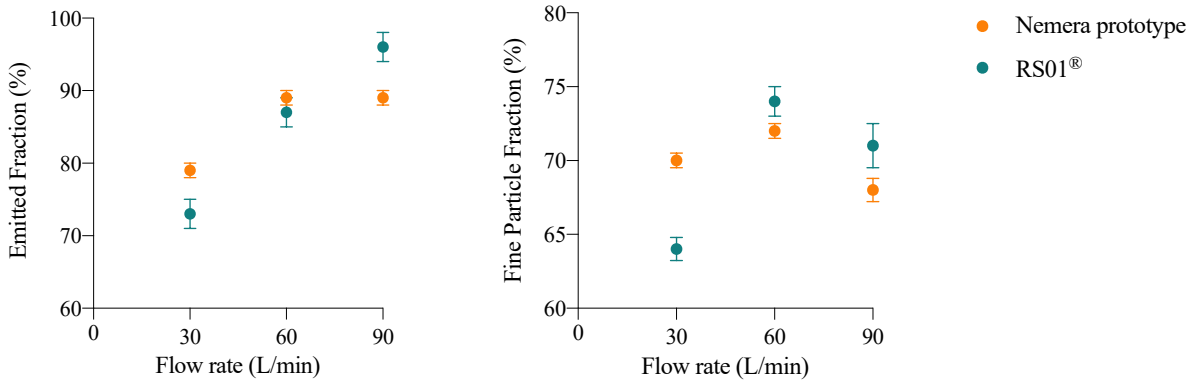

Figure 4.39 Emitted and Fine Particle fraction of Bronchitol® aerosolized by Nemera Prototype device and RS01® reference device at 30,60 and 90 L/min after 5 inhalation acts.

Both Ph.Eur. and USP suggest a pressure drop over the inhaler of 4 kPa as being broadly representative of the pressure drop generated during inhalation by patients using DPIs. The pressure drop created by the air drawn through an inhaler can be measured directly by measuring the absolute pressure downstream of the inhaler mouthpiece and comparing this directly with atmospheric pressure.

To measure the device resistance, flow through the inhalers was produced using a vacuum pump (Mod. 1000, Erweka GmbH, Langen, Germany) which created the aerosolization air flow and recorded using a digital Flow Meter DFM 2000 (Copley scientific Ltd, Nottingham, UK) tested over a range of airflow rates (30 to 100 L/min). To validate flow rate stability the critical (sonic) flow was assessed. This was confirmed by simply measuring the absolute pressure at a point on either side of the flow control valve. The pressure downstream of the

valve was less than half of the upstream pressure *i.e.* that the ratio $P_3/P_2 \leq 0.5$ then critical (sonic) flow has been assured and the flow rate can be assumed to be stable.

The device resistance was calculated as the slope of the plot of the square root of the measured pressure drop over the flow rate as reported by Clark and Hollingworth[186]. The pressure drop readings across Nemera device was measured with an empty capsule.

To assess the duration time (s) needed to allow that 4 L passed through the device, the following Equation was applied:

$$T = \frac{240}{Q} \quad (16)$$

Where T is the time in seconds, Q is the flow rate (L/min).

Applying Equation 16 the aerosolization time at 60 L/min was 4s.

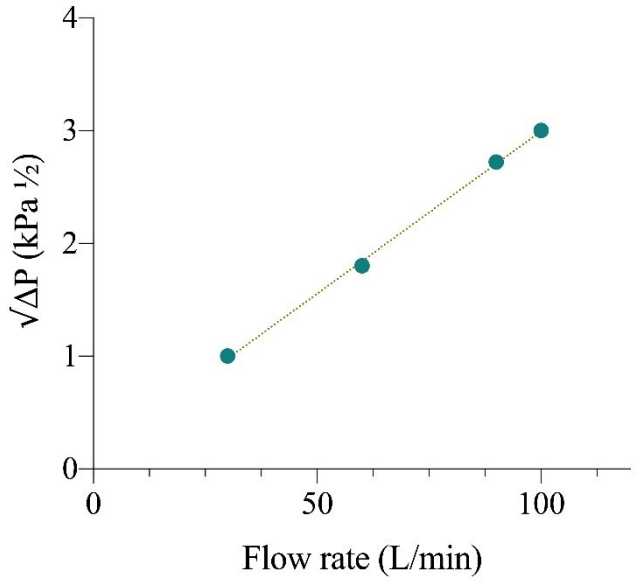

Figure 4.40 Relationship between airflow rate and generated pressure drop for Nemera device inhaler. Simple linear regression was assessed by Prism, Version 7.0a, GraphPad Software Inc., La Jolla, CA, USA).

The Nemera device resistance measured was 0.029 $kPa^{1/2}/L \cdot min^{-1}$ close to RS01® Medium resistance device (Figure 4.40).

The unloaded microparticles embedding CaPs were *in vitro* tested by Fast Screening Impactor (gravimetrically) using Nemera molded prototype. The RS01® MR was used as device reference since used for all aerodynamic assessment performed previous. A capsule of HPMC was loaded with 40 mg of powder and the air flow to 60 L/min was actuated. The test was performed on six different batches. The data reported in Table 4.23 showed that the powder was successfully emitted (EF over 90%) from the Nemera device after the first inhalation act

and was significantly higher compared to reference device. The Fine Particle Fraction was higher 50% when the novel DPIs was employed.

Table 4.23 Emitted Fraction and Fine particle Fraction of unloaded dpCaPs aerosolized by RS01® and Nemera molded prototype. The data are express as average values and standard deviation (N = 9).

Device		EF (%)	FPF (%)
RS01®	1 Inhalation act	83.8 ± 0.02	48.7 ± 0.03
	2 Inhalation acts	88.8 ± 0.02	51.1 ± 0.03
	3 Inhalation acts	90.5 ± 0.02	51.2 ± 0.04
Nemera prototype	1 Inhalation act	91.4 ± 0.02	53.8 ± 0.02
	2 Inhalation acts	92.2 ± 0.02	56.3 ± 0.02
	3 Inhalation acts	92.5 ± 0.02	58.3 ± 0.05

A user test has been conducted on 17 healthy volunteers, 7 women and 10 men. The age distribution was between 20 and 70 years old. The study goal was to get preliminary feedback from users on the device, in order to evaluate key strengths and key weaknesses of the novel device during use: get qualitative feedback (intuitiveness, aesthetics, handling, first impression), identify potential improvement and comparison vs a reference device. Overall, the Nemera device usability was fine for most participants (*e.g.,* steps, handling). They particularly appreciated the ergonomic aspect, with a suitable size on the device, especially on piercing buttons. This feedback, with a clear preference to the Nemera device compared to the RS01® reference device, (88% vs 12%) gives confidence about device use for clinical trials.

4.5 Scale up of microparticles embedding MP-loaded CaPs

4.5.1 Feasibility assessment of loaded with MP dpCaPs manufacturing

The spray dried MP/CaPs with a total solid content of 8.0 mg/mL and an MP/CaPs: Mannitol w/w ratio of 1:4 was regarded as the candidate for the technology transfer of inhalable microparticles production at pilot scale. Therefore, to prepare the microparticles embedding MP loaded CaPs at industrial level, the undiluted CaPs, *i.e.* concentration 1.6 mg/mL, were employed for the reason that the more concentrated dispersion will lead to reduce industrial time of drying procedure.

In collaboration with FIN Ceramica S.p.A. (Faenza, Italy), a Belgian company (Xedev, Zelzate, Belgium). having an approved pharmaceutical industrial environment, was selected as supplier to execute the industrial technology transfer on their industrial spray dryer (ProCepT spray dryer). The goal was to develop and optimize an industrial scaled up spray drying process with the objective to obtain a product with characteristics similar to those of lab production and a process at higher throughput and yield. The main transferred characteristics were particle size for inhalation ($Dv_{90} < 5$ μm) and a water content of lower than 3 % (w/w). In fact, the lab scale dpCaPs with a water content less than 3%, exhibited good respirability and acceptable shelf life of the formulated inhalable dry powder. Moreover, attention was paid to the peptide preserved content and ability of microparticles to restore nanoparticles in their original size. The spray-drying experiments were performed using the ProCepT spray-dryer. The ProCepT spray dryer has a different configuration/setting compared to the lab Mini Büchi B-290 Spray-dryer. The ProCepT SD was set-up with the extended column (Figure 4.41) equipped with a small cyclone, suitable for capturing small particles. During industrial process optimization, the small cyclone was exchanged with a medium cyclone in order to collect the dry powder. The extended drying chamber of the spray dryer increased the residence time in the drying heated air.

Under the best process conditions of the optimization study, two batches of 100 g dry loaded particles were produced. To collect the amount of dry powder envisaged, the feed solution consisted of a mix of six batches (3L each one) of CaP NPs in which the mannitol in ratio 1:4 was dissolved. During spray drying, samples were taken after 1 hour processing in order to evaluate PSD, recovery and RWC. Numerous attempts were performed; in Table 4.24 the conditions of spray-drying production relative to the most significant trials and final fixed

protocol are reported. A process with the 0.4 mm nozzle orifice was preferred to those of 0.6 mm, due to a higher observed process yield and product robustness.

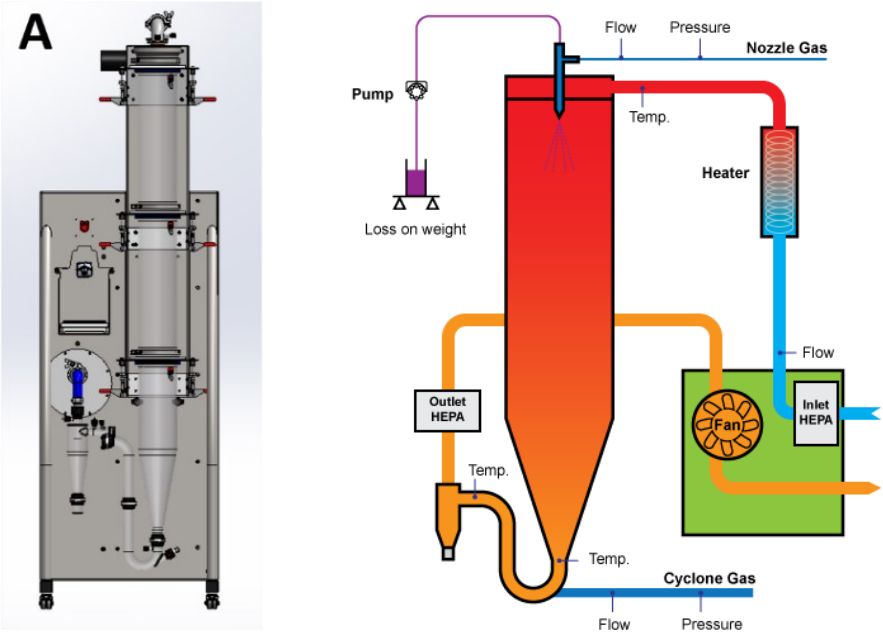

Figure 4.41 ProCepT spray dryer with extended column(A). Synoptic overview of the ProCepT spray dryer.

Table 4.24 An overview of the industrial SD process parameters of two optimization performed tests and final production. Inlet Temperature, Nozzle air and Airflow were varied during the two trials.

	Trial 1	Trial 2	Final production
Inlet temperature (°C)	135	160	160
Temperature chamber out (°C)	50	70	70
Temperature before cyclone (°C)	45	55	55
Airflow in (m^3/min)	0.35	0.35	0.4
Cyclone air (L/min)	200	200	200
Bi-Fluid Nozzle (mm)	0.4	0.4	0.4
Nozzle air(L/min)	6	4	6
Spray rate(g/min)	10	10	10
Yield (%)	82	84	90

The SD parameters Inlet Temperature, Air flow and Nozzle air were varied during the two trials and their influence on final product was evaluated in terms of mean volume diameter and residual water content (RWC). In traditional spray drying a cyclone separator is often included in a succeeding separation step, after spray drying chamber. The gas-solid cyclone separator is a separation device that separates solid particles from a gas phase using a centrifugal force field

depending on inlet air flow. Thus, the setting up of inlet cyclone air flow is an added value of ProCepT spray dryer critical for dried particle formation.

Firstly, since the use of high temperatures with 6 L/min nozzle air can have as consequence a too fast particle shell formation, the inlet temperature was set to 135°C, resulting in an Outlet temperature of 50°C. The process yield was 82%, but RWC was slightly high, namely 3.7% w/w. Therefore, higher temperatures are needed to obtain a dry product.
In the second trial, the Inlet temperature was set to 160°C, resulting in an Outlet temperature of 70°C and temperature before cyclone of 55°C. Then, the influence of the Nozzle Air on particle size and residual water content was determined as well. A decrease in nozzle air results usually in larger droplets, which led to larger particles, but, in case of low solid load, this effect usually is small. Using lower nozzle air rates can result in slower shell formation, whereby less water remains entrapped. Nozzle air rate was decreased from 6 L/min to 4 L/min (trial 1 and 2, respectively) resulting in particles with a mean volume diameter of 2.0 µm and 3.4 µm, respectively. The water content did decrease from 3.1% to 2.8% w/w respectively, which confirmed that slower drying of the particles results in drier product.

In summary, for the final production the Inlet temperature was set to 160°C, resulting in an Outlet temperature of 70°C; Nozzle air rate was kept at 4 L/min and the Inlet airflow was Increased from 0.35 m³/min to 0.4 m³/min. To lower the residual water content during longer processes, the medium size cyclone was installed. By using the medium size cyclone, higher Airflows (0.4 m³/min) can be used compared to the small cyclone together with the cyclone air (200 L/min). The higher Nozzle Air and Inlet Airflow had a positive influence on RWC, which dropped from 2.8% to 2.1%, whereas no influence on PSD was observed. The final production resulted in high recoveries of 90% for all batches.

4.5.2 Scaled loaded with MP dpCaPs characterization

In total 100.0 g of powder were obtained for each batch in a continuous process of less than 2 hours, compared to 1g/hours produced at lab scale. The PSD obtained displayed Dv_{10}, Dv_{50} and Dv_{90} of 0.53, 2.0 and 4.5 µm, respectively (Figure 4.42). The peptide content, that in CaPs before spray drying was 6.0 ± 0.2% w/w, in scaled microparticles was slightly lower than expected (*i.e.* 1.2 %w/w, the fifth of 6.0 %w/w since the microparticles consisting of a ratio CaPs: mannitol 1:4), namely 0.5 ± 0.2% w/w.

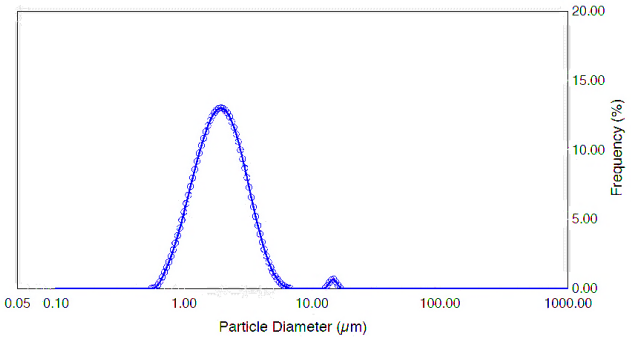

Figure 4.42 Particle size distribution (µm) in frequency (%) of industrial scaled batch of loaded with MP dpCaPs by laser light diffraction.

The SEM analysis confirmed the small particle volume diameter assessed by laser light diffraction. Roundish and rough dry particles were evidenced by morphology study, despite the lower peptide content than lab prepared microparticles. Moreover, the inner structure, by SEM-FIB analysis, confirmed the nanoporosity presence close to lab scale MP loaded dpCaPs (Figure 4.43).

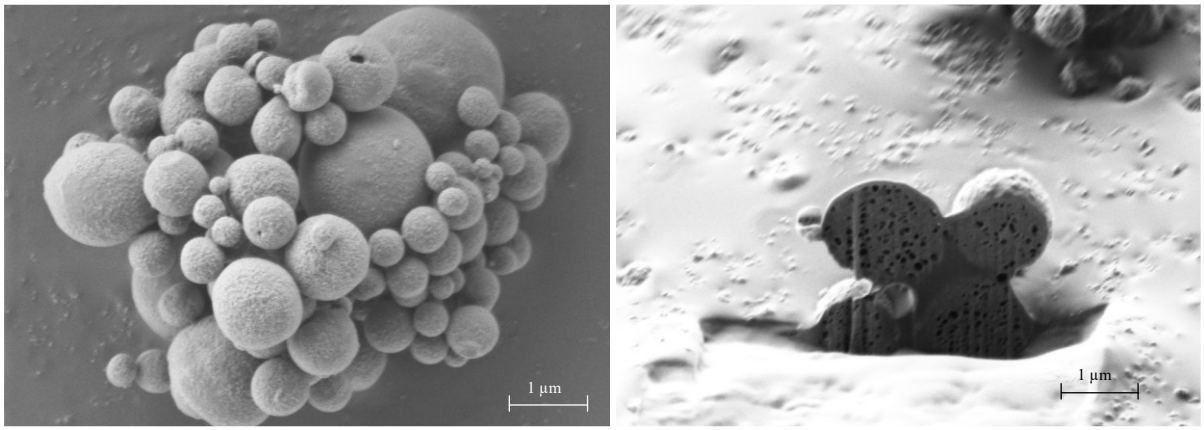

Figure 4.43 Rough surface and roundish shape SEM micrograph (left) and inner structure FIB/SEM photograph (right) of scaled microparticles embedding nanoparticles loaded with MP peptide.

For DPI products, bulk density is an important parameter with an opposite meaning for powders characteristics of aerosolization and flowability. A low value of bulk density is beneficial for powder aerosolization; while, at the same time, a higher value improves powder flow properties[39, 187]. Hence, the scaled spray dried powder was also characterized in terms of bulk and tapped density. Bulk (poured) density was 0.3 g/cm^3. Density, after mechanical tapping, showed an increase, *i.e.* 0.7g/cm^3. The true density measured by helium pycnometer was 1.6 ± 0.001 g/cm^3. From the determination of the poured bulk and tapped density according to Ph.

Eur. 9th ed. prescriptions, the powder flowability, a critical characteristic for capsule/vial filling and for their aerodynamic properties, was calculated by mean of the Carr's Index and Hausner ratio. The Equations 17 and 18 to calculate both these flowability indexes are reported as following:

$$Carr's\ Index\ (\%) = 100 \cdot \frac{\rho_T - \rho_B}{\rho_T} \quad (17)$$

$$Hausner\ ratio = \frac{\rho_T}{\rho_B} \quad (18)$$

where ρ_T is the tapped density and ρ_B the poured bulk density.

The micronized powder having Carr's Index of 57% and Hausner ratio of 2.3 has to be classified as poor flowable powder. Values higher than 25% and 1.25 for Carr's Index and Hausner ratio, respectively, are indication of poor flowability[188, 189].

In several papers, the bulk density values below 0.4 g/cm^3 are claimed as cut-off for providing good aerodynamic characteristics[39]. The scale up manufactured dpCaPs with a bulk density of 0.7 g/cm^3, revealed an interesting aerodynamic behaviour when aerosolized through Nemera prototype inhaler device. To assess aerodynamic behaviour with the NGI impactor, three capsules of size 3, loaded with 40 mg of powder, were actuated at air flow rate of 60 L/min for the duration of time to allow 4 L of air passing through the inhaler, as specified in USP_ 41. The Emitted fraction was 92.0 ± 0.1% of the metered dose, the Fine Particle Fraction 80.0 ± 0.3% (d_{ae} < 5 µm) of Emitted Dose, of which 54 ± 0.3% as Extra-Fine (d_{ae} < 3 µm) particles. The percentages of MP particles deposited in the device, induction port and in the different stages of NGI are reported in (Figure 4.44).

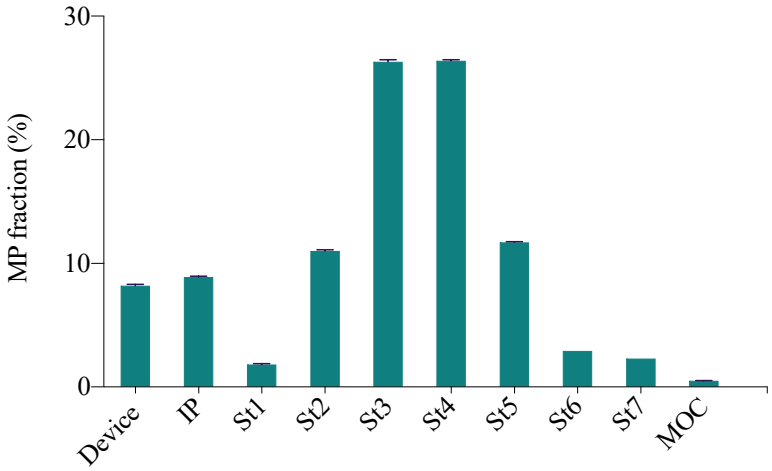

Figure 4.44 Bar graph shows the average values and standard deviation (N=3) of the percentage of MP deposited in the device, induction port, and in the different stages of the NGI.

The mass balance was within 15% of the labelled dose. The Mass Median Aerodynamic Diameter (MMAD) and Geometric Standard Deviation (GSD) were determined from the NGI data in Figure 4.45. The MMAD was 2.5 µm with GSD of 1.8. The calculation of the aerodynamic parameters was performed by using Prism, Version 7.0a (GraphPad Software Inc., La Jolla, CA, USA). MMAD and GSD were calculated based on the inverse normal of the cumulative percentage under the stated aerodynamic diameter versus the log of the effective cut-off diameter. Linear regression of the four data points closest to 50% of the cumulative particle mass that entered the impactor was performed to compute the MMAD and GSD.

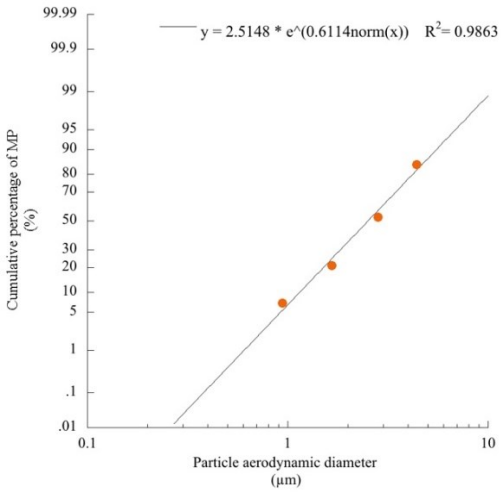

Figure 4.45 Plot of cumulative percentage of mimetic peptide mass less than stated aerodynamic dynamic diameter (probability scale) versus aerodynamic diameter (logarithmic scale). Data are reported as mean of 3 NGI experiments. Linear regression performed by (Prism, Version 7.0a, GraphPad Software Inc., La Jolla, CA, USA).

The *in vitro* aerodynamic assessment demonstrated that the first industrial product (MP powder and device inhaler) is very promising for the therapeutic application by inhalation. In particular, the Extra Fine Particle Fraction higher than 50% makes the formulation suitable for alveolar deposition.

In order to study the morphology of Extra Fine Particles, during NGI assessment a slice of carbon tape was stacked on the Micro Orifice Collector (MOC), on which the particles with aerodynamic diameter less than 0.34 µm at flow rate calibration of 60 L/min are deposited.

The spherical crumpled particles showed a geometric diameter less than 0.5 µm as expected as well as these fine particles exhibited a lot of small nano cavities in the inner structure (Figure 4.46).

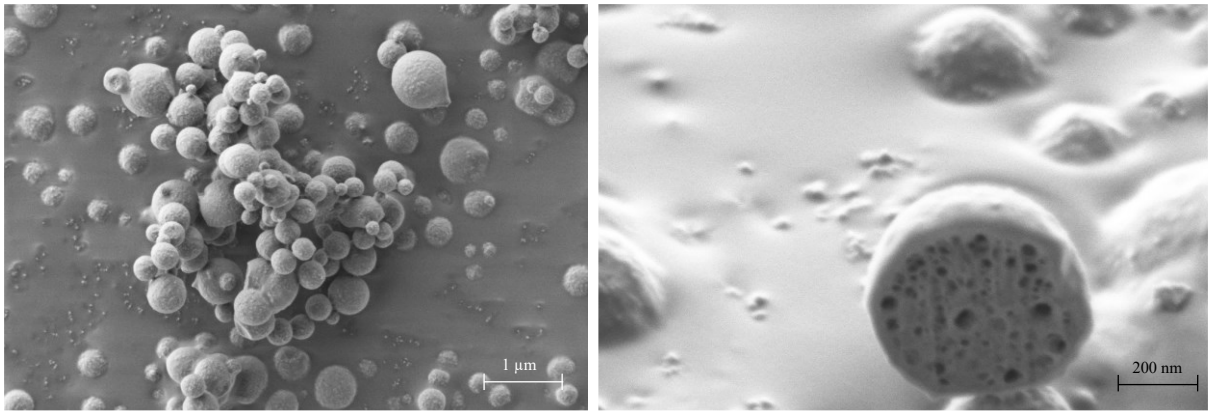

Figure 4.46 SEM (right) and FIB/SEM analysis of particles deposited on MOC of NGI.

When the MP loaded dpCaPs were dissolved in water at concentration of 0.5 mg/mL, the restored CaP NPs exhibit a Z-Average of 250 ± 50 nm with a Polydispersity index of 0.3. The restored size was higher compared to the original nanosize of nanoparticles before the spray drying, namely about 160 nm, likely due to some nanoparticles agglomerates. To collect more information on this interpretation, the number-based particle size distribution' was calculated by the DLS software. In Figure 4.47 the representation of MP/dpCaPs particle size distribution as number is reported. The histogram shows the particles frequency fractions distributed between two size values. The x-axis corresponds to the particle size values and the ordinate (y-axis) shows the fraction as number of particles having the correspondent size interval. The sigmoid curve represents the particle size values as cumulative undersize distribution. The cumulative distribution allows to identify the median size value (x=50.0) of the particle population as number distribution (Figure 4.47 blue line). It is the size of the particles that divides the particle population in two groups containing an equal number of particles. Based on particle size as number distribution, the median value of nanoparticles restored from loaded dpCaPs was 45±3 nm and the interval is between 10 and 100 µm. As reported in European Commission's recommendation for definition of nanomaterial: "if 50 % or more of the particles of a material in the number size distribution have one or more external dimension in the size range 1 nm to 100 nm, the material is a nanomaterial"[190].

The interest to use the number distribution instead than volume distribution is related to the meaning of the particle dimension related to their specific application. In environmental applications of micromeritics, the number of particles inhaled is critical for safety reasons. In pharmacy, the interest is towards the doses and therefore, the reference distribution has to be in volume or weight. Comparing the number distribution of a particle population with its volume distribution, the volume distribution shifts the distribution curve towards higher size

values. Therefore, considering our MP/dpCaPs particle populations, it is not surprising that a large difference exists between number and volume median values. This is due to the presence of some agglomerates (reversible particle clusters) in the sample under DLS analysis. Even if these clusters are few as number, as volume they represent an important fraction of the population, since the volume of the sphere from the diameter is calculated with a power of three, Therefore, not disregarding that the number distribution is the result of an algorithm applied to the hydrodynamic particle size distribution, it is not surprising that, in presence of few agglomerates, these structures are not visible in the population presented as number distribution. On the contrary, their contribution to the volume distribution become important.

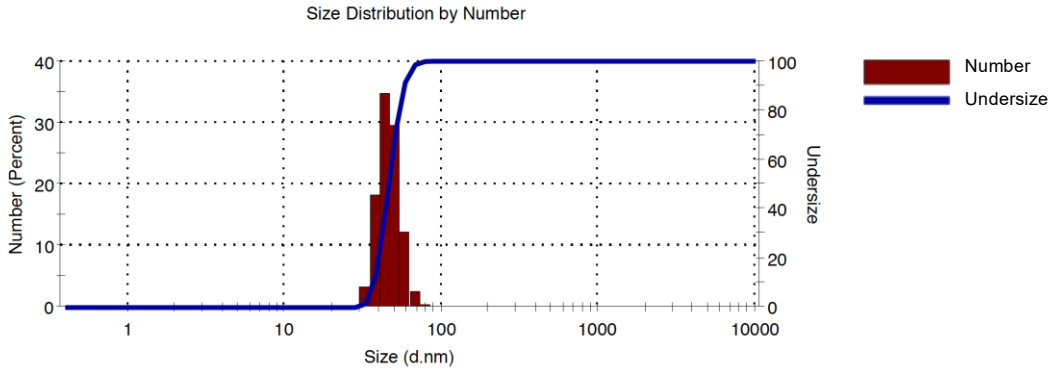

Figure 4.47 Particle size distributions of restored CaPs from scaled MP dpCaPs by DLS: histogram (red) and cumulative distribution (blue line). The median value of the number-based size distribution.

Finally, the Zeta Potential of -14 ± 4 mV communicates a negative surface charge enough close to those of NPs before SD, *i.e.* about -23 mV.

A summary of spray drying parameters and characteristics of both lab and industrial scaled microparticles embedding CaP NPs loaded with mimetic peptide is reported as below (Table 4.25 and Table 4.26).

Table 4.25 Spray drying parameters and production rates comparison of lab and pilot scale manufacturing. The feed concentration was for both SD process 8.0 mg/mL.

	Spray drying Parameters							
	Inlet T (°C)	**Outlet T (°C)**	**Atomization Flow (L/min)**	**Air flow (m^3/h)**	**Feed rate (L/min)**	**Nozzle (mm)**	**Yield (%)**	**Production rate (g/hours)**
Lab scale	125	70	10	35	0.035	0.7	63	1
Pilot scale	160	70	200	24	6	0.4	90	60

Table 4.26 Comparison of microparticles embedding CaPs loaded with MP manufactured at lab and pilot scale characterization.

	MP content (w/w%)	**Residual water (w/w%)**	**EF (%)**	**FPF (%)**	**Microparticle size (µm)**			**Restored Nanoparticles**	
					Dv_{10}	**Dv_{50}**	**Dv_{90}**	**Z-Average (nm)**	**Zeta Potential (mV)**
Lab scale	1.2	2.0	78.0	63.0	1.3	2.5	4.9	134.0	-15.0
Pilot scale	0.5	2.0	92.0	80.0	0.5	2.0	4.5	250.0	-14.0

4.6 Pulmonary and extra-pulmonary *in vitro* viability, cytotoxic and apoptotic levels following exposure to dpCaPs

The toxicity of microparticles embedding CaP nanoparticles has been assessed using pulmonary alveolar cells and HL-1 cardiac cells. *In vitro* cell models were target cells present in the respiratory unit, alveolar epithelial type 1 cells (immortalised human alveolar epithelial type 1 cell-like, TT1 cell), alveolar epithelial type 2 (AT2) cells (primary AT2) and primary human alveolar macrophages. Cells exposed to increasing concentrations of microparticles corresponding to the amount of CaPs (5, 10, 25, 50, 100, 250, 500 and 1000 µg/mL within the administered dpCaPs) were incubated for 24 hours at 37°C and 5% CO_2. dpCaPs were suspended in serum free DCCM-1 culture medium prior to applying to cells. The cells were analysed 24 hours after exposure. Cell viability/metabolic activity (MTT assay of mitochondrial activity), intracellular oxidative stress (ROS, Reactive Oxygen Species assay) and inflammatory cytokine mediator release (ELISA tests for IL-6 [pleiotropic action important regulator of inflammation and homeostasis] and IL-8 [chemoattraction of neutrophils and white blood cells] cytokines) have been assessed[191].

Zinc oxide (Zn Oxide) nanoparticles caused significantly cell death and was used as positive control. Lipopolysaccharide (LPS) was used as pro-inflammatory positive control. Results are presented according to the type of cell analysed: 1) Alveolar type 1 cells (TT1), 2) Alveolar type 2 cells (AT2) and 3) Alveolar macrophages. Results were analysed using Prism 7.0 software (GraphPad Software Inc., La Jolla, CA, USA).

4.6.1 Alveolar type 1 cells (TT1) viability

TT1 viability (MTT assay) following 24h exposure to dpCaPs TT1 cells monolayers were incubated for 24 hours at 37°C and 5% CO_2 with dpCaPs (CaP nanoparticles spray dried in mannitol carrier microparticle powder at 1:4 ratio) at increasing concentrations corresponding to the amount of CaPs *i.e.,* 5, 10, 25, 50, 100, 250, 500 and 1000 µg/mL were suspended in serum free DCCM-1 culture medium prior to applying to cells.

There was no change in TT1 cell viability/metabolic activity (Figure 4.48) after treatment with the concentrations 5 to 100 µg/mL CaP, compared to untreated cells. Interestingly, there was a significant (~20%) increase in cell viability/activation following treatment at higher concentrations (250, 500 and 1000 µg/mL), possibly due to the presence of mannitol enhancing cell metabolism. Future studies on cell incubation with mannitol alone will clarify this point.

dpCaPs microparticle concentrations were calculated in order for the x-axis to correspond to CaP concentrations, according the 1:4 CaP/mannitol carrier ratio. Data from unexposed TT1 cells were used as 100% of the control (CTR-) cell viability. Zinc oxide nanoparticles were suspended in serum-free cell medium as described for dpCaPs to obtain the final concentration of 50 µg/mL and used as positive control; as expected, these particles caused significant cell death ($p<0.0001$).

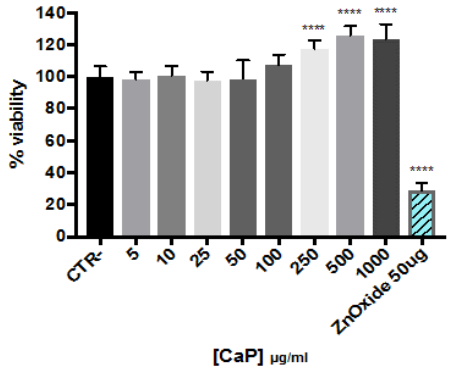

Figure 4.48 TT1 cell viability assessed by MTT assay. Cells were exposed for 24h to the dpCaPs formulation at increasing concentrations (5, 10, 25, 50, 100, 250, 500 and 1000 µg/mL corresponding to the bare CaPs included in the dpCaPs according the 1:4 CaP/mannitol carrier ratio). Data are expressed as % of unexposed TT1 cell control (CTR-). Zinc oxide (Zn Oxide) nanoparticles at 50 µg/mL were used as positive control. ****, $p<0.0001$. N=3 repeats performed in triplicate.

4.6.2 Intracellular TT1 cell ROS production

ROS can increase as a preliminary response that occurs before overt cell death, or to activate oxidative stress pathways for cell survival. The cell-permeant 2',7'-dichlorodihydrofluorescein diacetate probe (H_2DCFDA) was used as an indicator of intracellular ROS production after 24 hours treatment with increasing doses of dpCaPs (shown concentrations correspond to the amount of CaPs within the administered dpCaPs) (Figure 4.49).

There was no change in the level of intracellular ROS between 5 and 250 µg/mL CaP concentration exposure, compared to the unexposed TT1 negative control (CTR-). A small but significant decrease in fluorescent signal was observed at higher concentrations of 500 and 1000 µg/mL, which may be related to the increase in cellular mitochondrial activity observed at these concentrations, reported in the MTT results above (Figure 4.48). Further quantitative measures of ROS production at earlier time points (3h and 6h) are planned to determine whether ROS might have increased and subsided earlier in the exposure period.

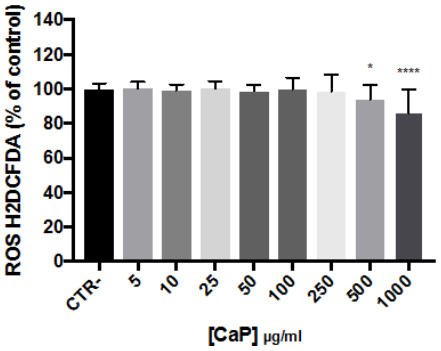

Figure 4.49 TT1 cell ROS production following 24h exposure to increasing concentration of dpCaPs formulation (5, 10 25, 50, 100, 250, 500 and 1000 µg/mL corresponding to the bare CaPs included in the dpCaPs according the 1:4 CaP/mannitol carrier ratio). H_2DCFDA probe analysis. Data are presented as a % of the unexposed control (CTR-). *, p<0.01; ****, p<0.0001. N=3 repeats performed in triplicate.

TT1 cell cytokine release following 24h exposure to dpCaPs IL-6 and IL-8 (markers of inflammation; assessed by ELISA) release into media during 24 hours exposure to dpCaPs showed barely detectable levels of these cytokines (<50 pg/mL) indicating no relevant pro-inflammatory stimulation by the nanoparticles at increasing concentrations (5, 10, 25, 50, 100, 250, 500 and 1000 µg/mL of equivalent bare CaPs within dpCaPs). Data from untreated TT1 cells were used as control (CTR-). There was a small dose-related response in IL-6 release at 1000 µg/mL CaP, the highest concentration studied (Figure 4.50).

Lipopolysaccharide (LPS/endotoxin), induces TT1 cell cytokine release[192] was used as a positive control. LPS was added to TT1 cells at 0.5 (IL-6 analysis) and 1 ng/mL (IL-8 analysis) suspended in 5% Newborn Calf Serum in DCCM-1 medium. The comparative data indicate that even the small but significant increase in IL6 release following 1000 µg/mL CaP is physiologically unimportant.

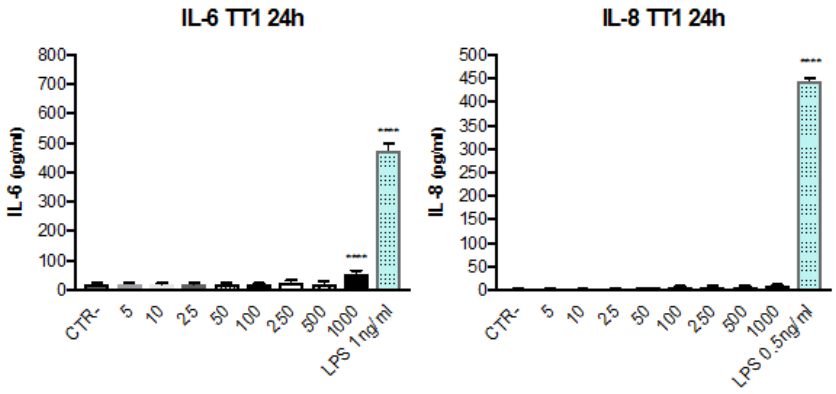

Figure 4.50 Effect of dpCaPs on IL-6 and IL-8 release by TT1 cells. TT1 were exposed for 24h to dpCaPs formulation at increasing concentrations (5, 10, 25, 50, 100, 250, 500 and 1000 µg/mL corresponding to the bare

CaPs included in the dpCaPs according the 1:4 CaP/mannitol carrier ratio). Data are expressed as pg/mL conditioned medium. LPS at 0.5 and 1 ng/mL concentration was used as pro-inflammatory positive control, as indicated. ****, p<0.0001. N=3 repeats performed in triplicate.

4.6.3 Alveolar type 2 cells (AT2), viability

AT2 cell monolayers were incubated for 24 hours at 37°C and 5% CO_2 with dpCaPs dry powder formulation at increasing dpCaPs concentrations corresponding to the amount of CaPs *i.e.,* 10, 25, 50, 100, 250 and 500 µg/mL, as described previously. dpCaPs were suspended in serum free DCCM-1 culture medium prior to applying to cells.

The AT2 cell viability/metabolic activity was not significant difference to untreated control (CTR-), up to 250 µg/mL dpCaPs exposure. A small but significant decrease in cell viability (~10% compared to untreated control) occurred at a higher dpCaPs exposure (500 µg/mL). Zinc oxide (Zn Oxide) nanoparticles caused significantly more cell death (~60%) at 10 µg/mL when used as positive control (Figure 4.51).

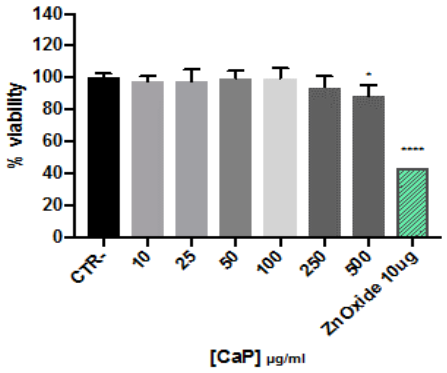

Figure 4.51 AT2 cell viability assessed by MTT assay. Cells were exposed for 24h to the dpCaPs formulation at increasing concentrations of CaP (10, 25, 50, 100, 250 and 500 µg/mL corresponding to the amount of CaPs within the administered dpCaPs). Data are expressed as % of unexposed cell control (CTR-). Zinc oxide nanoparticles at 10 µg/mL concentration used as positive control. *, p<0.05; ****, p<0.0001. N=3 subject samples, performed in triplicate.

Intracellular AT2 cell ROS production following 24h exposure to dpCaPs Intracellular ROS production was assessed on dpCaPs-exposed AT2 cell monolayers after 24 hours treatment with increasing concentrations of dpCaPs (Figure 4.52), as described above. There was a trend towards a concentration-dependent decrease (from 2.5 to 500 µg/mL) in ROS levels, compared to the unexposed AT2 control (CTR-). This became significant at the highest concentration of dpCaPs, 1000 µg/mL, although this decrease was only approximately 10%,

possibly reflecting cell loss due to cytotoxicity, shown in Figure 4.51. Further quantitative measures of ROS production at earlier time points (3h and 6h) are planned to determine whether ROS increased and declined at an earlier time interval.

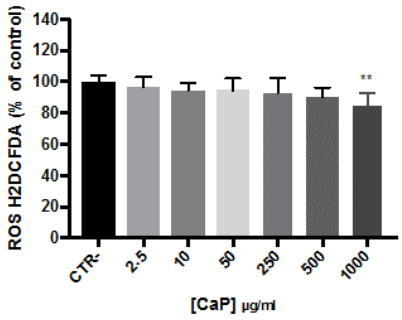

Figure 4.52 AT2 cell ROS production following 24h exposure to increasing concentration of dpCaPs formulation corresponding to the amount of CaPs 2.5, 10, 50, 250, 500 and 1000 µg/mL. H_2DCFDA probe analysis. Data are presented as a % of the unexposed control (CTR-). **, $p<0.01$, N=3 subject samples, performed.

AT2 cell cytokine release following 24h exposure to dpCaPs IL-6 and IL-8 release into the medium was determined (by ELISA assay) after 24 hours exposure to dpCaPs. There were no significant changes in release of either cytokine compared to the untreated control (CTR-). The highest cytokine concentration was less than 500 pg/mL for IL-6 and less than 130 pg/mL for IL-8 (Figure 4.53), significantly less than that observed with positive LPS (~1400 and 7500 pg/mL respectively). These results show no physiologically important pro-inflammatory stimulation of AT2 cells by the formulation up to CaP levels of 500 µg/mL.

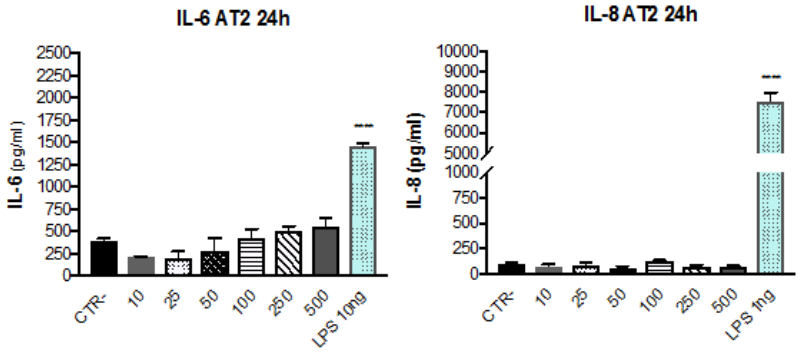

Figure 4.53 Effect of dpCaPs on IL-6 and IL-8 release by AT2 cells. AT2 exposed for 24h to dpCaPs formulation at increasing concentrations (10, 25, 50, 100, 250 and 500 µg/mL corresponding to the amount of CaPs within the administered dpCaPs). Data are expressed as pg/mL conditioned medium. LPS at 10 and 1 ng/mL concentration was used as inflammatory positive control, as indicated. ****, $p<0.0001$. N=3 subject samples, performed in triplicate.

4.6.4 Alveolar macrophages viability

Macrophage viability (MTT assay) following 24h exposure to dpCaPs Macrophages were incubated for 24 hours at 37°C and 5% CO_2 with dpCaPs dry powder formulation at increasing concentrations. Formulation was suspended in serum free RPMI-1640 culture medium prior to application to the cells. There was no change in cell viability/metabolic activity even at the highest concentrations, when compared to untreated cells (Figure 4.54).
These results show the same trends as those seen with AT1 cells, that dpCaPs are not toxic.

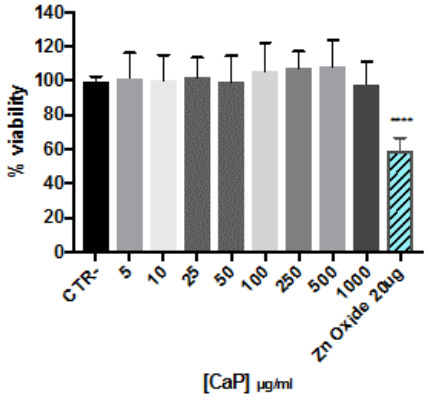

Figure 4.54 Macrophage viability assessed by MTT assay. Cells were exposed for 24h to dpCaP (left) formulation at increasing CaP concentrations (5, 10, 25, 50, 100, 250, 500 and 1000 µg/mL, corresponding for dpCaPs to the amount of CaPs within the administered dpCaPs. Data are expressed as % unexposed macrophage cell control (CTR-). Zinc oxide (Zn Oxide) nanoparticles at 20 µg/mL concentration was used as positive control. **, $p<0.01$; ****, $p<0.0001$. N=3 subject samples performed in triplicate.

4.6.5 Intracellular macrophage ROS production

Intracellular ROS production was assessed in dpCaPs-exposed macrophages monolayers after 24 hours incubation at 5, 10, 25, 50, 100, 250, 500 and 1000 µg/mL CaP, as described above. There was no significant change in ROS levels with increasing dpCaPs concentrations (Figure 4.55), compared to the unexposed control cells (CTR-). These data indicate that there is no overt increase in oxidative stress due to dpCaPs in human alveolar macrophages, in line with the lack of cytotoxicity.

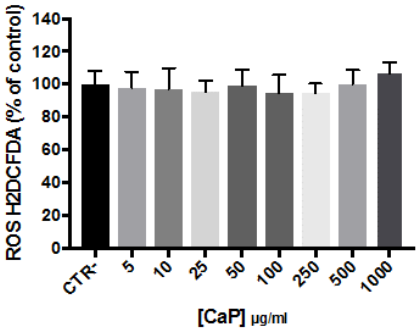

Figure 4.55 Macrophage ROS production following 24h exposure to increasing concentrations of dpCaPs formulation corresponding to the amount of CaPs 5, 10, 25, 50, 100, 250, 500 and 1000 µg/mL. H_2DCFDA probe analysis. Data are presented as a % of the unexposed control (CTR-). N=3 subject samples performed in triplicate.

4.6.6 Macrophage cytokine release

Conditioned media from macrophages were collected 24 hours after exposure to dpCaPs at increasing concentrations and assayed for IL-6 and IL-8 levels; LPS was used as pro-inflammatory control, as described above. There was no difference in the release of either cytokine (Figure 4.56), which was below 100 pg/mL, significantly less than the positive control (approximately 400 and 1100 pg/mL for IL-6 and IL-8, respectively). These results again suggest no physiologically important pro-inflammatory stimulation of human macrophages by the dpCaPs.

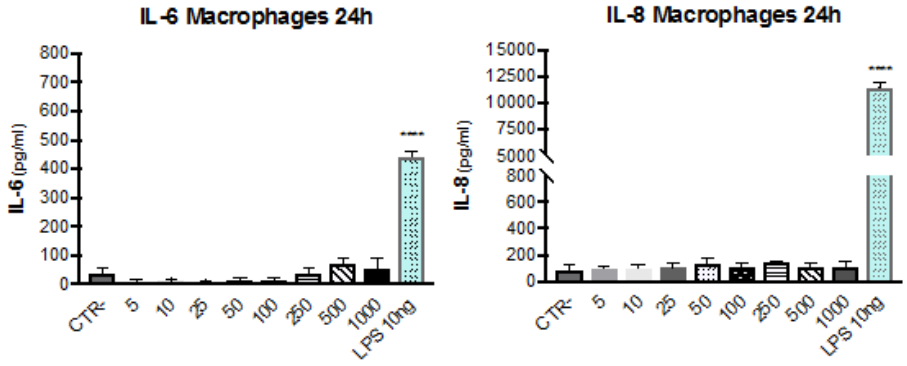

Figure 4.56 Release of IL-6 and IL-8 by macrophages exposed for 24h to dpCaPs formulation at increasing corresponding to the amount of CaPs 5, 10, 25, 50, 100, 250, 500 and 1000 µg/mL. Data are expressed as pg/mL conditioned medium. LPS at 10 ng/mL concentration was used as pro-inflammatory positive control, as indicated. ****, $p<0.0001$. N=3 subject samples performed in triplicate.

In addition to above tests performed in a series human lung cell models, further biocompatibility assays were performed in the HL-1 cardiac cell line.

4.6.7 HL-1 cardiac cells (TT1) viability, cytotoxic and apoptotic levels

HL-1 cardiac cells were subjected to incremental doses of dpCaPs and an analysis of viability, cytotoxicity and caspase 3/7 activity was performed. In addition, specific inhibitors of clathrin and dynamin, which are involved in the initial processes of CaP endocytosis and invagination from the plasma membrane[94], were also used. Confirming the above data in human lung cells, cardiac cells largely tolerated an acute administration of dpCaPs without showing any effect in terms of viability and sign of apoptosis and cytotoxicity up to 125 µg/mL after 24 h (Figure 4.57) and 48 h (Figure 4.58). Notably, the lower concentrations of 31.25, 62.5, and 125 µg/mL, showing high biocompatibility.

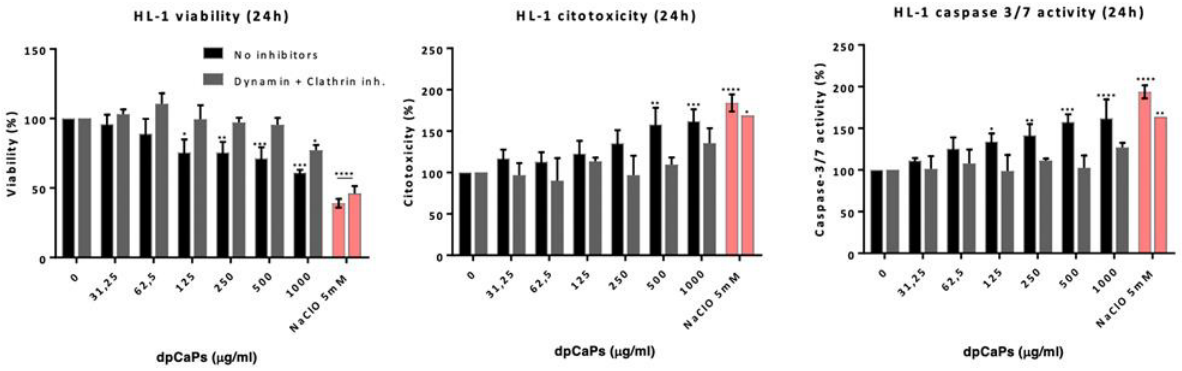

Figure 4.57 Correlation of viability (left), cytotoxic (middle), and apoptotic (right) levels' in HL-1 exposed to dpCaPs. Cells pretreated as indicated with clathrin and dynamin inhibitors and then with increasing concentrations of dpCaPs during 24 h. Data are presented as mean ± std.dev.; N = 9, in three independent experiments for each experimental condition. *p < 0.05, **p < 0.01, ***p < 0.001 and ****p < 0.0001 indicate significance for each dpCaPs dose compared with CTR using two-way ANOVA and Tukey's post hoc test. Assay was performed with ApoTox-Glo™ Triplex Assay (Promega).

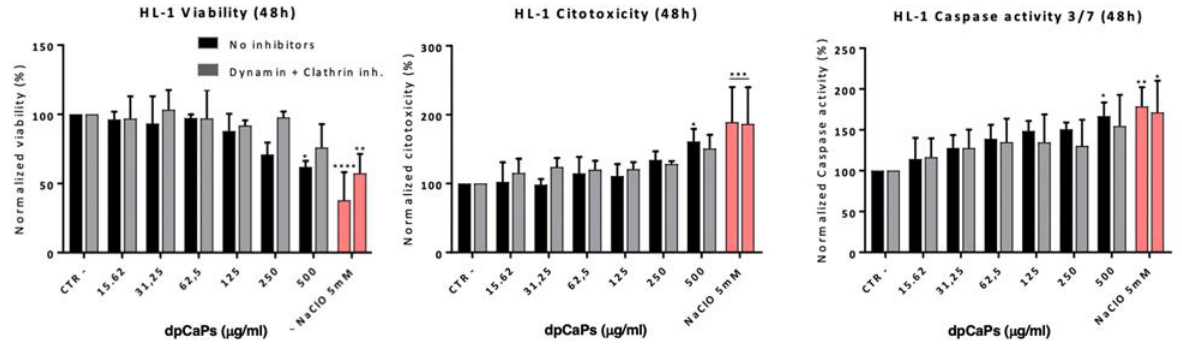

Figure 4.58 Correlation of viability (left), cytotoxic (middle), and apoptotic (right) levels' in HL-1 exposed to dpCaPs. Cells pretreated as indicated with clathrin and dynamin inhibitors and then with increasing concentrations of dpCaPs during 24 h. Data are presented as mean ± std.dev.; N = 9, in three independent experiments for each experimental condition. *p < 0.05, **p < 0.01, ***p < 0.001 and ****p < 0.0001 indicate significance for each dpCaPs dose compared with CTR using two-way ANOVA and Tukey's post hoc test. Assay was performed with ApoTox-Glo™ Triplex Assay (Promega).

4.7 *In vitro* studies of nanoparticle uptake and translocation across TT1 cells

The nanoparticle cell uptake studies performed firstly focused on nanoparticle-alveolar epithelial cell interactions, uptake and translocation of CaPs were then examined by TEM, following CaP treatment of a human alveolar type 1-like epithelial cell line (TT1 cells). Confocal microscopy was used to examine epithelial cell uptake of fluorescently labelled CaPs. Confocal fluorescence microscopy was used to establish intracellular CaPs localization using 3D image analysis of CaP-AF647. TT1 cells were grown to high confluence and exposed to 10, 25, and 50 µg/mL CaPs concentration in serum-free RPMI-1640 medium. Cells were washed to remove apical CaP excess then fixed with 4% paraformaldehyde. TT1 cells were stained with fluorescent dye DAPI for the nucleus (blue) and WGA-488 dye for the lipid component (green, cell membrane and endosomes, Figure 4.59).

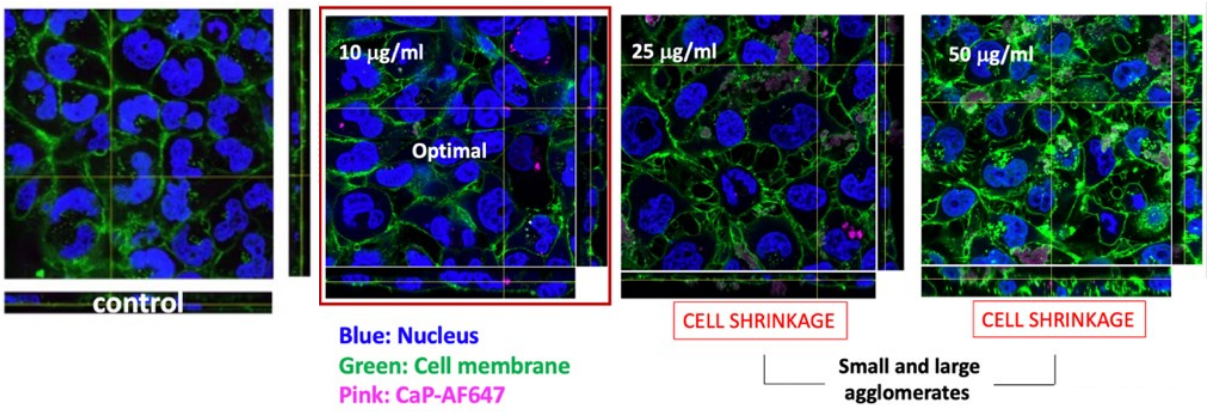

Figure 4.59 Intracellular uptake and distribution of CaP-AF647 NPs. TT1 cells were exposed to CaP-AF647 for 24 hours at 10 µg/mL and 25 µg/mL respectively. Z-stack images were taken from the top to the bottom of the cells and are presented from left-to-right. The nucleus is blue, cell membrane is green and CaP-AF647 is pink. Cell shrinkage occurred when TT1 cells were exposed to 25 and 50 µg/mL, compared to control (left), but this was not so clear after exposure to 10 µg/mL. Particle agglomerates (red arrowhead) can be seen at the higher particle exposure concentrations. Scale bar= 10 µm.

CaP-AF647 are purple against the green cell membrane staining. Cells were analyzed and 3D Z-stack images were taken along the entire height of the sample. There was a good fluorescence signal associated with CaPs showing some intracellular accumulation after 24h exposure. After exposure to 10 µg/mL, confocal analysis showed the presence of few fluorescent nanoparticle clusters within the cytoplasm of TT1 cells monolayer, confirmed from the orthogonal views of

the Z-stack images. However, not all cells internalized CaPs. 25 and 50 µg/mL treatment resulted in accumulation of large aggregates of CaPs (few microns) on the apical side of TT1 cell membranes and between the cells, suggesting that these aggregates were too large to be internalized by clathrin and caveolin uptake routes, normally used by TT1 cells. Furthermore, confocal images revealed an altered TT1 cell conformation (shrinkage/contraction) and cell stress with no visible cell death. High level of nanoparticle aggregation, leading to TT1 structural alterations, could explain the apparent decreased uptake observed at 25 µg/mL compared to that at 10 µg/mL. Thus, 10 µg/mL was considered the most biocompatible concentration in terms of detectability of fluorescence intensity (FI), sufficient intracellular CaP uptake, and lower nanoparticle external aggregation. Thus, it was selected as the maximal concentration to use in later studies of translocation with these specific nanoparticles.

4.7.1 CaP-AF647 nanoparticles fluorescence intensity extrapolation

A standard curve to measure CaP-AF647 (Figure 4.60) nanoparticle levels was generated using nanoparticle concentrations in serial dilution and determination of their relative fluorescence intensity. This curve was used to estimate NP concentrations contained within the apical, basal, and cellular compartments of the Transwell models by interpolation. RPMI-1640 medium was used as blank.

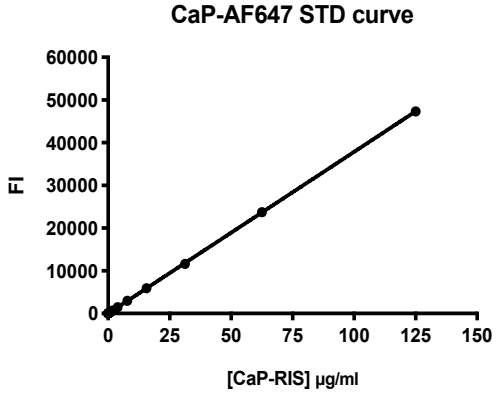

Figure 4.60 CaP-AF647 standard curve. Serial dilutions of nanoparticles from 0.004 to 125 µg/mL RPMI-1640 were generated and their fluorescence intensities (FI) were measured through a fluorescence 96-well plate reader at excitation/emission wavelengths of 580/20 and 635/20 nm.

Alveolar epithelial cell monolayers were cultured on commercial Transwell membrane inserts for fluorescence studies with fluorophore-conjugated CaP formulations. TT1 cells were grown on the PET membrane within the upper chamber compartment of the Transwell inserts for 2 days until full confluence, then fixed, stained and EM resin embedded. After resin

polymerization, semi-thin transverse sections (150 nm) were cut with ultra-microtome and stained with Toluidine blue dye to enhance the contrast before taking micrographs by light microscopy.

Following delivery to the apical chamber (upper compartment), CaP-AF647 nanoparticle levels were evaluated in both the lower compartment (translocated nanoparticles) and the cell-associated compartment (cytoplasmatic and attached to the cell membrane after washing) (Figure 4.61).

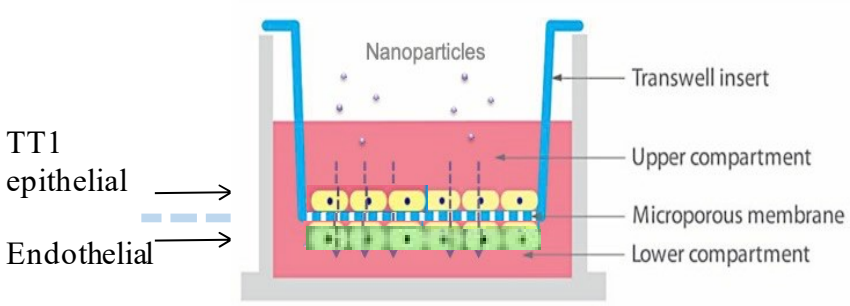

Figure 4.61 Diagram of the commercial Transwell insert model system to determine fluorescently labelled CaP uptake, translocation and fate at the alveolar air-liquid interface and across the model alveolar membrane. Transwell membrane insert characteristics: 24-well plate inserts (surface area ~0.3cm2, thickness 10 µm, pore size 0.4 µm, PET transparent membrane, pore density 4 x 106).

Taking into account the cell shrinkage effect observed on TT1 after 24h of incubation with CaPs, lower concentrations of CaP-AF647 were used. Concentration were reduced in order to avoid possible undesired paracellular NP translocation. Therefore, 200µl of CaP-AF647 (0.1 µg/well) in serum-free RPMI medium were added to the upper compartment at the apical surface of TT1 cells. 700 µl of serum-free RPMI medium were added to the lower compartment. Following 6h exposure there was 10% of cell-associated nanoparticles which rose to 15% after 24h (Figure 4.62, red bars).

Translocated nanoparticles (Figure 4.62, green bars) reached 42% after 24h of incubation; nanoparticle translocation through naked Transwell membrane inserts were ~48% at 6h and ~70% at 24h. No cytotoxicity nor reduced viability are associated to cells during these experiments.

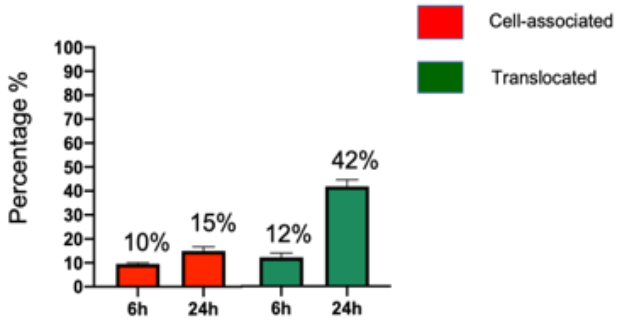

Figure 4.62 CaP-AF647 (0.5 µg/mL; 0.1 µg/well applied) uptake and translocation (6h and 24h) through overconfluent TT1 cell monolayer. CaP-AF647 uptake/cell-associated (RED) and translocation (GREEN) are shown, left bars represent 6 hours time point and right bars represent 24 hours incubation time point. Each experiment was carried out in triplicate, the data are shown as the mean. Error bars represent standard deviation (SD).

The CaPs are successfully internalized and translocate across TT1 cells, as shown further in TEM image (Figure 4.63). A proportion of TT1 cells showed active CaP endocytosis at the cell membrane level for small nanoparticle clusters; caveolin and clathrin coated pits were mostly observed. Endocytosis, mostly by caveolar vesicles, was observed as internalization of small clusters of CaPs less than 200 nm across.

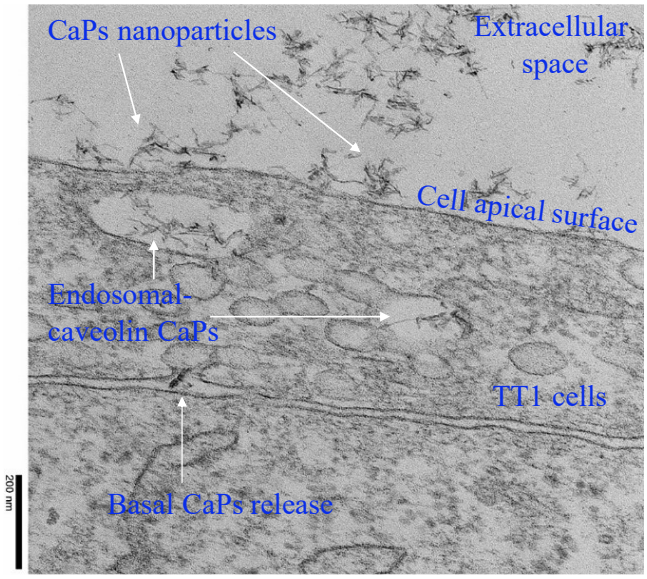

Figure 4.63 TT1 cells exposed to CaP NPs. CaPs were observed as clusters at the apical surface of the cell monolayer with a small percentage of single and small agglomerated particle. CaPs exhibit structures 5-10 nm thick with a variable length from 30 to 100 nm. Extracellular clusters showed a variable length ranging from a minimum of 100 nm up to few microns, resembling the morphology of the original CaPs (Figure 4.16). Blank arrowheads indicate nanoparticle within endocytic vesicle.

4.8*In vitro* cardiac functional test of Mimetic Peptide loaded dpCaPs

One of the main concerns in using CaP NPs is their potential interference with functional properties of excitable and contractile cells, such as cardiomyocytes. To assess the efficiency of microparticles embedding CaPs loaded with MP to deliver the active therapeutic peptide within cardiac cells, an *in vitro* functional assay for the evaluation of MP-dependent effect on enhancing/recovering the protein-protein interaction of LTCC subunits was performed on cardiac cells.

Murine cardiac muscle cells HL-1 were grown in Claycomb medium supplemented with 10% FBS, 1% of penicillin-streptomycin as ultraglutamine and 0.1 mM of norepinephrine in gelatin/fibronectin precoated T75 flasks.

The treatment with different concentrations of microparticles embedding MP CaP loaded and peptide R7W-MP, self-internalized by cardiomyocytes, used as positive control, was performed in serum-free medium (starvation). After 24 h of treatment, the Fluo-4 Direct Calcium Assay was assessed. HL-1 cells, were stimulated with Fluo-4Direct calcium reagent and signals were detected one hour post-treatment.

MP as it is, is not able to internalize cardiomyocytes. As shown in Figure 4.64, positive results were obtained. The effects were comparable to those obtained from the administration of a self-internalizing R7W-MP[96] that, in contrast to MP, is independent from CaP for its cell internalization. The microparticles embedding CaP nanoparticles allow the mimetic peptide internalization with a dose-dependent mechanism.

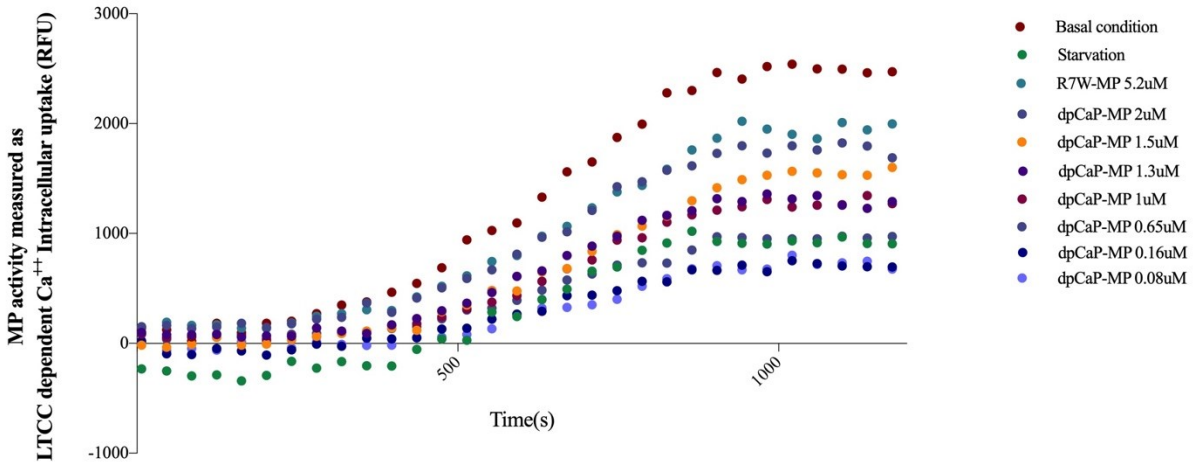

Figure 4.64 MP activity measured as L-Type Calcium Channel Complex dependent Ca^{++} intracellular uptake.

Notes: Basal condition is referred to HL-1 cells cultured in serum medium. Starvation is referred to HL-1 cells cultured in serum free medium. RFU is Relative Fluorescent Intensity was assessed after administration of R7W-MP positive control and dpCaPs at increasing concentration (from 0.08 μM to 5.2 μM) in serum free medium. Results were analyzed using (Prism, Version 7.0a; GraphPad Software Inc., La Jolla, CA, USA). Data are expressed as mean ± st.dev (N=3).

4.9 Therapeutic effect of Mimetic Peptide loaded dpCaPs formulation for the treatment of cardiovascular function in mini-pigs

The main study is currently ongoing. The preliminary results of the first dose-finding study, including some preliminary experiments on the *in vitro* administration of MP on muscle strips from HFrEF minipigs are here presented.

MP inhibits the intracytoplasmic degradation of LTCCs, improves the contractility of cardiomyocytes and thus exerts a positive inotropy. Hence, for preclinical proof-of-concept, microparticles embedding CaPs loaded with mimetic peptide were administered in a porcine model of heart failure with reduced ejection fraction (HFrEF). HFrEF is induced in Goettingen mini-pigs via tachypacing, according to the protocol represented below in Figure 4.65.

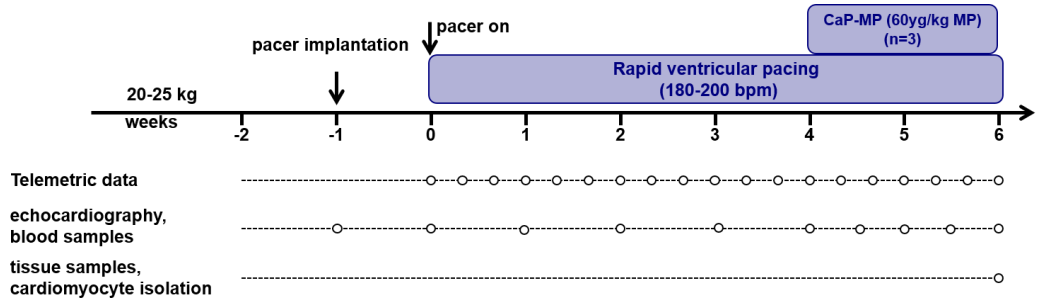

Figure 4.65 HFrEf induced in Goettingen mini pigs via tachypacing brief protocol.

The experiments performed have shown a pronounced phenotype with a left ventricular ejection fraction of 20-30% after 4 weeks of right ventricular tachypacing, as shown in the following short-axis views (Figure 4.66).

EF 60% EF 20%

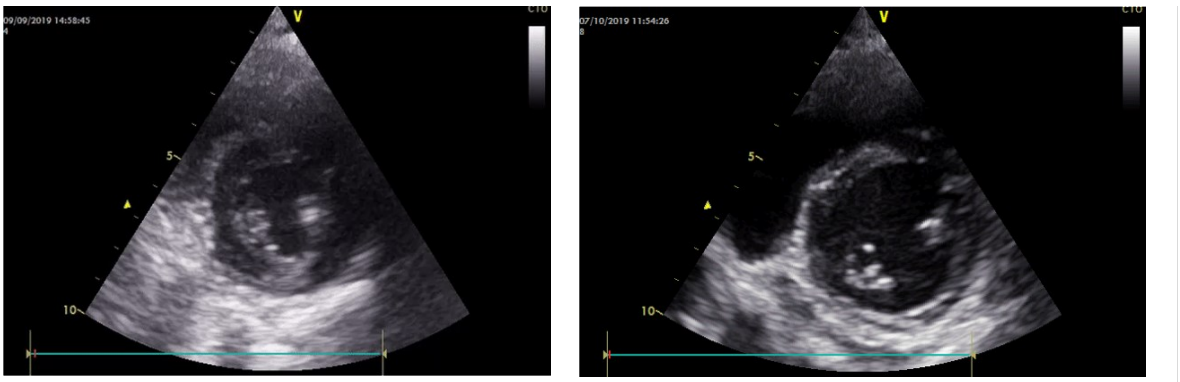

Figure 4.66 Echocardiography of Goettingen mini-pigs before (left) and after (right) tachypacing. EF: Ejection Fraction.

Before starting with the inhalation of dpCaP-MPs in the HFrEF mini-pigs, the effect of *in vitro* administration of MP (specifically, the cell penetrant R7W-MP) on muscle strips (n=6) derived from HFrEF mini-pigs after 4 weeks of pacing was assessed.

After surgical cardioplegia and heart explant, muscle strips were prepared under the microscope. Muscle strips were mounted on the muscle-strip setup and stimulated at a rate of 1 Hz, while force development was measured over 90 minutes. While measuring force in 4 muscle stripes (2 control vs 2 treated with R7W-MP at dose of 10 µM), further muscle strips were incubated with R7W-MP (same dose of 10 µM) 3-hours long before measurement. In these preliminary strips, the typical force-rundown over time was observed in the control but not in the R7W-MP group, suggesting a positive inotropic effect of R7W-MP on the HFrEF myocardium as represented in the Figure 4.67.

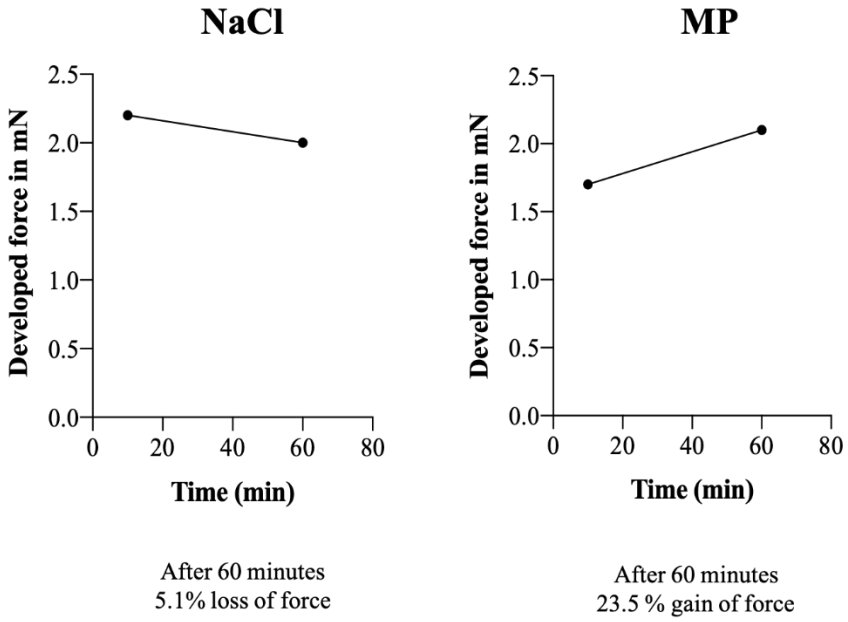

Figure 4.67 Force generation in HFrEF cardiac muscle stripes treated with either vehicle (NaCl) or R7W-MP.

With regard to the pilot study the dose of 12 mg/kg of microparticles loaded with 60 µg/kg of mimetic peptide through a mask for 14 days of treatment was tested in Goettingen mini-pigs with reduced ejection fraction from 60 to 20% induced via tachypacing. The preliminary data suggested that the treatment with microparticles improves cardiac contractility normalizing left ventricular Ejection Fraction as well as fractional shortening (data from 2 pigs shown in Figure

4.68). In line with these data, left ventricular dilatation as well as a surrogate of filling pressure (E/e´) were at least partially reversed by the treatment over 2 weeks. The treatment was well tolerated and no adverse events, including severe arrhythmias occurred. The main study comparing heart failure pigs exposed to loaded MP dpCaPs vs dpCaPs is ongoing and it will prove the efficacy of the treatment in the porcine model.

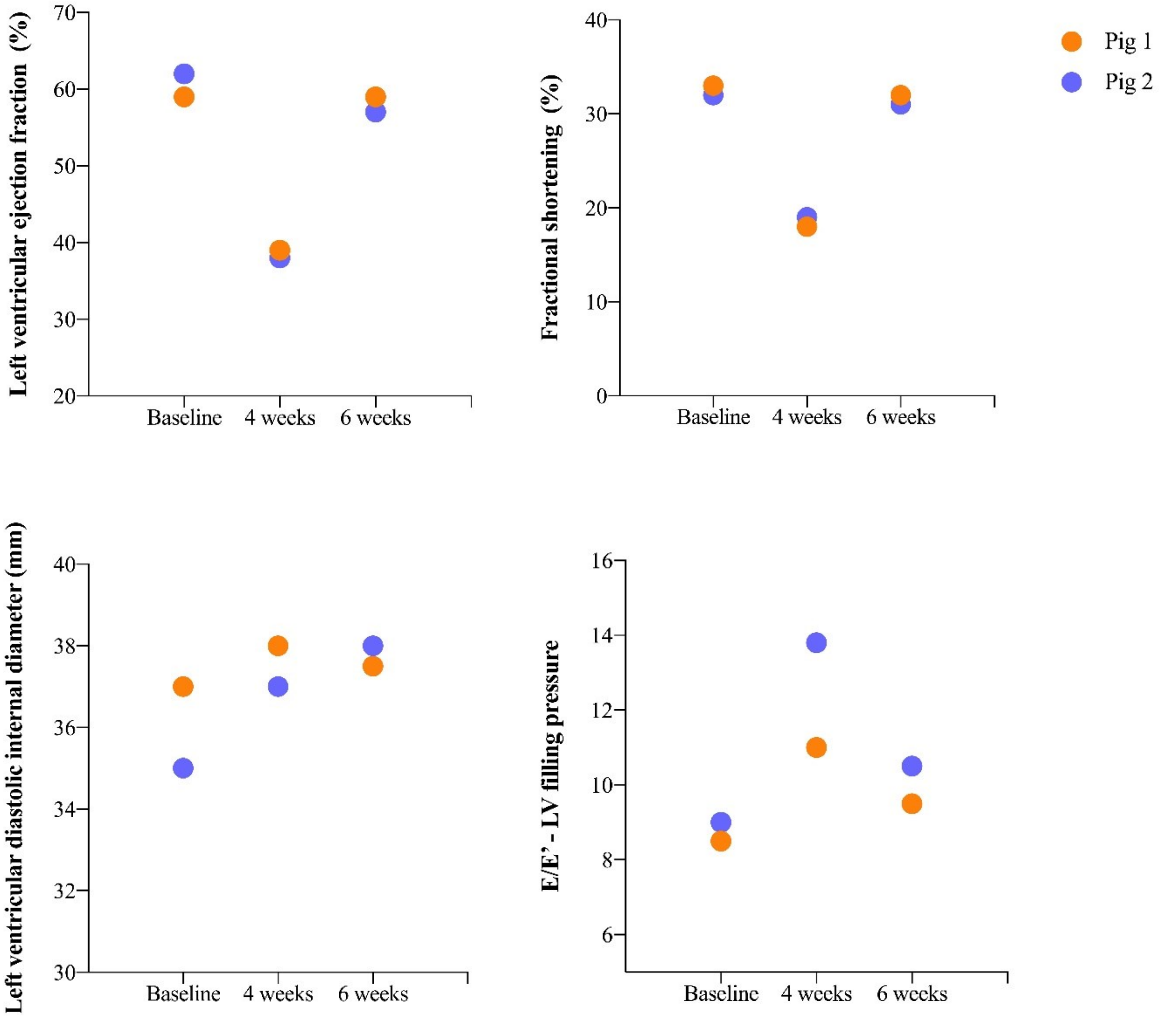

Figure 4.68 Left ventricular ejection fraction (%), fractional shortening (%), left ventricular diastolic internal diameter (mm) and left ventricular (LV) filling pressure (E/E´) of 2 treated pigs with MP dpCaPs over 6 weeks.

5 Calcium Phosphate Nanoparticle Precipitation by a Continuous Flow Process: A Design of Experiment Approach

Lorenzo Degli Esposti[1,†], Alessandro Dotti[2,†], Alessio Adamiano[1], Claudia Fabbi[2], Eride Quarta[3,4], Paolo Colombo[4], Daniele Catalucci[5,6], Claudio De Luca[2,*] and Michele Iafisco[1,*]

[1] Institute of Science and Technology for Ceramics (ISTEC), National Research Council (CNR), Via Granarolo 64, 48018 Faenza, Italy; lorenzo.degliesposti@istec.cnr.it (L.D.E.); alessio.adamiano@istec.cnr.it (A.A.)

[2] Fin-Ceramica Faenza SPA, Via Granarolo 177/3, 48018 Faenza, Italy; alessandro.dotti@finceramica.it (A.D.); claudia.fabbi@finceramica.it (C.F.)

[3] Food and Drug Department, University of Parma, Parco Area delle Scienze 27/A, 43124 Parma, Italy; Eride.quarta@studenti.unipr.it

[4] Plumestars srl, Strada Inzani 1, 43125 Parma, Italy; paolo.colombo@plumestars.com

[5] Humanitas Clinical and Research Center, IRCCS, 20089 Rozzano, Italy; daniele.catalucci@cnr.it

[6] Institute of Genetic and Biomedical Research (IRGB)-UOS, National Research Council (CNR), 20090 Milan, Italy

* Correspondence: michele.iafisco@istec.cnr.it (M.I.); cdeluca@finceramica.it (C.D.L.); Tel.: +39-054-669-9730 (M.I.); Tel.: +39-054-660-7314 (C.D.L.)

† These authors contributed equally to this work.

Published on October 2020, ***Crystals*** special issue
IF 2.4
Open access

Abstract: Calcium phosphate nanoparticles (CaP NPs) are an efficient class of nanomaterials mainly used for biomedical applications but also very promising in other sectors such as cosmetics, catalysis, water remediation, and agriculture. Unfortunately, as in the case of other nanomaterials, their wide application is hindered by the difficulty to control size, morphology, purity and degree of particle aggregation in the translation from laboratory to industrial scale production that is usually carried out in batch or semi-batch systems. In this regard, the use of continuous flow synthesis can help to solve this problem, providing more homogenous reaction conditions and highly reproducible synthesis. In this paper, we have studied with a design of experiment approach the precipitation of citrate functionalized CaP NPs aided by sonication using a continuous flow wet chemical precipitation, and the effect of some of the most relevant process factors (i.e. reactant flow rate, sonication amplitude, and maturation time) on the physico-chemical properties of the NPs were evaluated. From the statistical data analysis, we have found that CaP NP dimensions are influenced by the reactor flow rate, while the crystalline domain dimensions and product purity are influenced by the maturation process. This work provides a deeper understanding of the relationships between reaction process factors and CaP NP properties and is a relevant contribution for the scale-up production of CaP NPs for nanomedical or other applications.

Keywords: calcium phosphate; nanoparticles; design of experiment; continuous flow synthesis; nanomedicine

1. Introduction

Many domains of applied science and technology, especially health, energy, and environment, are facing an ever-growing demand for highly efficient materials. In this context, nanomaterials have emerged as a very attractive solution, because of their unique features and properties related to their small dimension, not shared by their bulk counterparts[1]. Indeed, nanomaterials are strongly impacting very different sectors and have been recently used for varies applications, such as diagnostic and therapeutic tools, smart fertilizers, energy storage units, or anti-pollution devices[2-5].

Calcium phosphate nanoparticles (CaP NPs) are one of the most investigated ceramic nanomaterials. Being chemically similar to the mineral phase of bone and teeth, CaP NPs have been mainly considered for biomedical use because of their excellent biological properties[6-9]. One of their main applications has been in hard tissues substitution and regeneration, but nowadays, they are also studied for drug and gene delivery, vaccination, imaging, and for the treatment of tumors, autoimmune and even cardiovascular diseases[10-16]. In addition, CaP NPs were recently advocated as promising nanomaterials for cosmetics, catalysis, water remediation, and agriculture[17-20].

Nevertheless, like many other nanomaterials, the wide application of CaP NPs is hindered by the low replicability and technical problems of their production process. The main challenge lies in the translation from laboratory to industrial scale production, well exemplified by the difficulties to control size, morphology, purity and degree of particle aggregation in order to achieve products with consistent specifications. When it comes to the large-scale synthesis of NPs with high-quality criteria for biomedical purposes, this challenge is even more critical as even small differences in stoichiometry, morphology or size can dramatically affect NP biological behavior.

Many methods have been studied to date for the large-scale production of CaP NPs, such as mechanochemical[21], sol–gel[22], chemical precipitation[23], sonochemical[24], and hydrothermal[25]. Wet chemical precipitation is one of the most widely applied methods for CaP NP synthesis due to the use of low-cost equipment and its ease of implementation[26]. However, chemical precipitation is usually carried out in batch or semi-batch systems, which provide limited amounts of material and require long reaction times. Moreover, batch precipitation reactions could yield NPs with a broad size distribution[27]. This is due to the rapid nucleation and growth of particles during precipitation generated by high levels of supersaturation combined with the low mixing efficiency of batch reactors. Indeed, insufficient mixing leads to a non-uniform

distribution of supersaturation that produces nuclei with different size and tendency to aggregate, thus affecting particle size distribution[28].

A possible solution to these problems is the synthesis of CaP NPs by the constant composition method or the continuous flow precipitation. The constant composition method, developed by Nancollas *et al.*, has the advantage of precisely regulate the conditions of supersaturation, thus allowing one to control the nature of precipitating solid during the whole process[29]. However, this method has the great disadvantage of not being suitable for industrial production because it requires a very low level of supersaturation that leads to limited product yield[30]. On the other hand, the continuous flow precipitation, where reactants are continuously mixed together and the precipitated NPs are quickly collected and removed from the reactor, can provide short reactants residence time, homogenous reaction conditions and thereby a more reproducible synthesis; moreover, differently from the constant composition method, it is suitable for scale up production of CaP NP[31,32]. Furthermore, the use of continuous flow reactors enables an optimal use of reactants, solvents, energy, and space, allowing the optimization of the synthesis yield while minimizing waste[31]. On the other hand, the setup of chemical precipitation by continuous flow synthesis is more complicated than in batch, since all the process parameters usually are interconnected. This is probably the reason why, to date, only few papers on the continuous flow production of CaP NPs are reported in the literature. These works were collected and analyzed in detail by Latocha *et al.*,[31] who concluded that, although these processes are complex and require thorough optimization, they are very promising for the industrial production of CaP NPs for biomedical application.

All the production processes, especially the continuous flow ones, are influenced by many parameters having a complex impact on the process output. Therefore, it is important to identify how a single factor or a combination of factors influences the process and the chemico-physical properties of the final material. This can be investigated from a statistical point of view thanks to the Design of Experiment (DoE) approach, where the influence of multiple parameters can be tested simultaneously[33].

Therefore, the main aim of this work is the study of a novel, simple and scalable synthesis of CaP NPs by wet chemical precipitation through a continuous flow process. In particular, we focused our efforts on the synthesis of citrate-functionalized CaP NPs, whose efficacy to deliver therapeutic molecules to the heart was already demonstrated in other works[10,11]. A tubular flow-through reactor is immersed in an ultrasonic bath was set, where calcium and phosphate precursors are continuously mixed for CaP NPs precipitation. The formation of NPs was aided by sonication because it could improve the homogenization of reagents, reduce

particle size and polydispersity, and avoid reactor tube clogging[34,35]. A DoE strategy was carried out to rationalize the study and optimize the number of experimental variables. The physical–chemical properties (size, surface charge, crystallinity, and composition) of the obtained CaP NPs have been thoroughly characterized, and the DoE was used to investigate the effect of the most relevant factors of the continuous flow process (i.e. reactants flow rate, sonication amplitude, and maturation time) on them. In addition, the physical–chemical properties of CaP NPs prepared by continuous flow precipitation were compared to the properties of CaP NPs prepared by batch precipitation with the same precursor reagents.

2. Materials and Methods

2.1. Materials

Sodium citrate tribasic dihydrate ($Na_3(C_6H_5O_7)\cdot 2H_2O$, ≥99.0% pure, hereafter named Na_3(Cit)), sodium phosphate dibasic dihydrate ($Na_2HPO_4\cdot 2H_2O$, ≥99.0% pure), sodium hydroxide (NaOH, ≥98.0% pure), and calcium chloride dihydrate ($CaCl_2\cdot 2H_2O$, ≥99.0% pure) were supplied by Sigma Aldrich (St. Luis, MO, USA). All the solutions were prepared with ultrapure water (18.2 MΩ × cm, 25 °C, Barnstead Nanopure™, Thermo Scientific, Waltham, MA, USA).

2.2. Description of the Continuous Flow Tube type Reactor

CaP NPs were precipitated in a continuous flow tube type reactor which was immersed in a water bath together with a sonicator probe. A scheme of the reactor is reported in Figure 1. In detail, the reactor was composed of three main parts: (i) two stirred reservoirs containing calcium or phosphate precursor solutions connected to two independent peristaltic pumps, and (ii) a Y-shaped connector placed before (iii) a tubular reactor (Static mixer, Koflo Corporation) consisting of a spiral tube (316 stainless steel) with 4.8 mm in inner diameter and 230 mm in length immersed in a water bath with a sonicator probe (UP400ST, Hielscher, 400 W, with amplitude ratio 1:2.55 and diameter of 14 mm). The first two components of the reactor mix thoroughly the reactants and pump them in the second part of the reactor, where the precipitation aided by sonication occurs. At the outlet of the reactor, the product is collected in a reservoir which is maintained under magnetic stirring for a defined time window.

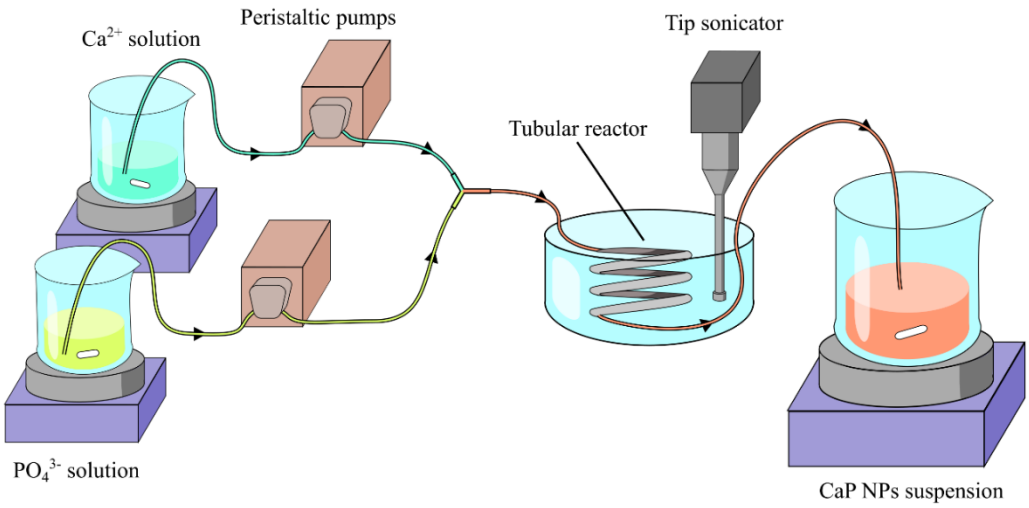

Figure 1 Schematic representation of the experimental apparatus.

2.3. Calcium Phosphate Nanoparticles Preparation

The synthesis of citrate functionalized CaP NPs was carried out similarly to the biomineralization-inspired strategy employed as discontinuous batch precipitation by Miragoli *et al.* and Di Mauro *et al.*[10,11]. Namely, it consists in the continuous mixing (1:1) at room temperature in the tubular reactor of two aqueous solutions (2 L each) of (i) $CaCl_2$ (100 mM) + Na_3Cit (400 mM) and (ii) Na_2HPO_4 (120 mM). The pH was adjusted to alkaline conditions by adding 320 mL of NaOH 0.1 M in both precursor solutions in order to reach a final volume of 2.32 L for each solution. After precipitation, the suspension was kept under stirring at room temperature for further maturation (see below). Finally, the obtained CaP NPs suspension was pelleted by centrifugation at 4500 RPM for 10 min (ROTOSILENTA 630 RS, Hettich GMBH, Tuttlingen, Germany). The collected solid fraction was washed one time with an equal volume of ultrapure water by centrifugation and redispersed again in water to the original volume. This suspension was then sonicated for 4 min (UP400ST, Hielscher, 400W) and stored at 4 °C. For the physico-chemical characterization of CaP NPs, an aliquot of the suspension was dried in ventilated oven at 70 °C for 72 h, then grinded and sieved with a 50 µm sieve in order to achieve a uniform granulometry. A control experiment was performed as discontinuous batch precipitation. In this case, the precursor solutions described above were mixed in a tank with the aid of magnetic stirring. After mixing, the suspension was kept under stirring at room temperature for 24 h. Finally, the obtained CaP NPs suspension was washed by centrifugation and stored as described above.

2.4. Design of Experiment

In the present study, the DoE approach was used to optimize the production and to study the influence of selected process factors on CaP NPs' physico-chemical properties. The DoE was conducted through a 2^3 full factorial design (3 factors with 2 levels each) that leads to eight different test runs, which were analyzed in triplicate. The selected process factors and levels were (i) the pump speed, hence the solution flow rate and thus the permanence time in the tubular reactor (FR, 0.7 and 2.8 mL s^{-1}); (ii) the power output of the probe sonicator, expressed as sonication amplitude (SA, 20 and 100%); and (iii) the maturation time of CaP NPs after synthesis (MT, 0 and 24 h). The levels of each factor and the description of each run of the DoE study are reported in Table 1. The CaP NPs' physico-chemical properties that were studied were the hydrodynamic diameter, size polydispersity, surface charge, crystallinity, crystalline domain size, Ca/P ratio, and yield of the CaP NPs. The values of each physico-chemical property (dependent variables) were analyzed using regression analysis in order to evaluate the influence of the process factors (independent variables). After a first regression analysis, the contribution of each process factor on the physico-chemical properties was calculated, and these results are reported in the Supplementary Materials. In the case that a two-factors combination had a very low incidence (<5%), it was excluded, and a new regression analysis on the remaining factors was performed. The effect of each factor was tested at the confidence limit of 95% (that corresponds to a p-value of 0.05). The factors having $p < 0.05$ were considered as "statistically significant". The standardized effect (which is the estimated effect divided by the standard error) of each factor for each dependent variable was reported as a Pareto chart graph. In all the Pareto charts reported below, the length of bars is proportional to the standardized effect of a factor, and a factor was considered as "statistically significant" if its bar exceeded the threshold of $p = 0.05$, indicated by a horizontal line. In addition, the plot of marginal means was also reported in order to graphically show the relationships between dependent and independent variables.

Table 1 Levels of factors and 2^3 experimental design matrix applied for the synthesis of calcium phosphate nanoparticles (CaP NPs).

Level	Sonication Amplitude (SA, %)	Flow Rate (FR, mL s^{-1})	Maturation Time (MT, h)
Level −1	20	0.7	0
Level +1	100	2.8	24
Sample code		**Design**	
Run 1	+1	+1	+1
Run 2	+1	+1	−1
Run 3	+1	−1	+1
Run 4	+1	−1	−1
Run 5	−1	+1	+1
Run 6	−1	+1	−1
Run 7	−1	−1	+1
Run 8	−1	−1	−1

2.5. Chemical, Morphological and Structural Characterization of the Samples

Powder X-ray diffraction (PXRD) patterns were recorded in the 2θ range from 10 to 80° with a step size (2θ) of 0.02 and a counting time of 1s with a D8 Advance diffractometer (Bruker, Karlsruhe, Germany) equipped with a Lynx-eye position sensitive detector using Cu Kα radiation (λ = 1.54178 Å) generated at 40 kV and 40 mA.

PXRD analysis was performed with the software TOPAS5[36]. In the case of the samples obtained through runs 1, 3, 5, and 7, a multiphase Rietveld refinement of the PXRD patterns was performed. The relative contents of hydroxyapatite, sodium citrate tribasic dihydrate, and halite were refined considering a three-phase system and using tabulated atomic coordinates[37-39]. For all the Rietveld refinements, anisotropic peak-broadening effects due to the anisotropic crystal shape were modeled using symmetrized spherical harmonics, while the pattern's background was modeled as 11^{th} order Chebychev function.

The average sizes of crystalline domains along the hydroxyapatite axis directions $D_{(002)}$ and $D_{(310)}$ were calculated with the software TOPAS5 as full-profile peak broadening evaluation, using the peak function of fundamental parameters. The instrumental contribution to peak broadening was evaluated by collecting the PXRD pattern of a LaB_6 standard sample.

Ca and P content was quantified by inductively coupled plasma optical emission spectrometer (ICP-OES) (ICAP 7400 DUO, Thermo Fisher Scientific Inc., Waltham, MA, USA). Atomic emission was measured at the following wavelengths: 422.673 nm for Ca, and 213.618 nm for P. Samples were prepared by dissolving an aliquot of powder in a 1 wt. % HNO_3 solution.

Fourier transform infrared (FT-IR) spectroscopy analyses were carried out on a Nicolet iN10 microscope with Nicolet iZ™10 FT-IR module (Thermo Fisher Scientific Inc., Waltham, MA, USA) with a resolution of 0.482 cm^{-1} by accumulation of 64 scans, using the KBr pellet method.

Dynamic light scattering (DLS) was used to determine hydrodynamic diameter and polydispersity index of the samples. NP size was measured with a Zetasizer Nano ZSP analyzer (Malvern, UK). DLS measurements were performed with backscatter detection (λ = 630 nm; θ = 173°) using as working parameters hydroxyapatite refractive index (1.63) for the CaP NPs, and water refractive index (1.33) and viscosity (0.887 cP) for the solvent. Measurements were performed at sample concentration of 0.5 mg/mL at unadjusted pH. Results were reported as Z-average and relative polydispersity indexes of three measurements of at least 10 runs for 10 s at 25 °C.

Electrophoretic mobility measurement (ζ-potential) was used to evaluate the surface charge of the CaP NPs at unadjusted pH using disposable folded capillary cells (DTS1061; Malvern, UK) at 25 °C. Three measurements (maximum of 100 runs each) were collected for each sample.

Transmission electron microscopy (TEM) was used to observe CaP NPs morphology. Micrographs were acquired with a Tecnai F20 microscope (Fei Corp., Hillsboro, OR, USA) operating at 120 kV. The powder samples were dispersed in ultrapure water by sonication, and then a few droplets of the slurry were deposited and dried on 200 mesh copper TEM grids were covered with thin amorphous carbon films. CaP NPs morphology analysis was performed with software ImageJ[40]. All the characterizations were performed in triplicate, and data were expressed as mean values ± standard deviation (SD) of independent analyses (n=3).

3. Results and Discussions

3.1. Crystallographic Features and Product Purity

PXRD patterns of the obtained powders are reported in Figure 2. All samples show the typical diffraction pattern of hydroxyapatite (HA, $Ca_5(PO_4)_3OH$, PDF card file 00-009-0432) as the main crystalline phase[41]. For all the runs, the diffraction peaks are broad and poorly defined, suggesting that CaP NPs are composed of HA crystals with reduced crystalline order and nano-sized crystalline domains[42]. The PXRD patterns of odd-numbered runs (Figure 2A) present additional peaks that were ascribed to the presence of minor crystalline phases that conversely are not present in even-numbered runs (Figure 2B). These secondary phases were indexed as sodium citrate tribasic dihydrate ($Na_3(C_6H_5O_7)\cdot 2H_2O$, abbreviated as Na_3(Cit), PDF card file

00-016-1170, marked with circles in Figure 2A) and halite (NaCl, PDF card file 00-005-0628, marked with squares in Figure 2A). Phase quantification was performed by multiphase Rietveld refinement (Table 2). Odd- and even- numbered runs differ for the MT factor, where the formers are (+1) MT level and the latter are (−1), respectively. The presence of secondary crystalline phases in the runs with (+1) MT level is probably due to a ripening effect in the final suspension, consisting of the dissolution and re-precipitation of CaP NPs together with halite and Na_3(Cit) during maturation. Interestingly, the highest content of impurities seems to be associated to high-level of FR. The presence of Na_3(Cit) and its increase with lower residence time were previously reported by Torrent-Burgués *et al.* for HA synthesized with similar precursors concentration and with a continuous process[43]. It is likely that the amount of water used in the washing step, that was minimized in order to avoid product losses, was not sufficient to remove these secondary products. As shown below, a high FR reduces particle size and increases particle number, thus, it is likely that in high FR runs, there is a higher number of particles where secondary phases can nucleate.

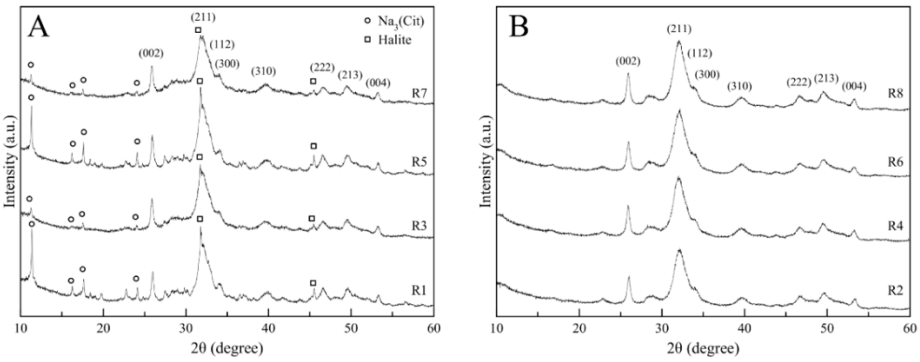

Figure 2. Powder X-ray diffraction (PXRD) patterns of the CaP NPs samples. (A) Odd-numbered runs and (B) even-numbered runs.

Table 2. Composition and crystallographic parameters of CaP NPs samples.

Sample Code	Composition (wt. %)			$D_{(002)}$ (nm)	$D_{(310)}$ (nm)	$D_{(002)}/D_{(310)}$	Splitting Factor [a]
	HA	$Na_3(Cit)$	Halite				
Run 1	64.8 ± 0.5	34.3 ± 0.5	0.9 ± 0.1	38.5 ± 1.9	7.2 ± 0.9	5.3 ± 0.4	4.2 ± 0.1
Run 2	100 ± 0.1	-	-	22.6 ± 1.1	6.1 ± 0.7	3.7 ± 0.5	4.2 ± 0.1
Run 3	87.6 ± 0.7	11.9 ± 0.7	0.5 ± 0.1	30.3 ± 1.5	6.1 ± 0.8	5.0 ± 0.6	4.3 ± 0.1
Run 4	100 ± 0.1	-	-	24.2 ± 1.2	5.7 ± 0.7	4.2 ± 0.4	4.2 ± 0.1
Run 5	69.9 ± 0.4	29.3 ± 0.4	0.9 ± 0.1	34.3 ± 1.7	6.1 ± 0.6	5.6 ± 0.6	4.6 ± 0.1
Run 6	100 ± 0.1	-	-	22.6 ± 1.2	5.5 ± 0.5	4.1 ± 0.3	4.3 ± 0.1
Run 7	90.2 ± 0.7	9.5 ± 0.7	0.4 ± 0.1	32.2 ± 1.6	5.0 ± 0.6	6.4 ± 0.5	4.2 ± 0.1
Run 8	100 ± 0.1	-	-	23.8 ± 1.2	6.1 ± 0.7	3.9 ± 0.3	4.4 ± 0.1
Batch	100 ± 0.1	-	-	24.0 ± 1.1	7.1 ± 0.5	3.4 ± 0.4	3.5 ± 0.1

[a] Calculated from FT-IR spectra: the measure consists on sum of the heights of the stretching of phosphates peaks at 603 and 560 cm^{-1} and divided by the height of the valley between them at ca. 588 cm^{-1}; all heights were measured above a baseline drawn from approximately 780–495 cm^{-1} [11].

The dimensions of HA crystalline domains were estimated along the [*00l*] and [*hk0*] directions by evaluation of the broadening of the non-overlapped (002) and (310) PXRD peaks, and are reported in Table 2 together with the aspect ratio of the crystalline domains, estimated as the $D_{(002)}/D_{(310)}$ ratio. For all the samples, the $D_{(002)}$ values (ranging from 23 to 39 nm) are higher than the corresponding $D_{(310)}$ values (ranging from 5 to 7.2 nm), indicating that all the crystalline domains are elongated along the *c*-axis, as also shown by the high aspect ratios. The presence of elongated crystalline domains was already reported in literature for HA synthesized in the presence of citrate in discontinuous batch conditions[42].

The ranking of all standardized effects of process factors and the possible cross effects for all responses on the crystallographic parameters are shown on the Pareto charts together with their cumulative relative incidence in Figure S1. According to the relative Pareto chart (Figure S1A), the combination of factors SA–MT has a very low incidence (<5%) on the crystallographic parameter $D_{(002)}$, and therefore was excluded from the regression analysis. A new regression analysis was applied without the SA–MT combination, and the ranking of standardized effects of the relevant factors on $D_{(002)}$ is shown on the Pareto charts in Figure 3A. The bars above the horizontal line indicate that the corresponding effects are statistically significant at $p = 0.05$. MT was found to be the only factor to be statistically significant on $D_{(002)}$ (p-value = 0.013). The plot of marginal means for $D_{(002)}$ (Figure 3B) shows that an increase in MT corresponds to an increase in the crystalline domain along the *c*-axis. On the other hand, the Pareto charts on the crystallographic parameter $D_{(310)}$ (Figures S1B and 3C) showed that all the factors were statistically unrelated to it (all p-values > 0.05), even if none of them could be excluded from the regression analysis. This finding suggests that the crystalline domains of HA nanoparticles increase significantly with MT along the *c*-axis but not along the *a*- and *b*-axes. This is also evident from the regression analysis applied to the aspect ratio $D_{(002)}/D_{(310)}$, where, according to the Pareto chart of all standardized effects of factors (Figure S1C), the combination of FR–MT factors has not been considered due to its low incidence (<5%). The regression analysis applied without the FR–MT combination (Figure 3E) shows that only MT is statistically significant (*p*-value = 0.011). Furthermore, in this case, the plot of marginal means for $D_{(002)}/D_{(310)}$ (Figure 3F) shows that an increase in MT induces an expansion of the crystalline domain aspect ratio. Overall, these data indicate that CaP NPs crystalline domain dimensions are regulated by MT, and, particularly, an increase in MT leads to an increase in the crystalline domain length and aspect ratio.

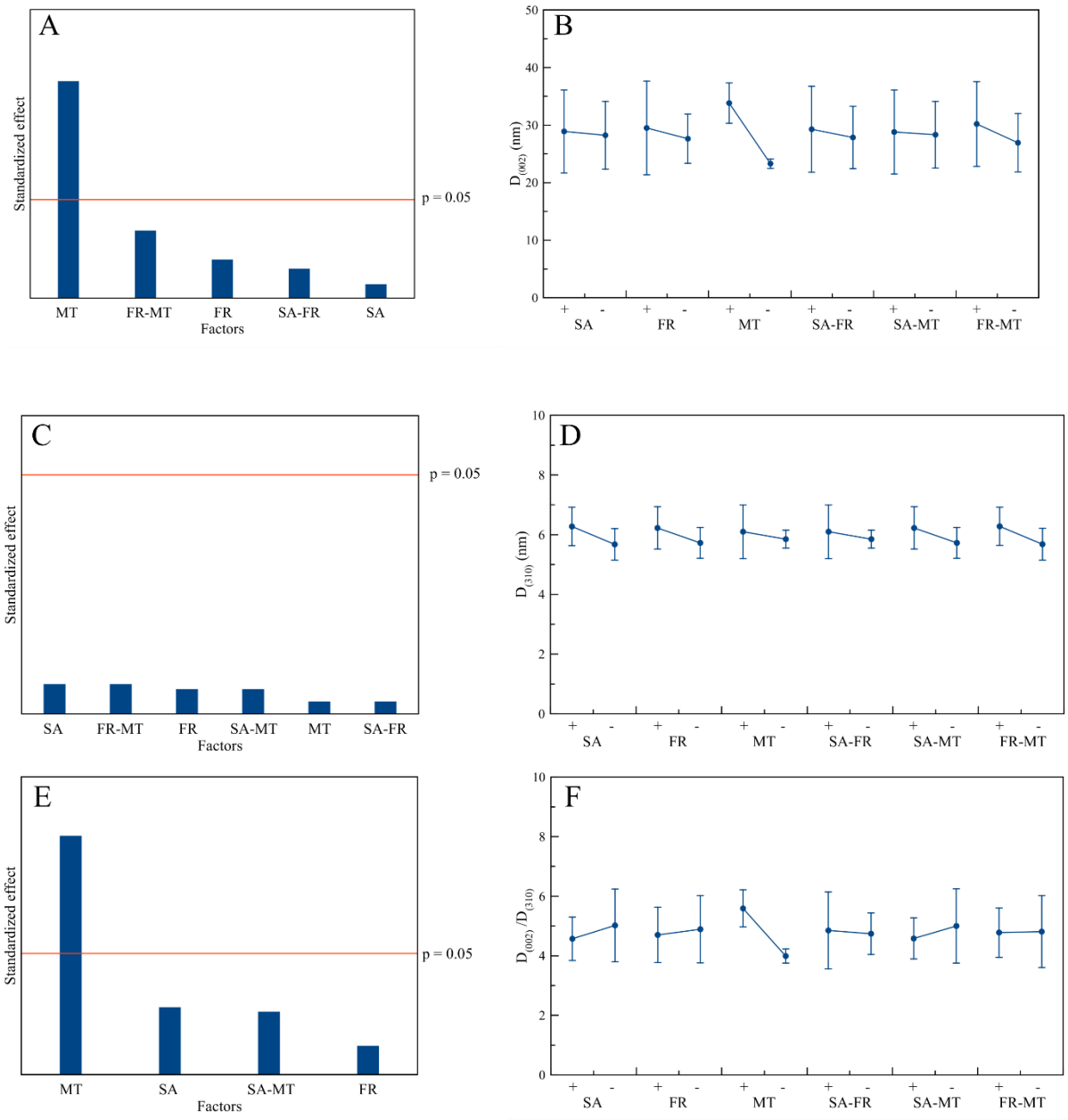

Figure 3 (A,C,E) Pareto chart of relevant standardized effects at the confidence limit of 95% and (B,D,F) plot of marginal means for (A,B) the $D_{(002)}$ crystalline domain, (C,D) the $D_{(310)}$ crystalline domain, and the (E,F) $D_{(002)}/D_{(310)}$ ratio.

These results were compared to the crystallographic features of CaP NPs prepared by discontinuous batch precipitation (Figure S2 and Table 2). It can be observed that batch CaP NPs do not present secondary crystalline phases. The size of crystalline domains of batch CaP NPs are similar to the samples prepared with the continuous flow precipitation at lower maturation time (even-numbered runs). This indicates that the continuous flow process

shortens the growth time of crystals, since with ca. 40 min of continuous flow precipitation, the crystalline domain sizes were comparable to those obtained after 24 h of maturation in batch.

3.2. Ca/P Ratio and Yield

The Ca/P molar ratio is a feature for CaP-based materials that is commonly used to evaluate composition and stoichiometry of the product[44,45]. Ca/P molar ratios of the eight runs are reported in Table 3 and are comprised between 1.48 and 1.59. The Ca/P values are lower than the stoichiometric value of HA (i.e. 1.67), indicating that all the samples are Ca-deficient, having Ca/P molar ratios close to biogenic apatite (1.5), which could enhance their biomimetic character[46]. A Ca/P value close to 1.5 is common for CaP NPs precipitated in presence of citrate[42], and similar values were observed for NPs both precipitated in discontinuous batch conditions and with continuous processes[43].

Table 3 Ca/P molar ratio of CaP NPs samples.

Sample Code	Ca/P	Yield (g L^{-1})	Corrected Yield (g L^{-1})
Run 1	1.50 ± 0.01	3.8 ± 0.4	2.5 ± 0.3
Run 2	1.53 ± 0.01	2.6 ± 0.3	2.6 ± 0.3
Run 3	1.52 ± 0.01	3.4 ± 0.4	3.0 ± 0.3
Run 4	1.52 ± 0.01	2.6 ± 0.3	2.6 ± 0.3
Run 5	1.49 ± 0.01	3.5 ± 0.2	2.5 ± 0.2
Run 6	1.54 ± 0.01	2.8 ± 0.3	2.8 ± 0.3
Run 7	1.51 ± 0.01	3.4 ± 0.3	3.1 ± 0.3
Run 8	1.59 ± 0.01	2.9 ± 0.3	2.9 ± 0.3
Batch	1.50 ± 0.01	1.6 ± 0.2	1.6 ± 0.2

Figure 4A–B shows the Pareto charts and plots of marginal means for the Ca/P ratios resulting from the statistical analysis. According to the Pareto chart of all standardized effects (Figure S3A), the combination of factors FR-MT has not been considered due to its low incidence. The regression analysis without FR-MT combination (Figure 4A) indicates that no factor has a significant effect on the Ca/P ratio, as also shown by the plot of marginal means (Figure 4B). In addition, also the CaP NPs prepared by discontinuous batch precipitation have a similar Ca/P ratio to those prepared by continuous flow precipitation. It is likely that the Ca/P ratio is dependent only to the stoichiometric ratios and concentration of the precursor reagents, as was reported in other works[47,48].

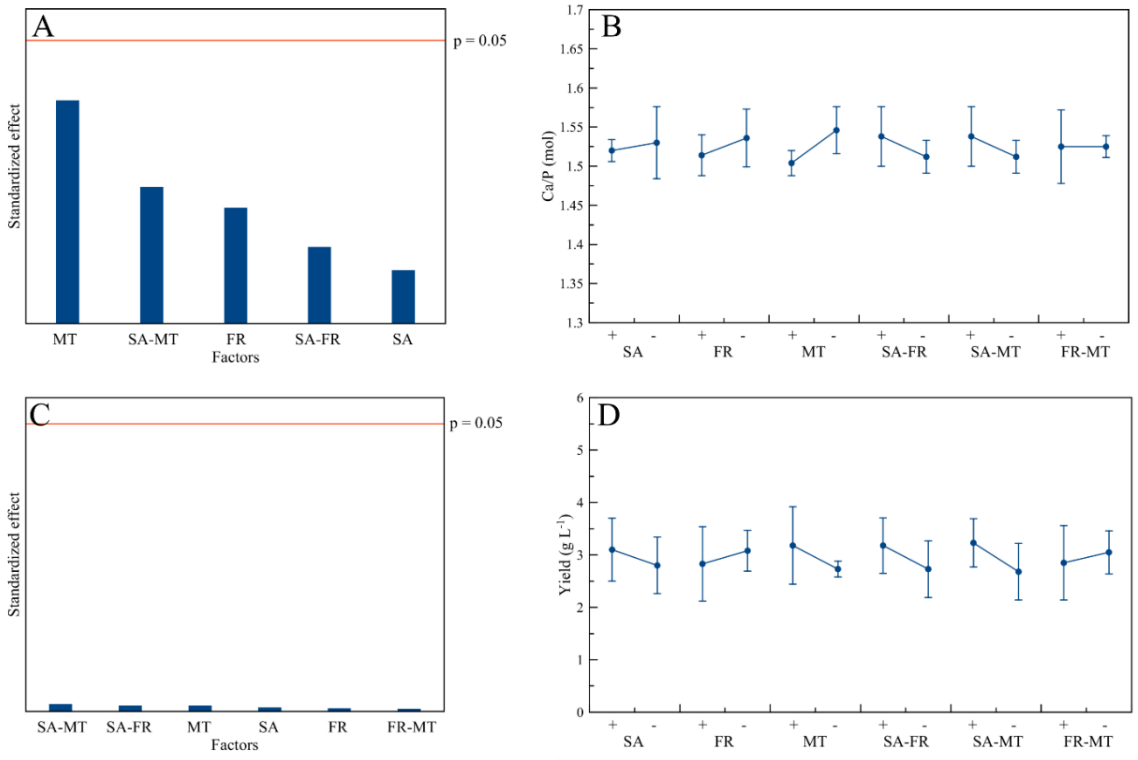

Figure 4 (A,C) Pareto chart of relevant standardized effects at the confidence limit of 95% and (B,D) plot of marginal means for (A,B) Ca/P ratio and (C,D) yield.

Of fundamental importance for the industrial development of CaP NPs is the process yield. Commonly, CaP NPs precipitation process is far from being a quantitative reaction, and in the presence of growth inhibitors like citrate, the yield is even lower due to the effect of calcium chelation. For this reason, it is essential to find the best compromise between the NPs properties and process yield. The production yields for the eight runs are reported in Table 3, and are comprised between 2.6 and 3.8 g L^{-1}. Taking into account that odd-numbered runs contains impurities, the yields were corrected on the basis of HA content estimated from the phase quantification by PXRD Rietveld refinement. Indeed, a main result of the flow-process is the ca. two-fold increase in yield in comparison to discontinuous batch precipitation process (1.6 g L^{-1}). The increase in yield is due to the highly efficient mixing of precursors in the continuous flow process that improves the consumption of reactants and precipitation of particles[49,50]. However, according to the Pareto charts, reported in Figure 4C and Figure S3B, none of the factors has a statistically significant influence on the syntheses yield. In addition, from the plot of marginal means that no clear trend was observed between corrected yield and all the factors.

3.3. Structural Characterization

The FT-IR spectra of the samples are reported in Figure 5 and S4; all samples display the same bands. The main band is a broad band at ca. 1030 cm^{-1} with shoulders at ca. 1046 and ca. 1075 cm^{-1}, and it corresponds to ν_3PO_4 vibration, which is the triply degenerated antisymmetric stretching mode of the apatitic phosphate groups. The other main bands are also due to the vibration of apatitic phosphate groups, which are at ca. 961 cm^{-1} (ν_1PO_4, symmetric stretching) and at 603, 574 (as a shoulder) and 564 cm^{-1} (ν_4PO_4, triply degenerated bending). All the runs present the bands associated to the vibrational and stretching mode of hydroxyl ions at 632 and 3570 cm^{-1}, respectively[51], confirming the presence of OH^- groups in the crystal lattice and thus the HA phase assignment. In the 1650–1350 cm^{-1} range, the signals of antisymmetric and symmetric stretching modes of carboxylate group (asym and sym ν_{stret} OCO, respectively) are present, together with a band due to adsorbed water (ca. 1640 cm^{-1}). The ν_{stret} OCO bands were assigned to the presence of citrate ions, since carbonate ions were not detected in the samples, as evinced by the absence of νCO_3 carbonate band at ca. 870 cm^{-1}. The relative intensity of citrate bands is higher in odd-numbered runs (Figure 5A) than in even-numbered ones (Figure 5B), suggesting a higher citrate content due to the presence of Na_3(Cit), as shown by PXRD. This is also confirmed by the presence of a small band at 840 cm^{-1} only in odd-numbered runs that was attributed to the signal of bending modes of carboxylate group (ν_{ben} OCO) typical of Na_3(Cit) crystals[52]. Apart from the differences in relative intensity of citrate bands, all samples have similar band positions and intensities. A FT-IR spectrum similar to the ones of odd-numbered runs was obtained for the discontinuous batch precipitation sample (Figure S2).

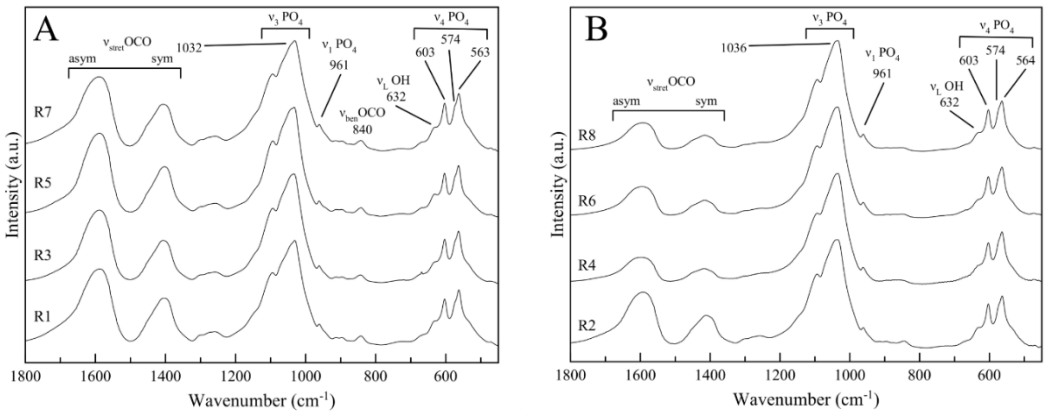

Figure 5 FT-IR spectra of the samples in the 1800–400 cm^{-1} region. (A) Odd-numbered runs and (B) even-numbered runs.

The FT-IR spectra were used to quantitatively evaluate the crystallinity of the products by means of the splitting factor (SF) (Table 2), a well-reported index for the evaluation of crystallinity degree of CaP-based materials[53]. All the samples have a SF between 4.2 and 4.6, suggesting that the crystallinity is comparable among the tested conditions. The SFs of the samples prepared by continuous flow precipitation are higher than that of CaP NPs synthesized through discontinuous batch precipitation (3.5), indicating that the flow-through precipitation aided by sonication improved particle crystallinity. From the Pareto charts on SF, reported in Figure S5, it is evident that the SA–MT combination can be excluded due to low incidence. The regression analysis without the SA–MT combination (Figure 6A) shows that no factor has a statistically significant influence on the SF. The plot of marginal means (Figure 6B) shows that a slightly higher SF value can be achieved with a lower SA.

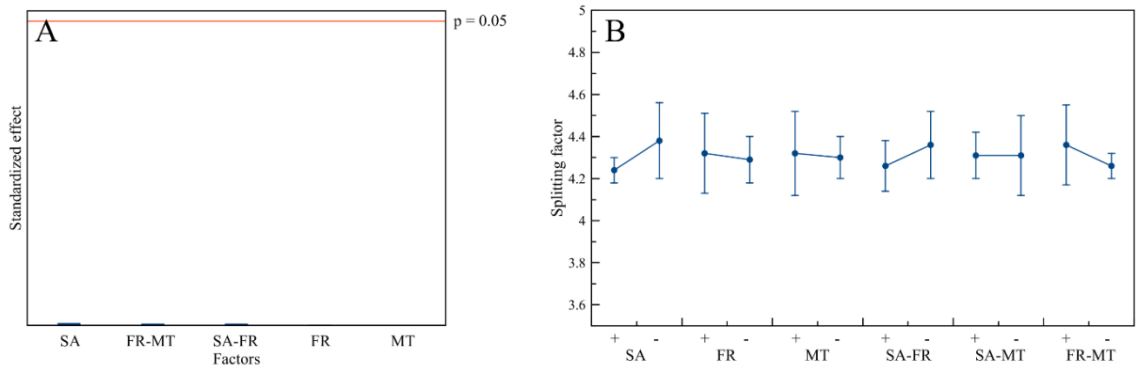

Figure 6 (A) Pareto chart of relevant standardized effects at the confidence limit of 95% and (B) plot of marginal means for the splitting factor.

3.4. Hydrodynamic Diameter, PdI, and ζ-Potential

CaP NPs dimensions, polydispersity, and surface charge are properties that are closely related to the biological behavior of the samples and affect essential processes such as cell and tissue penetration, translocation, cell compatibility, and protein binding. The hydrodynamic diameter (expressed as Z-average), the maximal particle size (expressed as $D_v(90)$, which is the diameter which encompasses the 90% in volume of the particles), the polydispersity index (PdI) and the ζ-potential of the samples are reported in Table 4. The obtained NPs have hydrodynamic diameters ranging from 60 to 140 nm (corresponding to a $D_v(90)$ ranging from 60 to 400 nm) with a relatively low PdI (from 0.25 to 0.5), and have a strongly negative surface charge in the range between −23 and −34 mV. Figures 7 and S6 shows the Pareto charts and plots of marginal

means for size and surface charge values resulting from the statistical analysis. According to the Pareto chart of all the standardized effects on Z-average (Figure S6A), the SA–MT combination factor has a low incidence and was excluded. The regression analysis without the SA–MT combination (Figure 7A) shows that NPs' hydrodynamic diameter is significantly dependent on FR (p = 0.003). Plots of marginal means (Figure 7B) show that size is notably lower with higher FR. The results suggest that a high FR, and thus the increase in pressure, led to the formation of a turbulent flow in the reactor, improving reactant mixing and nucleation and reducing particle aggregation. $D_v(90)$, being another expression of particle size, has the same Pareto charts and plots of marginal means of Z-average, and for sake of simplicity, was omitted. Even the PdI is significantly influenced only by FR (p = 0.011); according to the relative Pareto chart (Figure 7C), the two are inversely proportional (high FRs correspond to lower PdI) as shown by the plot of marginal means (Figure 7D). For PdI, the FR–MT combination factor was excluded before regression analysis due to its low incidence (Figure S6B). The results indicate that both NPs dimension and polydispersity are inversely proportional to flow rate through the reactor. The particle size reduction and homogenization by higher flow rates were previously reported in other works on HA NPs produced by continuous flow processes. In these works, it was found that high flow rates and low residence times (i) improved the mixing of precursor solutions, (ii) increased nucleation and decreased particle size, and (iii) decreased particle aggregation after nucleation[31,32,54]. Indeed, the Z-average and PdI values of run 1 and run 5 samples (i.e. prepared at higher FR with 24h of MT) are lower than those of CaP NPs prepared in batch conditions (24h of maturation). From Pareto charts on ζ-potential values, reported in Figure S6C, both SA–MT and FR–MT combination factors can be excluded due to low incidence. The regression analysis without these factors (Figure 7E) shows that no factor has a statistically significant influence on the surface charge. In our previous works, we have demonstrated that the negative surface charge of NPs is due to the presence of citrate ions on their surface[10,11]. CaP NPs prepared by discontinuous batch precipitation have a slightly lower ζ-potential value (−19 mV) than those prepared by continuous flow.

Table 4 Dynamic light scattering (DLS) and electrophoretic mobility analysis of CaP NPs samples.

Sample Code	Z-Average (nm)	$D_v(90)$ (nm)	PdI	ζ-Potential
Run 1	62 ± 2	61 ± 3	0.28 ± 0.04	−23.3 ± 4.6
Run 2	74 ± 4	70 ± 8	0.25 ± 0.01	−28.6 ± 0.7
Run 3	140 ± 12	398 ± 130	0.50 ± 0.02	−33.6 ± 2.3
Run 4	126 ± 5	336 ± 151	0.42 ± 0.01	−24.5 ± 1.3
Run 5	61 ± 4	62 ± 4	0.27 ± 0.05	−31.3 ± 4.7
Run 6	91 ± 8	97 ± 27	0.25 ± 0.01	−31.3 ± 2.7
Run 7	124 ± 12	175 ± 78	0.39 ± 0.02	−33.6 ± 0.5
Run 8	135 ± 36	151 ± 68	0.42 ± 0.01	−32.6 ± 1.4
Batch	87 ± 1	90 ± 9	0.41 ± 0.01	−19.1 ± 2.1

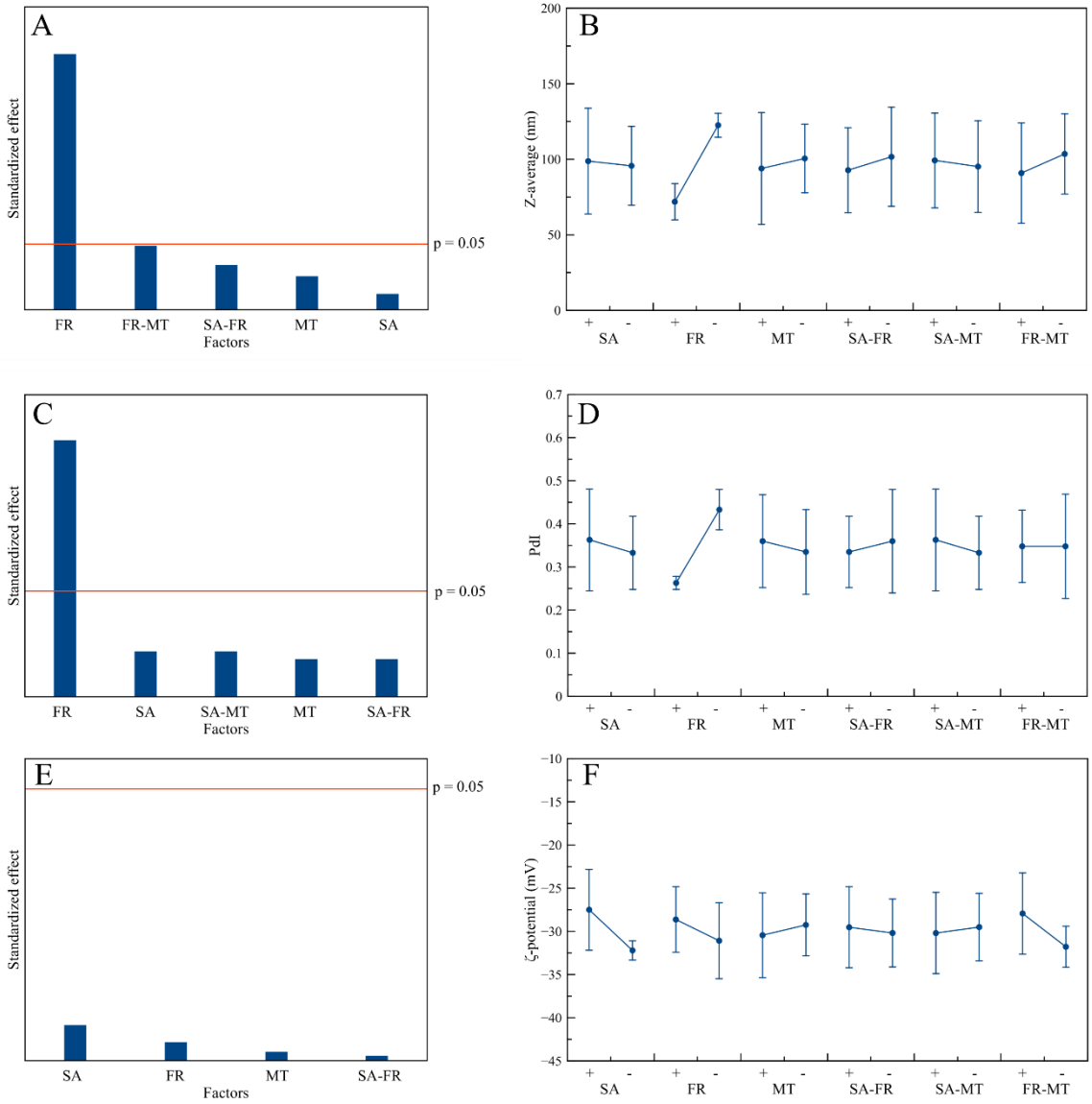

Figure 7 (A,C,E) Pareto chart of relevant standardized effects at the confidence limit of 95% and (B,D,F) plot of marginal means for (A,B) Z-average, (C,D) PdI, and (E,F) ζ-potential.

3.5. Influence of the Process Factors on CaP NPs' Physico-Chemical Properties

On the basis of the statistical data analysis, the significance of the factors on the CaP NPs' physico-chemical properties is reported in Table 5. Overall, the crystalline domain size and the crystalline domain aspect ratio are dependent on the MT factor. In particular, the higher maturation time induces the growth of the crystalline domains along the crystallographic *c*-axis, thus increasing the crystalline domain aspect ratio. Moreover, the same leads to the formation of Na_3(Cit) and halite secondary phases in the solid samples. It is important to remark that Na_3(Cit) and halite are water soluble phases that can be easily removed from the solid product, improving the washing steps.

Table 5 Summary of process factors and their significance on CaP NPs' physico-chemical properties. The arrows indicate whether an increase in the factor leads to an increase (↑) or a decrease (↓) in the physico-chemical properties.

Factors	**Response Parameter**								
	D(002)	**D(310)**	**D(002)/D(310)**	**Ca/P**	**Yield**	**Splitting Factor**	**Z-Average**	**PdI**	**ζ-Potential**
SA	-	-	-	-	-	-	-	-	-
FR	-	-	-	-	-	-	(↓)	(↓)	-
MT	(↑)	-	(↑)	-	-	-	-	-	-
SA-FR	-	-	-	-	-	-	-	-	-
SA-MT	-	-	-	-	-	-	-	-	-
FR-MT	-	-	-	-	-	-	-	-	-

On the other hand, all particle size parameters (Z-average, $D_v(90)$, and PdI) are controlled by FR, where higher flow rates—hence, higher pressure and more efficient mixing—lead to NPs with significantly smaller size due to higher nucleation, limited particle growth and lower aggregation. Finally, some CaP NPs properties ($D_{(310)}$, SF, Ca/P molar ratio, yield, ζ-potential) were not related to the herein studied process parameters. Additional DoE investigations will be carried out in the future to study the influence of reagents concentration and other synthesis parameters on the production of CaP NPs.

3.6. Morphological Investigation

In order to select the most suitable samples for a potential scale-up production, the following selection criteria were used, in decreasing order of relevance: (i) smallest hydrodynamic diameter, (ii) lowest PdI, (iii) highest ζ-potential, (iv) lowest content of impurities, (v) highest yield. According to these criteria, samples from run 2 and run 5 were selected as the most

interesting of the even- and odd-numbered runs, respectively, thus, they were analyzed by TEM. TEM micrographs (Figure 8) show that the two samples have similar morphology and are constituted by thin, needle-like nanoparticles. This morphology was previously observed for HA nanoparticles grown in the presence of citrate[42,55], where it was proved that HA nanocrystals have an anisotropic growth along the crystallographic *c*-axis and form platy, needle-like particles. Both run 5 and run 2 samples are constituted by NPs ca. 50 nm long and ca. 10 nm wide. No significant differences were observed between the two samples, meaning that MT has not influenced the morphology of the nanoparticles, as was indicated by DoE statistical data analysis.

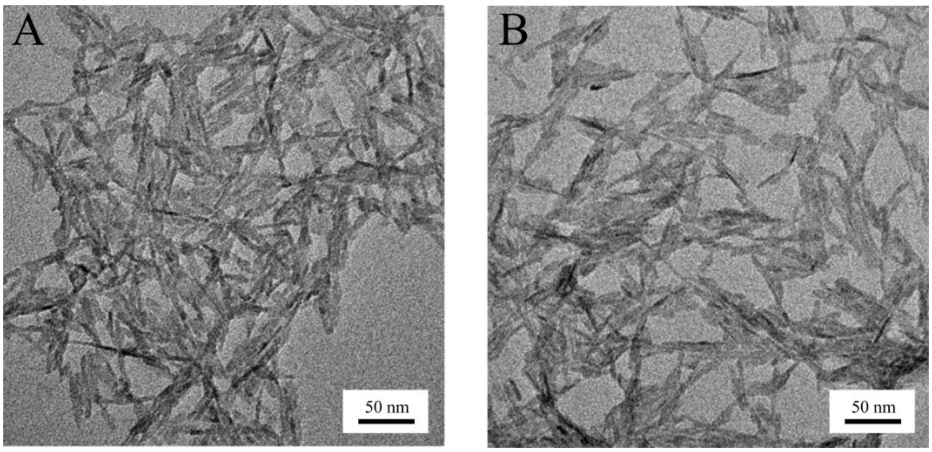

Figure 8 TEM micrograph of (A) run 5 and (B) run 2 samples.

4. Conclusions

The present work is among the first reports on the systematic evaluation by DoE of some of the most relevant process factors, i.e. maturation time, flow rate and sonication amplitude, on the production of CaP NPs obtained by continuous flow wet chemical precipitation aided by sonication. CaP NPs obtained by each of the tested runs were proven to be composed of poorly crystalline HA nanoparticles with small size and a high negative surface charge, associated, in some cases, with halite and Na_3(Cit) impurities. Through the statistical DoE data analysis, it was found that CaP NPs' dimensions are influenced mainly by reactor flow-through rate, while crystalline domain dimensions and crystalline domain anisotropy are influenced by the post-synthesis maturation process. It was also found that sonication amplitude does not have a statistically significant influence on any physico-chemical property in the tested conditions, and the NPs' stoichiometry, crystallinity, yield, and surface charge are not influenced by the analyzed process factors. In addition, it was shown that the continuous flow process in

comparison to batch precipitation allows one to achieve generally higher yields and shorter production times, and, in some cases, smaller and more homogenous CaP NPs.

The study here reported gives a proof of concept for the production of CaP NPs with suitable characteristics for nanomedical applications by a continuous precipitation process with larger yields in comparison to discontinuous batch reactions. The best conditions for achieving low CaP NPs size and polydispersity, and at the same time high purity, yield and surface charge, have been individuated and will be used as basis for further DoE experiments. The present work provides a deeper understanding of the relationships between reaction process factors and CaP NPs properties, and at the same time is a relevant contribution to the development of a cost-effective scalable process for the continuous production of CaP NPs for nanomedical or even other applications.

Supplementary Materials: The following are available online at www.mdpi.com/xxx/s1, Figure S1: Pareto chart of all standardized effects and their cumulative relative incidence for (A) the $D_{(002)}$ crystalline domain, (B) the $D_{(310)}$ crystalline domain, and (C) the $D_{(002)}/D_{(310)}$ ratio. Figure S2. (A) PXRD pattern and (B) FT-IR spectrum in the 4000–400 cm^{-1} region of the batch CaP NPs. Figure S3: Pareto chart of all standardized effects and their cumulative relative incidence for (A) the Ca/P ratio and (B) yield. Figure S4. FT-IR spectra of the samples in the 4000–400 cm^{-1} region. (A) Odd-numbered runs and (B) even-numbered runs. Figure S5: Pareto chart of all standardized effects and their cumulative relative incidence for the splitting factor. Figure S6: Pareto chart of all standardized effects and their cumulative relative incidence for (A) Z-average, (B) PdI, and (C) ζ-potential.

Author Contributions: Conceptualization, M.I. and C.D.L.; investigation, L.D.E., A.D., C.F., and A.A.; data analysis and interpretation, L.D.E., C.F., E.Q. and A.D.; writing—original draft preparation, L.D.E. and M.I.; writing—review and editing, all authors; supervision, M.I., C.D.L., P.C. and D.C.; funding acquisition, D.C. All authors have read and agreed to the published version of the manuscript.

Funding: This research was funded in part by the European Union's Horizon 2020 research and innovation program under project CUPIDO, grant agreement [No 720834].

Conflicts of Interest: The authors declare no conflict of interest.

References

1. Wagner, V.; Dullaart, A.; Bock, A.-K.; Zweck, A. The emerging nanomedicine landscape. *Nat. Biotechnol.* **2006**, *24*, 1211–1217.
2. Arico, A.S.; Bruce, P.; Scrosati, B.; Tarascon, J.-M.; Van Schalkwijk, W. Nanostructured materials for advanced energy conversion and storage devices. In *Materials for Sustainable Energy: A Collection of Peer-Reviewed Research and Review Articles from Nature Publishing Group*; World Scientific: Singapore, 2011; pp. 148–159.
3. Sattler, K.D. *Handbook of Nanophysics: Nanoelectronics and Nanophotonics*; CRC Press: Boca Raton, FL, USA, 2010.
4. Wang, P.; Lombi, E.; Zhao, F.-J.; Kopittke, P.M. Nanotechnology: A new opportunity in plant sciences. *Trends Plant Sci.* **2016**, *21*, 699–712.
5. Agarwal, A.; Joshi, H. Application of nanotechnology in the remediation of contaminated groundwater: A short review. *Recent Res. Sci. Technol.* **2010**, *2*, 51-57.
6. Dorozhkin, S.V. Bioceramics of calcium orthophosphates. *Biomaterials* **2010**, *31*, 1465–1485.
7. Dorozhkin, S.V.; Epple, M. Biological and Medical Significance of Calcium Phosphates. *Angew. Chem. Int. Ed.* **2002**, *41*, 3130–3146, doi:10.1002/1521-3773(20020902)41:17<3130::aid-anie3130>3.0.co;2-1.
8. Uskoković, V.; Wu, V.M. Calcium phosphate as a key material for socially responsible tissue engineering. *Materials* **2016**, *9*, 434.
9. Uskoković, V. Ion-doped hydroxyapatite: An impasse or the road to follow? *Ceram. Int.* **2020**, *46*, 11443–11465.
10. Miragoli, M.; Ceriotti, P.; Iafisco, M.; Vacchiano, M.; Salvarani, N.; Alogna, A.; Carullo, P.; Ramirez-Rodríguez, G.B.; Patrício, T.; Degli Esposti, L.; et al. Inhalation of peptide-loaded nanoparticles improves heart failure. *Sci. Transl. Med.* **2018**, *10*, eaan6205.
11. Di Mauro, V.; Iafisco, M.; Salvarani, N.; Vacchiano, M.; Carullo, P.; Ramírez-Rodríguez, G.B.; Patrício, T.; Tampieri, A.; Miragoli, M.; Catalucci, D. Bioinspired negatively charged calcium phosphate nanocarriers for cardiac delivery of MicroRNAs. *Nanomedicine* **2016**, *11*, 891–906, doi:10.2217/nnm.16.26.
12. Victor, S.P.; Kumar, T.S.S. Tailoring calcium-deficient hydroxyapatite nanocarriers for enhanced release of antibiotics. *J. Biomed. Nanotechnol.* **2008**, *4*, 203–209, doi:10.1166/jbn.2008.019.

13. Victor, S.P.; Paul, W.; Jayabalan, M.; Sharma, C.P. Supramolecular hydroxyapatite complexes as theranostic near-infrared luminescent drug carriers. *CrystEngComm* **2014**, *16*, 9033–9042, doi:10.1039/c4ce01137f.
14. Iafisco, M.; Drouet, C.; Adamiano, A.; Pascaud, P.; Montesi, M.; Panseri, S.; Sarda, S.; Tampieri, A. Superparamagnetic iron-doped nanocrystalline apatite as a delivery system for doxorubicin. *J. Mater. Chem. B* **2016**, *4*, 57–70, doi:10.1039/c5tb01524c.
15. Mostaghaci, B.; Loretz, B.; Lehr, C.M. Calcium Phosphate System for Gene Delivery: Historical Background and Emerging Opportunities. *Curr. Pharm. Des.* **2016**, *22*, 1529–1533, doi:10.2174/1381612822666151210123859.
16. He, Q.; Mitchell, A.; Morcol, T.; Bell, S.J. Calcium phosphate nanoparticles induce mucosal immunity and protection against herpes simplex virus type 2. *Clin. Diagn. Lab. Immunol.* **2002**, *9*, 1021–1024.
17. Ali, I. New generation adsorbents for water treatment. *Chem. Rev.* **2012**, *112*, 5073–5091.
18. Mori, K.; Yamaguchi, K.; Hara, T.; Mizugaki, T.; Ebitani, K.; Kaneda, K. Controlled synthesis of hydroxyapatite-supported palladium complexes as highly efficient heterogeneous catalysts. *J. Am. Chem. Soc.* **2002**, *124*, 11572–11573.
19. Yoon, H.Y.; Lee, J.G.; Esposti, L.D.; Iafisco, M.; Kim, P.J.; Shin, S.G.; Jeon, J.-R.; Adamiano, A. Synergistic Release of Crop Nutrients and Stimulants from Hydroxyapatite Nanoparticles Functionalized with Humic Substances: Toward a Multifunctional Nanofertilizer. *ACS Omega* **2020**, *5*, 6598–6610.
20. Ramírez-Rodríguez, G.B.; Dal Sasso, G.; Carmona, F.J.; Miguel-Rojas, C.; Pérez-de-Luque, A.; Masciocchi, N.; Guagliardi, A.; Delgado-López, J.M. Engineering Biomimetic Calcium Phosphate Nanoparticles: A Green Synthesis of Slow-Release Multinutrient (NPK) Nanofertilizers. *ACS Appl. Bio Mater.* **2020**, *3*, 1344–1353.
21. Rhee, S.-H. Synthesis of hydroxyapatite via mechanochemical treatment. *Biomaterials* **2002**, *23*, 1147–1152.
22. Kim, I.-S.; Kumta, P.N. Sol-gel synthesis and characterization of nanostructured hydroxyapatite powder. *Mater. Sci. Eng. B* **2004**, *111*, 232–236.
23. Drouet, C.; Bosc, F.; Banu, M.; Largeot, C.; Combes, C.; Dechambre, G.; Estournès, C.; Raimbeaux, G.; Rey, C. Nanocrystalline apatites: From powders to biomaterials. *Powder Technol.* **2009**, *190*, 118–122.
24. Jevtic, M.; Mitric, M.; Skapin, S.; Jancar, B.; Ignjatovic, N.; Uskokovic, D. Crystal structure of hydroxyapatite nanorods synthesized by sonochemical homogeneous precipitation. *Cryst. Growth Des.* **2008**, *8*, 2217–2222.

25. Di Chen, J.; Wang, Y.J.; Wei, K.; Zhang, S.H.; Shi, X.T. Self-organization of hydroxyapatite nanorods through oriented attachment. *Biomaterials* **2007**, *28*, 2275–2280.
26. Afshar, A.; Ghorbani, M.; Ehsani, N.; Saeri, M.; Sorrell, C. Some important factors in the wet precipitation process of hydroxyapatite. *Mater. Des.* **2003**, *24*, 197–202.
27. Kim, D.W.; Cho, I.-S.; Kim, J.Y.; Jang, H.L.; Han, G.S.; Ryu, H.-S.; Shin, H.; Jung, H.S.; Kim, H.; Hong, K.S. Simple large-scale synthesis of hydroxyapatite nanoparticles: In Situ observation of crystallization process. *Langmuir* **2010**, *26*, 384–388.
28. Chen, J.; Zheng, C.; Chen, G.A. Interaction of macro-and micromixing on particle size distribution in reactive precipitation. *Chem. Eng. Sci.* **1996**, *51*, 1957–1966.
29. Kazmierczak, T.; Schuttringer, E.; Tomažić, B.; Nancollas, G. Controlled composition studies of calcium carbonate and sulfate crystal growth. *Croat. Chem. Acta* **1981**, *54*, 277–287.
30. Uskokovic, V. Challenges for the modern science in its descend towards nano scale. *Curr. Nanosci.* **2009**, *5*, 372–389.
31. Latocha, J.; Wojasiński, M.; Sobieszuk, P.; Ciach, T. Synthesis of hydroxyapatite in a continuous reactor: A review. *Chem. Process Eng.* **2018**, 281–293-281–293.
32. Castro, F.; Ferreira, A.; Rocha, F.; Vicente, A.; Teixeira, J.A. Continuous-flow precipitation of hydroxyapatite at 37 C in a meso oscillatory flow reactor. *Ind. Eng. Chem. Res.* **2013**, *52*, 9816–9821.
33. Massart, D.L.; Vandeginste, B.G.; Buydens, L.; Lewi, P.; Smeyers-Verbeke, J.; Jong, S.D. *Handbook of Chemometrics and Qualimetrics*; Elsevier Science Inc.: Amsterdam, The Netherlands, 1998.
34. Giardina, M.A.; Fanovich, M.A. Synthesis of nanocrystalline hydroxyapatite from $Ca(OH)_2$ and H_3PO_4 assisted by ultrasonic irradiation. *Ceram. Int.* **2010**, *36*, 1961–1969.
35. Deng, S.; Lin, Z.T.; Tang, H.X.; Ullah, S.; Bi, Y.G. Rapid synthesis of hydroxyapatite nanoparticles via a novel approach in the dual-frequency ultrasonic system for specific biomedical application. *J. Mater. Res.* **2019**, *34*, 2796–2806.
36. Coelho, A. *Topas Academic V5*; Coelho Software: Brisbane, Australia, 2012.
37. Hughes, J.M.; Cameron, M.; Crowley, K.D. Structural variations in natural F, OH, and Cl apatites. *Am. Mineral.* **1989**, *74*, 870–876.
38. Walker, D.; Verma, P.K.; Cranswick, L.M.; Jones, R.L.; Clark, S.M.; Buhre, S. Halite-sylvite thermoelasticity. *Am. Mineral.* **2004**, *89*, 204–210.
39. Fischer, A.; Palladino, G. Trisodium citrate dihydrate. *Acta Crystallogr. Sect. E Struct. Rep. Online* **2003**, *59*, m1080–m1082.

40. Abràmoff, M.D.; Magalhães, P.J.; Ram, S.J. Image processing with ImageJ. *Biophotonics Int.* **2004**, *11*, 36–42.
41. Martínez-Casado, F.J.; Iafisco, M.; Delgado-López, J.M.; Martínez-Benito, C.; Ruiz-Pérez, C.; Colangelo, D.; Oltolina, F.; Prat, M.; Gómez-Morales, J. Bioinspired Citrate–Apatite Nanocrystals Doped with Divalent Transition Metal Ions. *Cryst. Growth Des.* **2015**, *16*, 145–153.
42. Delgado-López, J.M.; Iafisco, M.; Rodríguez, I.; Tampieri, A.; Prat, M.; Gómez-Morales, J. Crystallization of bioinspired citrate-functionalized nanoapatite with tailored carbonate content. *Acta Biomater.* **2012**, *8*, 3491–3499, doi:10.1016/j.actbio.2012.04.046.
43. Torrent-Burgués, J.; Gómez-Morales, J.; López-Macipe, A.; Rodríguez-Clemente, R. Continuous precipitation of hydroxyapatite from Ca/citrate/phosphate solutions using microwave heating. *Cryst. Res. Technol. J. Exp. Ind. Crystallogr.* **1999**, *34*, 757–762.
44. Dorozhkin, S.V. Calcium orthophosphates. *J. Mater. Sci.* **2007**, *42*, 1061–1095.
45. Iafisco, M.; Palazzo, B.; Martra, G.; Margiotta, N.; Piccinonna, S.; Natile, G.; Gandin, V.; Marzano, C.; Roveri, N. Nanocrystalline carbonate-apatites: Role of Ca/P ratio on the upload and release of anticancer platinum bisphosphonates. *Nanoscale* **2012**, *4*, 206–217.
46. Gómez-Morales, J.; Iafisco, M.; Delgado-López, J.M.; Sarda, S.; Drouet, C. Progress on the preparation of nanocrystalline apatites and surface characterization: Overview of fundamental and applied aspects. *Progress Cryst. Growth Charact. Mater.* **2013**, *59*, 1–46, doi:10.1016/j.pcrysgrow.2012.11.001.
47. Kawase, M.; Suzuki, T.; Miura, K. Growth mechanism of lanthanum phosphate particles by continuous precipitation. *Chem. Eng. Sci.* **2007**, *62*, 4875–4879.
48. Pieper, M.; Aman, S.; Hintz, W.; Tomas, J. Optimization of a continuous precipitation process to produce nanoscale $BaSO_4$. *Chem. Eng. Technol.* **2011**, *34*, 1567–1574.
49. Gecim, G.; Donmez, S.; Erkoc, E. Calcium deficient hydroxyapatite by precipitation: Continuous process by vortex reactor and semi-batch synthesis. *Ceram. Int.* **2020**, doi:10.1016/j.ceramint.2020.09.020.
50. Calabrese, G.S.; Pissavini, S. From batch to continuous flow processing in chemicals manufacturing. *AIChE J.* **2011**, *57*, 828–834.
51. Koutsopoulos, S. Synthesis and characterization of hydroxyapatite crystals: A review study on the analytical methods. *J. Biomed. Mater. Res.* **2002**, *62*, 600–612.
52. Lakhmanan, B. Infrared Absorption spectrum of sodium citrate. *J. Indian Inst. Sci.* **2013**, *39*, 27.

53. Termine, J.D.; Posner, A.S. Infra-red determination of the percentage of crystallinity in apatitic calcium phosphates. *Nature* **1966**, *211*, 268–270.
54. Kandori, K.; Kuroda, T.; Togashi, S.; Katayama, E. Preparation of calcium hydroxyapatite nanoparticles using microreactor and their characteristics of protein adsorption. *J. Phys. Chem. B* **2011**, *115*, 653–659.
55. Ivanchenko, P.; Delgado-López, J.M.; Iafisco, M.; Gómez-Morales, J.; Tampieri, A.; Martra, G.; Sakhno, Y. On the surface effects of citrates on nano-apatites: Evidence of a decreased hydrophilicity. *Sci. Rep.* **2017**, *7*, 8901.

6 Conclusions

In the specific framework of the cardiovascular disease treatment, this work addresses the novel objective of exploiting the lung as administration route to target the heart. The product studied in this thesis was a nanomedicine to be inhaled for heart disease treatment. A mimetic peptide (MP) or miRNA have been loaded in calcium phosphate nanoparticles to target heart failure.

The problems and the drawbacks of the prior art concerning the aerosol products containing nanoparticles have been overcome by creating a powder aerosol made by microparticles embedding the nanoparticles. The composite microparticles have been constructed by spray drying a mannitol water solution in which calcium phosphate nanoparticles loaded with therapeutic active substances have been dispersed. In an *in vivo* experiment, the composition and structure of spray dried microparticle successfully targeted the heart via their aerosol deposition in deep lung.

The therapy sequence proceeds with the formation of a powder aerosol by means of a dry powder inhaler, then, the microparticles are deposited in lung alveoli where the release of drug loaded nanoparticle takes place by microparticle dissolution. The restored nanoparticles translocate to the pulmonary veins blood and directly reach the heart. Here, CaP nanoparticles are internalized in cardiomyocytes where MP acts on the $Ca_V\beta 2$ subunit of the L-type calcium channel (LTCC) and miR-133 controls many components of the β1 adrenergic receptor transduction cascade, both drugs improving cardiac contractility.

The spray drying to transform the nanoparticle's droplet in dry microparticles was the crucial beginning of the nanomedicine preparation. For this nanomedicine pharmacology, physic-chemistry drug delivery and product manufacturing at industrial level have been successfully combined.

The first step of the CaP nanomedicine preparation was the selection of the carrier to allow the nanoparticles to be deposited in the deep lung. The use of the mannitol was selected essentially because it was already used as drug for inhalation. This carrier usually provides spherical smooth particles but used with CaPs microparticle rough surface were always obtained indicating an accumulation of nanoparticles at the surface during drying. The structure of these spray dried microparticles depends on the rate of solvent evaporation and on the carrier molecules' and nanoparticles' diffusion rate in the drying droplet. In fact, during drying, the volume reduction of the droplet accumulates the carrier molecules and nanoparticles at the surface, giving rise to a concentration gradient. Consequently, a mass transport process from

droplet surface to center takes place. It has been found that when the nanoparticles of calcium phosphate are unloaded, the spherical microparticles result empty inside. In fact, the diametral section of microparticle exhibited a central void. This is an important discovery since the spray dried mannitol microparticles in general collapse when a void space is formed internally.

The aerosols of microparticles having the rough surface and an internal void, possess a favorable respirability. It was found that these original structures depend on the solution composition, *i.e.* the amount of nanoparticle in the dispersion, the ratio between nanoparticles and carrier and spray drying parameter.

As revealed by a dedicated Design of Experiment study concerning the composition of the water dispersion/solution to spray dry, the ratio of calcium phosphate nanoparticles' content versus mannitol is critical for particle shape and consequently, respirability. It was found that CaPs nanoparticle embedded in mannitol microparticles at composition ratio 1:4 resists to collapse on the internal void and do not form the typical wrinkled raisin like structures. These microparticles perform well for the respirability and restoration of original nanoparticle size. On the contrary, decreasing the ratio between nanoparticles and carrier to 1:0.07, the microparticles assume a donut shape that assigns a still effective respirability, but slightly difficult restoration. Thus, ratio CaPs: mannitol has been fixed to 1:4.

The most important discovery of this thesis, object of a patent filing, was that, when the mimetic peptide or micro-RNA substances are loaded in the nanoparticles, the presence of these macromolecular substances determines a reorganization of the internal structure of dry microparticle. No more central void appeared but an even distribution of small voids inside microparticles was observed. Since both density and shape effects contribute to the aerodynamic properties, these novel microparticles embedding peptide and micro-RNA loaded CaP nanoparticles demonstrated an important deep lung or alveolar deposition. In fact, a high fraction of extra-fine particles (>50%) were revealed by *in vitro* aerodynamic assessment performed using the dedicated novel Nemera prototype device. In addition, following the microparticle dissolution, the released nanoparticles recovered their primary size and surface charge. Finally, the mannitol played a key role to disaggregate the dpCaPs, in particular when loaded with micro-RNA calcium phosphate nanoparticles.

The last part of the development work was dedicated to the industrial feasibility of this nanomedicine. CaPs loaded nanoparticles and microparticles were successfully produced at pilot scale. The tangential flow filtration will be tested to improve the efficiency of NPs purification. The improvement of scaled microparticles will aim to reduce peptide loss during

spray drying process. The industrial powder resulted stable at room temperature, both stored in capsules or glass vial, preserving the aerodynamic properties.

The final part of the research was dedicated to the *in vitro* evaluation of dpCaPs toxicity for human lung alveolar epithelial cells and macrophages and not induction of cytokine release. The microparticles embedding MP loaded CaPs nanoparticle *in vitro* tested in murine cardiac cells HL-1 allowed the peptide internalization in the myocytes increasing the intracellular calcium level with a dose dependent mechanism.

Finally, the most important result reached until now is that the dry powder formulation administered by inhalation *in vivo* to induced heart diseased mini pig was able to restore the normal heart contractility in all the animal tested, differently from a placebo powder.

Other diseases such as lung pathologies or vaccines can be targeted by the engineered composite microparticles. For example, lung cancer using drugs, as zoledronic acid or doxycycline or vincristine loaded on the calcium phosphate nanoparticles, can be efficiently inhaled in the described microparticles. Vaccines based on peptides or micro-RNAs substances can be efficiently prepared for inhalation.

Acknowledgments

First of all, I would like to thank the Innovative SME PlumeStars Srl for the High Research and training Apprenticeship opportunity and my professional and academic supervisors Professor Paolo Colombo and Professor Fabio Sonvico that guided me during every single step of this project, for your admirable supervision. You always giving me the best of your knowledge and support. Your competence and dedication inspired me. Thank you for trusting me and embracing all my projects.

I would also like to thank all Professors and colleagues of the Advanced Drug Delivery Research Laboratory of Food and Drug Science Department at University of Parma, especially Professor Ruggero Bettini, to openly received me in this lab and always been ready to listen and give essential advice, providing me all the support in the realization of this work and Prof. Francesca Buttini who always collaborated with prompt and important suggestions.

Special thanks to Professor Reinhard Vehring and his team, for kindly receiving me in his lab at Department of Mechanical Engineering, University of Alberta. He has been available to support me to conclude this work, unfortunately interrupted due to SARS-CoV-2 pandemic. I really hope for further collaboration.

I am grateful to the funding agencies: European Union for the EU H2020 RIA-funded project "CUPIDO – Cardiac Ultraefficient nanoParticles for Inhalation of Drug prOducts" (GA No. 720834) headed by the Project Coordinator Dr. Daniele Catalucci and a special acknowledgment to 12 partners of Cupido project who willingly shared knowledge and data the entire time of our collaboration. Thank you for the scientific and human contributions and constant (almost daily) collaboration during this challenging project.

Moreover, special thanks are given to Dr. Giovanna Trevisi and Francesca Rossi from the IMEM-CNR Institute in Parma for the electronic microscopy analysis.

Finally, it is really worth to remember the undergraduate and MSc students who contributed to this work: Chiara Ghirardi, Giada Paccagnella, Sara Tamborrino and Alexandros Filippakis.

7 References

1. Rau JL. The inhalation of drugs: advantages and problems. *Respir Care*. 2005;50(3):367-382.

2. Fröhlich E, Mercuri A, Wu S, Salar-Behzadi S. Measurements of Deposition, Lung Surface Area and Lung Fluid for Simulation of Inhaled Compounds. *Front Pharmacol*. 2016;7:181. doi:10.3389/fphar.2016.00181

3. Sanjar S, Matthews J. Treating Systemic Diseases via the Lung. *J Aerosol Medicine*. 2001;14(1, Supplement 1):51-58. doi:10.1089/08942680150506349

4. Cordts E, Steckel H. Formulation considerations for dry powder inhalers. *Ther Deliv*. 2014;5(6):675-689. doi:10.4155/tde.14.35

5. Labiris NR, Dolovich MB. Pulmonary drug delivery. Part I: Physiological factors affecting therapeutic effectiveness of aerosolized medications. *Brit J Clin Pharmaco*. 2003;56(6):588-599. doi:10.1046/j.1365-2125.2003.01892.x

6. Bustamante-Marin XM, Ostrowski LE. Cilia and Mucociliary Clearance. *Csh Perspect Biol*. 2017;9(4):a028241. doi:10.1101/cshperspect.a028241

7. Cheng YS. Mechanisms of Pharmaceutical Aerosol Deposition in the Respiratory Tract. *Aaps Pharmscitech*. 2014;15(3):630-640. doi:10.1208/s12249-014-0092-0

8. Tena AF, Clarà PC. Deposition of Inhaled Particles in the Lungs. *Archivos De Bronconeumología Engl Ed*. 2012;48(7):240-246. doi:10.1016/j.arbr.2012.02.006

9. Moon C, Smyth HDC, Watts AB, Williams RO. Delivery Technologies for Orally Inhaled Products: an Update. *Aaps Pharmscitech*. 2019;20(3):117. doi:10.1208/s12249-019-1314-2

10. Telko MJ, Hickey AJ. Dry powder inhaler formulation. *Respir Care*. 2005;50(9):1209-1227.

11. Hassan MS, Lau RWM. Effect of Particle Shape on Dry Particle Inhalation: Study of Flowability, Aerosolization, and Deposition Properties. *Aaps Pharmscitech*. 2009;10(4):1252. doi:10.1208/s12249-009-9313-3

12. Raula J, Thielmann F, Naderi M, Lehto V-P, Kauppinen EI. Investigations on particle surface characteristics vs. dispersion behaviour of l-leucine coated carrier-free inhalable powders. *Int J Pharmaceut*. 2010;385(1-2):79-85. doi:10.1016/j.ijpharm.2009.10.036

13. Ohsaki S, Mitani R, Fujiwara S, Nakamura H, Watano S. Effect of Particle–Wall Interaction and Particle Shape on Particle Deposition Behavior in Human Respiratory System. *Chem Pharm Bulletin*. 2019;67(12):1328-1336. doi:10.1248/cpb.c19-00693

14. Darquenne C. Encyclopedia of Respiratory Medicine. In: Article Titles: P. ; 2006:300-304. doi:10.1016/b0-12-370879-6/00289-1

15. Weers J, Clark A. The Impact of Inspiratory Flow Rate on Drug Delivery to the Lungs with Dry Powder Inhalers. *Pharmaceut Res*. 2017;34(3):507-528. doi:10.1007/s11095-016-2050-x

16. Heyder J. Deposition of Inhaled Particles in the Human Respiratory Tract and Consequences for Regional Targeting in Respiratory Drug Delivery. *Proc Am Thorac Soc*. 2004;1(4):315-320. doi:10.1513/pats.200409-046ta

17. Tekade RK. *Drug Delivery Systems. Advances in Pharmaceutical Product Development and Research*. (Elsevier, ed.).; 2019.

18. Dunnet S. *Filtration Mechanisms. In: Colbeck I., Lazaridis M. (Eds). 2014, Aerosol Science: Technology and Applications. Chichester, UK: Wiley, 89-119*. Vol 6.; 2014. doi:http://eu.wiley.com/WileyCDA/WileyTitle/productCd-1119977924.html

19. Carvalho TC, Peters JI, Williams RO. Influence of particle size on regional lung deposition – What evidence is there? *Int J Pharmaceut*. 2011;406(1-2):1-10. doi:10.1016/j.ijpharm.2010.12.040

20. Hofmann W. Modelling inhaled particle deposition in the human lung—A review. *J Aerosol Sci*. 2011;42(10):693-724. doi:10.1016/j.jaerosci.2011.05.007

21. Patton JS. Mechanisms of macromolecule absorption by the lungs. *Adv Drug Deliver Rev*. 1996;19(1):3-36. doi:10.1016/0169-409x(95)00113-l

22. Bailey MM, Berkland CJ. Nanoparticle formulations in pulmonary drug delivery. *Med Res Rev*. 2009;29(1):196-212. doi:10.1002/med.20140

23. Patton JS, Fishburn CS, Weers JG. The Lungs as a Portal of Entry for Systemic Drug Delivery. *Proc Am Thorac Soc*. 2004;1(4):338-344. doi:10.1513/pats.200409-049ta

24. Wichert P von, Seifart C. The Lung, an Organ for Absorption? *Respiration*. 2005;72(5):552-558. doi:10.1159/000087685

25. Patton JS, Byron PR. Inhaling medicines: delivering drugs to the body through the lungs. *Nat Rev Drug Discov*. 2007;6(1):67-74. doi:10.1038/nrd2153

26. Metered Dose Inhaler (MDI) and Dry Powder Inhaler (DPI) Products - Quality Considerations.

27. Negro RWD. Dry powder inhalers and the right things to remember: a concept review. *Multidiscip Resp Med*. 2015;10(1):13. doi:10.1186/s40248-015-0012-5

28. Lavorini F, Pistolesi M, Usmani OS. Recent advances in capsule-based dry powder inhaler technology. *Multidiscip Resp Med*. 2017;12(1). doi:10.4081/mrm.2017.236

29. Demoly P, Hagedoorn P, Boer AH de, Frijlink HW. The clinical relevance of dry powder inhaler performance for drug delivery. *Resp Med*. 2014;108(8):1195-1203. doi:10.1016/j.rmed.2014.05.009

30. Boer AH de, Hagedoorn P, Hoppentocht M, Buttini F, Grasmeijer F, Frijlink HW. Dry powder inhalation: past, present and future. *Expert Opin Drug Del*. 2016;14(4):1-14. doi:10.1080/17425247.2016.1224846

31. Sanjar S, Matthews J. Treating Systemic Diseases via the Lung. *J Aerosol Medicine*. 2001;14(1, Supplement 1):51-58. doi:10.1089/08942680150506349

32. Finlay WH. The Mechanics of Inhaled Pharmaceutical Aerosols. Published online 2019:133-182. doi:10.1016/b978-0-08-102749-3.00007-5

33. Cordts E, Steckel H. Formulation considerations for dry powder inhalers. *Ther Deliv*. 2014;5(6):675-689. doi:10.4155/tde.14.35

34. Weers JG, Miller DP. Formulation Design of Dry Powders for Inhalation. *J Pharm Sci*. 2015;104(10):3259-3288. doi:10.1002/jps.24574

35. Pilcer G, Amighi K. Formulation strategy and use of excipients in pulmonary drug delivery. *Int J Pharmaceut*. 2010;392(1-2):1-19. doi:10.1016/j.ijpharm.2010.03.017

36. Hoppentocht M, Hagedoorn P, Frijlink HW, Boer AH de. Technological and practical challenges of dry powder inhalers and formulations. *Adv Drug Deliver Rev*. 2014;75:18-31. doi:10.1016/j.addr.2014.04.004

37. Telko MJ, Hickey AJ. Dry powder inhaler formulation. *Respir Care*. 2005;50(9):1209-1227.

38. Lau M, Young PM, Traini D. A review of co-milling techniques for the production of high dose dry powder inhaler formulation. *Drug Dev Ind Pharm*. 2017;43(8):1-39. doi:10.1080/03639045.2017.1313858

39. Chougule M, Padhi B, Jinturkar K, Misra A. Development of Dry Powder Inhalers. *Recent Patents Drug Deliv Formulation*. 2007;1(1):11-21. doi:10.2174/187221107779814159

40. Salama AH. Spray drying as an advantageous strategy for enhancing pharmaceuticals bioavailability. *Drug Deliv Transl Re*. 2020;10(1):1-12. doi:10.1007/s13346-019-00648-9

41. Ameri M, Maa Y-F. Spray Drying of Biopharmaceuticals: Stability and Process Considerations. *Dry Technol*. 2007;24(6):763-768. doi:10.1080/03602550600685275

42. Ziaee A, Albadarin AB, Padrela L, Femmer T, O'Reilly E, Walker G. Spray drying of pharmaceuticals and biopharmaceuticals: Critical parameters and experimental process optimization approaches. *Eur J Pharm Sci*. 2018;127:300-318. doi:10.1016/j.ejps.2018.10.026

43. Maa Y, Nguyen P, Sit K, Hsu CC. Spray-drying performance of a bench-top spray dryer for protein aerosol powder preparation. *Biotechnol Bioeng*. 1998;60(3):301-309. doi:10.1002/(sici)1097-0290(19981105)60:3<301::aid-bit5>3.0.co;2-l

44. Vehring R. Pharmaceutical Particle Engineering via Spray Drying. *Pharmaceut Res*. 2008;25(5):999-1022. doi:10.1007/s11095-007-9475-1

45. Gradon L, Sosnowski TR. Formation of particles for dry powder inhalers. *Adv Powder Technol*. 2014;25(1):43-55. doi:10.1016/j.apt.2013.09.012

46. Singh A, Mooter GV den. Spray drying formulation of amorphous solid dispersions. *Adv Drug Deliver Rev*. 2016;100:27-50. doi:10.1016/j.addr.2015.12.010

47. Belotti S, Rossi A, Colombo P, et al. Spray-dried amikacin sulphate powder for inhalation in cystic fibrosis patients: The role of ethanol in particle formation. *Eur J Pharm Biopharm*. 2015;93:165-172. doi:10.1016/j.ejpb.2015.03.023

48. Vehring R, Foss WR, Lechuga-Ballesteros D. Particle formation in spray drying. *J Aerosol Sci*. 2007;38(7):728-746. doi:10.1016/j.jaerosci.2007.04.005

49. Seville PC, Learoyd TP, Li H-Y, Williamson IJ, Birchall JC. Amino acid-modified spray-dried powders with enhanced aerosolisation properties for pulmonary drug delivery. *Powder Technol*. 2007;178(1):40-50. doi:10.1016/j.powtec.2007.03.046

50. Ansari MT, Sunderland VB. Solid dispersions of dihydroartemisinin in polyvinylpyrrolidone. *Arch Pharm Res*. 2008;31(3):390. doi:10.1007/s12272-001-1169-6

51. Weers JG, Miller DP. Formulation Design of Dry Powders for Inhalation. *J Pharm Sci*. 2015;104(10):3259-3288. doi:10.1002/jps.24574

52. Ellenberger D, O'Donnell KP, Williams RO. Formulating Poorly Water Soluble Drugs. Published online 2016:41-120. doi:10.1007/978-3-319-42609-9_2

53. Lechanteur A, Evrard B. Influence of Composition and Spray-Drying Process Parameters on Carrier-Free DPI Properties and Behaviors in the Lung: A review. *Pharm*. 2020;12(1):55. doi:10.3390/pharmaceutics12010055

54. Suhag Y, Nayik GA, Nanda V. Effect of gum arabic concentration and inlet temperature during spray drying on physical and antioxidant properties of honey powder. *J Food Meas Charact*. 2016;10(2):350-356. doi:10.1007/s11694-016-9313-4

55. Bosquillon C, Lombry C, Préat V, Vanbever R. Influence of formulation excipients and physical characteristics of inhalation dry powders on their aerosolization performance. *J Control Release*. 2001;70(3):329-339. doi:10.1016/s0168-3659(00)00362-x

56. Sahoo NG, Abbas A, Judeh Z, Li CM, Yuen K. Solubility enhancement of a poorly water-soluble anti-malarial drug: Experimental design and use of a modified multifluid nozzle pilot spray drier. *J Pharm Sci*. 2009;98(1):281-296. doi:10.1002/jps.21399

57. Ståhl K, Claesson M, Lilliehorn P, Lindén H, Bäckström K. The effect of process variables on the degradation and physical properties of spray dried insulin intended for inhalation. *Int J Pharmaceut*. 2002;233(1-2):227-237. doi:10.1016/s0378-5173(01)00945-0

58. Tonon RV, Brabet C, Hubinger MD. Influence of process conditions on the physicochemical properties of açai (Euterpe oleraceae Mart.) powder produced by spray drying. *J Food Eng*. 2008;88(3):411-418. doi:10.1016/j.jfoodeng.2008.02.029

59. Maury M, Murphy K, Kumar S, Shi L, Lee G. Effects of process variables on the powder yield of spray-dried trehalose on a laboratory spray-dryer. *Eur J Pharm Biopharm*. 2005;59(3):565-573. doi:10.1016/j.ejpb.2004.10.002

60. Elversson J, Millqvist-Fureby A, Alderborn G, Elofsson U. Droplet and particle size relationship and shell thickness of inhalable lactose particles during spray drying. *J Pharm Sci*. 2003;92(4):900-910. doi:10.1002/jps.10352

61. Elkinton HW. Economic control of quality of manufactured product by W. A. Shewhart, Ph.D., Member of the Technical Staff, Bell Telephone Laboratories, Inc., 501 pages, tables, diagrams, 8vo. New York, D. Van Nostrand Company, Inc., 1931. Price $6.50. *J Frankl Inst*. 1932;213(3):336-337. doi:10.1016/s0016-0032(32)91043-6

62. Buttini F, Rozou S, Rossi A, Zoumpliou V, Rekkas DM. The application of Quality by Design framework in the pharmaceutical development of dry powder inhalers. *Eur J Pharm Sci*. 2018;113:64-76. doi:10.1016/j.ejps.2017.10.042

63. Korakianiti E, Rekkas D. Statistical Thinking and Knowledge Management for Quality-Driven Design and Manufacturing in Pharmaceuticals. *Pharmaceut Res*. 2011;28(7):1465-1479. doi:10.1007/s11095-010-0315-3

64. Grangeia HB, Silva C, Simões SP, Reis MS. Quality by Design in Pharmaceutical Manufacturing: a systematic review of current status, challenges and future perspectives. *Eur J Pharm Biopharm*. 2019;147:19-37. doi:10.1016/j.ejpb.2019.12.007

65. Yu LX, Amidon G, Khan MA, et al. Understanding Pharmaceutical Quality by Design. *Aaps J*. 2014;16(4):771-783. doi:10.1208/s12248-014-9598-3

66. Schneider H, Stamatis DH. Failure Mode and Effect Analysis: FMEA from Theory to Execution. *Technometrics*. 1996;38(1):80. doi:10.2307/1268911

67. Politis SN, Colombo P, Colombo G, Rekkas DM. Design of experiments (DoE) in pharmaceutical development. *Drug Dev Ind Pharm*. 2017;43(6):1-36. doi:10.1080/03639045.2017.1291672

68. Buttini F, Rozou S, Rossi A, Zoumpliou V, Rekkas DM. The application of Quality by Design framework in the pharmaceutical development of dry powder inhalers. *Eur J Pharm Sci*. 2018;113:64-76. doi:10.1016/j.ejps.2017.10.042

69. Mishra V, Thakur S, Patil A, Shukla A. Quality by design (QbD) approaches in current pharmaceutical set-up. *Expert Opin Drug Del*. 2018;15(8):737-758. doi:10.1080/17425247.2018.1504768

70. Moghimi SM, Hunter AC, Murray JC. Nanomedicine: current status and future prospects. *Faseb J*. 2005;19(3):311-330. doi:10.1096/fj.04-2747rev

71. Bailey MM, Berkland CJ. Nanoparticle formulations in pulmonary drug delivery. *Med Res Rev*. 2009;29(1):196-212. doi:10.1002/med.20140

72. Esposti LD, Carella F, Adamiano A, Tampieri A, Iafisco M. Calcium phosphate-based nanosystems for advanced targeted nanomedicine. *Drug Dev Ind Pharm*. 2018;44(8):1-34. doi:10.1080/03639045.2018.1451879

73. Davda J, Labhasetwar V. Characterization of nanoparticle uptake by endothelial cells. *Int J Pharmaceut*. 2002;233(1-2):51-59. doi:10.1016/s0378-5173(01)00923-1

74. Moghimi SM, Hunter AC, Murray JC. Long-circulating and target-specific nanoparticles: theory to practice. *Pharmacol Rev*. 2001;53(2):283-318.

75. Zhang Y-W, Shi J, Li Y-J, Wei L. Cardiomyocyte death in doxorubicin-induced cardiotoxicity. *Arch Immunol Ther Ex*. 2009;57(6):435-445. doi:10.1007/s00005-009-0051-8

76. Moreno-Sastre M, Pastor M, Salomon CJ, Esquisabel A, Pedraz JL. Pulmonary drug delivery: a review on nanocarriers for antibacterial chemotherapy. *J Antimicrob Chemoth*. 2015;70(11):2945-2955. doi:10.1093/jac/dkv192

77. Davis ME, Chen Z (Georgia), Shin DM. Nanoparticle therapeutics: an emerging treatment modality for cancer. *Nat Rev Drug Discov*. 2008;7(9):771-782. doi:10.1038/nrd2614

78. Iafisco M, Alogna A, Miragoli M, Catalucci D. Cardiovascular nanomedicine: the route ahead. *Nanomedicine-uk*. 2019;14(18):2391-2394. doi:10.2217/nnm-2019-0228

79. Dorozhkin SV. Calcium Orthophosphate Bioceramics. *Eurasian Chem J*. 2010;12(3-4):247-258. doi:10.18321/ectj52

80. Epple M. Review of potential health risks associated with nanoscopic calcium phosphate. *Acta Biomater*. 2018;77:1-14. doi:10.1016/j.actbio.2018.07.036

81. Esposti LD, Carella F, Adamiano A, Tampieri A, Iafisco M. Calcium phosphate-based nanosystems for advanced targeted nanomedicine. *Drug Dev Ind Pharm*. 2018;44(8):1-34. doi:10.1080/03639045.2018.1451879

82. Mauro VD, Iafisco M, Salvarani N, et al. Bioinspired negatively charged calcium phosphate nanocarriers for cardiac delivery of MicroRNAs. *Nanomedicine-uk*. 2016;11(8):891-906. doi:10.2217/nnm.16.26

83. Rodríguez-Ruiz I, Delgado-López JM, Durán-Olivencia MA, et al. pH-Responsive Delivery of Doxorubicin from Citrate–Apatite Nanocrystals with Tailored Carbonate Content. *Langmuir*. 2013;29(26):8213-8221. doi:10.1021/la4008334

84. Hu Y-Y, Rawal A, Schmidt-Rohr K. Strongly bound citrate stabilizes the apatite nanocrystals in bone. *Proc National Acad Sci*. 2010;107(52):22425-22429. doi:10.1073/pnas.1009219107

85. Victor SP, Paul W, Jayabalan M, Sharma CP. Supramolecular hydroxyapatite complexes as theranostic near-infrared luminescent drug carriers. *Crystengcomm*. 2014;16(38):9033-9042. doi:10.1039/c4ce01137f

86. Iafisco M, Drouet C, Adamiano A, et al. Superparamagnetic iron-doped nanocrystalline apatite as a delivery system for doxorubicin. *J Mater Chem B*. 2015;4(1):57-70. doi:10.1039/c5tb01524c

87. Nadar RA, Margiotta N, Iafisco M, Beucken JJJP van den, Boerman OC, Leeuwenburgh SCG. Bisphosphonate-Functionalized Imaging Agents, Anti-Tumor Agents and Nanocarriers for Treatment of Bone Cancer. *Adv Healthc Mater*. 2017;6(8):1601119. doi:10.1002/adhm.201601119

88. Steichen SD, Caldorera-Moore M, Peppas NA. A review of current nanoparticle and targeting moieties for the delivery of cancer therapeutics. *Eur J Pharm Sci*. 2013;48(3):416-427. doi:10.1016/j.ejps.2012.12.006

89. Zhang G, Liu T, Chen Y-H, et al. Tissue Specific Cytotoxicity of Colon Cancer Cells Mediated by Nanoparticle-delivered Suicide Gene In vitro and In vivo. *Clin Cancer Res*. 2009;15(1):201-207. doi:10.1158/1078-0432.ccr-08-1094

90. Lee MS, Lee JE, Byun E, et al. Target-specific delivery of siRNA by stabilized calcium phosphate nanoparticles using dopa–hyaluronic acid conjugate. *J Control Release*. 2014;192:122-130. doi:10.1016/j.jconrel.2014.06.049

91. Hu Y, Haynes MT, Wang Y, Liu F, Huang L. A Highly Efficient Synthetic Vector: Nonhydrodynamic Delivery of DNA to Hepatocyte Nuclei in Vivo. *Acs Nano*. 2013;7(6):5376-5384. doi:10.1021/nn4012384

92. Roy I, Mitra S, Maitra A, Mozumdar S. Calcium phosphate nanoparticles as novel non-viral vectors for targeted gene delivery. *Int J Pharmaceut*. 2003;250(1):25-33. doi:10.1016/s0378-5173(02)00452-0

93. Porru M, Zappavigna S, Salzano G, et al. Medical treatment of orthotopic glioblastoma with transferrin-conjugated nanoparticles encapsulating zoledronic acid. *Oncotarget*. 2014;5(21):10446-10459. doi:10.18632/oncotarget.2182

94. Mauro VD, Iafisco M, Salvarani N, et al. Bioinspired negatively charged calcium phosphate nanocarriers for cardiac delivery of MicroRNAs. *Nanomedicine-uk*. 2016;11(8):891-906. doi:10.2217/nnm.16.26

95. Miragoli M, Ceriotti P, Iafisco M, et al. Inhalation of peptide-loaded nanoparticles improves heart failure. *Sci Transl Med*. 2018;10(424):eaan6205. doi:10.1126/scitranslmed.aan6205

96. Rusconi F, Ceriotti P, Miragoli M, et al. Peptidomimetic Targeting of Cavβ2 Overcomes Dysregulation of the L-Type Calcium Channel Density and Recovers Cardiac Function. *Circulation*. 2016;134(7):534-546. doi:10.1161/circulationaha.116.021347

97. Romanelli A, Affinito A, Avitabile C, et al. An anti-PDGFRβ aptamer for selective delivery of small therapeutic peptide to cardiac cells. *Plos One*. 2018;13(3):e0193392. doi:10.1371/journal.pone.0193392

98. Miragoli M, Ceriotti P, Iafisco M, et al. Inhalation of peptide-loaded nanoparticles improves heart failure. *Sci Transl Med*. 2018;10(424):eaan6205. doi:10.1126/scitranslmed.aan6205

99. Golshahi L, Tian G, Azimi M, et al. The Use of Condensational Growth Methods for Efficient Drug Delivery to the Lungs during Noninvasive Ventilation High Flow Therapy. *Pharmaceut Res*. 2013;30(11):2917-2930. doi:10.1007/s11095-013-1123-3

100. Perinel S, Leclerc L, Prévôt N, et al. Micron-sized and submicron-sized aerosol deposition in a new ex vivo preclinical model. *Respir Res*. 2016;17(1):78. doi:10.1186/s12931-016-0395-7

101. Hoet PH, Brüske-Hohlfeld I, Salata OV. Nanoparticles – known and unknown health risks. *J Nanobiotechnol*. 2004;2(1):12. doi:10.1186/1477-3155-2-12

102. Wiebert P, Sanchez-Crespo A, Falk R, et al. No Significant Translocation of Inhaled 35-nm Carbon Particles to the Circulation in Humans. *Inhal Toxicol*. 2008;18(10):741-747. doi:10.1080/08958370600748455

103. Mills NL, Amin N, Robinson SD, et al. Do Inhaled Carbon Nanoparticles Translocate Directly into the Circulation in Humans? *Am J Resp Crit Care*. 2006;173(4):426-431. doi:10.1164/rccm.200506-865oc

104. Oberdörster G, Sharp Z, Atudorei V, et al. EXTRAPULMONARY TRANSLOCATION OF ULTRAFINE CARBON PARTICLES FOLLOWING WHOLE-BODY INHALATION EXPOSURE OF RATS. *J Toxicol Environ Heal Part*. 2002;65(20):1531-1543. doi:10.1080/00984100290071658

105. NEMMAR A, VANBILLOEN H, HOYLAERTS MF, HOET PHM, VERBRUGGEN A, NEMERY B. Passage of Intratracheally Instilled Ultrafine Particles from the Lung into the Systemic Circulation in Hamster. *Am J Resp Crit Care*. 2001;164(9):1665-1668. doi:10.1164/ajrccm.164.9.2101036

106. Takenaka S, Karg E, Roth C, et al. Pulmonary and Systemic Distribution of Inhaled Ultrafine Silver Particles in Rats. *Environ Health Persp*. 2001;109:547. doi:10.2307/3454667

107. Kato T, Yashiro T, Murata Y, et al. Evidence that exogenous substances can be phagocytized by alveolar epithelial cells and transported into blood capillaries. *Cell Tissue Res*. 2003;311(1):47-51. doi:10.1007/s00441-002-0647-3

108. Geiser M, Schürch S, Gehr P. Influence of surface chemistry and topography of particles on their immersion into the lung's surface-lining layer. *J Appl Physiol*. 2003;94(5):1793-1801. doi:10.1152/japplphysiol.00514.2002

109. Iafisco M, Delgado-Lopez JM, Varoni EM, et al. Cell Surface Receptor Targeted Biomimetic Apatite Nanocrystals for Cancer Therapy. *Small*. 2013;9(22):3834-3844. doi:10.1002/smll.201202843

110. Iafisco M, Varoni E, Foggia MD, et al. Conjugation of hydroxyapatite nanocrystals with human immunoglobulin G for nanomedical applications. *Colloids Surfaces B Biointerfaces*. 2012;90:1-7. doi:10.1016/j.colsurfb.2011.09.033

111. Iafisco M, Catalucci D. Bio-Inspired Regenerative Medicine Materials, Processes, and Clinical Applications. Published online 2016:47-83. doi:10.1201/b19914-4

112. Mostaghaci B, Loretz B, Lehr C-M. Calcium Phosphate System for Gene Delivery: Historical Background and Emerging Opportunities. *Curr Pharm Design*. 2016;22(11):1529-1533. doi:10.2174/1381612822666151210123859

113. Lomis N, Gaudreault F, Malhotra M, Westfall S, Shum-Tim D, Prakash S. Novel Milrinone Nanoformulation for Use in Cardiovascular Diseases: Preparation and in Vitro Characterization. *Mol Pharmaceut*. 2017;15(7):2489-2502. doi:10.1021/acs.molpharmaceut.7b00360

114. Castaldi A, Zaglia T, Mauro VD, et al. MicroRNA-133 Modulates the β1-Adrenergic Receptor Transduction Cascade. *Circ Res*. 2014;115(2):273-283. doi:10.1161/circresaha.115.303252

115. Castaldi A, Zaglia T, Mauro VD, et al. MicroRNA-133 Modulates the β1-Adrenergic Receptor Transduction Cascade. *Circ Res*. 2014;115(2):273-283. doi:10.1161/circresaha.115.303252

116. Savi M, Rossi S, Bocchi L, et al. Titanium dioxide nanoparticles promote arrhythmias via a direct interaction with rat cardiac tissue. *Part Fibre Toxicol*. 2014;11(1):63. doi:10.1186/s12989-014-0063-3

117. Novak P, Shevchuk A, Ruenraroengsak P, et al. Imaging Single Nanoparticle Interactions with Human Lung Cells Using Fast Ion Conductance Microscopy. *Nano Lett*. 2014;14(3):1202-1207. doi:10.1021/nl404068p

118. Dvir T, Bauer M, Schroeder A, et al. Nanoparticles Targeting the Infarcted Heart. *Nano Lett*. 2011;11(10):4411-4414. doi:10.1021/nl2025882

119. Thorley AJ, Ruenraroengsak P, Potter TE, Tetley TD. Critical Determinants of Uptake and Translocation of Nanoparticles by the Human Pulmonary Alveolar Epithelium. *Acs Nano*. 2014;8(11):11778-11789. doi:10.1021/nn505399e

120. Torge A, Grützmacher P, Mücklich F, Schneider M. The influence of mannitol on morphology and disintegration of spray-dried nano-embedded microparticles. *Eur J Pharm Sci*. 2017;104:171-179. doi:10.1016/j.ejps.2017.04.003

121. Melani AS, Bonavia M, Cilenti V, et al. Inhaler mishandling remains common in real life and is associated with reduced disease control. *Resp Med*. 2011;105(6):930-938. doi:10.1016/j.rmed.2011.01.005

122. Problems with inhaler use: A call for improved clinician and patient education.

123. Mäkelä MJ, Backer V, Hedegaard M, Larsson K. Adherence to inhaled therapies, health outcomes and costs in patients with asthma and COPD. *Resp Med*. 2013;107(10):1481-1490. doi:10.1016/j.rmed.2013.04.005

124. Hole P, Sillence K, Hannell C, et al. Interlaboratory comparison of size measurements on nanoparticles using nanoparticle tracking analysis (NTA). *J Nanopart Res*. 2013;15(12):2101. doi:10.1007/s11051-013-2101-8

125. Wright M. Nanoparticle Tracking Analysis for the Multiparameter Characterization and Counting of Nanoparticle Suspensions. Methods in Molecular Biology (Methods and Protocols), vol 906. *Methods Mol Biology Clifton N J*. 2012;906:511-524. doi:10.1007/978-1-61779-953-2_41

126. Politis SN, Colombo P, Colombo G, Rekkas DM. Design of experiments (DoE) in pharmaceutical development. *Drug Dev Ind Pharm*. 2017;43(6):1-36. doi:10.1080/03639045.2017.1291672

127. Ich. ICH Topic Q2 (R1) Validation of Analytical Procedures : Text and MethodologyEuropean Medicines Agency. Published online 1995.

128. Rogers DF, Donnelly LE, Witherden IR, Tetley TD. Human Airway Inflammation, Sampling Techniques and Analytical Protocols. *Methods Mol Medicine*. 2001;56:137-146. doi:10.1385/1-59259-151-5:137

129. Kemp SJ, Thorley AJ, Gorelik J, et al. Immortalization of Human Alveolar Epithelial Cells to Investigate Nanoparticle Uptake. *Am J Resp Cell Mol*. 2008;39(5):591-597. doi:10.1165/rcmb.2007-0334oc

130. Alogna A, Schwarzl M, Manninger M, et al. Acute stimulation of the soluble guanylate cyclase does not impact on left ventricular capacitance in normal and hypertrophied porcine hearts in vivo. *Am J Physiol-heart C*. 2018;315(3):H669-H680. doi:10.1152/ajpheart.00510.2017

131. Mauro VD, Iafisco M, Salvarani N, et al. Bioinspired negatively charged calcium phosphate nanocarriers for cardiac delivery of MicroRNAs. *Nanomedicine-uk*. 2016;11(8):891-906. doi:10.2217/nnm.16.26

132. Iafisco M, Esposti LD, Ramírez-Rodríguez GB, et al. Fluoride-doped amorphous calcium phosphate nanoparticles as a promising biomimetic material for dental remineralization. *Sci Rep-uk*. 2018;8(1):17016. doi:10.1038/s41598-018-35258-x

133. Ou S-F, Chiou S-Y, Ou K-L. Phase transformation on hydroxyapatite decomposition. *Ceram Int*. 2013;39(4):3809-3816. doi:10.1016/j.ceramint.2012.10.221

134. Guo Y. Handbook of Stability Testing in Pharmaceutical Development, Regulations, Methodologies, and Best Practices. Published online 2009:241-261. doi:10.1007/978-0-387-85627-8_12

135. Esposti LD, Dotti A, Adamiano A, et al. Calcium Phosphate Nanoparticle Precipitation by a Continuous Flow Process: A Design of an Experiment Approach. *Crystals*. 2020;10(10):953. doi:10.3390/cryst10100953

136. Richards JM, Kunitake JAMR, Hunt HB, et al. Crystallinity of hydroxyapatite drives myofibroblastic activation and calcification in aortic valves. *Acta Biomater*. 2018;71:24-36. doi:10.1016/j.actbio.2018.02.024

137. Weiner S, Bar-Yosef O. States of preservation of bones from prehistoric sites in the Near East: A survey. *J Archaeol Sci*. 1990;17(2):187-196. doi:10.1016/0305-4403(90)90058-d

138. Rey C, Combes C, Drouet C, Glimcher MJ. Bone mineral: update on chemical composition and structure. *Osteoporosis Int*. 2009;20(6):1013-1021. doi:10.1007/s00198-009-0860-y

139. Delgado-López JM, Iafisco M, Rodríguez I, Tampieri A, Prat M, Gómez-Morales J. Crystallization of bioinspired citrate-functionalized nanoapatite with tailored carbonate content. *Acta Biomater*. 2012;8(9):3491-3499. doi:10.1016/j.actbio.2012.04.046

140. Lamarche Y, Malo O, Thorin E, et al. Inhaled but not intravenous milrinone prevents pulmonary endothelial dysfunction after cardiopulmonary bypass. *J Thorac Cardiovasc Surg*. 2005;130(1):83-92. doi:10.1016/j.jtcvs.2004.09.011

141. Kozlowski LP. IPC – Isoelectric Point Calculator. *Biol Direct*. 2016;11(1):55. doi:10.1186/s13062-016-0159-9

142. Frisken BJ. Revisiting the method of cumulants for the analysis of dynamic light-scattering data. *Appl Optics*. 2001;40(24):4087. doi:10.1364/ao.40.004087

143. Filipe V, Hawe A, Jiskoot W. Critical Evaluation of Nanoparticle Tracking Analysis (NTA) by NanoSight for the Measurement of Nanoparticles and Protein Aggregates. *Pharmaceut Res*. 2010;27(5):796-810. doi:10.1007/s11095-010-0073-2

144. Carpenter DK. Dynamic Light Scattering with Applications to Chemistry, Biology, and Physics (Berne, Bruce J.; Pecora, Robert). *J Chem Educ*. 1977;54(10):A430. doi:10.1021/ed054pa430.1

145. Sokolova V, Ludwig A-K, Hornung S, et al. Characterisation of exosomes derived from human cells by nanoparticle tracking analysis and scanning electron microscopy. *Colloids Surfaces B Biointerfaces*. 2011;87(1):146-150. doi:10.1016/j.colsurfb.2011.05.013

146. Modi S, Anderson BD. Determination of Drug Release Kinetics from Nanoparticles: Overcoming Pitfalls of the Dynamic Dialysis Method. *Mol Pharmaceut*. 2013;10(8):3076-3089. doi:10.1021/mp400154a

147. Bruschi ML. *Strategies to Modify the Drug Release from Pharmaceutical Systems*. Vol 5. (Elsevier, ed.).; 2015. doi:10.1016/b978-0-08-100092-2.00005-9

148. Duret C, Wauthoz N, Sebti T, Vanderbist F, Amighi K. Solid dispersions of itraconazole for inhalation with enhanced dissolution, solubility and dispersion properties. *Int J Pharmaceut*. 2012;428(1-2):103-113. doi:10.1016/j.ijpharm.2012.03.002

149. Rahimpour Y, Kouhsoltani M, Hamishehkar H. Alternative carriers in dry powder inhaler formulations. *Drug Discov Today*. 2014;19(5):618-626. doi:10.1016/j.drudis.2013.11.013

150. Dormenval C, Lokras A, Cano-Garcia G, et al. Identification of Factors of Importance for Spray Drying of Small Interfering RNA-Loaded Lipidoid-Polymer Hybrid Nanoparticles for Inhalation. *Pharmaceut Res*. 2019;36(10):142. doi:10.1007/s11095-019-2663-y

151. LeClair DA, Cranston ED, Xing Z, Thompson MR. Optimization of Spray Drying Conditions for Yield, Particle Size and Biological Activity of Thermally Stable Viral Vectors. *Pharmaceut Res*. 2016;33(11):2763-2776. doi:10.1007/s11095-016-2003-4

152. Forbes RT, Davis KG, Hindle M, Clarke JG, Maas J. Water vapor sorption studies on the physical stability of a series of spray-dried protein/sugar powders for inhalation. *J Pharm Sci*. 1998;87(11):1316-1321. doi:10.1021/js9800811

153. Maa Y-F, Nguyen P-A, Andya JD, et al. Effect of Spray Drying and Subsequent Processing Conditions on Residual Moisture Content and Physical/Biochemical Stability of Protein Inhalation Powders. *Pharmaceut Res*. 1998;15(5):768-775. doi:10.1023/a:1011983322594

154. Armstrong RA. When to use the Bonferroni correction. *Ophthal Physl Opt*. 2014;34(5):502-508. doi:10.1111/opo.12131

155. Kim H-Y. Statistical notes for clinical researchers: post-hoc multiple comparisons. *Restor Dent Endod*. 2015;40(2):172-176. doi:10.5395/rde.2015.40.2.172

156. Islam MA, Barua S, Barua D. A multiscale modeling study of particle size effects on the tissue penetration efficacy of drug-delivery nanoparticles. *Bmc Syst Biol*. 2017;11(1):113. doi:10.1186/s12918-017-0491-4

157. Wang Y, Beck-Broichsitter M, Yang M, Rantanen J, Bohr A. Investigation of nanocarriers and excipients for preparation of nanoembedded microparticles. *Int J Pharmaceut*. 2017;526(1-2):300-308. doi:10.1016/j.ijpharm.2017.05.008

158. Mudalige T, Qu H, Haute DV, Ansar SM, Paredes A, Ingle T. Nanomaterials for Food Applications. Published online 2019:313-353. doi:10.1016/b978-0-12-814130-4.00011-7

159. Keil TWM, Feldmann DP, Costabile G, Zhong Q, Rocha S da, Merkel OM. Characterization of spray dried powders with nucleic acid-containing PEI nanoparticles. *Eur J Pharm Biopharm*. 2019;143:61-69. doi:10.1016/j.ejpb.2019.08.012

160. Belotti S, Rossi A, Colombo P, et al. Spray dried amikacin powder for inhalation in cystic fibrosis patients: A quality by design approach for product construction. *Int J Pharmaceut*. 2014;471(1-2):507-515. doi:10.1016/j.ijpharm.2014.05.055

161. Belotti S, Rossi A, Colombo P, et al. Spray-dried amikacin sulphate powder for inhalation in cystic fibrosis patients: The role of ethanol in particle formation. *Eur J Pharm Biopharm*. 2015;93:165-172. doi:10.1016/j.ejpb.2015.03.023

162. Vehring R. Pharmaceutical Particle Engineering via Spray Drying. *Pharmaceut Res*. 2008;25(5):999-1022. doi:10.1007/s11095-007-9475-1

163. Peng T, Zhang X, Huang Y, et al. Nanoporous mannitol carrier prepared by non-organic solvent spray drying technique to enhance the aerosolization performance for dry powder inhalation. *Sci Rep-uk*. 2017;7(1):46517. doi:10.1038/srep46517

164. Littringer EM, Mescher A, Schroettner H, Achelis L, Walzel P, Urbanetz NA. Spray dried mannitol carrier particles with tailored surface properties – The influence of carrier surface roughness and shape. *Eur J Pharm Biopharm*. 2012;82(1):194-204. doi:10.1016/j.ejpb.2012.05.001

165. Boel E, Koekoekx R, Dedroog S, et al. Unraveling Particle Formation: From Single Droplet Drying to Spray Drying and Electrospraying. *Pharm*. 2020;12(7):625. doi:10.3390/pharmaceutics12070625

166. Muddana HS, Morgan TT, Adair JH, Butler PJ. Photophysics of Cy3-Encapsulated Calcium Phosphate Nanoparticles. *Nano Lett*. 2009;9(4):1559-1566. doi:10.1021/nl803658w

167. Höistad M, Chen KC, Nicholson C, Fuxe K, Kehr J. Quantitative dual-probe microdialysis: evaluation of [3H]mannitol diffusion in agar and rat striatum. *J Neurochem*. 2002;81(1):80-93. doi:10.1046/j.1471-4159.2002.00791.x

168. Gomez M, McCollum J, Wang H, et al. Development of a formulation platform for a spray-dried, inhalable tuberculosis vaccine candidate. *Int J Pharmaceut*. Published online 2020:120121. doi:10.1016/j.ijpharm.2020.120121

169. Tsapis N, Dufresne ER, Sinha SS, et al. Onset of Buckling in Drying Droplets of Colloidal Suspensions. *Phys Rev Lett*. 2005;94(1):018302. doi:10.1103/physrevlett.94.018302

170. Marty G, Tsapis N. Monitoring the buckling threshold of drying colloidal droplets using water-ethanol mixtures. *European Phys J E*. 2008;27(2):213. doi:10.1140/epje/i2008-10375-6

171. Kwon Y-B, Kang J-H, Han C-S, Kim D-W, Park C-W. The Effect of Particle Size and Surface Roughness of Spray-Dried Bosentan Microparticles on Aerodynamic Performance for Dry Powder Inhalation. *Pharm*. 2020;12(8):765. doi:10.3390/pharmaceutics12080765

172. Wang H, Nobes DS, Vehring R. Particle Surface Roughness Improves Colloidal Stability of Pressurized Pharmaceutical Suspensions. *Pharmaceut Res*. 2019;36(3):43. doi:10.1007/s11095-019-2572-0

173. Chew NYK, Tang P, Chan H-K, Raper JA. How Much Particle Surface Corrugation Is Sufficient to Improve Aerosol Performance of Powders? *Pharmaceut Res*. 2005;22(1):148-152. doi:10.1007/s11095-004-9020-4

174. Candioti LV, Zan MMD, Cámara MS, Goicoechea HC. Experimental design and multiple response optimization. Using the desirability function in analytical methods development. *Talanta*. 2014;124:123-138. doi:10.1016/j.talanta.2014.01.034

175. Sosnik A, Seremeta KP. Advantages and challenges of the spray-drying technology for the production of pure drug particles and drug-loaded polymeric carriers. *Adv Colloid Interfac*. 2015;223:40-54. doi:10.1016/j.cis.2015.05.003

176. You Y, Zhao M, Liu G, Tang X. Physical characteristics and aerosolization performance of insulin dry powders for inhalation prepared by a spray drying method. *J Pharm Pharmacol*. 2007;59(7):927-934. doi:10.1211/jpp.59.7.0003

177. Elversson J, Millqvist-Fureby A. Particle size and density in spray drying—effects of carbohydrate properties. *J Pharm Sci*. 2005;94(9):2049-2060. doi:10.1002/jps.20418

178. Datta S, Grant DJW. Crystal structures of drugs: advances in determination, prediction and engineering. *Nat Rev Drug Discov*. 2004;3(1):42-57. doi:10.1038/nrd1280

179. Kou X, Chan LW, Steckel H, Heng PWS. Physico-chemical aspects of lactose for inhalation. *Adv Drug Deliver Rev*. 2012;64(3):220-232. doi:10.1016/j.addr.2011.11.004

180. Kaialy W, Martin GP, Ticehurst MD, Momin MN, Nokhodchi A. The enhanced aerosol performance of salbutamol from dry powders containing engineered mannitol as excipient. *Int J Pharmaceut*. 2010;392(1-2):178-188. doi:10.1016/j.ijpharm.2010.03.057

181. Botez CE, Stephens PW, Nunes C, Suryanarayanan R. Crystal structure of anhydrous δ-D-mannitol. *Powder Diffr*. 2003;18(3):214-218. doi:10.1154/1.1582460

182. Cares-Pacheco MG, Vaca-Medina G, Calvet R, et al. Physicochemical characterization of d-mannitol polymorphs: The challenging surface energy determination by inverse gas chromatography in the infinite dilution region. *Int J Pharmaceut*. 2014;475(1-2):69-81. doi:10.1016/j.ijpharm.2014.08.029

183. Smith RR, Shah UV, Parambil JV, Burnett DJ, Thielmann F, Heng JYY. The Effect of Polymorphism on Surface Energetics of D-Mannitol Polymorphs. *Aaps J*. 2017;19(1):103-109. doi:10.1208/s12248-016-9978-y

184. Hulse WL, Forbes RT, Bonner MC, Getrost M. The characterization and comparison of spray-dried mannitol samples. *Drug Dev Ind Pharm*. 2009;35(6):712-718. doi:10.1080/03639040802516491

185. Raut DilipM, Mahajan T, K.V.Pavan, Allada R, Deshpande G, Patil DP and A. WATER AND TEMPERATURE INDUCED POLYMORPHIC TRANSFORMATIONS OF MANNIT. *International Journal of Current Research*. Published online 2011.

186. CLARK AR, HOLLINGWORTH AM. The Relationship Between Powder Inhaler Resistance and Peak Inspiratory Conditions in Healthy Volunteers — Implications for In Vitro Testing. *J Aerosol Medicine*. 1993;6(2):99-110. doi:10.1089/jam.1993.6.99

187. Hickey AJ, Mansour HM, Telko MJ, et al. Physical characterization of component particles included in dry powder inhalers. II. Dynamic characteristics. *J Pharm Sci*. 2007;96(5):1302-1319. doi:10.1002/jps.20943

188. Hao T. Understanding empirical powder flowability criteria scaled by Hausner ratio or Carr index with the analogous viscosity concept. *Rsc Adv*. 2015;5(70):57212-57215. doi:10.1039/c5ra07197f

189. Seville PC, Learoyd TP, Li H-Y, Williamson IJ, Birchall JC. Amino acid-modified spray-dried powders with enhanced aerosolisation properties for pulmonary drug delivery. *Powder Technol*. 2007;178(1):40-50. doi:10.1016/j.powtec.2007.03.046

190. Rauscher(1) H, Roebben(2 G, 3), et al. *An Overview of Concepts and Terms Used in the European Commission's Definition of Nanomaterial*.; 2019.

191. Sweeney S, Leo BF, Chen S, et al. Pulmonary surfactant mitigates silver nanoparticle toxicity in human alveolar type-I-like epithelial cells. *Colloids Surfaces B Biointerfaces*. 2016;145:167-175. doi:10.1016/j.colsurfb.2016.04.040

192. Thorley AJ, Ford PA, Giembycz MA, Goldstraw P, Young A, Tetley TD. Differential Regulation of Cytokine Release and Leukocyte Migration by Lipopolysaccharide-Stimulated Primary Human Lung Alveolar Type II Epithelial Cells and Macrophages. *J Immunol*. 2007;178(1):463-473. doi:10.4049/jimmunol.178.1.463